Droplet-based giant unilamellar vesicles as a tool for pore-spanning membrane preparation and transmembrane protein reconstitution

Dissertation

for the award of the degree

Doctor rerum naturalium

of the Georg-August-Universität Göttingen

within the doctoral program

IMPRS for Physics of Biological and Complex Systems

submitted by

Kristina Kramer

from Leer

Göttingen 2022

Members of the thesis committee

Prof. Dr. Claudia Steinem
Institute of Organic and Biomolecular Chemistry,
Georg-August-Universität Göttingen

Prof. Dr. Helmut Grubmüller
Theoretical and Computational Biophysics
Max Planck Institute for Biophysical Chemistry Göttingen

Prof. Dr. Nils Brose
Molecular Neurobiology
Max-Planck Institute of Experimental Medicine Göttingen

Members of the examination board

Prof. Dr. Claudia Steinem
Institute of Organic and Biomolecular Chemistry,
Georg-August-Universität Göttingen

Prof. Dr. Helmut Grubmüller
Theoretical and Computational Biophysics
Max Planck Institute for Biophysical Chemistry Göttingen

Prof. Dr. Nils Brose
Molecular Neurobiology
Max-Planck Institute of Experimental Medicine Göttingen

Prof. Dr. Peter J. Walla
Institute of Physical and Theoretical Chemisty
Technische Universität Braunschweig

Prof. Dr. Burkhard Geil
Institute of Physical Chemistry
Georg-August-Universität Göttingen

Jun.-Prof. Dr. Nadja A. Simeth
Institute of Organic and Biomolecular Chemistry
Georg-August-Universität Göttingen

Date of Oral Examination: 22nd April 2022

Declaration

I, Kristina Kramer,

hereby certify that my doctoral thesis entitled "Droplet-based giant unilamellar vesicles as a tool for pore-spanning membrane preparation and transmembrane protein reconstitution" has been written independently and with no other sources and aids than quoted.

Göttingen 2022   _____   _____
                              (Date)   (Kristina Kramer)

Abstract. Model membranes represent a central tool to decipher complex processes of living cells. Giant unilamellar vesicles (GUVs) are of particular interest as they are cell-like in size, observable with optical microscopy and starting point for the formation of pore-spanning membranes (PSMs). The latter combines merits of solid-supported and free-standing membranes as they provide high stability, separate two aqueous compartments and offer optimal conditions for studying e.g. transmembrane proteins. Thus, developing strategies for GUV production and simultaneous protein reconstitution under physiological conditions is of great interest. In this work, droplet-based microfluidics were employed as a tool for producing droplet-stabilized GUVs (dsGUVs) by encapsulation of large unilamellar vesicles (LUVs) in water-in-oil droplets. Subsequent de-emulsification allowed to release GUVs in an aqueous phase. Basically, a defined interplay of surfactants, ions and lipids was found to be essential for dsGUV assembly. It was shown that the method ensures flexible choice of the constituents allowing to adjust physiological conditions. Moreover, microfluidic-GUVs served for the formation of PSMs. Investigating the biophysical properties like lipid mobility and mechanics of microfluidic-derived membranes revealed that the lipid diffusion coefficient and bending modulus were unaltered compared to membranes derived from electroformation. In contrast, the lateral membrane tension of microfluidic-PSMs was found to be 1.5-fold decreased suggesting an impact of residual surfactants in the membranes. Moreover, reconstitution of two model transmembrane proteins ($TF_O F_1$ ATP synthase, synaptobrevin 2) in (ds)GUVs was probed. Initial detergent-mediated reconstitution in LUVs revealed that the choice of detergent influences the success of the following dsGUV assembly from the proteo-LUVs. Analysing the protein activity and reconstitution efficiency revealed loss of the reconstituted proteins during the microfluidic preparation and de-emulsification. Thus, the microfluidic approach appears to be promising for GUV production under biomimetic conditions, yet the reconstitution of proteins requires further adaptions. Besides, activity of $TF_O F_1$ was characterized in depth after functional reconstitution in LUVs by luminescence-based ATP synthesis assays as a function of the applied ΔpH across the lipid bilayer and thus of the proton motive force (pmf). Resulting turnover rates ranged from $0.042\,s^{-1}$ to $13.0\,s^{-1}$. Quantification of the acidification step of the ATP synthesis assay (required to generate the pmf) was performed by a pyranine-based proton influx assay and revealed incomplete acidification of the intravesicular volume. Hereby, it was shown that misinterpretation of the pmf and thus the protein activity may occur by applying common acid-base transition.

Zusammenfassung. Modellmembranen sind ein zentrales Instrument zur Entschlüsselung komplexer Prozesse lebender Zellen. Riesige unilamellare Vesikel (*giant unilamellar vesicles*, GUVs) sind von besonderem Interesse, da sie eine zellähnliche Größe haben, mit optischer Mikroskopie beobachtet werden können und Ausgangspunkt für Porenüberspannende Membranen (*pore-spanning membranes*, PSMs) sind. Letztere vereinen die Vorzüge von festkörperunterstützten und freistehenden Membranen, da sie eine hohe Stabilität aufweisen, zwei wässrige Kompartimente trennen und optimale Bedingungen für die Untersuchung von z.B. Transmembranproteinen bieten. Daher ist die Entwicklung von Strategien für die GUV-Produktion und Rekonstitution von Proteinen unter physiologischen Bedingungen von großem Interesse. In dieser Arbeit wurden tropfenstabilisierte GUVs (*droplet-stabilized* GUVs, dsGUVs) ausgehend von großen unilamellaren Vesikeln (*large unilamellar vesicles*, LUVs) mittels tropfenbasierter Mikrofluidik hergestellt. Durch anschließende Demulgierung konnten die GUVs in eine wässrigen Phase freigesetzt werden. Es wurde festgestellt, dass ein definiertes Zusammenspiel von Tensiden (*Surfactants*), Ionen und Lipiden für die dsGUV-Assemblierung von wesentlicher Bedeutung ist. Die genutzte Methode ermöglichte eine flexible Auswahl der Lipide und Pufferbestandteile und damit das beibehalten physiologischer Bedingungen während der gesamten Präparation. Außerdem dienten mikrofluidische GUVs zur Hestellung von PSMs. Die Untersuchung der diffusiven und biomechanischen Eigenschaften der mikrofluidischen Membranen ergab, dass sowohl der Lipiddiffusionskoeffizient als auch der Biegemodul im Vergleich zu den durch Elektroformation hergestellten Membranen unverändert blieben. Im Gegensatz dazu wurde festgestellt, dass die laterale Membranspannung von mikrofluidischen PSMs um das 1,5-fache verringert war, was auf einen Einfluss von *surfactant*-Rückständen in der Membran hindeutet. Außerdem wurde die Rekonstitution von zwei Modell-Transmembranproteinen ($TF_O F_1$ ATP-Synthase, Synaptobrevin 2) in (ds)GUVs untersucht. Die vorherige Detergensvermittelte Rekonstitution in LUVs zeigte, dass die Wahl des Detergens den Erfolg der anschließenden dsGUV-Assemblierung ausgehend von Proteo-LUVs beeinflusst. Die Analyse der Proteinaktivität und der Rekonstitutionseffizienz machte einen Verlust der rekonstituierten Proteine während der mikrofluidischen Präparation und der Demulgierung deutlich. Der mikrofluidische Ansatz scheint vielversprechend für die GUV-Produktion unter biomimetischen Bedingungen zu sein, jedoch erfordert die Rekonstitution von Proteinen weitere Anpassungen. Außerdem wurde die Aktivität der $TF_O F_1$ ATP synthase nach der funktionellen Rekonstitution in LUVs durch

lumineszenzbasierte ATP-Synthese*assays* als Funktion des angelegten ΔpH über der Membran und damit der protonenmotorischen Kraft (*proton motive force*, *pmf*) eingehend charakterisiert. Die resultierenden Umsatzraten reichten von $0{,}042\,\mathrm{s}^{-1}$ bis $13{,}0\,\mathrm{s}^{-1}$. Die Quantifizierung des Azidifizierungsschritts des ATP-Synthese*assays* (der für die Erzeugung der *pmf* erforderlich ist) wurde mit einem auf pyraninbasierten Protoneneinstrom*assay* durchgeführt und ergab eine unvollständige Azidifizierung des intravesikulären Volumens. Hierdurch konnte gezeigt werden, dass eine Fehlinterpretation des *pmf* und damit der Proteinaktivität durch die Anwendung des üblichen Säure-Basen-Übergangs erfolgen kann.

Contents

1 Introduction

1.1 Investigating processes at biological membranes

Biological membranes serve in living systems as permeability barriers, where highly selective protein-mediated substance transport, membrane fusion, enzymatic catalysis and signal transduction take place.[1] Due to the high complexity of the cellular membrane, investigating these processes requires deconstruction of living cells in a top-down fashion or bottom-up assembly of artificial membrane systems. The top-down approach is based on eliminating certain biological components or pathways by knock-out or knock-down mutations of genes.[2,3] In the past, this technique was successfully applied for various aims including biosynthesis of drug precursors or creation of multifunctional materials.[4] In contrast, the bottom-up creation of artificial cells or cell-like systems is less established but of steadily increasing interest in recent years.[5] While top-down deconstruction of living material deals with the high complexity of metabolic and regulatory pathways in living cells, designing synthetic cells or cell-like compartments from scratch allows to focus on a minimal set of biological components.[4] In general, artificial cells are composed of a boundary (membrane) and a limited number of components featuring for instance metabolism, energy supply and genetic replication, respectively (cf. figure 1.1).[3] It is noteworthy, that artificial cells or cell-like compartments are not inevitably meant to be "alive" but to provide a robust and minimal system for studying individual components and their interplay omitting unwanted interference of metabolic background processes.[2] Moreover, some studies differentiate between entirely artificial cells and semi-artificial cells. The latter contain biological components isolated from living organisms such as DNA, RNA and proteins[3] and are referred to as artificial or synthetic cells in this work.[3] The minimality and robustness of these artificial cells allow a wide variety of applications for instance in biomedical or -technical research.[2] Building-up synthetic cells relies mostly on the preparation of giant unilamellar vesicles as they are cell-like in size ($1\,\mu\mathrm{m}$ to $100\,\mu\mathrm{m}$)[6] and the subsequent encapsulation and reconstitution of genetic information, (transmembrane) proteins and/or cytoskeletal filaments.[7] In particular, mimicking living cells requires reconstitution of proteins for energy supply like ATP synthases that are able to convert electrochemical gradients into ATP.[7] Thereby, photosynthetic artificial organelles equipped with an ATP synthase and a light-driven proton pump encapsulated in GUVs enabled production of proteins

or the polymerization of actin.[8,9] Finally, advanced systems are equiped with a variety of components like for example ion channels, pore-forming or receptor proteins allowing signal transduction, communication or transport of diverse molecules or ions between artificial cells or artificial and living cells, respectively.[4,7,10–12] Moreover, cell-cell connection via gap junctions[13] and cell-cell adhesion via cadherins[14] allow assembly of threedimensional networks and thus the formation of artificial tissues.
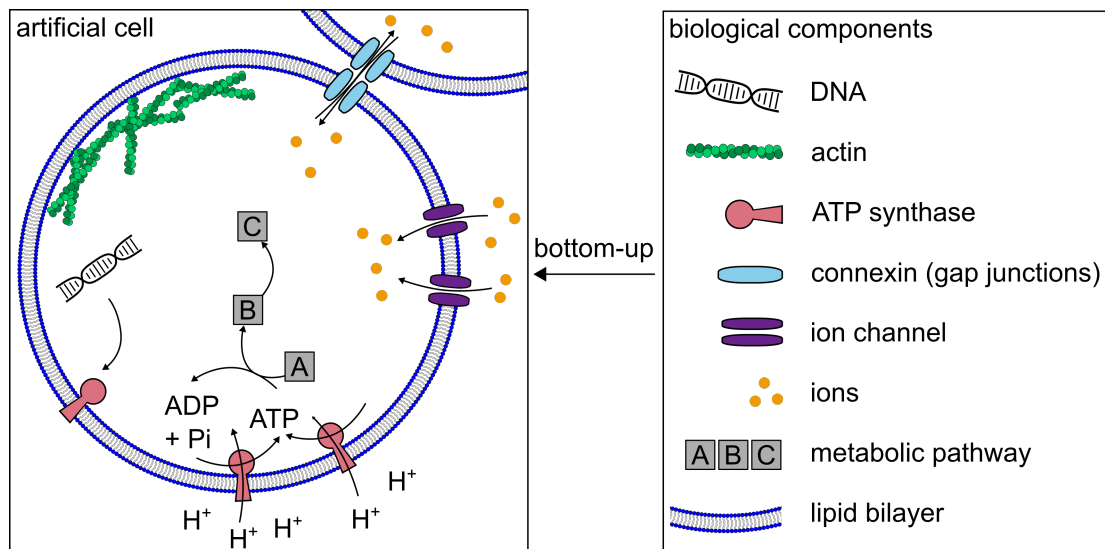
Figure 1.1: Schematic illustration of an artificial cell. Artificial cells are composed of a boundary (membrane) and defined set of further biological components like genetic information, proteins for energy supply or intercellular communication and cytoskeletal components, respectively.

1.2 Model membrane systems

A variety of model membrane systems was established during the past decades allowing quantitative investigation of biological processes at and with lipid bilayers in a defined and biomimetic environment including membrane fusion,[15] cellular organization[16] or transport of ions or molecules,[17] to name a few. This abundance of processes at cellular membranes causes a high research interest for membrane-associated proteins as potential drug targets. For example inhibitors or cytostatics for proton- or ion-pumping transmembrane proteins like Na^+/H^+ echangers are highly discussed in cancer therapy.[18] Therefore, model membranes are an important tool to

analyze impact of drugs on the protein of interest and furthermore membrane-drug interactions.[19]

Investigating cellular processes requires reconstitution of the involved biological components (e.g. proteins) in artificial lipid bilayers. In the following, an overview of selected model membrane systems will be presented with respect to certain merits and drawbacks. Lipid vesicles are one of the most common model membrane systems featuring different sizes and structures. In this work, the focus lies on small, large and giant unilamellar vesicles (SUVs, LUVs, GUVs). Reconstituting proteins isolated from native membranes in SUVs and LUVs ($d_{SUV} \approx 20\,nm$ to $100\,nm$, $d_{LUV} \approx 100\,nm$ to $1\,\mu m$)[20,21] can be performed basically by two different approaches relying both on the use of detergents. Proteins are directly inserted into detergent-destabilized preformed vesicles (direct reconstitution) or proteoliposomes are formed from ternary compositions of lipids, proteins and detergents (mixed micelles). Detergent removal is an essential step in both methods to gain proteoliposomes and can be realized by a variety of procedures like dialysis, size exclusion or polystyrene beads depending on the used detergent and its critical micelle concentration (CMC).[22,23] Direct reconstitution allows to reach a mostly uniform orientation of asymmetric proteins harboring a water-soluble part like $F_O F_1$ ATP synthases (cf. chapter 1.4) as crossing the hydrophobic core of the bilayer is unfavorable for the hydrophilic F_1 unit. In contrast, preparation of proteoliposomes from mixed micelles results in less uniform oriented proteins.[22–26] Due to small vesicle sizes in particular of SUVs the membranes are highly curved and thus subjected to a high tension and in a metastable state.[27] In contrast, the size of GUVs ($d_{GUV} > 1\,\mu m$), being similar to native cells, relieves them from curvature-effects. Moreover, the larger size of GUVs allows to access them with optical microscopy and to micromanipulate them for instance by electrical fields, micropipettes or optical traps.[15,28] Assembling GUVs can be performed on the basis of different materials including phospholipids, block co-polymers, phospholipid-polymere-mixtures (hybrid membranes) and cell-membrane derived components (cf. figure 1.2 A).[29] While usage of phospholipids represents the highest biocompatibility, amphiphilic block co-polymer-based membranes reveal modulated properties like elasticity, lateral mobility or permeability. Altered biophysical behavior of polymer- and hybrid-membranes can be attributed to the increased membrane thickness of $5\,nm$ to $50\,nm$ compared to phospholipid bilayers exhibiting a height of only $3\,nm$ to $5\,nm$.[29] Although the (partial) application of block co-polymers for GUV production improves their stability, the comparability to cellular systems is

greatly reduced.[29] In general, preparation of GUVs and the insertion of (transmembrane) proteins can be realized by a multitude of methods which will be highlighted in greater detail in chapter 1.3. In addition to artificial vesicles, giant plasma membrane vesicles (GPMVs), obtained from so-called membrane blebs, provide a complement to artificial membrane systems for studying cellular membranes and associated processes.[30,31] GPMVs offer the possibility to analyze biochemical and biophysical properties and organization of cellular membranes, however high complexity and lack of compositional control limit the applicability of the system.[30]
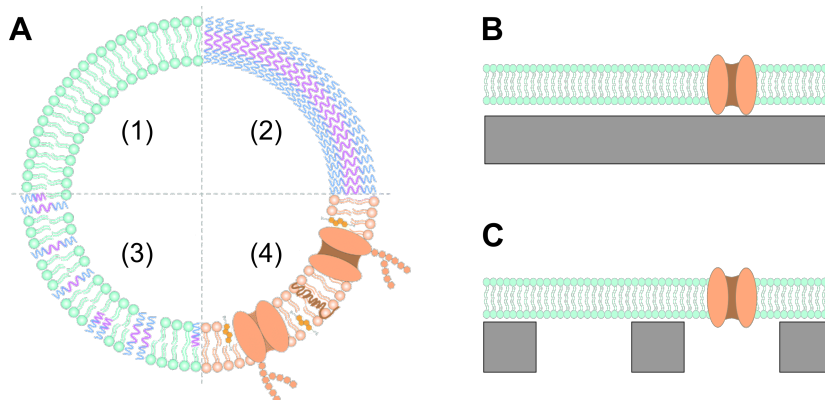
Figure 1.2: Schematic illustration of model membrane systems. A: Giant unilamellar vesicles (GUVs) can be composed of phospholipids (1), amphiphilic block co-polymers (2) or a hybrid composition of the former two components (3). Reconstitution of components extracted from native cells in GUVs or formation of GPMVs (4) enables to investigate protein-associated processes. Figure modified from Lu et al.[29] Spreading (proteo-)LUVs or (proteo-)GUVs allows formation of planar membrane systems like solid-supported lipid bilayers (SLBs, **B**) or pore-spanning membranes (PSMs, **C**).

Another common model membrane system is represented by solid-supported lipid bilayers (SLBs, cf. figure 1.2 B) composed of planar membranes supported by hydrophilic substrate (e.g. glass, silica or mica).[15,16,30] Preparing SLBs relies basically on two techniques: (a) the Langmuir-Blodgett transfer and (b) spreading of vesicles (SUVs, LUVs).[16,30,32] The latter approach is based on adsorption of SUVs or LUVs ($\sim 25\,\mathrm{nm}$ to $100\,\mathrm{nm}$)[16] to the support where they rupture and fuse upon high surface coverage leading to an (almost) defect-free membrane.[16,32] In contrast to free-standing bilayers like GUVs, SLBs offer a high stability upon changing ambient conditions (e.g. solution or temperature) and accessibility with atomic force microscopy (AFM) and surface plasmon resonance (SPR) spectroscopy in addition

to optical microscopy.[30,32] A thin water layer ($\sim 1\,\mathrm{nm}$ to $2\,\mathrm{nm}$) between support and membrane mostly preserves mobility of incorporated components, however diffusion of lipids or proteins can be reduced or even fully prevented due to lipid-surface or protein-surface interactions.[15,33,34] Spreading vesicles on so-called cushions (polymer-functionalized substrates) enhances distance of lipids and support and thus may decrease interactions.[15] A more sophisticated approach combining merits of free-standing GUVs and SLBs are pore-spanning membranes (PSMs, cf. figure 1.2 C). PSMs consist of planar membranes covering an array of highly ordered pores or closed cavities providing accessibility from two sides, good long-term stability, lateral mobility of the lipids and thus represent a promising mimic of native membranes.[35–37] The separation of two compartments allows in contrast to SLBs the entrapment of molecules in atto- to picoliter sized cavities and the investigation of protein- or peptide-mediated transport processes across lipid bilayers in a highly parallel manner.[35,38] Moreover, PSMs serve as a platform to analyze phase behavior of a lipid bilayer,[39] its mechanical properties (e.g. lateral tension, viscoelasticity, bending)[40,41] and SNARE-mediated fusion processes[36,42]. Formation of PSMs requires well-considered surface-functionalizations of the porous substrates providing either a hydrophobic surface of the pore rims for the formation of so-called hybrid-PSMs or a hydrophilic surface serving as support for continous lipid bilayer.[35] Generating PSMs can be performed basically by two different preparational techniques, either by a solvent-mediated lipid painting strategy or by spreading GUVs on a functionalized porous substrate.[35] As the latter offer the possibility for creation of biomimetic solvent-free PSMs, spreading GUVs appears to be the more preferable procedure. Thus, investigating biological processes in PSMs requires their previous reconstitution in GUVs.[42] Production of GUVs with a defined lipid composition and functional insertion of proteins may by an essential bottle-neck that will be tackled in the following chapter in greater detail.

1.3 Protein reconstitution in giant unilamellar vesicles

Among all model membrane systems, the GUV is one of the most promising to mimick living cells and to investigate functions of membrane-associated proteins in a reduced and well-defined environment. To retain functionality of proteins, encapsulation (e.g. cytoskeletal components) or reconstitution (e.g. transmembrane proteins) has to

be conducted under physiological conditions.[7] In the following, an overview of a selection of methods for production of transmembrane protein-containing GUVs will be given with respect to their benefits and drawbacks.
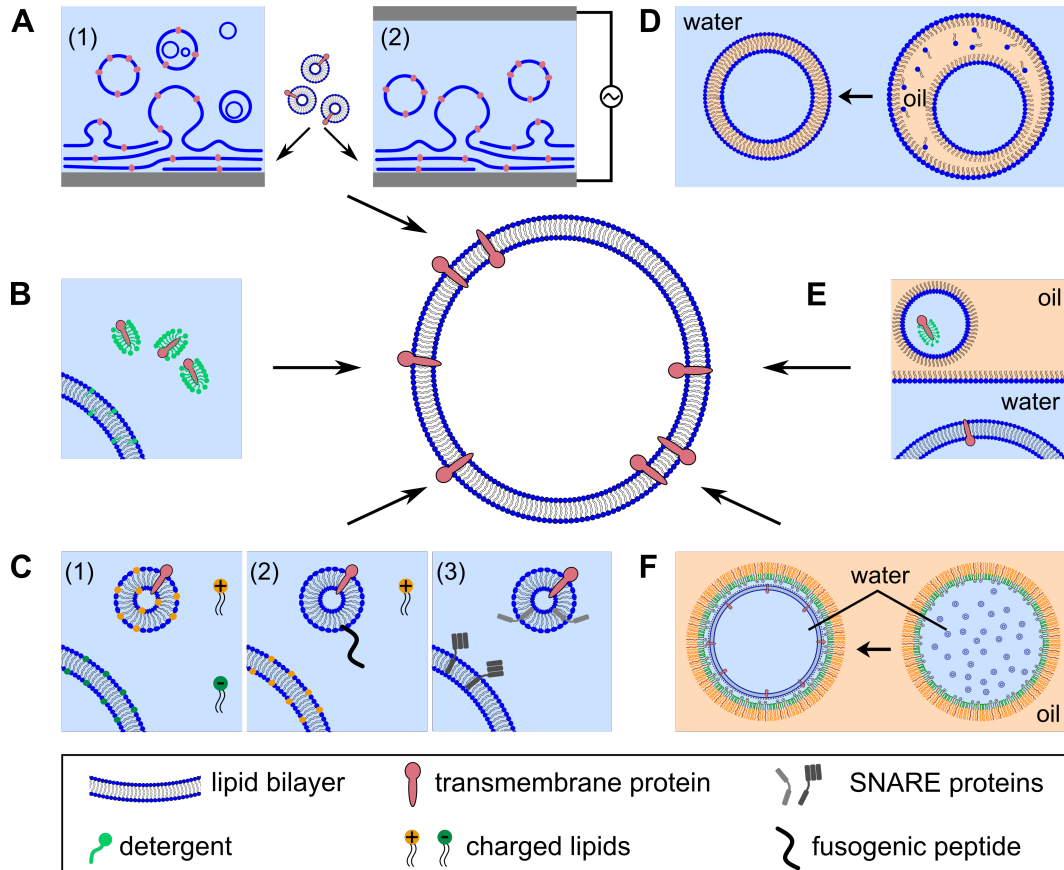
Figure 1.3: Schematic illustration of preparational methods yielding proteo-GUVs. A: The lipid hydration-based approach relies on swelling of dried and layered lipid films yielding partially multilamellar GUVs (gentle hydration, 1). The process can be improved by applying an electric field (electroformation, 2). **B:** During direct (or direct-detergent) based protein reconstitution in GUVs detergent-solubilized proteins are added to GUVs preformed from lipids or lipid-detergent mixtures. **C:** Fusion-based methods like charge-mediated fusion (1), peptide-induced fusion (2) or SNARE-mediated fusion (3) rely on fusion of preformed proteoliposomes and GUVs. **D:** Double-emulsion technigues generate w/o/w emulsions using microfluidic chips. Lipids in the oil phase assemble at the interfaces (monolayers) and form a bilayer upon removal of the volatile oil. **E:** The droplet-transfer method is based on sedimentation of water droplets coated with a lipid monolayer through an oil-water interface spanned a further lipid monolayer resulting in a GUV. Detergent-solubilized proteins can be added either in the water droplet or the bulk solution. **F:** Droplet-based microfluidics rely on formation of surfactant-stabilized droplets. Encapsulated (proteo-)liposomes adhere and spread at a charged interface forming a (proteo-) GUV that can be released in an aqueous enviroment by de-emulsification.[7,43–45]

Most commonly used methods are the lipid hydration- (or swelling-) based approaches (cf. figure 1.3 A). Initially, either drying of lipids dissolved in chloroform or partial dehydration of preformed proteoliposomes on a solid surface (e.g. glass) is required to form stacks of bilayer sheets. Addition of an aqueous solution induces the hydration (or swelling) process by penetration of water in the interlamellar region yielding partially GUVs.[6,7,43] However, this method, called gentle hydration or spontaneous swelling, lacks control about size and lamellarity of the resulting GUVs and presupposes certain conditions like low ionic strength and ideally addition of charged lipids.[6,7] Application of an externally applied electrical field during rehydration of the dried lipid film was found to improve formation of unilamellar vesicles. Performing this method, called electroformation, requires drying of lipid films mostly on conductive indium tin oxide coated glass (or platinum wires) and results in higher yields of more homogenous vesicles. Depending on the exact protocol, electroformation of GUVs may be severely hindered by high ionic strength or charged lipids.[7,43] Reconstitution of two transmembrane proteins, a Ca^{2+} ATPase and bacteriorhodopsin, in GUVs via electroformation was performed by Girard et al. via detergent-mediated production of small proteoliposomes, their partial dehydration on a conductive surface and subsequent rehydration of the bilayer stacks by an externally applied electric field.[46] Various more proteins were reconstituted in GUVs during the past years using optimized electroformation protocols.[36,47,48] However, the critical dehydration step may hamper functional reconstitution especially of complex transmembrane proteins and restrictions concerning buffer and lipid compositions limit the universal applicability of the method.[43] Further approaches for insertion of transmembrane proteins were the direct and direct-detergent mediated reconstitution of proteins in preformed GUVs (cf. figure 1.3 B). While Kreir et al. and Battle et al. incubated detergent-solubilized proteins with GUVs, Dezi et al. produced detergent-destabilized GUVs and subsequently added the respective detergent-solubilized protein. Detergents were removed by addition of polystyrene beads as described previously for protein reconstitution in LUVs.[49–51] Although these detergent-based procedures appear to be simple, resulting instability of GUVs may lead to low yields of proteo-GUVs.[43] Fusion-based approaches rely on charge- or fusogenic peptide-mediated fusion of preformed GUVs and proteoliposomes obtained for example from detergent-mediated reconstitution in SUVs or LUVs (cf. figure 1.3 C).[43] Biner et al. were able to co-reconstitute an ATP synthase and a *bo₃* oxidase in GUVs by electrostatic interactions of oppositely charged lipids incorporated in the

membrane of GUVs and proteoliposomes. However, high amounts of unphysiological positively charged lipids (30 mol%) were required lowering the biocompatibility of the approach.[52] A similar problem is faced by peptide-induced fusion of GUVs and proteoliposomes, in which the negatively charged fusogenic peptides interact with positively charged lipids of the counterpart.[53] Microfluidic double emulsion approaches for GUV production rely on the formation of water droplets encapsulated in an oil phase which again is surrounded by an outer aqueous phase (w/o/w). Lipids dissolved in the oil phase assemble with their hydrophilic headgroups facing to the aqueous phases and with their lipophilic tails pointing towards the oil phase. Thereby, removing the volatile oil yields GUVs. However, residual amounts of oil within the bilayer are nearly inevitable and reconstitution of transmembrane proteins remains difficult, both limiting the applicability of the technique.[43,44] Nevertheless, recently established droplet-based microfluidics represent a promising advancement. Surfactant-stabilized water-in-fluorocarbon oil droplets provide a negative net charge at the interface due to the addition of anionic surfactants at which preformed liposomes adhere, spread and fuse yielding a continuous lipid bilayer at the droplet periphery. Resulting dsGUVs can be biofunctionalized by injection of proteoliposomes or water soluble molecules like cytoskeletal components via the so-called picoinjection technology within preformed dsGUVs. Subsequently, the release of GUVs from the oil phase is feasible by de-emulsification.[45,54] In contrast to double emulsion approaches, no trace amounts of residual oil within the released GUVs were found.[45] Thus, droplet-based microfluidics represent a promising approach for the reconstitution and investigation of (transmembrane) proteins in GUVs, their transfer in PSMs and formation of artificial cells.[45] Further techniques like spontanous or SNARE-mediated fusion (cf. figure 1.3 C3), droplet-transfer (cf. figure 1.3 E) or micro-jetting are mentioned here only for the sake of completeness and are limited by trace amounts of oil or solvents in the bilayer, low yields and/or low reconstitution rates.[29,43,44,55] Finally, reconstituting transmembrane proteins requires to consider that many of them exhibit a directional mode of action (e.g. directional transport processes). Thus, control of their orientation in the GUV bilayer is required. While swelling methods most likely lead to a symmetrical orientation, fusion-based reconstitution retains the preferential protein orientation of the small proteoliposomes.[43,51,52] Direct reconstitution in GUVs resembles the equivalent method in LUVs and a preferential orientation can be achieved.[51] Until now, protein orientation in GUVs performed by droplet-based microfluidics was not specified.[45]

1.4 Transmembrane proteins: Structure and function of F-type ATP synthases

Structure of F-type ATP synthases

Adenosine triphosphate (ATP) plays a pivotal role in living cells as it is the main energy currency driving multiple biochemical reactions and processes like membrane transport, mechanical movement and metabolism. Thus, continuous regeneration of ATP from ADP and anorganic phosphate is inevitable. ATP synthesis in native cells is mainly conducted by F-type (or $F_O F_1$) ATP synthases which are ubiquitous and highly conserved among all species.[56] The ATP synthase is driven by the translocation of H^+ or Na^+-ions along their electrochemical gradients as postulated initially from Mitchell.[57] Consequently, coupling to enzymes that are able to produce electrochemical gradients is required.[58]
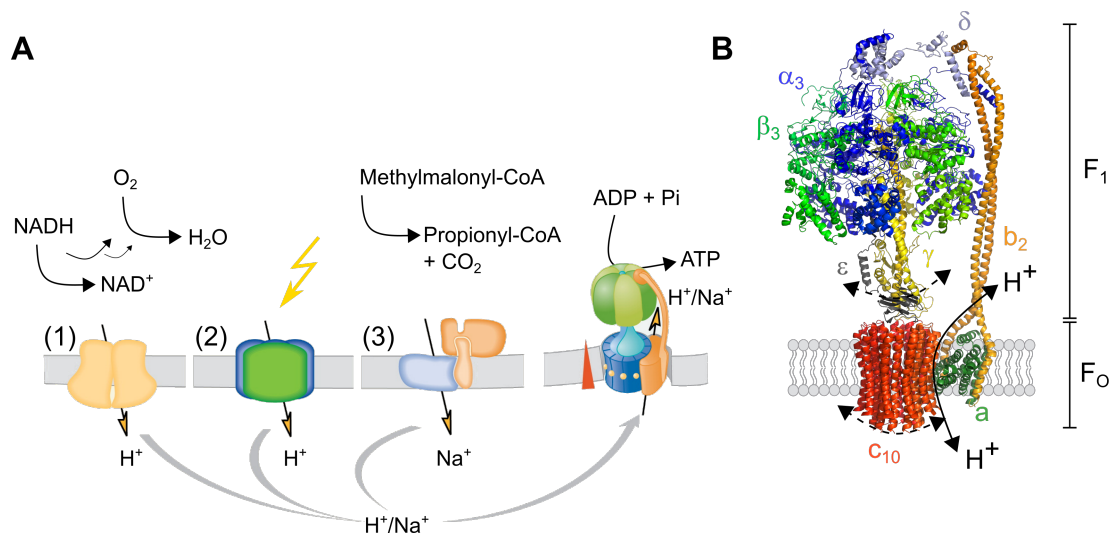
Figure 1.4: Schematic illustration of ion channels coupled to ATP synthases in biological membranes. A: Electrochemical gradients were generated in aerobic bacteria and mitochondria by respiratory chain enzymes (1), in phototrophic bacteria and chloroplasts by photosynthesis (2) and in anaerobic bacteria by decarboxylation reactions. Resulting H^+/Na^+ gradients were utilized by F-type ATP synthases for biosynthesis of ATP. Figure modified from von Ballmoos et al.[58] **B:** Structure of the *E. coli* $F_O F_1$ ATP synthase (PDB: 5T4O) determined by cryo-electron microscopy.[59,60] The protein is assembled from a water-soluble F_1-unit ($\alpha_3\beta_3\gamma\delta\epsilon$, $\sim 380\,kDa$) and a membrane-spanning F_O-unit (ab_2c_{10-15}, $\sim 120\,kDa$). Proton translocation through the c-ring of F_O induces rotation of the γ-stalk and concomitant conformational changes in the catalytically active centers of F_1 causing ATP synthesis.

In mitochondria and aerobic bacteria the metabolism of nutrients yields reducing equivalents which can be used in the respiratory chain to build up a proton gradient. Within the framework of photosynthesis, chloroplasts and phototrophic bacteria are able to transform energy from light into a proton gradient. In contrast, anaerobic bacteria like *Propionigenium modestum* realize formation of electrochemical sodium gradients by decarboxylation reactions (cf. figure 1.4 A).[56,58] The interconversion between energy supplied by ATP and an electrochemical potential is enabled by a defined interplay of the two rotary motors F_O ($ab_2c_{10\text{-}15}$, $\sim 120\,kDa$) and F_1 ($\alpha_3\beta_3\gamma\delta\epsilon$, $\sim 380\,kDa$).[61] Both entities are able to exchange energy by rotational motion. During ATP synthesis, the electrical nanomotor F_O converts the electrochemical gradient in a rotary torque inducing ATP synthesis in the F_1-unit. Vice versa, the chemical nanomotor F_1 is able to convert energy from ATP hydrolysis into a contrary torque inducing active proton transport across the membrane in the reverse direction. In general, F_OF_1 ATP synthases preliminary synthesize instead of hydrolyse ATP since the F_O-nanomotor produces the larger torque under native conditions.[56] Nevertheless, an exceptional case is represented for example by fermenting bacteria using the proton-pumping activity of the protein for generating membrane potentials or for maintaining neutral cytoplasmic pH in alkaline solutions.[62] The overall structure of the F_OF_1 ATP synthase is illustrated in figure A.4 B. The F_1-unit contains a hexamer of alternating α- and β-subunits. The nucleotide binding sites are formed within the three catalytic β-subunits facing towards the surface of the α-subunits. An intrinsic asymmetry is evoked by the interaction of the β-subunits with the rotary γ-stalk. The δ- and ϵ-subunits connect the two entities of the overall protein.[56] Moreover, the *C*-terminal ϵ-domain has a regulatory function and is able to inhibit the ATP hydrolysing activity of the F_1-unit and of the entire F_OF_1-complex by a conformational change and subsequent stretching of its α-helices along γ-subunit and towards the $\alpha_3\beta_3$ hexamer.[56,63] Interestingly, several studies additionally revealed a suppression of the ATP synthesis activity mediated from the *C*-terminal domain of the ϵ-subunit. However, this phenomen is not fully understood until now.[64,65] The membrane embedded F_O-nanomotor consists of the statory subunits a/b_2 and an oligomeric c-ring composed of 10-15 individual subunits depending on the originating species. For instance, the oligomeric c-ring of *Escherichia coli* or *Bacillus* PS3 ATP synthases harbor ten c-monomers. It is assumed that proton (or ion) translocation is performed at the interface of the a- and c-subunits producing the torque applied to the γ-stalk.[56] Connection of the

b-subunits from F_O and the α-subunits from F_1 is mediated via the δ-subunit, while the γ-stalk and the c-ring are connected by the *N*-terminal domain of ϵ.[56,63] The subunits γ, ϵ and $c_{10\text{-}15}$ can be defined as rotary part of the ATP synthase while remaining subunits represent the so-called stator ($\alpha_3\beta_3\delta ab_2$).

Function of the rotary F_1-unit

Proton translocation through the $c_{10\text{-}15}$-ring along the electrochemical gradient induces its rotation which is translated to the γ-stalk. The rotation of the γ-stalk causes conformational changes in the catalytic core of the $\alpha_3\beta_3$ hexamer which results in alternating closing and opening of the catalytic sites in the $\alpha\beta$-subunits and ATP synthesis. Vice versa, ATP hydrolysis induces conformational changes in the $\alpha\beta$-subunits pushing the γ-stalk in the reverse direction.[58,66,67] The binding-change model was developed by studying the intramolecular processes in the F_1-unit during ATP hydrolysis while the mechanism of ATP synthesis was assumed to follow the reverse pathway. A possible scheme for the occupancy of the binding sites within the $\alpha\beta$-subunits of the two reversable processes is illustrated in figure 1.5 A. During ATP hydrolysis (or synthesis) the rotor turns anticlockwise (or clockwise) in steps of $120\,°$ which can be further devided in four substeps. The detailed processes during these substeps are exemplified for the ATP hydrolysis reaction in figure 1.5 B. For the sake of simplicity, the $\alpha\beta$ binding sites will only be referred to as β below. In general, three different conformations are possible: closed (C), half-closed (C') or open (O). In stage 1, the angular position of the γ-stalk is defined to be $0\,°$. β_1 is existent in its open-conformation (O) and devoid of a nucleotide. In the following ATP binding dwell (stages 1-2), ADP is released from β_3 (C') and ATP enters the β_1-site. The latter causes a fast $80\,°$ rotation of the γ-stalk (stages 2-3) inducing conformational changes in β_1 (C) and β_3 (O). During the catalytic dwell (stages 3-4), ATP hydrolysis in β_2 (C) occurs and the remaining phosphate is released from β_3 (O). As a consequence, a $40\,°$ rotation of the γ-stalk happens (stages 4-5) finalizing the aforementioned anticlockwise $120\,°$ rotation. The β_3-site (O) is empty and ready for ATP binding. Further rotation of the γ-stalk by $80\,°$ (overall $200\,°$ rotation) requires hydrolysis of the ATP molecule bound to the β_1-site (C). Stepwise release of respective ADP (C') and phosphate (O) causes a rotation of the γ-stalk to $240\,°$ and $320\,°$. Rotation by $360\,°$ is reached upon hydrolysis of ATP bound to β_3 (C). Thus a total $360\,°$ rotation of the γ-stalk requires hydrolysis of three ATP molecules.[58,67]
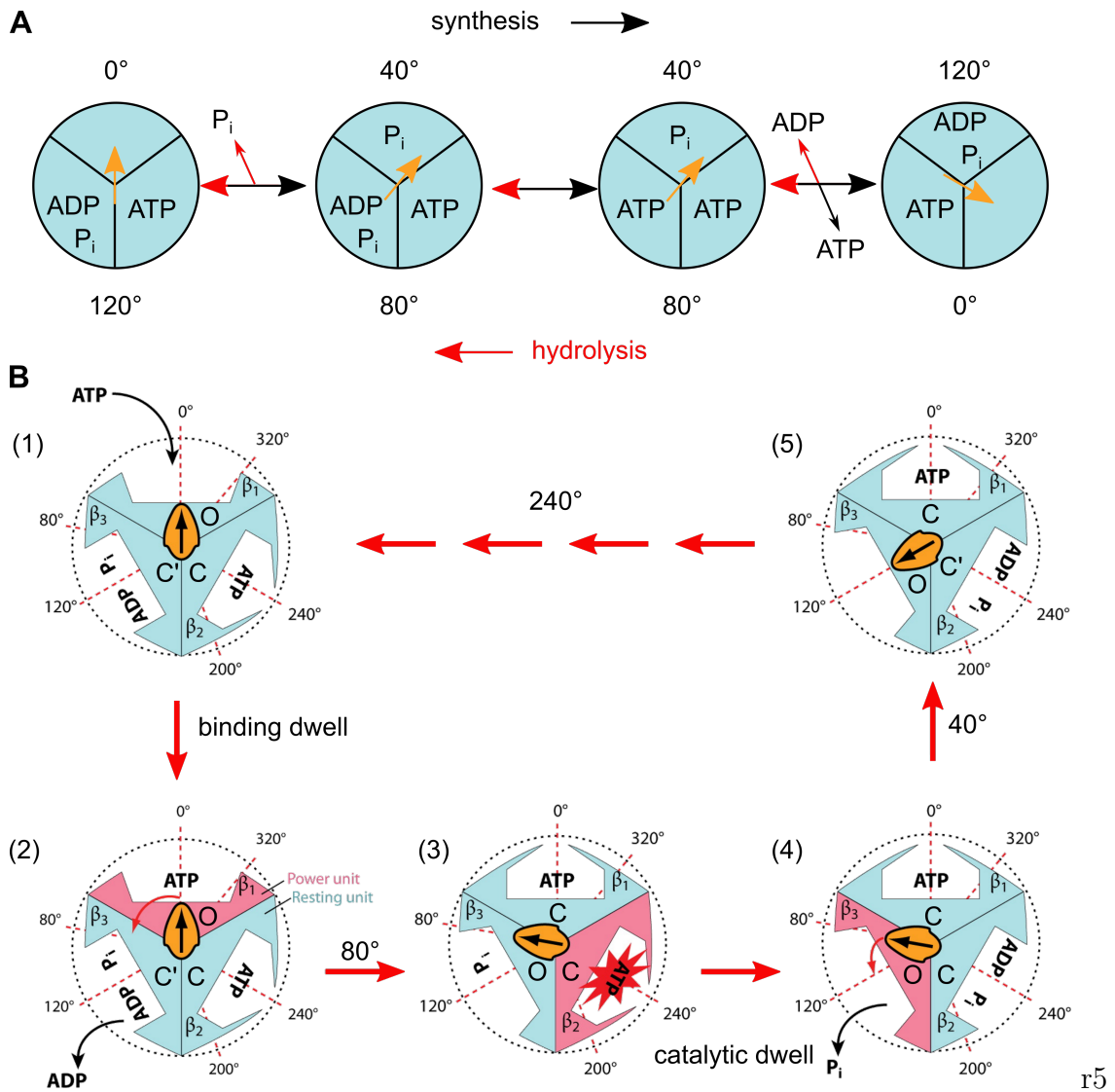
Figure 1.5: Schematic illustration of the binding site occupancy during synthesizing and hydrolyzing activity of F-type ATP synthases. A: Scheme of the mechanism of ATP synthesis (black arrows) or hydrolysis (red arrows). The three αβ-binding sites are shown in light blue and the γ-stalk is represented by an orange arrow indicating its angular orientation. Figure partially adapted from Xu et al.[67] **B:** Detailed illustration of the binding change mechanism of ATP hydrolysis. $β_{1-3}$ represent the αβ-interfaces in their possible conformations: closed (C), half-closed (C'), and open (O). In stage 1, the angular orientation of γ is defined to 0°. ATP binding in $β_1$ and ADP release in $β_3$ occurs during the so-called binding dwell (stage 2-3) inducing 80° rotation of γ. ATP hydrolysis happens during the catalytic dwell (stage 3-4) in $β_2$ followed by release of residual phosphate from $β_3$. Rotation by further 40° completes 120° of γ. Hydrolysis of a particular ATP causes 360° rotation of γ. 0°: ATP binding, 200°: ATP cleavage, 240° and 320°: release of ADP and phosphate and 360°: empty binding site. The figure is modified from von Ballmoos et al.[58] The F_1 unit is displayed from the membrane side in **A** and **B**.

The presented mechanism can be assumed for bacterial (and yeast) ATP synthases. The human variant slightly differs in the angles of the individual substeps, which, however, accumulate as well to rotational steps of $120\,°$.[67]

Function of the rotary F_O-unit

The oligomeric c-ring and its neighboring a- and b-subunits form the F_O-nanomotor. The stoichiometry of the subunits has an essential influence on the bioenergetic properties of the protein as the number of c-subunits predicts the number of protons per $360\,°$ rotation. Thus, the TF_OF_1 ATP synthase from *E. coli* and *Bacillus* PS3 featuring a c_{10}-ring translocates ten protons per total rotation implying an ATP/H^+ ratio of 3.3. The structural basics of proton translocation through the F_O-nanomotor are still elusive.[56,58] However, several charged and highly conserved amino acids like aspartate and glutamate in the c-subunits and arginine in the a-subunits were identified. The most accepted proposal for the mechanism is presented by the two-channel model. It is suggested that the a-subunit has two proton transport pathways (half-channels) each spanning half of the lipid bilayer and thus connecting the proton binding site in the adjacent c-subunits with both sides of the membrane. Briefly, a proton entering the first halfchannel is transported to the c-subunit where it protonates and thus neutralizes a carboxylate residue (Glu or Asp). The uncharged residue allows the c-subunit to move towards the hydrophobic membrane core and thereby induces rotation of the overall c-ring. A neighboring c-subunit enters the second halfchannel where it releases a proton that leaves the half-channel at the opposite membrane side.[66] Rotation of the c-ring is accompanied by rotation of the γ-stalk causing conformational changes in the catalytic αβ hexamer as described above.[56,58]

The proton motive force

ATP production by F-type ATP synthases is driven by the so-called transmembrane electrochemical proton potential $\Delta\tilde{\mu}_{H+}$ which is defined as

$$\Delta\tilde{\mu}_{H+} = F\Delta\psi + RT\ln\left(\frac{[H_p^+]}{[H_n^+]}\right) \tag{1.1}$$

where F is the Faraday constant ($96{,}485\,\mathrm{C\,mol^{-1}}$), R is the molar gas constant ($8.3145\,\mathrm{J\,K^{-1}\,mol^{-1}}$) and T the temperature. The potential difference is mainly

composed of the electrochemical potential $\Delta\psi$ and the gradient between high (p) and low (n) proton concentrations at the two different sides of the membrane. For simplification, however, the proton motive force is employed resulting from dividing $\Delta\tilde{\mu}_{H+}$ by F.[58,68]

$$pmf = \frac{\Delta\tilde{\mu}_{H+}}{F} = \Delta\psi + 2.3\frac{RT}{F}\Delta pH \tag{1.2}$$

At room temperature ($T = 25\,°C$) equation 1.2 can be reduced to $pmf = \Delta\psi + 60 \cdot pH$. ATP synthesis occurs when the energy stored in ΔpH and $\Delta\psi$ is larger than the required Gibbs free energy $G_{ATP} = 50\,kJ\,mol^{-1}$ (with $G^0_{ATP} = 30.5\,kJ\,mol^{-1}$).[69] Considering the stoichiometric ratio H^+/ATP (x) of different ATP synthases, which ranges from 3.3 for the *Bacillus* PS3 protein to 4.7 for the chloroplast protein,[58] the required $\Delta\tilde{\mu}_{H+}$ and pmf can be theoretically determined by equation 1.3.

$$x \cdot \Delta\tilde{\mu}_{H+} = G_{ATP} = G^0_{ATP} + RT\ln\frac{[ATP]}{[ADP] \cdot [P_i]} \tag{1.3}$$

Thus, a $\Delta\tilde{\mu}_{H+}$ between $11\,kJ\,mol^{-1}$ and $15\,kJ\,mol^{-1}$ ($\sim 110\,mV$ to $160\,mV$) can be assumed to be necessary for realizing ATP synthesis. The determined pmf of biological membranes contributing to ATP synthesis amounts to $120\,mV$ to $200\,mV$.[68]

2 Scope of thesis

Understanding complex processes of biological membranes requires the development of simplified model membranes to shed light on the activity and interactions of individual membrane-associated components (e.g. transmembrane proteins). Among all model systems, giant unilamellar vesicles (GUVs) represent particular convenience as they are cell-like in size, observable with optical microscopy and the starting point for producing pore-spanning membranes (PSMs). The latter consists of a lipid bilayer covering an array of ordered pores combining merits of solid-supported and freestanding lipid bilayers and are considered to be well-suited for studying i.e. transport processes across membranes. Both, GUVs and PSMs open up unique opportunities to investigate the activity of transmembrane proteins like ATP synthases.

In recent decades, a variety of methods for GUV production was developed, all of which involve more or less non-physiological conditions. However, reconstituting proteins in artificial membranes under physiological conditions is pivotal to maintain their functionality. In this work, an approach based on the encapsulation of large unilamellar vesicles in water-in-oil droplets (droplet-based microfluidics) and their subsequent charge-mediated spreading and fusion at the droplet periphery will be probed as a tool for formation of protein-containing GUVs. Droplet-stabilized GUVs, which can be released in an aqueous phase by de-emulsification, will be produced under different buffer- and lipid compositions to evaluate the flexibility of this method. Moreover, resulting GUVs will be used as starting point for the formation of PSMs. The biophysical properties like membrane mechanics and lipid mobility of these model membranes will be analyzed using atomic force microscopy, fluorescence recovery after photobleaching and fluorescence correlation sprectroscopy. To assess the feasibility of the microfluidic reconstitution approach two different transmembrane proteins (TF$_O$F$_1$ ATP synthase, synaptobrevin 2) will be employed as model proteins. Functional and efficient reconstitution in GUVs will be analyzed either by activity assays (TF$_O$F$_1$) or by fluorescence-based quantification of the reconstitution efficiency (syb 2) in GUVs. Moreover, the activity of the TF$_O$F$_1$ ATP synthase in LUVs, which are simultaneously employed for dsGUVs production, will be systematically analyzed by means of luminescence-based ATP synthesis assays.

In the future, functional reconstitution of transmembrane proteins like ATP synthases in GUVs will pave the way for fabricating protein-containing PSM or for creating artificial cells allowing *in situ* ATP-production to drive further processes.

3 Materials and methods

3.1 Proteins and biochemical methods

3.1.1 Biossynthetic production of the TF_OF_1 ATP synthase in *Escherichia coli* and purification

Biosynthetic production of the TF_OF_1 ATP synthase

The development of novel artificial membrane systems intended to study protein activities requires stable proteins that are amenable to easy purification. The TF_OF_1 ATP synthase ($530\,kDa$, pI $= 5.8$)[70,71] from the *thermophillic Bacillus* PS3 is a remarkably stable and well studied ATP synthase (physiological temperature of $60\,°C$) consisting of the subunits α, β, γ, δ, ϵ (F1, $356\,kDa$) as well as the subunits a, b and c (F_O, $174\,kDa$).[70,72–75]

The expression system used in this work is based on the work of Suzuki et al. and uses a transformed *Escherichia coli* (*E. coli*) DK8 strain with the pTR-ASDS plasmid encoding for thermophillic F_OF_1 ATPase.[72] The lack of the endogenous ATP synthase subunits in *E. coli* DK8 allows the overproduction and clean purification of the protein of interest.[76] The TF_OF_1 ATPase with its *N*-terminal His$_{10}$-Tag of the three β-subunits was produced and purified according to previous works.[55,77]

Pre-cultures in $30\,L$ terrific broth medium (TB medium) supplied with ampicillin ($100\,\mu g\,mL^{-1}$) were inoculated from cryostocks ($-80\,°C$, $50\,\%$ glycerol) and incubated at $37\,°C$ and $120\,rpm$ over night. TB medium was prepared as described below. The following day, eight main cultures of TB medium ($250\,mL$ each) were supplemented with each $100\,\mu g\,mL^{-1}$ of ampicillin as well as $5\,mL$ of the pre-culture and incubated at $37\,°C$ and $120\,rpm$. The optical density ($\lambda = 600\,nm$, OD_{600}) was monitored over time (cf. figure 3.1 A). $1\,mM$ isopropyl β-D-1-thiogalactopyranosid (IPTG) was added at an OD_{600} of 0.6 to 0.7. When reaching an OD_{600} of 1.7 to 2.0, cells were centrifuged for 15 min at $4\,°C$ and $4{,}000\,g$ and thus harvested. The cell pellets were stored at $-80\,°C$ over night.

Preparation of TB medium

The TB medium ($12\,g\,L^{-1}$ tryptone, $24\,g\,L^{-1}$ yeast extract, $0.4\,\%$ (v/v) glycerol) and TB salts ($23.1\,g\,L^{-1}$ KH_2PO_4, $125.4\,g\,L^{-1}$ K_2HPO_4) were prepared in ultrapure water and autoclaved. Upon reaching room temperature, the TB salts were sterile filtered and added in a ratio of 1:10.
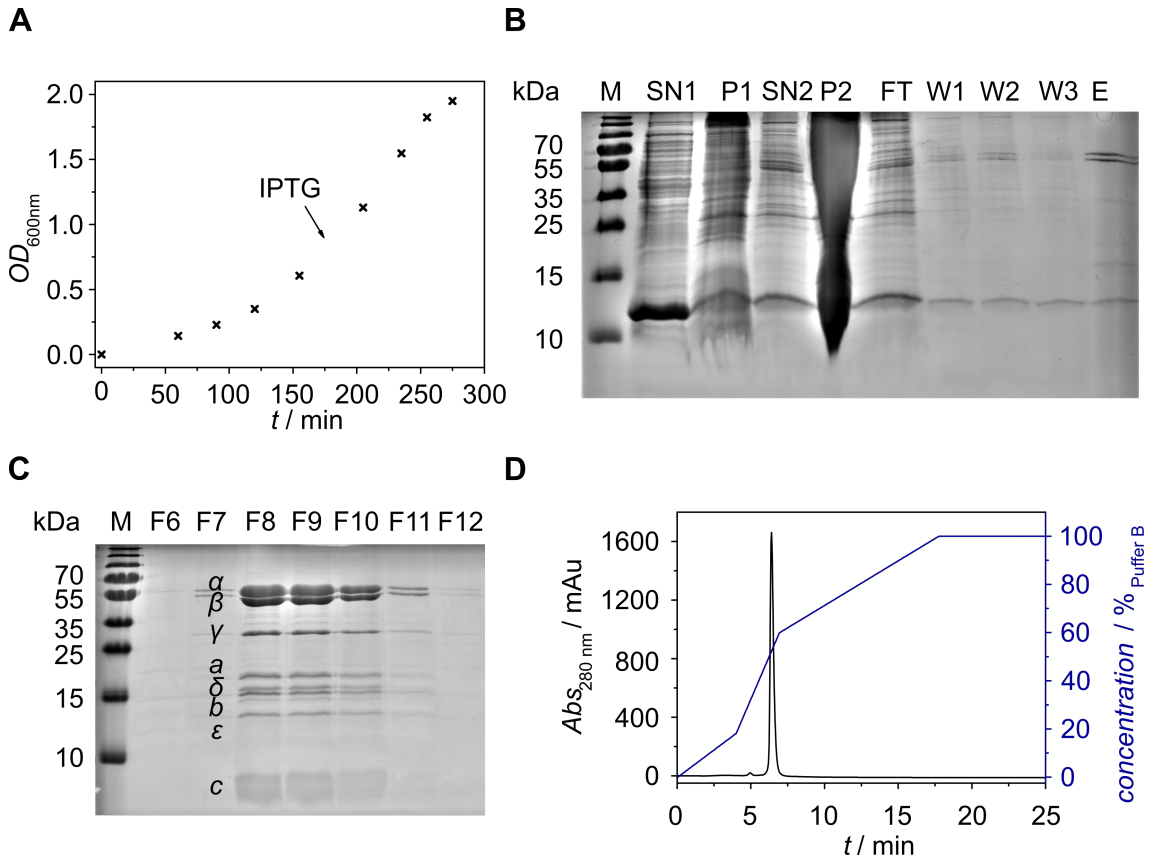
Figure 3.1: Isolation and Purification of the TF_OF_1 ATP synthase. A: Growth curve of *E. coli* DK8 containing the pTR-ASDS plasmid. The OD_{600} was plotted against the time (min). At an OD_{600} of 0.7 the biosynthetic production of the protein was induced by adding of IPTG. Cells were harvested at an OD_{600} of 2.0. **B:** SDS PAGE of the isolation of the TF_OF_1 ATP synthase and purification via Co^{2+} affinity chromatography (IMAC) with M: marker, SN: supernatant, P: pellet, FT: supernatant of the IMAC, W: wash fractions, E: elution fraction. **C:** SDS PAGE of the elution fractions F6 to F12, corresponding to an elution time of 5 to 7 min (elution rate $1\,mL\,min^{-1}$), of the anion exchange chromatography. All subunits of the TF_OF_1 ATP synthase are visible and can be assigned on the basis of the literature.[72] (M: marker). **D:** Anion exchange chromatogram of the elution of the TF_OF_1 ATP synthase and the gradient of buffer B (1 M NaCl). The course of the elution suggests an elution at $52\,\%$ buffer B ($29\,mS\,cm^{-1}$, 616 mM NaCl).

Purification of the TF$_O$F$_1$ ATP synthase

The resuspension of the cell pellets in 150 mL lysis buffer was followed by an incubation of the respective suspension at 37 °C for 30 min. All buffers used for purification are listed in table 3.1. After adding MgCl$_2$ (5 mM) and DNaseI solved in DNase buffer (150 µL) the cell suspension was stirred for 30 min at room temperature. Three cycles (1,000 bar) in an ice-cooled microfluidizer LM10 (Microfluidics, Westwood, USA) were used for the mechanical lysis of the cells. After adding Na$_2$SO$_4$ (150 mM) and sodium cholat (65.8 mM) the suspension was stirred for 20 min at 25 °C. Centrifugation for 30 min at 20,000 g and 4 °C resulted in a supernatant (SN1) and a Pellet (P1). Samples for the SDS PAGE were taken (cf. figure 3.1 B). The supernatant was discarded whereas the pellet was resuspended with HEPES buffer. The suspension was stirred for 45 min at room temperature. A second centrifugation step (20,000 g, 4 °C, 30 min) resulted in a pellet (P2) and a supernatant (SN2) (cf. figure 3.1 B). Purification of the protein from the supernatant was performed via immobilized metal ion chromatography (IMAC) based on Co^{2+} ions. The supernatant was incubated for 2 h at 4 °C with pre-equilibrated TALON Metal Affinity Resin (Clontech, Takara Bio Europe, Saint-Germain-en-Laye, France) while gently mixing on a tube roller. Prior to usage, the TALON Metal Affinity Resin was treated with equilibration buffer. For this purpose, a bed volume of 2.5 mL of the TALON Metal Affinity Resin was resuspended with 25 mL of equilibration buffer and a centrifugation for 2 min at 4 °C was performed. The supernatant was discarded and the previous two steps were repeated once. The incubated resin was then centrifuged for 2 min at 700 g and 4 °C. The supernatant (FT, cf. figure 3.1 B) was removed from the resin and 20 mL of wash buffer were added. The suspension was incubated for 10 min at 4 °C under gentle agitation on a tube roller. The supernatant was separated from the resin by centrifugation (W1, cf. figure 3.1 B) (5 min, 700 g, 4 °C). The washing step was repeated once (W2, cf. figure 3.1 B). To resuspend and transfer the resin in a gravity flow column, 2.5 mL of wash buffer were added. After rinsing with 7.5 mL wash buffer (W3, cf. figure 3.1 B), the TF$_O$F$_1$ ATP synthase was eluted with elution buffer (E, cf. figure 3.1 B). Afterwards, the TALON Metal Affinity Resin was regenerated with 12.5 mL of regeneration buffer, 12.5 mL ultrapure water and stored in 20 % ethanol supplemented with 0.1 % NaN$_3$. Samples were taken from all steps of the IMAC for an SDS PAGE (cf. figure 3.1 B). According to the SDS PAGE, no significant impurities were present in the elution fraction (E, cf. figure 3.1 B). The eluted fraction was dialyzed (molecular weight cut-off of 5 kDa) over night in buffer A at 4 °C.

Table 3.1: List of buffers used for the isolation and purification of the TF$_O$F$_1$ ATP synthase.

lysis buffer	50 mM Tris, 5 mM MgCl$_2$, 0.5 mM EDTA, 1 mg mL^{-1} Lysozym*, 1 tablet/50 mL cOmplete^{TM} protease inhibitor cocktail*, pH 8.0
DNase buffer	20 mM Tris, 1 mM MgCl$_2$, 5 mg mL^{-1} DNase, 50 % glycerol (w/v), pH 7.5
HEPES buffer	20 mM HEPES,100 mM KCl, 20 mM imidazole, 5 mM MgCl$_2$, 1 % (w/v) n-dodecyl-β-D-maltoside(DDM), pH 7.6
wash buffer	20 mM HEPES, 100 mM KCl, 20 mM imidazole, 5 mM MgCl$_2$, 0.08 % (w/v) DDM, pH 7.6
elution buffer MgCl$_2$,	20 mM HEPES, 50 mM KCl, 250 mM imidazole, 5 mM 0.05 % (w/v) DDM, pH 7.4
equilibration buffer	50 mM Na$_3$PO$_4$, 300 mM NaCl, pH 7.4
regeneration buffer	20 mM MES, 300 mM NaCl, pH 5.0
buffer A	20 mM HEPES, 20 mM NaCl, 5 mM MgCl$_2$, 0.05 % (w/v) DDM**, pH 7.4
buffer B	20 mM HEPES, 1 M NaCl, 5 mM MgCl$_2$, 0.05 % (w/v) DDM, pH 7.4
	*added immediately before isolation **omitted for dialysis step

Since the concentration of the eluted sample was low, an anion exchange chromatography with a MonoQ5/50 column (ÄKTA Purifier 10, GE Healthcare Europe, Freiburg, Germany) was required (cf. chapter 3.1.3). A gradient of NaCl was created using buffer A (20 mM) and buffer B (1 M NaCl). The percentage of buffer B (1 M NaCl) was gradually increased for the first four column volumes (1 CV = 1 mL, 1 mL min^{-1}) from 0 to 18 %, for the following three column volumes from 18 to 60 % and for the last eleven column volumes from 60 to 100 %. Protein elution was controlled by the absorption at 280 nm (cf. figure 3.1 D). The TF$_O$F$_1$ ATP synthase eluted at 52 % buffer B (29 mS cm^{-1}, 616 mM NaCl). Running an SDS PAGE of the fractions corresponding to the protein peak (F6 to F12, t = 5 to 7 min) revealed the successful concentration (cf. figure 3.1 C). In addition, all eight subunits of ATP synthase (α,

β, γ, δ, ε, a, b, c) are visible and can be assigned on the basis of the literature.[72] Protein concentration was determined by means of UV/Vis spectroscopy (Nanodrop2000c, Thermo Fisher Scientific, Waltham, USA, chapter 3.1.5). The pooled fractions (F8-F10) of the examplary protein purification, which is shown here, had a concentration of $2.4 \, \mathrm{mg \, mL^{-1}}$ ($4.9 \, \mathrm{\mu M}$).

SDS PAGE according to Laemmli was performed after completion of purification as described in chapter 3.1.4.

3.1.2 Biosynthetic production of Synaptobrevin 2 in *Escherichia coli* and purification

Biosynthetic production of synaptobrevin 2 in *E. coli* and purification

For further investigation of new model membrane systems, simple proteins that do not consist of multiple subunits and are easily accessible for modifications, such as a fluorescent tag, are indispensable. The v-SNARE synaptobrevin 2 with an additional cystein residue on position 117 (1-117 Cys, syb 2) was used for this purpose. The protein is composed of an α-helical transmembrane domain (95-114), an α-helical water soluble domain and a β-sheet (25-28).[78]

Synaptobrevin 2 ($12.8 \, \mathrm{kDa}$, pI = 7.8)[79], originating from *Rattus norvegicus*, was produced in *E. coli* BL21(DE3) as host. The protein was equipped with a $\mathrm{His_6}$-tag and purified analogously to previous works.[79–81] Pre-cultures consisting of $100 \, \mathrm{mL}$ lysogeny broth medium (LB medium) were supplemented with ampicillin ($100 \, \mathrm{\mu g \, mL^{-1}}$), inoculated from cryostocks ($-80 \, \mathrm{°C}$, $50 \, \%$ glycerol) and incubated over night at $37 \, \mathrm{°C}$ and $140 \, \mathrm{rpm}$. LB medium was prepared as described below. The following day, ten main cultures TB medium ($250 \, \mathrm{mL}$ each, prepared as described in chapter 3.1.1) were supplemented with ampicillin ($100 \, \mathrm{\mu g \, mL^{-1}}$) and $5 \, \mathrm{mL}$ of the pre-culture. The main cultures were incubated at $37 \, \mathrm{°C}$ and $140 \, \mathrm{rpm}$ until the OD_{600} amounted to 0.9 (cf. figure 3.2). The protein production started after addition of the inducer $1 \, \mathrm{mM}$ IPTG. The cells were collected by centrifugation ($15 \, \mathrm{min}$, $700 \, g$, $4 \, \mathrm{°C}$) after reaching an OD_{600} of approximately 2.0. The resulting pellets were isolated from the supernatant, resuspended (resuspension buffer), frozen and stored over night at $-80 \, \mathrm{°C}$.

Preparation of LB medium

LB medium was prepared as described in chapter 3.1.1. LB medium, composed of $10\,g\,L^{-1}$ Trypton, $5\,g\,L^{-1}$ yeast extract and $5\,g\,L^{-1}$ NaCl, was prepared in ultrapure water and autoclaved afterwards.

A **B**
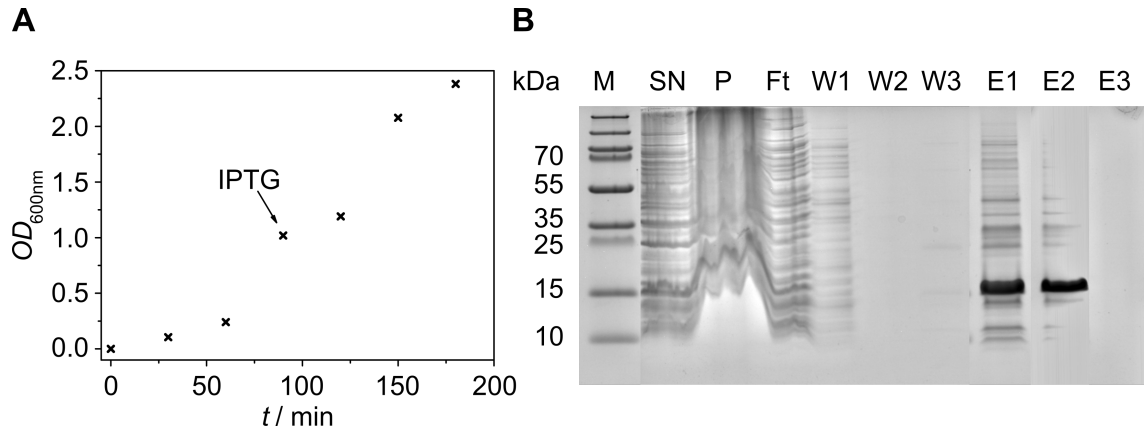
Figure 3.2: Isolation of synaptobrevin 2 (1-117Cys). A: Growth curve *E. coli* BL21(DE3). The OD_{600} is plotted against the time (min). At an OD_{600} of 0.9 the production of syb 2 was induced by supplementing IPTG. Cells were harvested at an OD_{600} of 2.0. **B:** SDS PAGE of the isolation of syb 2 and purification via Ni^{2+} affinity chromatography (IMAC) with M: marker, SN: supernatant, P: pellet, Ft: flowthrough, W1-3: wash fractions, E1-E3: elution fractions.

Isolation of syb 2

The frozen suspension was thawed on ice. All used buffers are listed in table 3.2. Lysozyme (4 mg per 1 L main culture), $MgCl_2$ (1 mM), DNaseI (2 mg) and cOmplete^{TM} protease inhibitor cocktail (2 tablets) were added and the suspension was incubated for 30 min at room temperature to induce cell lysis. After homogenization, the cells were mechanically lysed in the ice-cooled microfluidizer LM10 (Microfluidics, Westwood, USA, 1,000 bar, 3 cycles, 4 °C). The addition of extraction buffer (1:1, *v/v*) and urea (6 M) to the lysat was followed by its incubation for 30 min at room temperature. After centrifugation (60 min, 20,000 *g*, 4 °C) the resulting pellet (P) was separated from the supernatant (S). Samples for an SDS-PAGE were taken immediatly (cf. figure 3.2 B).

The purification was performed by immobilized metal ion chromatography (IMAC) based on Ni^{2+} ions. The supernatant was added to prepared Ni^{2+}-NTA agarose beads (5-6 mL bed volume) and incubated for 3 h at 4 °C on a tube roller. Before usage, 10-12 mL of resuspended Ni^{2+}-NTA agarose beads (stored in 30 % ethanol)

were centrifuged at 700 g and 4 °C for 2 min. The supernatant was discarded, the beads were resuspended in syb-wash buffer 1 and centrifuged (700 g, 4 °C, 2 min). The last step was repeated twice. The bead suspension incubated with protein was transferred in a gravity flow column after the incubation period had been completed. A sample for an SDS PAGE was collected of the flowthrough (FT, cf. figure 3.2 B). For separation of the target protein from unspecifically bound proteins, four rounds of syb-wash buffer 1 (50 mL, W1, cf. figure 3.2 B) and two rounds of syb-wash buffer 2 (50 mL, W2 and W3, cf. figure 3.2 B) were flushed through the beads. For the elution of syb 2, the beads were resuspended with 10 mL of syb-elution buffer and incubated for 10 min at 4 °C. The protein was eluted afterwards from the column. The elution step was repeated for twice (E1-E3, cf. figure 3.2 B).

Table 3.2: List of buffers used for the isolation and purification of syb 2.

resuspension buffer	20 mM Tris, 500 mM NaCl, 20 mM imidazole, pH 7.4
extraction buffer	20 mM Tris, 500 mM NaCl, 20 mM imidazole, 10 % (w/v) sodium cholat, pH 7.4
syb-wash buffer 1	20 mM Tris, 500 mM NaCl, 20 mM imidazole 1 % (w/v) sodium cholat, pH 7.4
syb-wash buffer 2	20 mM Tris, 500 mM NaCl, 40 mM imidazole, 1 % (w/v) CHAPS, pH 7.4
syb-elution buffer	20 mM Tris, 500 mM NaCl, 400 mM imidazole, 1 % (w/v) CHAPS, pH 7.4
syb-dialysis buffer	20 mM HEPES, 150 mM NaCl, 1 mM EDTA, 0.1 mM TCEP 1 % (w/v) CHAPS, pH 7.4
syb-buffer A	20 mM HEPES, 0.1 mM TCEP, 1 mM EDTA, 1 % (w/v) CHAPS, pH 7.4
syb-buffer B	20 mM HEPES, 0.1 mM TCEP, 1 mM EDTA, 1 M NaCl, pH 7.4

Cleavage of His$_6$ tag

Fractions from the elution with a high syb 2 concentration (E1 and E2, cf. figure 3.2 B) were pooled, injected into a dialysis tube (molecular weight cut off: 5 kDa) and supplemented with thrombin (0.08 mg mL^{-1}). The tube was incubated in syb-dialysis buffer for 1 h at room temperature and cooled down to 4 °C over night. A successful cleavage of the His$_6$ tag was illustrated by a decreased protein molecular mass (cf. figure 3.3, bC: before cleavage, aC: after cleavage).
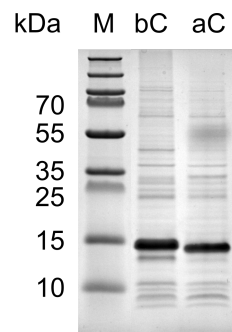
Figure 3.3: SDS PAGE of thrombin cleavage of syb 2 to separate protein and His$_6$ tag. The bands before (bC) and after (aC) cleavage show a decrease in the molecular mass of approximately 2 kDa. (M: marker).

For further purification the solution was injected to the ÄKTA Purifier 10 (GE Healthcare Europe, Freiburg, Germany) performing a cation exchange chromatography with a MonoS5/50 column (chapter 3.1.3). The percentage of syb-buffer B was gradually increased to 100 % in 29 column volumes (1 CV = 1 mL, 2 mL min^{-1}). The elution of the protein was controlled by the absorption at 280 nm (cf. figure 3.4 A). Cleaved Syb 2 eluted from 20-60 % Syb-buffer B (14-50 mS cm^{-1}, 0.2-0.6 M NaCl). An SDS PAGE of the fractions corresponding to the protein peak (F4 to F10, 1.5 to 5 min) proves the success of the purification (cf. figure 3.4 B). The concentration of the protein was analyzed by UV/Vis spectroscopy (Nanodrop2000c, Thermo Fisher Scientific, Waltham, USA, chapter 3.1.5). Fraction F5 and F6 were pooled and had an overall concentration of 3.4 mg mL^{-1} (263 µM).

SDS PAGE according to Schägger was performed after completion of purification as described in chapter 3.1.4.
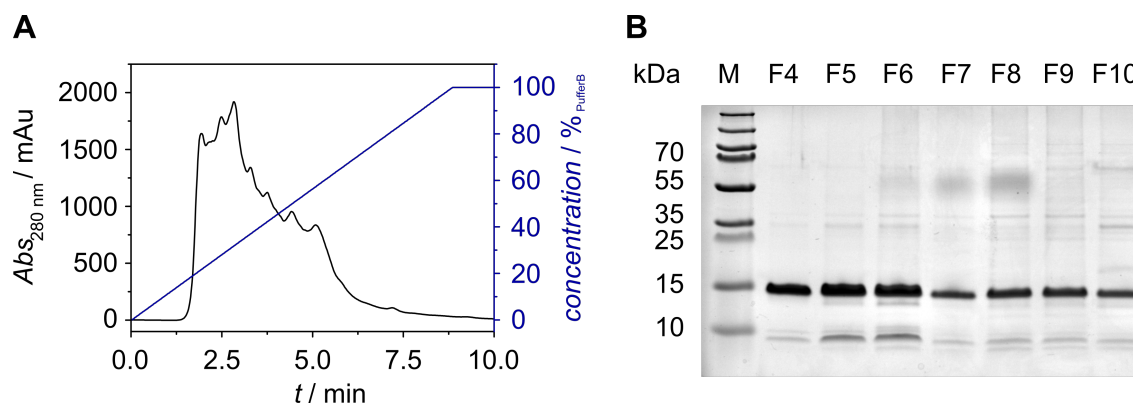
Figure 3.4: Purification of syb 2 (1-117Cys) via cation exchange chromatography. A: Chromatogram of syb 2 using a MonoS5/50 column. Syb 2 eluted between 14 to $60\,\mathrm{mS\,cm^{-1}}$. **B:** SDS PAGE of fraction F4 to F10 corresponding to an elution time of 1.5 to 5 min (elution rate $2\,\mathrm{mL\,min^{-1}}$).

3.1.3 Chromatography

Immobilized metal ion chromatography (IMAC)

Immobilized metal ion chromatography (IMAC) was performed as the first purification step of the supernatants. The proteins isolated in this work were biosynthesized from cloned genes and thus equipped with a His$_x$-tag ($x_{\mathrm{TFOF1}} = 10$, $x_{\mathrm{syb\,2}} = 6$) that can bind to immobilized metal ions.[69] TALON Metal Affinity Resin (Clontech, Takara Bio Europe, Saint-Germain-en-Laye, France) based on cobalt ions ($\mathrm{Co^{2+}}$, chapter 3.1.1) was used for the purification of ATP synthase. Syb 2 was isolated using a nickel based resin ($\mathrm{Ni^{2+}}$-NTA, chapter 3.1.2).

Ion exchange chromatography

Ion exchange chromatography was used further to separate the proteins of interest from impurities respectively to increase the protein concentration. The method is founded on the different binding affinities of proteins to a stationary phase depending on their net charge. If the pI value of the protein differs from the pH value of the mobile phase, a net charge is present and the protein can bind to an oppositely charged stationary matrix. Positively charged proteins were purified by a negatively charged matrix (cation exchanger) while negatively charged proteins were purified by a negatively charged matrix (anion exchanger). By increasing the ionic strength of the mobile phase in a controlled manner, bound proteins are eluted depending on their pI and thus separated from each other.[69]

In this work, the ion exchange chromatography was performed with the help of an ÄKTA purifier 10 (GE Healthcare Europe, Freiburg, Germany). The protein was dialyzed or diluted to obtain a low salt concentration to allow the protein to bind to the stationary matrix of the column. An anion exchange column (MonoQ5/50) was utilized for the purification of TF_OF_1 and a cation exchange column (MonoS5/50) for the purification of syb 2. First, the column was rinsed with the low salt buffer and then loaded with the protein solution. The salt concentration was then increased by adding the high-salt buffer. The gradient was previously optimized for the respective protein. The elution was detected by measuring the absorption at 280 nm.

3.1.4 SDS Polyacrylamide gel electrophoresis

The sodium dodecyl polyacrylamide gel electrophoresis (SDS PAGE) was used for the verification of the success of the protein isolation and purification steps as well as the quantification of the reconstitution efficiency after vesicle flotation assays (chapter 3.2.2.4).

The anionic detergent SDS is able to unfold the structure of proteins and creates a constant mass to charge ratio by binding to the amino acid chain. Thus, the intrinsic charge of the proteins can be neglected. After being added to a polyacrylamid gel and the application of an electric field, the velocity of the negatively charged proteins towards the anode is only dependent on their mass. This leads to a separation of the proteins within the sample. In this work, SDS PAGE according to Laemmli was used for studies of TF_OF_1, while for syb 2 the method according to Schägger was applied, as this is particularly suitable for the separation of smaller proteins.[82–84]

SDS PAGE according to Laemmli

The prepared gel consists of a stacking and a resolving gel differing in the pH value and the mesh size. The stacking gel provides a small mesh size and a low pH (5 % acrylamide, pH 6.8) compared to the resolving gel (17 % acrylamide, pH 8.8). In the stacking gel, the proteins contained in the sample are focused on a sharp protein band before entering the resolving gel. This is caused by the ions of the tank buffer diffusing into the gel. Glycine ions (trailing ions) are found as zwitterions in the stacking gel (pH 6.8) and therefore hardly migrate towards the anode, while the chloride ions (leading ions) have a high velocity in the electric field. The result is a potential difference between leading and trailing ions. Therefore the proteins migrate between

leading and trailing ions with an equal velocity. Entering the resolving gel, this effect is reversed by deprotonation of the glycine. Thus, the protein-SDS-complexes are separated by mass in the smaller meshes of the resolving gel.[82]

The resolving gel was prepared as described below (cf. table 3.4), overlayed with isopropanol and polymerized for 30 min. The stacking gel was prepared and added atop of the resolving gel after discarding the isopropanol. To form the sample wells a comb was inserted and the gel was polymerized for 30 min. The gel was stored at 4 °C for up to two weeks or directly mounted into an electrophoresis device filled with tank buffer (cf. table 3.3). The samples were mixed with the respective sample buffer and incubated for 5 min at 85 °C in an Eppendorf® ThermoMixer Compact(Eppendorf AG, Hamburg, Germany). 2 × sample buffer was used for analysis of the protein isolation and purification steps, while 6 × sample buffer was used for the analysis of flotation assays (cf. chapter 3.2.2.4). DTT was present in the sample buffer as a reducing agent to break disulfide bonds allowing a complete linearization and unfolding of the proteins by SDS. Samples and a molecular weight standard (PageRuler™prestained protein ladder) were loaded into the gel and the elektrophoresis was conducted at 200 V for approximately (45-60) min. Afterwards the gel was washed two times with ultrapure water by heating up to 100 °C and incubating for 1 min. The protein bands in the gel were visualized by heating up the gel to 100 °C in a staining solution containing solvent-free Coomassie Brilliant Blue G-250. After incubating for 5 min the staining solution was removed, the gel was washed in ultrapure water and photographed with an Azure c300 gel imaging system (Azure Biosystems, Inc., Dublin, USA).

Table 3.3: Solutions and buffers used for SDS-PAGE according to Laemmli.

2x sample buffer	125 mM Tris, 100 mM DTT, 20 % (v/v) glycerol, 2 % (w/v) SDS, 0.02 % (w/v) bromphenol blue, pH 6.8
6x sample buffer	375 mM Tris, 300 mM DTT, 60 % (v/v) glycerol, 6 % (w/v) SDS, 0.06 % (w/v) bromphenol blue, pH 6.8
tank buffer	25 mM Tris, 192 mM glycine, 0.1 % (w/v) SDS
stacking gel buffer	1 M Tris, pH 6.8
resolving gel buffer	1 M Tris, pH 8.8
staining solution	0.8 % (w/v) Coomassie Brilliant Blue G-250, 35 mM HCl

Table 3.4: Composition of stacking and resolving gel for the SDS-PAGE according to Laemmli.

stacking gel	0.33 mL acrylamide/bisacrylamide (29:1, 30 %), 1.4 mL ultrapure H_2O, 0.25 mL stacking gel buffer, 0.1 % (w/v) SDS, 0.1 %(w/v) APS, 2 µL TEMED
resolving gel	2.3 mL acrylamide/bisacrylamide (29:1, 30 %), 0.65 mL ultrapure H_2O, 1 mL resolving gel buffer, 0.1 % (w/v) SDS, 0.1 %(w/v) APS, 4 µL TEMED

SDS PAGE according to Schägger

The SDS PAGE according to Schägger is the preferred system to separate proteins smaller than 30 kDa. In this method, glycine ($pK_a = 9.6$) is replaced by tricine ($pK_a = 8.15$). The differences in pK_a value cause the upper stacking limit to be reduced in tricine SDS-PAGE.[83,84]

Stacking and resolving gel were composed as described in table 3.6. The further preparation of the gels proceeded similarly to the preparation according to Laemmli. The polyacrylamide gel was then mounted into the electrophoresis chamber. The inner compartment was filled with cathode buffer, whereas the outer compartment was loaded with anode buffer (cf. table 3.5). Sample preparation and loading to the gel were as described above and the same buffers were used as for Laemmli SDS PAGE (cf. table 3.3). The electrophoresis was started for 10 min at 70 V allowing the formation of a sharp protein band in the stacking gel. Subsequently the voltage was raised to 200 V for approximately 45-60 min. The staining and destaining were accomplished as described above.

Table 3.5: Solutions and buffers used for SDS-PAGE according to Schägger.

cathode buffer	0.1 M Tris, 0.1 M tricine, 1 % (w/v) SDS, pH 8.25
anode buffer	0.2 M Tris, pH 8.9
Schägger gel buffer	3 M Tris, 0.3 % (w/v) SDS, pH 8.45

Table 3.6: Composition of stacking and resolving gel for the SDS-PAGE according to Schägger.

stacking gel	1.23 mL ultrapure H_2O, 500 µL Schägger gel buffer, 267 µL acrylamide/bisacrylamide (29:1, 30 %), 0.1 % (w/v) APS, 2.65 µL TEMED
resolving gel	570 µL ultrapure H_2O, 1.06 mL glycerol (50 % (v/v)), 1.68 mL Schägger gel buffer, 1.66 mL acrylamide/ bisacrylamide (29:1, 30 %), 0.1 % (w/v) APS, 3 µL TEMED

3.1.5 Quantification of protein concentration

UV/Vis spectroscopy (Nanodrop 2000c, Thermo Fisher Scientific, Waltham USA) was used for the determination of the protein concentration and the degree of labeling (*DOL*, cf. chapter 3.1.6) on the basis of Lambert-Beers law (cf. equation 3.1) and the absorbance properties of the aromatic amino acids tryptophane, tyrosine, phenylalanine and histidine at a wavelength of 280 nm. The concentration (c) of an aqueous solution of proteins can be evaluated by the absorbance at 280 nm (A_{280}) and the specific thickness (l) of the cuvette.

$$A_{280} = \varepsilon_{280} \cdot c \cdot l \tag{3.1}$$

The extinction coefficient of the TF_OF_1 ATP synthase was taken from Usukara et al. (253,000 M cm^{-1}).[70] The extinction coefficient of syb 2 was calculated by the online tool ProtParam (13,980 M cm^{-1}).[85]

3.1.6 Protein labeling

For the visualization by means of fluorescence microscopy measurements, synapto-brevin 2 (1-117Cys, syb 2) was labeled with the fluorescent dye Atto488 maleimide (Atto-Tec GmbH, Siegen, Germany). The approach used in this work is based on the thiol reactivity of cystein residues and their rarity in the proteome. This requires a single and accessible cysteine residue without a function for the protein folding or activity. In the case of syb 2 an engineered cysteine at position 117 in

the amino acid sequence was used. The thiol group is able to attack the maleimide function of the fluorophore in the course of a modification of the Michael addition (cf. figure 3.5).[86,87]
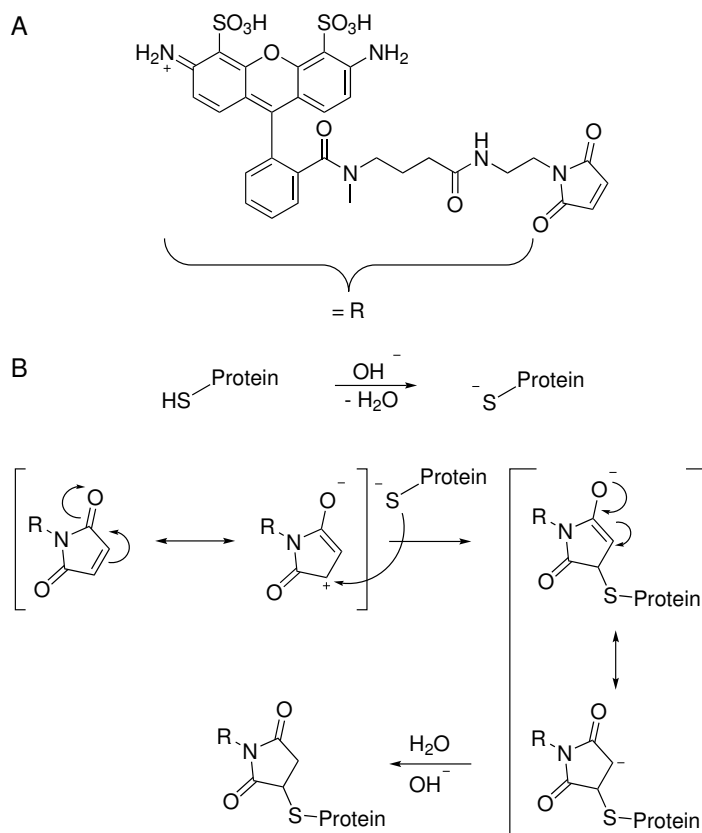
Figure 3.5: Reaction mechanism of the maleimide-thiol-addition (Michael addition). A: Chemical structure of Atto488 maleimide. **B:** In an alkaline environement, the thiol group of a cysteine of the protein is deprotonated and is thus able to attack the β carbon atom. The resulting negatively charged carbanion is protonated.

In an alkaline environment, the thiol group of a cysteine is deprotonated and thus able to attack the β carbon atom of an α, β unsaturated carbonyl, resulting in a carbanion with a delocalized negative charge. The carbanion accepts a proton from a water molecule regenerating the catalyst and resulting in syb 2 coupled to the fluorophore.[87]

Protein fractions with high concentrations and purity were pooled (F5 and F6 cf. figure 3.4) and used for labeling under light-free conditions. A molar excess (1.8 ×) of Atto488 maleimide (0.9 μmol) was solved in 100 μL of syb-buffer A (cf. table 3.2), added to the syb 2 solution (0.5 μmol) and incubated for 2 h at room

temperature. The labeled protein was separated from the excess fluorophore by dialysis over 24 h against syb-buffer A. The outer buffer was changed five times during the dialysis.

The degree of labeling (DOL) was analyzed by applying UV/Vis spectroscopy. The protein concentration was determined by equation 3.2 using the absorbance at 280 nm (A_{280}), the extinction coefficient of syb 2 ($\varepsilon_{\text{syb 2}} = 13{,}980 \,\text{M}\,\text{cm}^{-1}$), the thickness of the cuvette (l), the maximal absorbance (A_{max}) and the correction factor of the Atto488 label ($CF_{280} = 0.09$). Next, the DOL was determined as the fraction of the concentration of the labeled protein ($c_{\text{prot, label}}$) and the overall protein concentration (c_{prot}) (cf. equation 3.3). The extinction coefficient of the Atto488 label ($\varepsilon_{\text{Atto488}} = 90{,}000 \,\text{M}\,\text{cm}^{-1}$) was required.

$$c_{\text{prot}} = \frac{A_{280} - A_{\text{max}} \cdot CF_{280}}{\varepsilon_{\text{prot}} \cdot l} \tag{3.2}$$

$$DOL = \frac{c_{\text{prot, label}}}{c_{\text{prot}}} = \frac{A_{\text{max}} \cdot \varepsilon_{\text{prot}}}{(A_{280} - A_{\text{max}} \cdot CF_{280}) \cdot \varepsilon_{280}} \tag{3.3}$$

The mean DOL was 0.92 at a protein concentration of 231 µM.
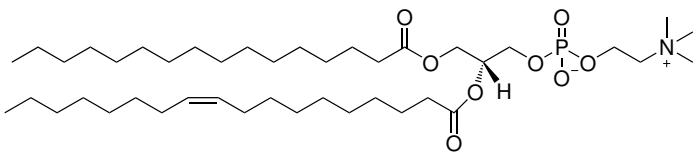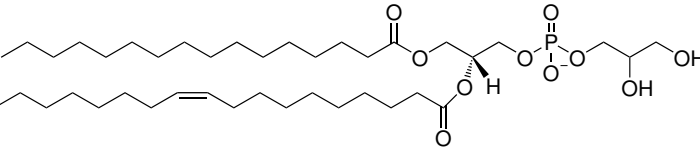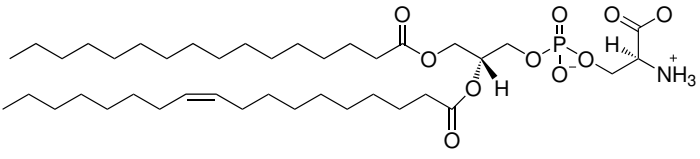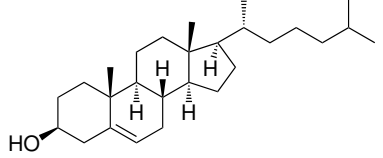
3.2 Preparative methods

3.2.1 Vesicle preparation
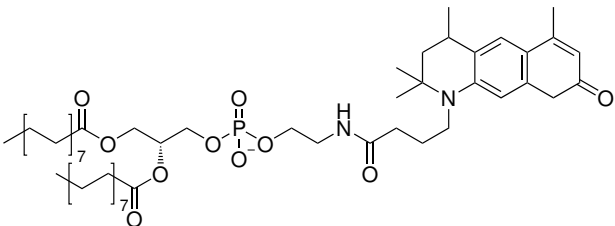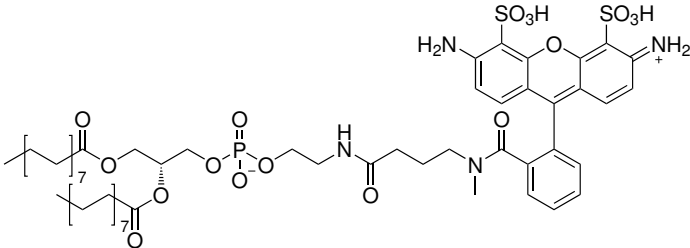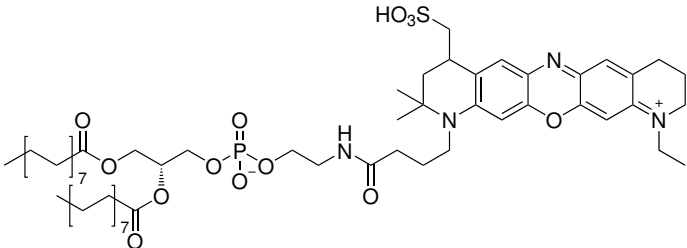
3.2.1.1 Lipids and lipid coupled fluorophores

Different phospholipids and cholesterol served for the preparation of model membrane systems in this work. Table 3.7 summarizes the chemical structures of 1-palmitoyl-2-oleoyl-*sn*-glycero-3-phosphocholin (POPC), 1-palmitoyl-2-oleoyl-*sn*-glycero-3-phospho-*rac*-1-glycerol (POPG), 1-palmitoyl-2-oleoyl-*sn*-glycero-3-phospho-L-serine (POPS) and Cholesterol (Chol).

Table 3.7: Overview of the lipids used in this work. For the preparation of artificial membrane systems POPC, POPG, POPS and cholesterol in different compositions were combined.

Lipids	Molecular mass
 1-Palmitoyl-2-oleoyl-*sn*-glycero-3-phosphocholin (POPC)	$760.1\,\mathrm{g\,mol^{-1}}$
 1-Palmitoyl-2-oleoyl-*sn*-glycero-3-phospho-*rac*-1-glycerol (POPG)	$747.1\,\mathrm{g\,mol^{-1}}$
 1-Palmitoyl-2-oleoyl-*sn*-glycero-3-phospho-L-serine (POPS)	$761.1\,\mathrm{g\,mol^{-1}}$
 Cholesterol (Chol)	$386.7\,\mathrm{g\,mol^{-1}}$

Table 3.8: Overview of the most important lipid coupled fluorophores used in this work.

Lipids	Molecular mass
Atto390 1,2-dipalmitoyl-*sn*-glycero-3-phosphoethanolamine (Atto390 DPPE)	$1014.4\,\mathrm{g\,mol^{-1}}$
Atto488 1,2-dipalmitoyl-*sn*-glycero-3-phosphoethanolamine (Atto488 DPPE)	$1264.0\,\mathrm{g\,mol^{-1}}$
Atto655 1,2-dipalmitoyl-*sn*-glycero-3-phosphoethanolamine (Atto655 DPPE)	$1201.6\,\mathrm{g\,mol^{-1}}$

While POPC served as basis for all lipid bilayers prepared in this work, the amounts of POPG, POPS and cholesterol variied, depending on the experimental aim. Fluorophores coupled to the head group of 1,2-dipalmitoyl-*sn*-glycero-3-phosphoethanolamine (DPPE), 1,2-dihexadecanoyl-*sn*-glycero-3-phosphoethanolamine (DHPE) or 1,2-dioleoyl-*sn*-glycero-3-phosphoethanolamine (DOPE) (cf. table 3.8) were implemented for fluorescence microscopic imaging and characterization of the systems by means of fluorescence recovery after photobleaching (FRAP) or fluorescence correlation spectroscopy (FCS). Atto390 DPPE ($\lambda_{\mathrm{ex/em}} = 390/476\,\mathrm{nm}$) and

Atto488 DPPE ($\lambda_{\text{ex/em}}$ = 500/520 nm) were used for FRAP experiments due to their lower photostability. For fluorescence correlation spectroscopy, bilayers were doped with Atto 655 ($\lambda_{\text{ex/em}}$ = 633/680 nm) coupled to the head group of DOPE and DPPE, respectively. Additionally, in rare cases, OG488 DHPE (Oregon Green 488 1,2-dihexadecanoyl-*sn*-glycero-3-phosphoethanolamine, $\lambda_{\text{ex/em}}$ = 508/534 nm) and TxR DHPE (Texas Red 1,2-dihexadecanoyl-*sn*-glycero-3-phosphoethanolamine, $\lambda_{\text{ex/em}}$ = 595/615 nm) (not illustrated) were utilized for fluorescence labeling of bilayer systems.

3.2.1.2 Preparation of large unilamellar vesicles

Large unilamellar vesicles (LUVs) were prepared via extrusion of a suspension of lipids through a polycarbonate membrane (LiposoFast Basic, Avestin, Ottawa, Canada). Depending on the experiment, different compositions of the lipids and lipid-coupled fluorophores described in chapter 3.2.1.1 were used.

First, lipid films (2.5 mg total) were produced from lipid stock solutions of defined concentrations. The desired lipids and lipid-coupled fluorophors were added to 400 µL of chloroform. The solvent was removed thoroughly for 30 min at 30 °C by a constant flow of nitrogen. To get rid of any remaining solvent, the sample tubes containing the lipid mixture were placed for 2 h *in vacuo* at room temperature. The dried lipid films were hydrated in the desired buffer for 30 min at room temperature and resuspended through agitating on a vortex mixer three times for 30 s in 5 min intervals. A suspension of multilamellar vesicles was obtained. By extrusion (31×) through the polycarbonate membrane with a nominal pore diameter of 100 nm LUVs were otained. The overall lipid concentration was determined afterwards by a phosphate test as described in chapter 3.2.1.4.

3.2.1.3 Preparation of giant unilamellar vesicles via electroformation

As mentioned initially (cf. chapter 1.3), giant unilamellar vesicles (GUVs) can be prepared in a variety of ways.[6,7,43] GUVs prepared by the well-established electroformation technique served as a control compared to microfluidic-prepared GUVs introduced in this work.

Lipid films (0.2 mg total) were prepared directly on two glass slides coated with

indium tin oxide (ITO slides) and dried for 2 h *in vacuo* at room temperature. To assemble the electroformation chamber, two teflon spacers, each equipped with a selfadhesive copper stripe, and a silicon ring were placed between two ITO slides. The self-adhesive copper stripes were used as contacts. The cavity was loaded with sucrose solution ($300\,\text{mOsm}\,\text{kg}^{-1}$, $V = 1.7\,\text{mL}$) and a frequency of 5 Hz and an AC (alternating current) voltage of 3 V (peak-to-peak) was applied over night. The GUVs suspension was collected afterwards and used for the desired control experiments.

3.2.1.4 Determination of lipid concentration

For the determination of the total lipid concentration, 15 µL of a sample, doped with 200 µL of perchloric acid (70 %), and calibration samples of known NaH_2PO_4 concentrations were heated up to 240 °C for 30 min. The remaining inorganic components were treated with 700 µL of solution A and solution B (cf. table 3.9). The solution was incubated for 10 min at 80 °C. The absorption of the samples was measured at 820 nm via spectrophotometry and the concentration of phosphate within in the sample was determined from the calibration curve allowing to calculate the total lipid concentration of the sample.[88]

Table 3.9: Solutions used for the determination of the total lipid composition via a phosphate test.

solution A	12.6 % (w/v) $HClO_4$, 0.45 % (w/v) NaH_4MoO_4
solution B	1.7 % (w/v) L-ascorbic acid
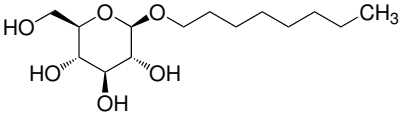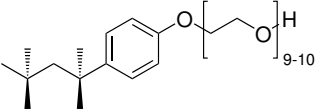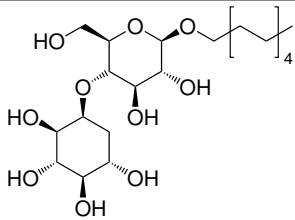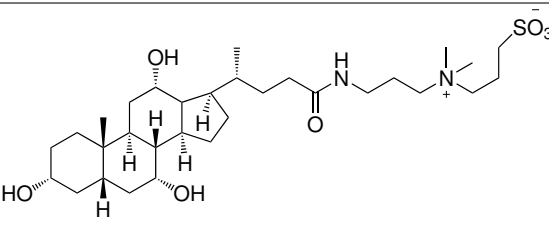
3.2.2 Protein reconstitution in large unilamellar vesicles

Transmembrane proteins are stabilized in aqueous solutions by detergents. These detergents are able to assemble with their hydrophobic parts towards the hydrophobic transmembrane domain (TMD) of a protein and thereby protect the protein from denaturation, misfolding or aggregation. Many of these membrane proteins are stable in a limited selection of detergents, however, different of proteins also demand the presence of different detergents. The optimization of reconstitution protocols individually tailored to the target protein is therefore essential.[22]

Two different methods can be used to reconstitute transmembrane proteins: the

direct reconstitution of proteins into preformed LUVs solubilized by detergents and the comizellization method. The latter is based on mixed lipid-protein-detergent micelles. In both methods, the proteoliposomes are ultimately obtained by removing the detergent. Detergents with a high critical micelle concentration (CMC) can be removed by dialysis or gel filtration, while detergents with a low CMC have to be removed by the addition of polystyrene beads (Bio-Beads SM-2®) or cyclodextrins for complexation.[22,23] A summary of all detergents used in this work is presented in table 3.10.

Table 3.10: Overview of surfactants used in this work.[22]

Surfactants	Molecular mass	CMC (at 25 °C)
n-octyl-β-D-glucoside (*n*OG)	$292.4\,\mathrm{g\,mol^{-1}}$	20-25 mM
2-[4-(2,4,4-trimethylpentan-2-yl) phenoxy]ethanol (Triton™X-100)	$630.0\,\mathrm{g\,mol^{-1}}$	0.17-0.3 mM
dodecyl-β-D-maltoside (DDM)	$510.6\,\mathrm{g\,mol^{-1}}$	0.15 mM
3-[(3-cholamidopropyl)dimethylammonio]- 1-propanesulfonate (CHAPS)	$614.5\,\mathrm{g\,mol^{-1}}$	6.5 mM

3.2.2.1 Reconstitution of TF$_O$F$_1$ ATP synthase in LUVs

The TF$_O$F$_1$ ATP synthase was solubilized in aqueous environment by dodecyl-β-D-maltoside (DDM) and inserted by direct reconstitution in the bilayer of LUVs with two different approaches using n-octyl-β-D-glucoside (nOG)[55] or Triton™X-100, respectively.[89,90] Various lipid compositions were used for the preparation of proteoliposomes. The standard protocols for both detergents are described below. Any changes are noted at the appropriate place in the chapter results.

Direct reconstitution of the TF$_O$F$_1$ ATP synthase with Triton™X-100

LUVs (5 mg mL^{-1}) were prepared as described in chapter 3.2.1.2 and the resulting lipid concentration was checked by a phosphate test (cf. chapter 3.2.1.4). For this purpose, reconstitution buffer R1 (cf. table 3.11) was used unless otherwise indicated. Triton™X-100 stored under Argon atmosphere was added to the suspension to a final concentration of 4 mM. After adding the protein in the desired theoretical protein to lipid ratio (p/l) the suspension was incubated for 60 min at room temperature. A theoretical p/l of 1/20,000 (n/n) was used if not described differently. Subsequently, Bio-Beads SM-2® (40 mg per 1 mg Triton™X-100) were added followed by an incubation for another 60 min at room temperature under gentle agitation. Prior to usage, the Bio-Beads were equilibrated and washed using methanol and ultrapure water. The Bio-Beads were removed yielding in the final proteoliposome suspension.

Direct reconstitution of the TF$_O$F$_1$ ATP synthase with nOG

Another reconstitution method known from the literature is based on the detergent n-octyl-β-D-glucoside (nOG).[55] LUVs (5 mg mL^{-1}) were prepared as described before with R1 or R2 buffer unless described differently. The preformed LUVs were destabilized for 30 min with a final concentration of nOG of 26 mM under gentle rotation at room temperature. TF$_O$F$_1$ ATP synthase was added in a theoretical p/l of 1/20,000 (n/n) if not indicated differently and incubated for 30 min at 4 °C followed by dialysis (cut-off 14 kDa) over night against the used reconstitution buffer supplemented with Bio-Beads SM-2®. The next day, heptakis(2,6-di-O-methyl)-$β$-cyclodextrin (DM$β$CD) was added for complexation of n-dodecyl-β-D-maltosid (DDM) in an equimolar amount. The suspension was incubated for 1 h at 4 °C. The proteoliposomes were separated from residual detergents by size exclusion

chromatography using a Sephadex G-25 prepacked illustra NAP-25 column (GE Healthcare Life Science, Solingen, Germany).

Table 3.11: Buffers used for the reconstitution of the TF_OF_1 ATP synthase in LUVs.

rec. buffer R1	20 mM Tricine, 20 mM succinic acid, 0.6 mM KCl, 2.5 mM MgCl$_2$, pH 8.0
rec. buffer R2	20 mM Tris, 1 mM KCl, 2.5 mM MgCl$_2$, pH 8.0

3.2.2.2 Reconstitution of synaptobrevin 2 in LUVs

Synaptobrevin 2 (1-117Cys) labeled with Atto488 (syb 2-Atto488) was solubilized by 3-[(3-Cholamidopropyl)dimethylammonio]-1-propanesulfonate (CHAPS) and inserted in LUVs by direct reconstitution as well as comicellization as explained below.

Direct reconsitution of syb 2-Atto488

LUVs (5 mg mL^{-1}) were prepared in reconstitution buffer R3 (cf table 3.12). Protein reconstitution was performed in a similar way as described in chapter 3.2.2.1 using nOG. A destabilization of the LUVs with 26 mM nOG was followed by an incubation at room temperature for 30 min. Unless otherwise indicated, syb 2-Atto488 was added in a theoretical p/l of 1/500 (n/n). The suspension was incubated under gentle rotation for 30 min at 4 °C. To remove the detergent a dialysis (cut-off 5 kDa) was performed over night at 4 °C against the respective buffer. The next day, a size exclusion chromatography using a Sephadex G-25 prepacked illustra NAP-25 column (GE Healthcare Life Science, Solingen, Germany) was performed resulting in proteoliposomes.

Co-micellisation

Another method for the reconstitution of syb 2-Atto488 is the comicellization. A lipid film (2.5 mg) was incubated for 30 min at room temperature with 500 µL of reconstitution buffer R3 supplemented with 52 mM nOG. The suspension was vortexed three times for 30 s in time intervals of 5 min. Syb 2-Atto488 was added in a p/l of 1/500 (n/n) unless otherwise indicated and incubated for another 30 min at room temperature. The detergent was removed by exclusion chromatography using a

Sephadex G-25 prepacked illustra NAP-25 column (GE Healthcare Life Science, Solingen, Germany) resulting in the proteoliposomes.

Table 3.12: Buffers used for the reconstitution of syb 2-Atto488 in LUVs.

rec. buffer R3	20 mM HEPES, 100 mM KCl, 10 mM MgCl$_2$, 50 mM sucrose, pH 8.0

3.2.2.3 Determination of the vesicle size by dynamic light scattering

Dynamic light scattering measurements were performed to determine the intensity weighted size distribution of liposomes using a Zetasizer NanoS (Malvern Instruments, Herrenberg, Germany) with a laser wavelength of 633 nm. The liposome suspension was diluted to a final concentration of approximately 0.01-0.02 mg mL^{-1} with the respective buffer or ultrapure water. The measurements were performed at 25 °C and evaluated with the corresponding Zetasizer Software.

3.2.2.4 Determination of reconstitution efficiency by a flotation assay

Densitiy gradient centrifugation of proteoliposomes (flotation assay) was used to verify the success of a protein reconstitution and determine the reconstitution efficiency. Lipsomes float, due to their aqueous lumen, after a centrifugation on top of a density gradient while non-reconstituted proteins, having a higher density, conglumerate at the bottom of the gradient. Thus, proteoliposomes can be separated from free protein and the reconstitution process can be quantitatively analyzed by an SDS-PAGE of fractions taken from the density gradient.

The gradient (0 %-40 %, w/v, cf. figure 3.6 A) was prepared with non-ionic Nycodenz ($M = 821$ g mol^{-1}).[91] Two solutions of Nycodenz (30 % and 80 %, w/v) were prepared in the same buffer used for the reconstitution of the respective protein. 40 µL of the proteoliposome-sample were gently mixed with the same volume of the 80 % (w/v) solution. The resulting solution (40 %, w/v) was transferred in a small centrifuge tube and overlayed with the 30 % (w/v) solution. 20 µL of the respective buffer were pipetted on top and a centrifugation at 300,000 g and 4 °C for 1.5 h was peformed. Seven fractions (20 µL) were collected from the gradient and subjected to SDS PAGE

for further analysis (cf. chapter 3.1.4, figure 3.6). Application of samples to the SDS PAGE with known protein concentrations allowed accurate determination of the mass of the protein in the fractions from the flotation assay. Proteoliposomes were expected in the upper three to four fractions. The ImageJ feature *Analyze Gel* (Version 1.45s, W. Rasband, NIH, USA) was used for the evaluation of the SDS PAGE. The intensities of the protein bands were analyzed and converted into intensity profiles for each gel column. For further investigation, the peak area of the intensity profiles was determined and converted into the mass of the protein in the fraction with the help of the protein standard. Since the TF_OF_1 ATP synthase consists of several subunits, for simplification only the α- and β-subunits were used. The determination of the protein to lipid ratio (p/l) was completed by a phosphate test (cf. chapter 3.2.1.4).
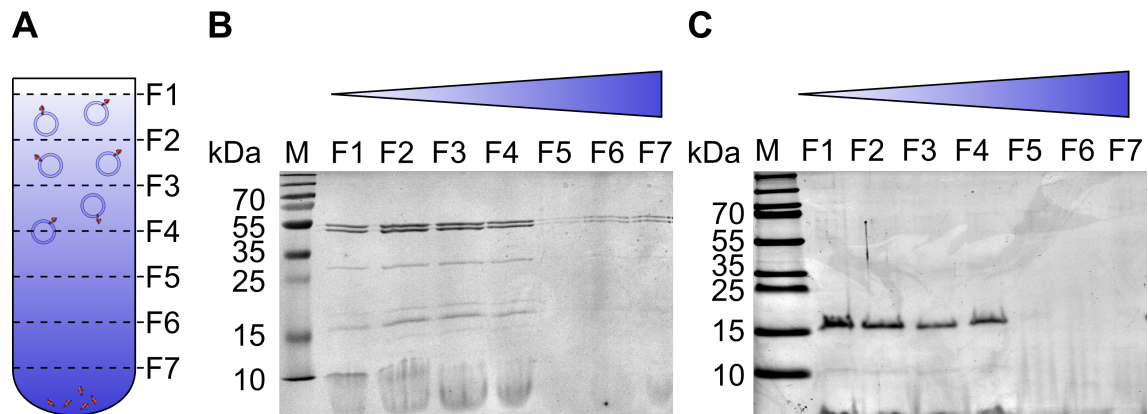
Figure 3.6: Density gradient centrifugation (flotation assay) for the determination of the reconstitution of proteins in vesicles. A: The density gradient (Nycodenz, 0 %-40 %) was prepared in the buffer used for preparation of the proteoliposomes. After centrifugation with a sample of proteoliposomes, the gradient was splitted in seven fractions. Exemplary gels of an SDS PAGE with the TF_OF_1 ATP synthase (**B**) and syb 2 (**C**) visualize the presence of proteins in fraction F1-F4.

3.2.3 Droplet-based microfluidics

3.2.3.1 Production of microfluidics devices

In this work, a microfluidic approach was used to investigate a new way to produce (droplet-stabilized) giant unilamellar vesicles (dsGUVs, GUVs) serving as artifical membrane system. The principle is based on a three-dimensional network of channels in micrometer range, arranged in a suitable geometry and adapted to the respective project. Photo- and soft lithography were used to fabricate the microfluidic devices from polydimethylsiloxane (PDMS). This can be achieved by transferring the desired geometry from a film or chrome mask, designed by computer-aided design (CAD) software, to a silicon wafer (master mold) using a photoresist (photolithography, cf. figure 3.7). The structures were molded into PDMS (soft lithography cf. figure 3.8 A), which is then attached to a glass substrate. [92–94]

Basically, microfluidic devices rely on small channel dimensions ($1\,\mu$m-$1000\,\mu$m) connected to flow driving pumps or pressure suppliers. [95] The Reynolds number R_e, which depends on the flow rate ν, hydraulic diameter D_h, viscosity μ and density ρ of the fluids and can be determined via

$$R_e = \frac{\rho \nu D_h}{\mu},\tag{3.4}$$

is typically < 2300 indicating the preponderance of a laminar compared to a turbulent flow. [95] In this work, a mask design from Mazutis et al. was used with slight modifications (cf. figure 3.8 B, C). [96] The design features one inlet for the oil (continuous phase) and two inlets for the aqueous phases (cf. figure 3.8 C1,2). All three inlets are equipped with structures that serve to filter out particles and other impurities that could interfere with the flow. Since only one inlet for an aqueous phase was required in this work, the second was left closed. The structure includes a flow-focusing junction (cf. figure 3.8 C4), allowing the generation of monodisperse droplets at medium to high capillary numbers ($C_a \geq 0.05$) and a low oil-to-water flow rate. [96–98] Fluid resistors (cf. figure 3.8 C3) are positioned after the inlet of both the continuous and the aqueous phase to reduce fluctuations. Produced droplets subsequently leave the device through its outlet and can be collected in a tube. [96]

Fabrication of the master mold (photolithography)

The fabrication of the master mold was performed together with Dr. Laura Turco at the Max-Planck-Insitute for Dynamics and Self-Organization (Göttingen) in the departement of Prof. Dr. Eberhard Bodenschatz.

The fabrication of a master mold is shown schematically in figure 3.7. A silicon wafer was covered with a layer of the negative photoresist SU8-3050 by spin-coating (500 rpm for 15 s, 3000 rpm for 30 s), resulting in a thickness of 30-40 µm. For the soft bake process, the wafer was incubated for one min at 65 °C, for 15 min at 95 °C and for another min at 65 °C. The wafer was cooled down and exposed to UV light (250 mJ cm^{-2}, 11 s) through the photomask leading to a polymerization of the photoresist in the uncovered areas, followed by the exposure bake process (1 min at 65 °C, 5 min at 95 °C, 1 min at 65 °C). After cooling down, the desired design can be obtained by removing the uncured photoresist several times by incubating in the developer (1-methoxy-2-propanol acetate) under gentle agitation. The wafer can be cleaned with isopropanol and the thickness of the structures was checked interferrometrically.
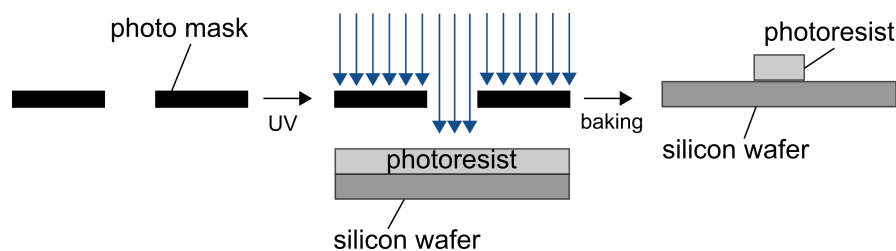
Figure 3.7: Schematic overview of the photolithographic process of the master mold production for microfluidic devices. A film mask was used to expose the photoresist SU8-3050, applied to a silica wafer, in specific areas to UV light. Soft and post baking processes as well as cleaning with the respective developer lead to the final master mold.

Fabrication of the microfluidic device (soft lithography)

To produce the microfluidic device, the PDMS base was mixed thoroughly with the curing agent in a ratio of 10:1 (w/w) and added on top of the master mold (cf. figure 3.8 A). The PDMS mixture was degassed for at least 30 min *in vacuo* and cured for 45 min at 75 °C. The cured PDMS was separated from the master

mold, cut to obtain individual channels and equipped with ports of a diameter of 0.75 mm by a puncher (Electron Microscopy Science, Hatfield, USA) serving as inlets for the aqueous and the oil phase respectively the outlet. The PDMS and a glass cover slip were rinsed with ultrapure water and isopropanol. After the treatment of both, the PDMS and the glass cover slip, with oxygen plasma (1 %-2 % relative power, 5 s, Zepto, Diener electronic, Ebhausen, Germany) the PDMS was fixed irreversibly to the glass surface leading to a channel width of 25 μm and height of 35 μm. To hydrophobize the inner surface of the channel, the system was treated with Sigmacoat (Sigma Aldrich, St. Louis, USA) for at least 30 s preventing the inversion of microemulsions. Prior to usage the channels were cleaned with ultrapure water and dried with air.
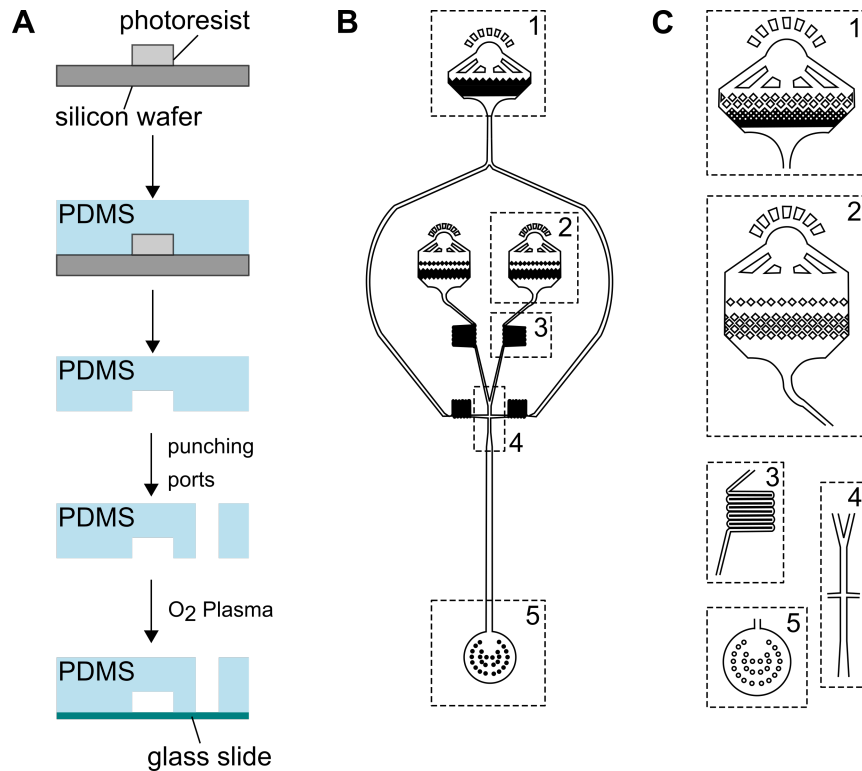
Figure 3.8: Soft lithographic fabrication and design of microfluidic devices for the production of droplet-stabilzed giant unilamellar vesicles (dsGUVs). A: Microfluidic devices were fabricated via soft lithography. PDMS was poured over the master mold and cured by baking at 75 °C. PDMS was separated from the wafer, equipped with ports and fixed on a glass substrate. **B:** Design of the microfluidic device used for the production of dsGUVs consisting of the inlet for the oil phase (**C**1), two inlets for the aqueous phases (**C**2), fluid resistors (**C**3), the flow focussing junction (**C**4) and the outlet (**C**5). Figure adapted from Mazutis et al. [96]

3.2.3.2 Production of droplet-stabilized giant unilamellar vesicles

Theoretical background of the formation of dsGUVs

As described previously (cf. chapter 1.2), the generation of giant unilamellar vesicles (GUVs) is, due to their resemblance to natural membrane systems, an obligatory part of research on membrane proteins and synthesis of artificial minimal cell compartements, as well as a tool for the formation of more advanced model membrane systems such as pore-spanning membranes (PSMs). Droplet-based microfluidics were developed as a novel platform for the formation of GUVs, that is not limited by the presence of high salt concentrations and charged lipids, which are essential for mimicking physiological conditions. Recently, Weiss et al. presented a microfluidic method for the production of spherical bilayers supported by water-in-oil droplets, originating from LUVs encapsulated within these droplets. Moreover, they revealed a way for subsequent biofunctionalization of the dsGUVs (picoinjection) with various proteins and presented a method for releasing GUVs from the oil phase into an aqueous, physiological environment.[45]

One essential parameter of the droplet-based microfluidic technology is the stabilization and modification of the emulsion by surface active agents (surfactants). The formation of emulsions of water and fluorocarbon oil is thermodynamically unfavored in the absence of surfactants. An oil-surfactant mixture was used in this work, reducing the interfacial tension and hereby stabilizing the droplet and preventing coalescence. For effective stabilization of the emulsion, a reduction of the interfacial tension to $20\,\mathrm{mN\,m^{-1}}$ or lower is mandatory.[99,100] The reduction of the interfacial tension is dependent on the amount of the surfactant adsorbed at the water-oil-interface as described in equation 3.5 from the Gibbs adsorption isotherm of diluted solutions. Γ is the excess surface concentration of the surfactant, c the bulk concentration, γ the interfacial tension, T the temperature and R the ideal gas constant.[100–102]

$$\Gamma = -\frac{c}{RT}\frac{\mathrm{d}\gamma}{\mathrm{d}c} \tag{3.5}$$
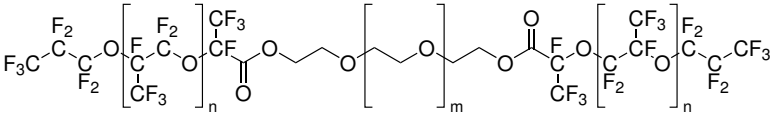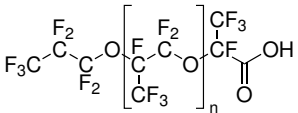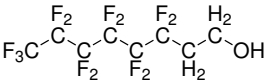
Moreover, the prevention of coalescence is mediated on the one hand by surfactant gradients, that are formed at the water-oil-interface and create an energy barrier,

and, on the other hand, by steric repulsion of the surfactants, which is increased with a higher molar weight of the molecules.[99,101]

One of the most widely used surfactants for stabilizing water-in-oil emulsions is the triblock copolymer perfluoropolyether-polyethylene glycol (PFPE-PEG-PFPE or 008-Fluorosurfactant, cf. table 3.13), which was also used here for the production of dsGUVs (cf. figure 3.9). Wagner et al. achieved a decrease of the interfacial tension between aqueous phase and fluorinated oil phase from $54.8\,\mathrm{mN\,m^{-1}}$ to $4.2\,\mathrm{mN\,m^{-1}}$ by adding the PEG triblock copolymer.[99] The PEG moiety represents the head group facing to the aqueous phase and providing an inert and biocompatible inner surface for the droplets while the PFPE tails point to the outer oil and mediate the stabilization of the droplets (cf. figure 3.9 B).[103] The encapsulation of LUVs in droplets leads to a multicompartment system which can be transferred into a single compartment system (dsGUV) in the presence of the charged surfactant Krytox (poly perfluoropropylene glycol carboxylate, PFPE-carboxylate, cf. table 3.13, figure 3.9 B). The LUVs spread and fuse at the water-oil interface which is mediated by divalent cations and facilitated by using negatively charged lipids.[54,94]

Table 3.13: Overview of surfactants used in this work.

Surfactants	Molecular mass
008-FluoroSurfactant*	$1{,}000\text{-}20{,}000\ \mathrm{g\,mol^{-1}}$
Krytox*	$2{,}500\text{-}7{,}500\ \mathrm{g\,mol^{-1}}$
1H,1H,2H,2H-Perfluoro-1-octanol	$364.1\,\mathrm{g\,mol^{-1}}$

*Polymer lengths (*n*, *m*) were not published.
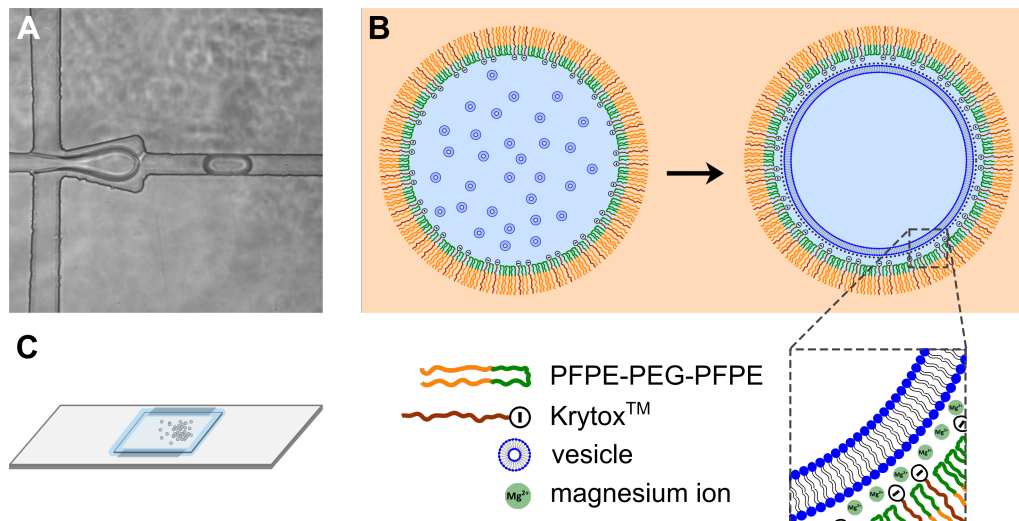
Figure 3.9: Production of droplet-stabilized GUVs mediated by surfactants.
A: Light microscopic image of the flow focusing junction of the microfluidic device.
B: Schematic illustration of the formation of droplet-stabilized GUVs mediated by surfactants. LUVs are encapsulated within droplets, stabilized by PFPE-PEG-PFPE. The formation of a dsGUVs was triggered by the presence of Krytox, divalent cations (magnesium ions) and negatively charged lipids. **C:** Chamber for the imaging and analysis of dsGUVs constructed from a glass slide and a cover slip.

Experimental procedure

For the production of dsGUVs a microfluidic device (cf. figure 3.8 B) with a flow focusing junction (cf. figure 3.9 A) was used. Tubes with an inner diameter of 0.3 mm connected the inlets of the device with the fluorocarbon oil (HFE-7500) supplemented with the uncharged PFPE-PEG-PFPE surfactant (1.4 wt%) and the charged PFPE-carboxylate surfactant (9 mM, 4.2 wt%, Krytox) respectively the LUV suspension (0.75 mg mL^{-1}). LUVs (POPC/POPG/Chol/lipid-coupled dye, 70-x/15/15/x, n/n) were produced as described in chapter 3.2.1.2 with droplet-buffer (cf. table 3.14) and, depending on the experiment, reconstituted with protein as described in chapter 3.2.2. The continous oil phase and the aqueous phase were flushed into the microfluidic chamber using a pressure controller system (OB 1 MK3, Elveflow Microfluidics, Paris, France) and applying pressures of 300 mbar and 250 mbar. The formation of droplets was observed by an inverted microscope (Axiovert 200, Zeiss, Oberkochen, Germany) and a high-speed camera (Fastcam SA1.1, Photron, Tokyo, Japan). The resulting droplets were collected in an eppendorf tube, using the aforementioned tubing connected to the outlet. Prior to usage, the droplets were incubated over night to allow the formation of a continuous bilayer at the water-oil interface. For

imaging and analysis the dsGUVs were transferred in a chamber contructed from a glass slide and cover slip as illustrated in figure 3.9 C.

Table 3.14: Buffers used for the production of dsGUVs and release of GUVs.

droplet buffer	20 mM HEPES, 100 mM KCl, 50 mM Sucrose, 10 mM MgCl$_2$, pH 7.4
release buffer	20 mM HEPES, 100 mM KCl, 80 mM Glucose, pH 7.4

3.2.3.3 Release of giant unilamellar vesicles

The release of GUVs from the continuous oil phase in an aqueous buffer phase was achieved by the destabilizing agent 1H,1H,2H,2H-perfluoro octanol (PFO, cf. table 3.13). Short-chain surfactants (C$_6$ to C$_{10}$) are not capable of creating long-term stability for microemulsions and are therefore used for de-emulsification.[103] PFO added in excess to the emulsion is able to displace the triblock copolymers from the water-oil interface decreasing the stability.[104] The higher polarity of the headgroup results in a lower surface activity due to uncontrolled agglomeration within the oil phase while the lower molecular mass results in a less effective steric stabilization of the droplets.[99]
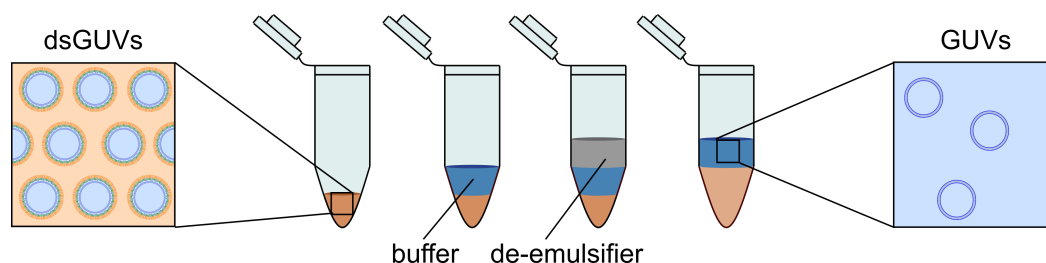
Figure 3.10: Bulk release of GUVs from a continuous oil phase in a physiological aqueous environement. A microemulsion containing dsGUVs (left) was overlayed carefully with buffer and a de-emulsifier (PFO) in a ration of 1:1:1 (*v/v/v*) resulting in GUVs in an aqueous environement (right).

These properties were exploited in this work for the release of GUVs as described previously.[54,94] The procedure is shown schematically in figure 3.10. 50 μL of the emulsion containing the dsGUVs were thoroughly overlayed 1:1:1 (*v/v/v*) with 50 μL release buffer (cf. table 3.14) and 50 μL of the PFO in fluorinated oil (30 % *v/v*)

resulting in the formation of an aqueous phase on top of the oil phase containing released GUVs. The GUVs were carefully separated from the oil phase by pipetting.

3.2.4 Pore-spanning membranes

To prepare pore spanning membranes (PSMs), GUVs obtained from droplet-based microfluidics or electroformation, respectively, were spread on functionalized porous substrates (Aquamarijn B. V., Zutphen, Netherlands) as depicted in figure 3.11. The 5 x 5 mm substrates were made of Si (0.9 mm) with a top layer of Si_3N_4 (0.5 μm) and had a porosity of (35-40) %. The porous pattern was composed of a hexagonal array of open pores with pore diameters of 1.2 μm or 5 μm and a height of 0.8 μm, stabilized by a surrounding rim of 1 mm. In this work, the substrates were functionalized by two different methods using gold and a self-assembled monolayer (SAM) from 6-mercapto-1-hexanol (6MH) on the one hand and SiO_x on the other hand (cf. figure 3.11 B, C).[79,105]
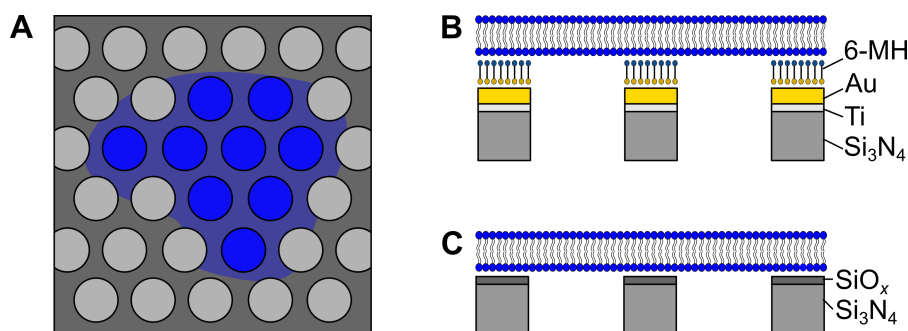
Figure 3.11: Illustration of pore-spanning membranes on top of functionalized Aquamarijn substrates. A: Illustration of a membrane patch on an Aquamarijn substrate with a hexagonal array of open pores. Substrates were functionalized prior to the spreading of GUVs with AU/6MH (**B**) or SiO_x (**C**).

Prior to the functionalization, substrates were cleaned with Argon plasma (0.2 mbar, 30 s, 60 % relative power) with a plasma cleaner (Zepto, Diener Electronic, Ebhausen, Germany). The functionalization proceeded in two different routes as described below.

Functionalization with Au/6MH

Rinsed substrates were coated with a thin layer of titanium in a sputter coater (Cressington Sputter Coater108auto, Watford, UK) for 30 s at 40 mA and 0.4 mbar

in an Argon atmosphere. After the exposure to ambient air, the titanium layer was oxidized immediatly to titanium dioxide, serving as adhesion promoter for the gold coating. Subsequently a thin layer of gold ($\sim 30\,\text{nm}$) was applied orthogonally by thermal vapor deposition under vacuum ($(0.3\text{-}0.4)\,\text{nm}\,\text{s}^{-1}$, $6 \cdot 10^{-6}\,\text{mbar}$, $62\,\text{A}$, MED020 coating system, Bal-Tec, Balzers, Lichtenstein). The functionalization was finalized by incubating the substrates in an *n*-propanolic solution of $1\,\text{mM}$ 6-mercapto-1-hexanol (6MH) over night at $4\,°\text{C}$. A hydrophilic surface was formed by exploiting the strong thiol-gold bond. The substrates were stored in the same solution until usage at $4\,°\text{C}$. For preparing PSMs, the substrates were cleaned with *n*-propanol and PSM buffer ($20\,\text{mM}$ HEPES, $140\,\text{mM}$ KCl, pH 7.4) and fixed to the bottom of a petri dish using a two-component glue. It was ensured that the substrates were wetted with liquid at each stage in order to impede that air can enter the pores. A chamber made of steel was used for fluorescence correlation spectroscopy (cf. chapter 3.3.3.4).

Functionalization with SiO$_x$

Cleaned substrates were functionalized with a $30\,\text{nm}$ laxer of silicon monooxide by thermal evaporation under vacuum ($(0.3\text{-}0.4)\,\text{nm}\,\text{s}^{-1}$, $6 \cdot 10^{-6}\,\text{mbar}$, $95\,\text{A}$, MED020 coating system, Bal-Tec, Balzers, Lichtenstein). An incubation for $1\,\text{h}$ in ultrapure water ($55\,°\text{C}$) resulted in the formation of a highly hydrophilic surface of SiO$_x$ ($1 \geq x \geq 2$).[105,106] Immediately thereafter, the substrates were cleaned with *n*-propanol and the PSM buffer and mounted on a petri dish or clamped in a teflon or steel chamber for further processing.

Preparation of pore-spanning membranes

After mounting the substrate in the measuring chamber or petri dish, buffer was filled on top. GUVs obtained from droplet-based microfluidics (cf. chapter 3.2.3) or electroformation (cf. chapter 3.2.1.3) were used to prepare PSMs. Care was taken to ensure that all buffers and solutions used were iso-osmolar.
For the preparation of PSMs derived from the microfluidic approach, GUVs were released from droplets in PSM buffer as described in chapter 3.2.3.3. $50\,\mu\text{L}$ of the GUV suspension were pipetted carefully on top of the substrate and incubated for $2\,\text{h}$ to allow spreading. GUVs adhere to the functionalized surface and a spontaneous rupture occurs resultig in the formation of PSMs. Electroformed GUVs were spread on porous substrates with a sedimentation method using a $5\,\text{mL}$ Eppendorf tip.

100 µL of the GUV suspension were added into the tip, filled with PSM buffer, serving as a column to separate vesicles from impurities. The column was placed centrally above the substrate and the GUVs sedimented for one minute. GUVs were allowed to spread for 30 min. Afterwards the substrates were cleaned with PSM buffer (10×1 mL).

3.3 Biophysical methods

3.3.1 Bioluminescence spectroscopy

Bioluminescence of the luciferin-luciferase system

The term luminescence includes various processes, in which energy supplied from the environment converts a physical system into an excited state. Returning into its ground state, photons are emitted. Energy can be supplied for instance in the form of photons (photoluminescence: fluorescence and phosphorescence) or through chemical reactions (chemiluminescence) catalyzed by enzymes from living organisms (bioluminescence). In bioluminescence, the enzyme (luciferase) catalyzes the formation of the high-energy transition state of its substrate (luciferin). Luciferases from different organisms are not homologous and the luciferins are chemically different. However, all of them form a luciferase-bound peroxy-luciferin intermediate, the degradation of which provides the energy for excitation.[107–109] In this work, the luciferin-luciferase system from the american firefly (*Photinus pyralis*) was exploited to detect ATP in a highly sensitive, specific and quantitative manner.

Firefly luciferin is a benzothiazoyl-thiazole, whose crucial high-energy intermediate state is a dioxetanone similar to other luciferins of various organisms.[109] The exact mechanism of the light emitting reaction is shown in figure 3.12. In the first step, the luciferase catalyzes the condensation of D-luciferin (I) with ATP under elimination of pyrophosphate resulting in an intermediate bound to AMP (II). After the elimination of two protons (III), a reaction with oxygen follows, resulting in the formation of a peroxide (IV), which cyclizes after the elimination of AMP (V). The subsequent decarboxylation is responsible for the release of the energy (approximately $210\,\mathrm{kJ\,mol^{-1}}$) required to form oxyluciferin (VI) in its first singlet excited state (S_1).[109,110] Relaxation to the ground state (S_0, VII) leads to an emission of light with high efficiency. The emission wavelength depends not only on the structure of the substrate but also on the protein environment since the substrates are typically protein-bound. The system from *Photinus pyralis* exhibits am emission wavelength of 562 nm with a quantum yield of 0.88.[109–111]
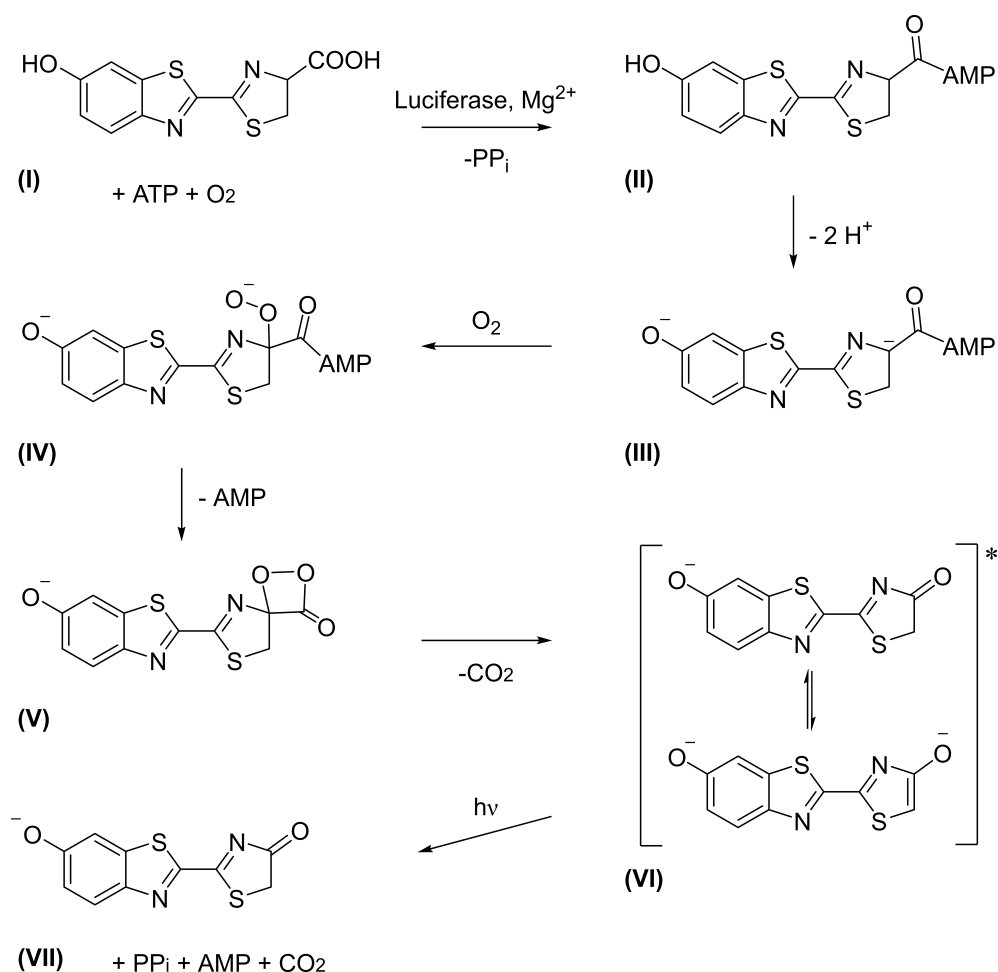
Figure 3.12: Mechanism of the firefly luciferin luciferase reaction. Luciferin (I) reacts with ATP in the presence of Mg^{2+} to an AMP-bound intermediate (II). Deprotonation and subsequent formation of a peroxide result in intermediates (III) and (IV), respectively. The latter cyclizes after the elimination of AMP and yields in intermediate (V). Decarboxylation leads to the exited state of oxyluciferin (VI) which is transferred into the ground state (VII) by emitting light.

Purification of ADP

Conventional commercially available ADP contains residues of ATP, which can interfere with the ATP synthesis assay. To reduce this effect, ADP was purified from ATP impurities prior to the ATP synthesis assay by an approach using a hexokinase. 100 mM ADP solved in hexokinase buffer (20 mM Tris, 100 mM $MgCl_2$, 10 mM glucose, 10 units mL^{-1} hexokinase, pH 7.5) were incubated at 37 °C overnight, resulting in the degradation of ATP to ADP and phosphate catalyzed by the hexokinase. Subsequently, the protein was removed by twofold centrifugation filtration (molecular

weight cut off 10 kDa). The purified ADP stock (100 mM) was aliquoted and stored at $-20\,°\text{C}$ until usage.

3.3.1.1 ATP synthesis assay in LUVs

Experimental procedure of the ATP synthesis assay using chemiluminescence

As mentioned in chapter 1.4, the $\text{TF}_\text{O}\text{F}_1$ ATP synthase is a reversible protein, which is able to actively transport protons across the membrane consuming ATP, as well as to produce ATP by proton translocation in the opposite direction.[70] Here, ATP synthesis by the $\text{TF}_\text{O}\text{F}_1$ ATP synthase was determined, which is induced by the proton motive force (*pmf*) depending on a pH- and a K^+-gradient across the membrane. The luciferin-luciferase system from *photinus pyralis* was employed for the determination of the ATP synthesis from $\text{TF}_\text{O}\text{F}_1$. In general, the light emitting reaction can occur in two different types. Either it proceeds in a so-called flash type reaction, in which the light emission reaches its maximum within a few seconds and then decays rapidly, or in a glow type reaction, in which the light signal is sustained for several minutes. In this work, a glow type luciferin-luciferase system (ATP Bioluminescence Assay Kit CLS II, Roche, Basel, Suisse) was used. The system was optimized for kinetic measurements and has a working range from 10^{-6} M to 10^{-11} M ATP and is thus optimal for the requirements desired here.[112–114]
The $\text{TF}_\text{O}\text{F}_1$ activity assay was carried out as described below using a microplate luminometer (LB centro 960, Berthold Technologies, Bad Wildbach, Germany). The system is equipped with a temperature control unit and three high-power injectors. Injector 3 is placed in a direct measuring position, allowing kinetic measurements immediately after the addition of reactants without loss of data. Luminescence of the samples can be detected in 96-well plates with a low-noise photon multiplier in single photon counting mode and a spectral range of 340 nm to 630 nm offering a high sensitivity (< 4 amol ATP, < 2 zmol firefly luciferase).

The $\text{TF}_\text{O}\text{F}_1$ ATP synthase was reconstituted in LUVs as described in chapter 3.2.2.1 with reconstitution buffer R1. Figure 3.13 illustrates the practical procedure of the ATP synthesis assay. In the first step, the lumenina of the proteoliposomes were acidified using acidification buffer (A_pH, cf. table 3.15) of various pH values (pH 4.0, 4.7, 5.0, 5.2, 5.4, 5.6, 5.8, 6.0, 7.0), containing ADP (0.1 mM), NaH_2PO_4 (5 mM)
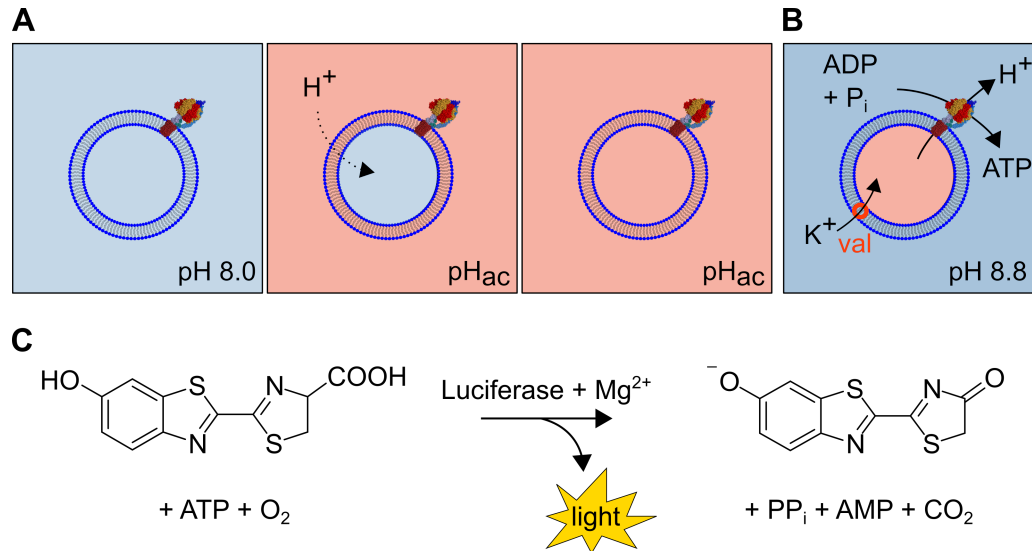
Figure 3.13: Schematic illustration of the ATP synthesis assay based on a luciferin-luciferase system. A: The lumenina of proteoliposomes were acidified by incubation in acidification buffer (pH $\leq$ 7.0) until an equilibration of outer and inner pH occured. **B:** Addition of assay buffer (pH 8.8) resulted in the formation of an H^+- and a K^+-gradient inducing ATP production of TF_OF_1 and proton translocation in the outer environment. The ionophore valinomycin enabled charge compensation by transport of K^+ in the opposite direction. **C:** ATP was visualized by a luciferin-luciferase system. In the presence of ATP, D-luciferin was converted to oxyluciferin, releasing a luminescence signal.

and valinomycin (20 µM, *val/l* 40:1, *n/n*), by incubating 10 µL of the proteoliposome suspension with 40 µL of the respective acidification buffer for three minutes at room temperature. Protons were translocated in the proteoliposomes lumen resulting in a pH decrease (cf. figure 3.13 A). 50 µL of the acidified proteoliposome suspension were transferred in a well of a non-binding microplate, which was inserted in the luminometer. Immediatly after starting the measurement, the plate entered the luminometer and a baseline was monitored for 10 s. To initiate the activity of the TF_OF_1 ATP synthase, 100 µL of the luminescence assay buffer containing the luciferin-luciferase reagent (1:5 *v/v*) with a pH value of 8.8 and a K^+ concentration of 160 mM ($L_{8.8}$) were added by injector 3 of the luminometer and a time course was measured for 60 s. The pH- and K^+-gradients across the membrane together generate a membrane potential (ψ) and the proton motive force (*pmf*, cf. equations 3.7 and 3.6) which directly influence the protein activity.[75,115]

$$\Delta\psi = \frac{TR}{F} \cdot ln\frac{[K_{out}^+]}{[K_{in}^+]} = 135 \text{ mV} \tag{3.6}$$

$$pmf = \Delta\psi + 2.3 \cdot \frac{k_B T}{e} \cdot \Delta pH = \Delta\psi + 60\text{mV} \cdot \Delta pH \tag{3.7}$$

T is the temperature, R the gas constant, F the Faraday constant, k_B the Boltzmann constant and e the elementary charge. All measurements were performed at a constant temperature of 27.5 °C. The K$^+$ gradient and thus the membrane potential ψ were kept constant at 135 mV, while the proton gradient and thus the *pmf* were varied. This leads to the simplification of the formulas as described in equation 3.7. Subsequently, 15 pmol ATP (10 µL of a 15 µM stock) were injected to the assay mixture and the luminescence signal was detected allowing to translate the emitted luminescence signal into an ATP concentration. Liposomes without TF$_\text{O}$F$_1$ were used as a negative control in analogy to the described procedure.

Table 3.15: Buffers used for the ATP synthesis assay.

buffer A$_{4.0-5.8}$	20 mM succinic acid, 0.6 mM KCl, 5 mM NaH$_2$PO$_4$, 2.5 mM MgCl$_2$, 0.1 mM ADP*, 20 µM valinomycin*, pH 4.0-5.8
buffer A$_{6.0-7.0}$	20 mM bis-tris, 0.6 mM KCl, 5 mM NaH$_2$PO$_4$, 2.5 mM MgCl$_2$, 0.1 mM ADP*, 20 µM valinomycin*, pH 6.0-7.0
buffer L$_{8.8}$	200 mM tricine, 160 mM KOH, 5 mM NaH$_2$PO$_4$, 2.5 mM MgCl$_2$, 0.1 mM ADP*, pH 8.8
	*add immediately before usage

Evaluation of data

The turnover number v_cat was determined as presented in figure 3.14. Extracted luminescence intensity values ($I_\text{raw, 0-60 s}$, figure 3.14 A, black) had to be background corrected (I_bg) by means of the control measurement (cf. figure 3.14 A, grey) as shown in equation 3.8). The background intensity results from the addition of the assay buffer L$_{8.8}$ containing the luciferin-luciferase kit. Nonspecific luminescence emission occurs due to low residual ATP impurities in the ADP stock.

$$I_\text{corr}(t) = I_\text{raw,0-60 s}(t) - I_\text{bg} \tag{3.8}$$
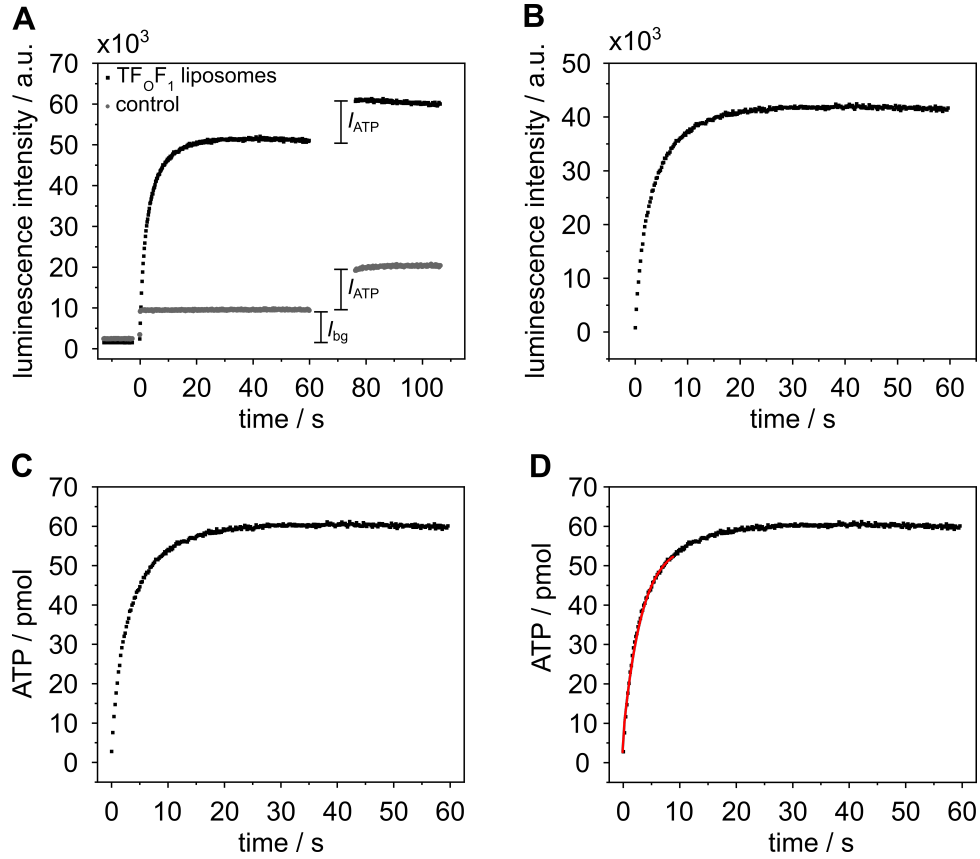
Figure 3.14: Exemplary evaluation of the ATP synthesis assay to determine the ATP production per second from the $\mathbf{TF_O F_1}$ ATP synthase. A: Raw data of an ATP synthesis assay with proteliposomes (black) and lipsomes (negative control, grey). I_{bg} represents the luminescence intensity of background after addition of buffer $L_{8.8}$ containing the luciferin-luciferase kit. I_{ATP} describes the increase of the luminescence intensity after ATP (15 pmol) addition. **B:** Background corrected luminescence intensity against time of the ATP synthesis assay. **C:** The luminescence intensity was normalized to the produced ATP using the ATP standard. **D:** Exponential fit of the first 5-10 s for the determination of the initial slope at $t = 0$ s. (cf. equations 3.8 to 3.12).

To normalize the corrected luminescence signal (I_{corr}, cf. figure 3.14 B) to a defined amount of ATP, an ATP standard (15 pmol) was added after each measurement. All measurements were performed in triplicates. The luminescence signal of the ATP standards (I_{ATP}) of all measurements were averaged and used for normalization as shown in equation 3.9.

$$n_{ATP}(t) = I_{corr}(t) \cdot \frac{15 \text{ pmol}}{I_{ATP}} \tag{3.9}$$

The normalized curve (cf. figure 3.14 C) was fitted with the exponential function described in equation 3.10. The first (5-10) seconds were used for this purpose (cf. figure 3.14 D). The obtained parameters can be used to calculate the slope at time $t = 0$ s (v) according to equation 3.11.

$$f(t) = a \cdot \exp\left(-\frac{t}{b}\right) + c + d \cdot t \tag{3.10}$$

$$v = -\frac{a}{b} + d \tag{3.11}$$

The flotation assay (cf. chapter 3.2.2.4) allows for the determination of the exact amount of the TF_OF_1 ATP synthase per assay (n_{TFOF1}). As described in equation 3.12, the turnover rate v_{cat} per single protein was calculated from the overall ATP synthesis rate v.

$$v_{cat} = \frac{v}{n_{TFOF1}} \tag{3.12}$$

3.3.1.2 ATP synthesis assay in dsGUVs

In addition to the activity analysis of TF_OF_1-LUVs, the activity of the TF_OF_1 ATP synthase reconstituted in dsGUVs and released GUVs was studied in the context of this work. Protein reconstitution into LUVs (POPC/POPG/Chol/TxR DHPE, 69/15/15/1, n/n) proceeded as described in chapter 3.2.2.1, but $MgCl_2$ concentration was increased to $10\,mM$ in each case prior to subsequent microfluidic production of proteo-dsGUVs (cf. chapter 3.2.3.2). Unless otherwise described, proteo-GUVs were released (cf. chapter 3.2.3.3) in modified release buffer, iso-osmolar to the reconstitution buffer ($20\,mM$ HEPES, $16\,mM$ KCl, pH 7.4). While the activity detection of released GUVs was carried out analogously to the procedure described above, a different approach was chosen for dsGUVs due to the surrounding oil phase. As described from Weiss et al., the proton gradient ($\Delta pH = 3$) required for the *pmf* was induced by an acidic oil phase.[45] To achieve this, trifluoroacetic acid (TFA) was dissolved in the fluorinated oil at a ratio of 1:1,000 (v/v). TF_OF_1 ATP synthase was reconstituted in LUVs (cf. chapter 3.2.2.1) and subsequently dsGUVs (cf. chapter 3.2.3.2) were produced, using the respective reconstitution

buffer supplemented with $0.1\,\text{mM}$ ADP and $5\,\text{mM}$ NaH_2PO_4. $100\,\mu L$ of dsGUVs were mixed with $20\,\mu L$ of the acidified oil and incubated for $2\,\text{min}$ to $5\,\text{min}$ allowing the synthesis of ATP inside the dsGUVs. As described in chapter 3.2.3.3, the content of the droplets was released into $100\,\mu L$ buffer (modified release buffer) using the de-emulsifier PFO ($30\,\%$, v/v) and transferred in a well of a 96 well plate placed in the luminometer. After injection of $100\,\mu L$ droplet buffer, containing $20\,\mu L$ of the luciferin-luciferase system, the luminescence intensity of the sample was measured for $60\,\text{s}$.

3.3.2 Fluorescence spectroscopy

The activity of the TF_OF_1 ATP synthase basically depends on the acidification step of the ATP synthesis assay. A fluorescence-based acidification assay was designed for further elucidation. Fluorescence is the emission of light resulting from transitition of a molecule in an excited singlet state (S_1, S_2,...) into its ground state (S_0). In contrast to bioluminescence, the energy for the excitation is not provided by a chemical reaction, but by light of a specific wavelength (excitation wavelength, λ_{ex}). Returning into the ground state, light shifted to longer wavelengths (λ_{em}, Stokes-shift), is emitted from the system. Typical molecules operating as fluorophors possess more or less distinct π-systems.[116]

To determine the vesicle acidification in dependence of the outer pH, the pH-sensitive, membrane-impermeable and water soluble fluorophor pyranine (1-hydroxypyrene-3,6,8-trisulfonate, HPTS) was used (cf. figure 3.15 A). Pyranine represents a group of fluorophores differing in the pK_a values for their ground and excited state. The pK_a is decreased from 7.2 for the ground state to 0.4 for the excited state, explaining the different shapes of absorption and emission spectra in the pH range between 7.2 and 0.4. At a lower pH ($7.2 \geq$ pH $\geq$ 0.4), pyranine is protonated and the absorption spectrum shows the vibrational structure of a hydrocarbon molecule. In contrast, the electronically excited species is deprotonated due to its lower pK_a resulting in completely different shaped emission spectrum.[116,117]

Experimental procedure of the acification assay

The change of the absorption spectrum of pyranine, depending on the protonation state of its 8-hydroxyl group, was exploited here. The excitation maximum shifts

from 458 nm (deprotonated species) to 405 nm (protonated species) as depicted in figure 3.15 B, leading to an emission maximum at 512 nm.
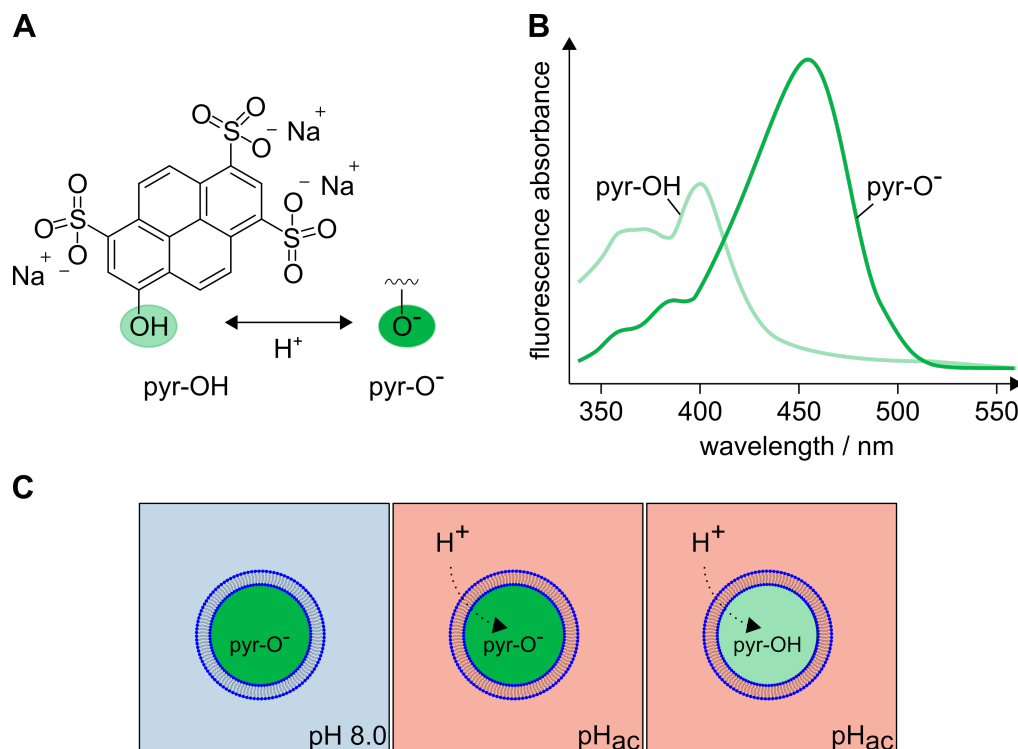
Figure 3.15: Illustration of the acidification assay. A: Chemical structure of pyranine in its protonated (light green) and deprotonated (dark green) state. **B:** Absorption spectra of protonated (light green) and deprotonated (dark green) pyranine. The absorption maximum $\lambda_{ex,max}$ shifts from 405 nm to 458 nm upon protonation of the 8-hydroxyl group. **C:** Schematic illustration of the acidification assay using pyranine. Incubating pyranine-filled liposomes (pH 8.0) in acidification buffer (pH $\leq$ 7.0) leads to the spontaneous influx of protons. The decrease pH_{in} results in a decrease of the pyranine fluorescence emission ($\lambda_{ex/em} = 458/512$ nm).

Vesicles were prepared as described in chapter 3.2.1.2 in reconstitution buffer R1 (cf. chapter 3.2.2.1) doped with 500 μM pyranine. To get rid of extravesicular pyranine, a size exclusion chromatography (illustra NAP-25, GE Healthcare Life Science, Solingen, Germany) was performed. Vesicles were diluted in reconstitution buffer R1 to a final lipid concentration of 50 μM and a volume of 400 μL and transferred to a quartz cuvette. The acidification assay was conducted as depicted in figure 3.15 C. Pyranine fluorescence was monitored with a fluorimeter (FP-6500, Jasco Germany GmbH, Groß-Umstadt, Germany) at $\lambda_{ex} = 458$ nm and $\lambda_{em} = 512$ nm. A baseline was monitored for 100 s prior to the addition of 1.6 mL of acidification buffer

A_{pH} lacking valinomycin and ADP (cf. chapter 3.3.1.1, table 3.15) to the vesicle suspension. After 200 s, vesicles were lysed with 32.5 µL of a 3 % (w/v) solution of lauryldimethylamine oxide (LDAO) and the emission was detected for another 60 s. Additional measurements were performed in the presence of valinomycin, which was added to the acidification buffer at a val/l ratio of 1/40. For evaluation, all data points measured after addition of the acidification buffer were multiplied by a factor of 5 due to the given dilution (dilution factor). The curves were normalized to the baseline after addition of the pyranine vesicles.

pK_a determination of pyranine in liposomes

To determine the pK_a value of pyranine, LUVs (POPC, nominal diameter 100 nm) were prepared as described before in reconstitution buffer R1$_{pH}$ (table 3.16) differing the pH (8.0, 7.0. 6.0, 5.8, 5.0, 4.0). The lipsomes were diluted with the respective buffer (pH$_{in}$ = pH$_{out}$) to a final concentration of 50 µM and a volume of 400 µL and transferred into a quartz cuvette. The samples were excited at λ_{ex} = 458 nm and emission spectra were measured from 480-650 nm. The emission maxima at λ_{em} = 512 nm were extracted, normalized to the maximum at pH = 8.0 and plotted against the pH values. To determine the pK_a value, a variant of the Henderson-Hasselbalch equation was fitted to the data (cf. chapter 4.3.1.2).[118,119]

Table 3.16: Buffers used for determination of the pK_a value of pyranine.

rec. buffer R1$_{8.0}$	20 mM Tricine, 20 mM succinic acid, 0.6 mM KCl, 2.5 mM MgCl$_2$, pH 8.0
rec. buffer R1$_{7.0/6.0}$	20 mM Bis-Tris, 20 mM succinic acid, 0.6 mM KCl, 2.5 mM MgCl$_2$, pH 7.0/6.0
rec. buffer R1$_{5.8/5.0/4.0}$	40 mM succinic acid, 0.6 mM KCl, 2.5 mM MgCl$_2$, pH 5.8/5.0/4.0

3.3.3 Fluorescence microscopy

3.3.3.1 Principle of confocal laser scanning microscopy

For the visualization of a specimen doped with a fluorescent dye, confocal laser scanning microscopy (CLSM) was used. In contrast to epifluorescence microscopy,

CLSM is not based on the illumination of the entire sample, but the point by point scanning and exclusion of out-of-focus light enabling a higher resolution of the overall image to be constructed afterwards.[120]
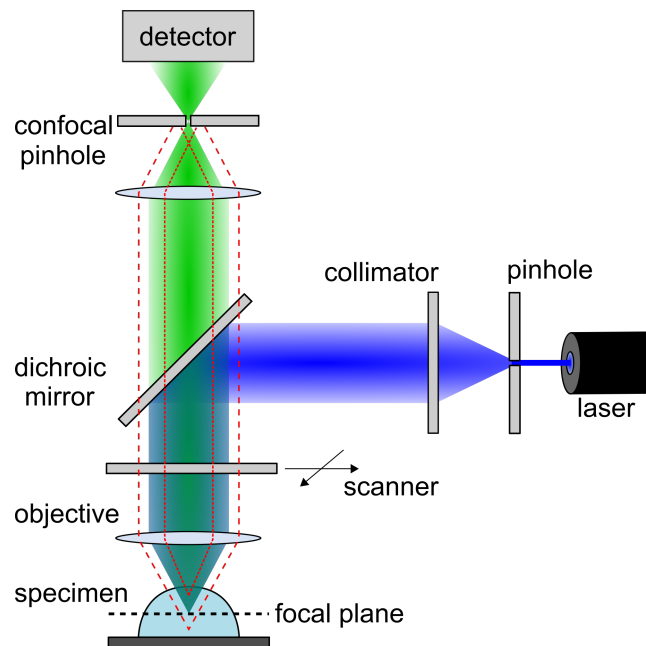
Figure 3.16: Schematic illustration of a confocal laser scanning microscope.
Light of a specific wavelength, created by a laser and an excitation filter, is focussed through a pinhole and reflected by a dichroic mirror on a specimen containing fluorescent molecules. Emitted light passes the dichroic mirror and a second pinhole before reaching the detector.

The setup of a CLSM is illustrated in figure 3.16. Excitation light is provided by a laser emitting several wavelengths. The desired wavelength is selected by an excitation filter, the beam is focussed by a first pinhole, collimated and reflected by a dichroic mirror, creating a reduced image of the pinhole in the specimen. Due to the diffraction at the pinhole aperture, an airy disk is created at the focus point. Scanning mirrors enable step-by-step screening of the specimen. The emitted, red-shifted light from the fluorophores in the sample is allowed to pass the dichroic mirror and is focussed by a second confocal pinhole to the detector. Detection occurs typically with low-noise and fast-response photomultiplier tubes (PMT). While the first pinhole enhances the x-y confocality, the second pinhole excludes out-of focus information, thus optimizing the z confocality.[120] In this work, confocal laser scanning microscopy was used to image dsGUVs, GUVs and PSMs doped with fluorescently labeled lipids and proteins. In addition, fluorescence recovery after photobleaching (FRAP) and

fluorescence correlation spectroscopy (FCS) experiments were performed to determine the lateral mobility of the labeled compounds.

3.3.3.2 Immobilization of GUVs via Biotin/Neutravidin interactions

To simplify the imaging and further investigation of GUVs, their immobilization on a functionalized glass surface via the biotin-NeutrAvidin interaction was expedient, depending on the experiment. Glass slides ((22×22) mm, ThermoFisher Scientific, Brunswick, Germany) were rinsed thoroughly with ultrapure water and ethanol (p.a.) and treated with oxygen plasma at $60\,\%$ relative power and 0.4 mbar for 30 s (Zepto, Diener Electronic, Ebbhausen, Germany). 3-glycidyloxipropyltrimethoxysilane was added between two glass slides, creating stacks to reduce the contact of the surface with atmospheric water. The glass slides were incubated for 1 h at $80\,°C$. After the incubation, the glass slides were separated and cleaned with aceton and dried via a nitrogen stream. α-methoxy-ω-amino-PEG (2 kDa) and α-amino-ω-biotin-PEG (3 kDa) were mixed in a ratio of 9:1 (n/n), melted at $85\,°C$ and spreaded between the two pre-heated glass slides. The resulting stacks were incubated over night at $80\,°C$. After being rinsed (ultrapure water, ethanol (p.a.)), the separated glass slides were dried under nitrogen stream and stored at $4\,°C$.[119,121]

Prior to usage, glass slides were fixed to the bottom of a petri dish and incubated with a NeutrAvidin solution (0.1 mg mL^{-1}) for at least 15 min. After cleaning with the respective buffer (10×1 mL), 50 to 100 µL of released GUVs doped with 0.1 mol% biotinyl-cap-DOPE were added. The GUVs were allowed to sediment and bind for 2 h.

3.3.3.3 Fluorescence recovery after photobleaching (FRAP)

Fluorescence recovery after photobleaching (FRAP) describes the regeneration of the fluorescence intensity after a bleaching event in order to study diffusion of fluorescently labeled lipids or proteins in native or model systems. In this work, FRAP experiments were performed to characterize the lateral mobility of lipids and proteins (syb 2-Atto488) in dsGUVs, GUVs and the solid supported part of pore-spanning membranes (s-PSM). The theoretical fluorescence time-course of a typical FRAP experiment is illustrated schematically in figure 3.17.
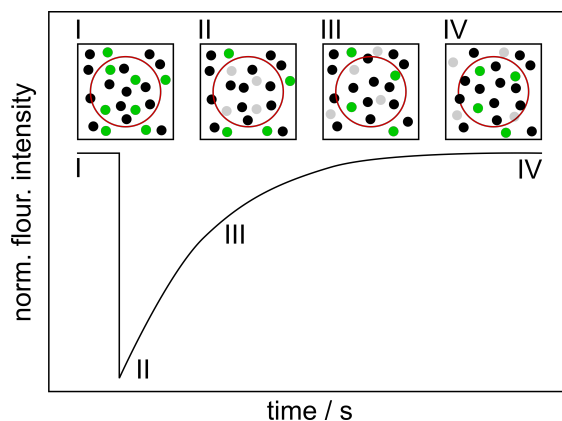
Figure 3.17: Schematic ilustration of the fluorescence recovery after photo-bleaching. The fluorescence intensity of fluorophores (green) is observed in a region of interest (red circle) of a 2D plane (I). A high intensity laser stimulus leads to an irreversible photobleaching of the fluorophores (grey) and a decrease in fluorescence intensity (II). The fluorescence intensity recovers over time due to lateral diffusion (III, IV).

To perform a FRAP experiment, the fluorescence intensity is monitored in a region of interest (ROI), before fluorescent molecules (labeled lipids or proteins) are irreversibly and photochemically bleached by a high-intensity laser stimulus. The fluorescence intensity is greatly decreased. As a function of the lateral mobility, unbleached fluorophores diffuse into and bleached fluorophores diffuse out of the ROI, resulting in a regeneration of the fluorescence intensity over time and allowing the determination of the diffusion coefficient D. If the observed fluorescent molecules are entirely mobile, the final fluorescence intensity returns to the level of intensity prior to the bleaching stimulus after a sufficiently long time. A difference indicates an immobile fraction of these fluorophors. According to the investigated model system, different procedures are required for the quantitative evaluation of the recovery curve. However, for the isotropic 2D systems studied in this work, the diffusion of fluorophores can be described by means of Fick's second law:

$$\frac{\partial c_{x,i}(x,t)}{\partial t} = D_i \nabla^2 c_{x,i}(x,t).$$ (3.13)

x is the radial distance, t the time and c_i the concentration of fluorophores of the ith species with different diffusion coefficients D_i.[122,123]

Determination of the lateral mobility in dsGUVs and GUVs

The lateral mobility of fluorescent lipids was determined using dsGUVs and released GUVs as model systems, prepared as described in chapter 3.2.3 (POPC/POPG/Chol/ Atto488 DPPE, 69/15/15/1, n/n). Studying the diffusion of fluorescently labeled syb 2, coupled to Atto488 or Atto647N, within these systems, proteoliposomes (POPC/POPG/Chol/Atto390 DPPE, 69/15/15/1, n/n) were prepared as specified in chapter 3.2.2.2. The microfluidic production of proteo-dsGUVs and proteo-GUVs was carried out analogously to the protocol without proteins. Unless otherwise described, biotin-cap-DOPE was incorporated into the lipid bilayer for the immobilization of the released GUVs on a functionalized glass surface (cf. chapter 3.3.3.2). dsGUVs were injected in a chamber consisting of a glass slide and a cover slip for further analyzation. FRAP experiments were carried out on the top plane of the GUVs and the bottom plane of the dsGUVs, respectively, to avoid an influence of the glass surface (cf. figure 3.18 A). A FluoView 1200 CLSM (Olympus, Tokyo, Japan) equipped with a dry objective (LUCPLFLN 40X, NA 0.6, Olympus, Tokyo, Japan) and a water immersion objective (LUMFLN 60XW, NA 1.1, Olympus, Tokyo, Japan). The settings used in the FRAP experiments are described in table 3.17.

Table 3.17: Settings used for the performance of FRAP experiments.

laser power	(5-10) % (20 mW)
frame time	64.9 ms
frames	200
resolution	256×256 pixel
stimulus duration	(64.9-90) ms
stimulis power	100 % (20 mW)
nominal radius r_n	(1.2-2.9) µm

The evaluation of the fluorescence recovery curves was performed as described previously.[124–126] An isotropic and two dimensional system was assumed as well as a circular stimulus area, where bleaching of fluorophors happened, which resulted in a Gaussian intensity profile. The stimulus area was assumed to be small compared to the overall model system. These premises were applied to the systems used here, whereby the bottom plane of a dsGUV an the top plane of a GUV, respectively, was assumed to be a 2D plane.[126] The fluorescence intensity $F(t)$ of the ROI over

the time t had to be corrected regarding the background intensity (F_{bg}) and the effect of photofading over time ($F_{\mathrm{f}}(t)$) and normalized by the prebleach fluorescence intensity ($F_{\mathrm{corr,initial}}$) as described in equations 3.14 and 3.15.[125,126] F_{bg} corresponds to a reference ROI adjacent to the GUV/dsGUV while $F_{\mathrm{f}}(t)$ can be obtained from an unbleached ROI on the GUV/dsGUV.

$$F_{\mathrm{corr}}(t) = \frac{F(t) - F_{\mathrm{bg}}}{F_{\mathrm{f}}(t) - F_{\mathrm{bg}}} \tag{3.14}$$

$$F_{\mathrm{corr,norm}}(t) = \frac{F_{\mathrm{corr}}(t)}{F_{\mathrm{corr,initial}}} \tag{3.15}$$

Equation 3.16 was fitted to the corrected fluorescence recovery over time ($F_{\mathrm{corr}}(t)$) to determine the half time of the fluorescence recovery $\tau_{1/2}$. It is crucial to note that the fit should be applied between the first frame after bleaching stimulus ($t = 0\,\mathrm{s}$) to the first point of full recovery.[79,125,126]

$$F_{\mathrm{corr,norm}}(t) = Ae^{-2\tau_{1/2}/t}[I_0(2\tau_{1/2}/t) + I_1(2\tau_{1/2}/t)] \tag{3.16}$$

I_0 and I_1 are modified Bessel functions of 0th and 1st order. The extracted half time of the fluorescence recovery $\tau_{1/2}$ was used for evaluating the diffusion coefficient D according to equation 3.17 described by Kang et al.:[126]

$$D = \frac{r_{\mathrm{e}}^2 + r_{\mathrm{n}}^2}{8\tau_{1/2}}. \tag{3.17}$$

The diffusion coefficient is dependent on $\tau_{1/2}$, the nominal bleach radius (r_{n}) and the effective bleach radius (r_{e}). The nominal bleach radius is the radius set by the user to $(1.2\text{-}2.9)\,\mu\mathrm{m}$ (cf. table 3.17). The determination of the effective bleach radius is dictated by the chosen measurement method. A Gaussian bleach profile was generated by a tornado-shaped laser stimulus. During the bleaching stimulus up to the acquisition of the first frame, unbleached fluorophores can diffuse into and bleached fluorophores out of the ROI. Thus, r_{e} is larger than r_{n}. The effective bleach radius was determined from the normalized postbleach profile obtained from circular averaging of the fluorescence intensity (cf. figure 3.18 B). The ImageJ plugin

"Radial profile Plot" was consulted for this purpose. r_e was determined from a linear interpolation of the radial fluorescence intensity data with a bleach depth K at $0.86K$.[126]
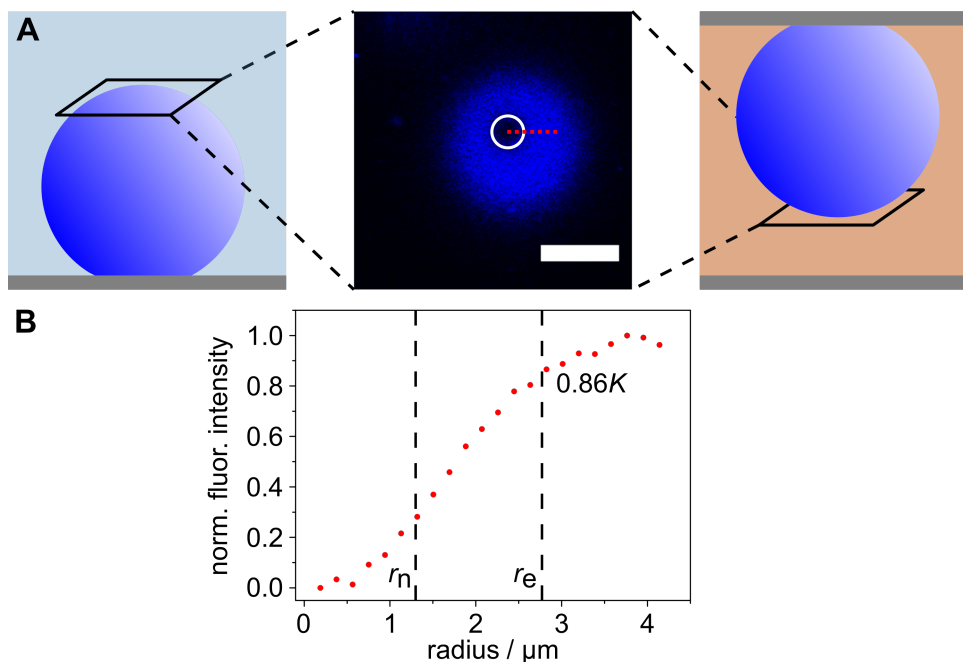
Figure 3.18: Schematic illustration of the post bleach profile of FRAP experiments with GUVs and dsGUVs. A: The top plane of a GUV (left) and the bottom plane of a dsGUV (right), respectively, was assumed as a 2D system for performing FRAP experiments. The fluorescence micrograph of post bleach profile (middle) was used to determine the effective bleach radius from the normalized radial intensity profil. The white circle highlights the nominal ROI while the red dashed line represents the radius used for the extraction of the radial intensity profile. Scale bar: 10 μm. **B:** Normalized integrated radial intensity. The nominal radius was user set while the effective radius was extracted from a linear interpolation at $0.86K$.

The mobile fraction F_m of the fluorescent molecules was extrated from the fluorescence intensity after recovery (F_∞), the intensity prior to ($F_{initial}$) and immediately after bleaching (F_0) according to equation 3.18.[79]

$$F_m = \frac{F_\infty - F_0}{F_{initial} - F_0} \qquad (3.18)$$

Determination of the lateral mobility in s-PSMs

Finite element simulations (FEM, COMSOL Multiphysics v4.4) were performed together with Dr. Ingo P. Mey from the Institute of Organic and Biomolecular Chemistry (IOBC, Göttingen) from the working group of Prof. Dr. Claudia Steinem.

The diffusion of lipids in the solid supported part of PSMs (s-PSMs) was analyzed by indirect FRAP experiments with the aid of finite element simulation (FEM, COMSOL Multiphysics v4.4, Göttingen, Germany) as described in the works from Jan Kuhlmann and Peter Mühlenbrock.[36,79,81] The quenching of fluorescence intensity on the pore rim as a function of the surface coating (SiO$_x$ or Au) precludes the determination of $D_{s\text{-PSM}}$ via common FRAP experiments or fluorescence correlation spectroscopy (FCS).[127–130] For an indirect FRAP experiment the free-standing part of a PSM (f-PSM) has to be irreversibly bleached. The resulting shape of the fluorescence recovery is mainly dependent on the diffusion of fluorophores from the s-PSM into the f-PSM but also on the diffusion within the f-PSM. Thus, the diffusion coefficients of the s-PSM and f-PSM have to be considered for the evaluation. Moreover, the evaluation method described for FRAP experiments with dsGUVs and GUVs is infeasible here, since the determination of the effective radius r_e is affected as well by the quenching phenomen on the rim. Thus, a semi-quantitative method of combined experimental and simulated FRAP experiments was developed from Jan Kuhlmann.[81]

For gaining the experimental data, GUVs were produced via droplet-based microfluidics according to chapter 3.2.3 (POPC/POPG/Chol/ Atto488 DPPE, 69/15/15/1, n/n) and spread on porous substrates as described in chapter 3.2.4 (pore diameter: 5 µm). For FRAP measurements, the bleaching ROI was placed in the area of an entire f-PSM. Experimental settings were described in table 3.18 using a FluoView 1200 CLSM (Olympus, Tokyo, Japan) equipped with a water immersion objective (LUMFLN 60XW, NA 1.1, Olympus, Tokyo, Japan). Experimental data were corrected and normalized as described by equations 3.14 and 3.15. The background intensity (F_{bg}) was determined from a ROI on top of an uncovered pore, while the photofading ($F_f(t)$) was extracted from a ROI on top of an adjacent f-PSM.

Table 3.18: Settings used for the performance of FRAP experiments on s-PSMs.

laser power	(5-10) % (20 mW)
frame time	64.9 ms
frames	200
resolution	256 × 256 pixel
stimulus duration	64.9 ms
stimulis power	100 % (20 mW)
nominal radius r_n	(2.2-2.3) µm

FEM simulations solving Fick's second law (cf. equation 3.13) were employed to anticipate the shape of fluorescence recovery curves for different diffusion coefficients D_i for molecules in the s- and f-PSM. The diffusion coefficient for the f-PSM was kept constant at a value extracted from fluorescence correlation spectroscopy data (FCS, cf. chapter 3.3.3.4, $D_\text{f-PSM} = 13.5\,\mu\text{m}^2\,\text{s}^{-1}$) while the diffusion coefficient of the s-PSM was variied from $0.5\,\mu\text{m}^2\,\text{s}^{-1}$ to $3\,\mu\text{m}^2\,\text{s}^{-1}$. The simulated system was mainly optimized in accordance to the experimental conditions, assuming a total surface area of $60 \times 60\,\mu\text{m}^2$ possessing a hexagonal array of pores with a diameter of $5\,\mu\text{m}$ and an overall porosity of 36 %. The simulated radius of the bleaching ROI was set to $2.2\,\mu\text{m}$ (r_sim). The concentration of molecules in the ROI after a bleaching stimulus with a Gaussian intensity profile was modeled based on the work of Jönsson et al. by equation 3.19 with $c_\text{eq} = 1$, $K = 2$ and $t = 0$.[122]

$$c(r,0) = c_\text{eq} \cdot \left(1 - K \cdot \exp\left(\frac{-r^2}{r_\text{sim}}\right)\right) \tag{3.19}$$

Subsequently, the fluorescence recovery was modeled as a function of time resulting in simulated curves for different theoretical diffusion coefficients of the s-PSM ($0.5\,\mu\text{m}^2\,\text{s}^{-1}$ to $3\,\mu\text{m}^2\,\text{s}^{-1}$). Comparing simulated curves with corrected and normalized experimental curves allowed the semi-quantitative determination of the diffusion coefficient.

3.3.3.4 Fluorescence correlation spectroscopy (FCS)

Theoretical background

Lateral lipid diffusion is an essential factor to describe the dynamic properties of biological or artificial membrane systems.[131] Besides FRAP experiments (cf. chapter 3.3.3.3) for the determination of diffusion coefficients within dsGUVs, released GUVs and the s-PSM, the lipid diffusion coefficient within the free-standing part of the PSM (f-PSM) was adressed in this work by fluorescence correlation spectroscopy (FCS) using a confocal laser scanning microscope.

The principle of FCS is based on the detection of time traces of the fluorescence intensity $F(t)$ within a confocal volume of the sample at high temporal resolution as illustrated in figure 3.19.[131]
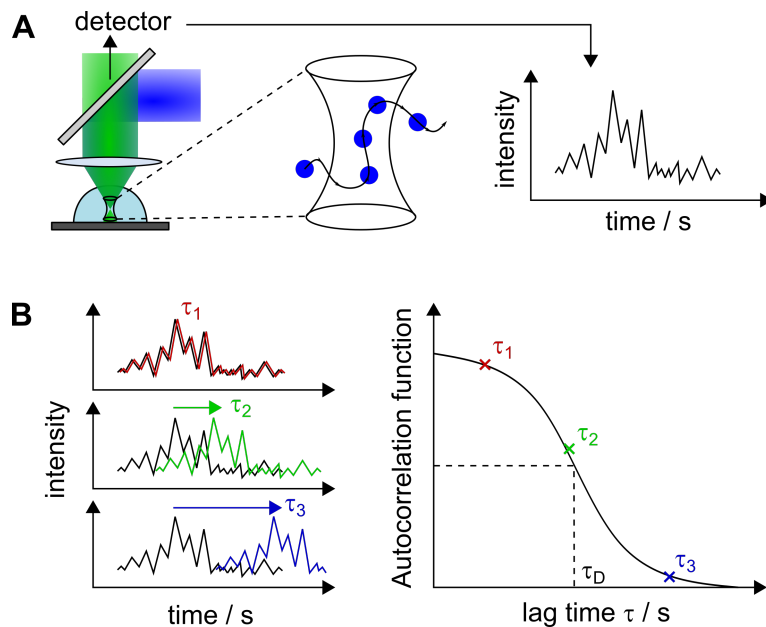
Figure 3.19: Schematic illustration of fluorescence correlation spectrosopy.
A: Fluorophores diffusing through the confocal volume emit photons leading to a fluorescence intensity time trace. The confocal volume is defined by the focus of a CLSM. **B:** The time trace is correlated with copy of itself which is shifted by the lag time τ. The diffusion time τ_{D} can be extracted to evaluate the diffusion coefficent D.

The ellipsoidal geometry of the observed volume can be approximated with help of the Gaussian point spread function (PSF) with the peak intensity F_0, the radial positions x and y, the axial position z and the the radial and axial radii ω_{xy} and ω_z:[131–134]

$$F(x, y, z) = F_0 \exp\left(-\frac{2(x^2 + y^2)}{\omega_{xy}^2}\right) \exp\left(-\frac{2z^2}{\omega_z^2}\right). \tag{3.20}$$

Fluorescent molecules diffusing through the confocal volume are excited and emit photons of higher wavelengths. Fluorescence intensity time traces are monitored with a suitable detector requiring a readout rate which is several orders of magnitude higher compared to the residence time of the fluorescent molecules within the focus (cf. figure 3.19 A). The resulting fluorescence intensity time trace is correlated to a copy of itself shifted by a lag time τ using the autocorrelation function $G(\tau)$ (cf. equation 3.21).[105,135]

$$G(\tau) = \frac{\langle F(t)F(t+\tau)\rangle}{\langle F(t)\rangle^2} \tag{3.21}$$

The pointed brackets describe an average of all values over time. The resulting shape of $G(\tau)$ provides information about the fluctuating processes of the sample caused by diffusion and photochemical and -physical processes, like for example triplet state dynamics, photon antibunching and more. The latter, however, operate on faster time scales (nanosecond to microsecond)[136] and can therefore be distinguished from diffusive processes in the millisecond to second range.[131]

In this work, FCS measurements were performed in a two-dimensional system of a planar bilayer (f-PSM, cf. figure 3.20 A). The detection volume is defined by the cross section of the focus and the plane of the sample. Thus, the detection area is actually described as a two-dimensional Gaussian profile and $G(\tau)$ for Brownian diffusion in a three-dimensional system, which is described with

$$G_{\text{3D}}(\tau) = 1 + \frac{\gamma}{N}\left(\frac{1}{1 + (\tau/\tau_{\text{D}})}\right)\left(\frac{1}{1 + (\tau/\tau_{\text{D}})(\omega_{\text{xy}}/\omega_{\text{z}})}\right)^{0.5} \tag{3.22}$$

can be reduced in a plane system to

$$G_{\text{2D}}(\tau) = 1 + \frac{\gamma}{N}\left(\frac{1}{1 + (\tau/\tau_{\text{D}})}\right), \tag{3.23}$$

where γ is defining a correction factor for the focal intensity profile, N the number of particles and τ_{D} the diffusion time.[135,137] The following relation allows to extract

the lateral diffusion coefficient D from τ_D:[131]

$$D = \frac{\omega_{xy}^2}{4\tau_\mathrm{D}}.$$

(3.24)

FCS of two-dimensional systems can lead to erroneous assumptions about the diffusion coefficient if the plane of the system is not located exactly in the center of the focus. Measuring outside the focal plane leads to a larger detection area and thus to a higher number of detected particles and a longer diffusion time. Z-scan FCS is a suitable method to overcome this challenge by measuring fluorescence intensity time traces and thus determining autocorrelation functions in different positions along the optical z-axis above and below the f-PSM (cf. figure 3.20).[131,138]
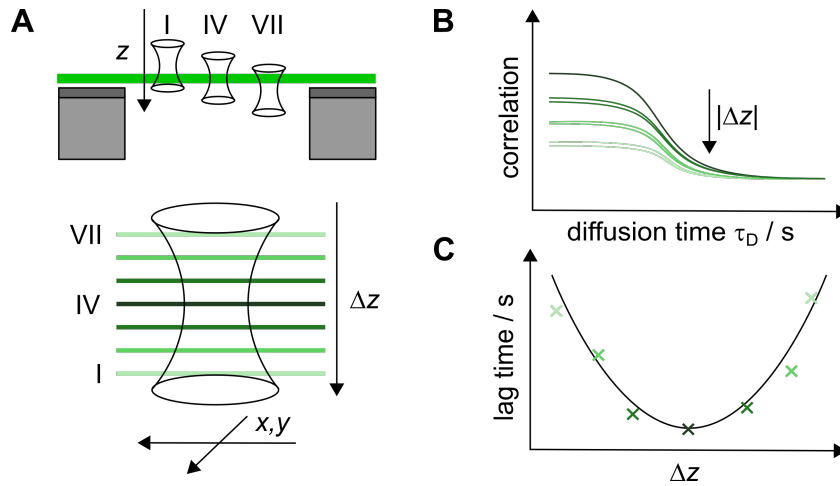
Figure 3.20: Schematic illustration of z-scan FCS. A: FCS measurements were performed in different position along the the optical axis z. **B:** Autocorrelation curves obtained from a z-scan FCS represent a change in the temporal decay and the amplitude dependent distance of sample plane and focal waist (Δz). **C:** Extracted diffusion are quadratically dependent on the z-position.

The diffusion time τ_D as well as the particle number N is quadratically dependent on the distance Δz between the plane of the sample and the focus waist as described with equations 3.25 and 3.26:

$$\tau_\mathrm{D}(\Delta z) = \frac{\omega_{xy}}{4D}\left(1 + \frac{\lambda^2 \Delta z^2}{\pi^2 n_\mathrm{r}^2 \omega_{xy}^4}\right)$$

(3.25)

71

$$N(\Delta z) = N_0 \left(1 + \frac{\lambda^2 \Delta z^2}{\pi^2 n_{\mathrm{r}}^2 \omega_{xy}^4} \right), \tag{3.26}$$

where λ is the excitation wavelength, n_{r} is the refractive index of the solution and $N_0 = \pi \omega_{xy} c$ is the particle number in the focus waist dependent on the concentration c of diffusing fluorescent molecules.[131,138]

Experimental procedure

PSMs (POPC/POPG/Chol/Atto390 DPPE/Atto655 DOPE, 68.999/15/15/1/0.001, n/n) were prepared as described in chapter 3.2.4 by spreading electroformed (cf. chapter 3.2.1.3) or microfluidically produced GUVs (cf. chapter 3.2.3) on porous substrates (pore diameter 5 μm). Z-scan FCS was performed in the center of an f-PSM using a LSM 880 (Carl Zeiss Microscopy GmbH, Oberkochen, Germany) equipped with a water immersion objective (40X A Plan Apochromat, NA 1.0, Carl Zeiss Microscopy GmbH, Oberkochen, Germany). The fluorophore Atto390 DPPE was used to visualize the membrane while Atto655 DOPE was used for the determination of the diffusion coefficient by z-scan FCS. By observing the measured count rate, the waist of the focus was adjusted to approximately coincide with the membrane plane. Z-scan FCS was measured in steps of 200 nm from 1 μm below to 1 μm above the position of maximal count rate. At each position two measurements of 60 s duration were recorded and averaged for the evaluation. The instrumental settings are described in table 3.19. Fluorescence intensity time traces were autocorrelated using equation 3.23 with the ZEN software (Carl Zeiss Microscopy GmbH, Oberkochen, Germany). For the determination of D the resulting diffusion times per z position were fitted by equation 3.25.

Table 3.19: **Settings used for the performance of z-scan FCS.**

laser power (633)	1 % (5 mW)
measurement time	60 s
repetitions	2
z range	± 1 μm
step size	200 nm

3.3.3.5 Quantitative analysis of confocal fluorescence micrographs

Quantitative analysis of the diameter and peak intensities of dsGUVs and GUVs

In this work, dsGUVs and GUVs, produced as described in chapter 3.2.3, were analyzed in terms of their diameter and membrane peak fluorescence intensity. For this purpose, fluorescence micrographs were captured at the equatorial plane using a FluoView 1200 CLSM (Olympus, Tokyo, Japan) equipped with a dry objective (LUCPLFLN 40X, NA 0.6, Olympus, Tokyo, Japan) and a water immersion objective (LUMFLN 60XW, NA 1.1, Olympus, Tokyo, Japan). For the quantitative evaluation a Matlab script written by Dr. Jeremias Sibold[105] and modified by Nils Liebe (Georg-August-Universität Göttingen) was used. The fluorescence intensity $I(x)$ was extracted from profile lines placed through the center of each dsGUV/GUV (cf. figure 3.21) and plotted against the distance x. The data were fitted using equation 3.27.[105]

$$I(x) = a_1 \exp\left(- \left(\frac{x - b_1}{c} \right)^2 \right) + a_2 \exp\left(- \left(\frac{x - b_2}{c} \right)^2 \right) + e \qquad (3.27)$$

The parameters a_1 and a_2 describe the maximal intensity of the two peaks at the positions b_1 and b_2 with a peak width of c while e describes the background intensity. The absolute value of the difference between b_1 and b_2 allows to draw conclusions about the diameter d of the analyzed objects.

Quantitative analysis of the reconstitution efficiency of syb 2 in GUVs

The reconstitution efficiency R_{GUV} of syb 2-Atto488 in GUVs produced by droplet-based microfluidics was investigated by a procedure described by Aimon et al. and Mühlenbrock et al. with modifications.[36,47] The determination of the amount of reconstituted protein was based on the correlation of the peak intensity of the membrane and the percentage of fluorophore within the lipid bilayer. GUVs were produced by droplet-based microfluidics containing known concentrations of Atto488 DPPE. Confocal images of the equatorial plane of the vesicles were analyzed using the aforementioned Matlab skript. Linear regression of the maximal peak intensity plotted against the fluorophore concentration allowed the generation of a calibration curve with the slope m. Vesicles reconstituted with syb 2-Atto488 were treated
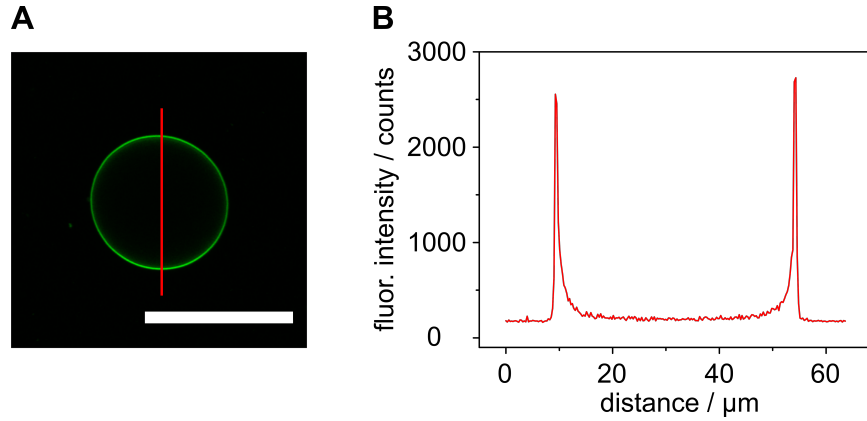
Figure 3.21: Illustration of the quantitative analysis of fluorescence micrographs of dsGUVs and GUVs. A: Representative fluorescence micrograph of a GUV (0.1 mol% Atto488 DPPE). The red line indicates an exemplary profile line. Scale bar = 50 μm. **B:** Representative extracted fluorescence intensity profile.

in an analogous manner. The maximal peak fluorescence intensity $I_{\text{peak,syb2}}$ of proteo-GUVs, the degree of labeling (DOL, cf. chapter 3.1.6) and the initial concentration of protein c_{initial} were used to determine the reconstituion efficiency R_{GUV} by equation 3.28.[36,47]

$$R_{\text{GUV}} = \frac{I_{\text{peak,syb2}}}{m \cdot DOL \cdot c_{\text{initial}}} \cdot 100. \tag{3.28}$$

The initial protein concentration in the LUVs used for the droplet-based microfluidics was determined previously by flotation assays (cf. chapter 3.2.2.4).

GUVs and proteo-GUVs (POPC/POPG/Chol/Atto390 DPPE/ Atto488 DPPE, $69.5 - x/15/15/0.5/x$, n/n) were produced by droplet-based microfluidics (cf. chapter 3.2.3). The preparation of LUVs and the protein reconstitution were performed as described in chapter 3.2.1.2 and 3.2.2.2. Atto390 DPPE was added in a constant concentration for labeling the bilayer of proteo-GUVs and GUVs. Atto488 DPPE, lacking in the bilayer of proteo-GUVs, served in different concentrations in the bilayer of the GUVs for the calibration curve. GUVs respectively proteo-GUVs were release in a BSA passivated petri dish using iso-osmolar buffers. Imaging was performed using a FluoView 1200 CLSM (Olympus, Tokyo, Japan) equipped with a water immersion objective (LUMFLN 60XW, NA 1.1, Olympus, Tokyo, Japan). Instrumental settings (PMT gain, pixel dwell time, resolution, laser power) were kept constant for all measurements (cf. table 3.20).

Table 3.20: Settings used for quantitative analysis of fluorescence micrographs for the determination of the reconstitution efficiency.

laser power	10 % (20 mW)
PMT gain	450
pixel dwell time	$10\,\mu\mathrm{s\,pixel}^{-1}$
resolution	$1024 \times 1024\,\mathrm{pixel}$

Quantitative analysis of intensities of oil and aqueous phase in dsGUVs

The production of dsGUVs was performed under varying buffer and surfactant conditions. A parameter to characterize the resulting dsGUVs is the amount of fluorophore leaking into the oil phase. A vertical profile line (cf. figure 3.22 A, red line) was drawn to determine the fluorescence intensity of both, the oil phase and the aqueous phase. The extracted averaged intensity data for the oil phase $I_{\mathrm{oil,norm}}$ and the aqueous phase $I_{\mathrm{aq,norm}}$, respectively, were normalized to the maximum peak intensity of the bilayer (cf. equation 3.29).

$$I_{\mathrm{oil/aq,n}} = \frac{I_{\mathrm{oil/aq}}}{I_{\mathrm{peak}}} \tag{3.29}$$
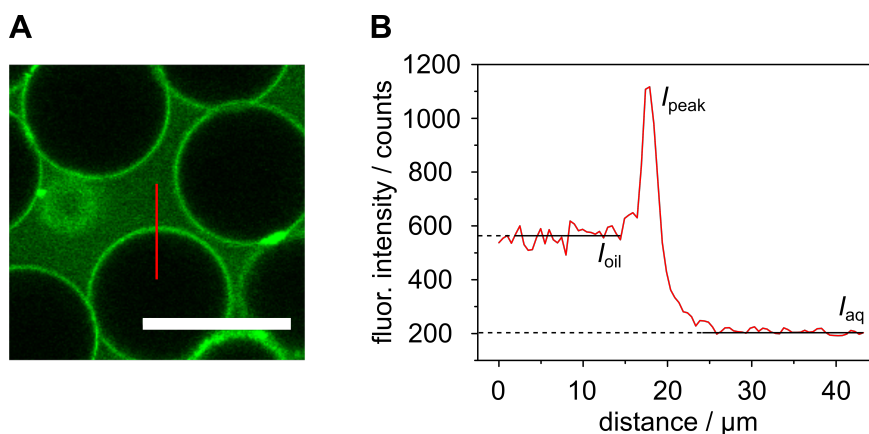
Figure 3.22: Illustration of the quantitative analysis confocal images of dsGUVs. A: Representative fluorescence micrograph dsGUVs. The red line indicates an exemplary profile line. Scale bar = 50 μm. **B:** Representative extracted fluorescence intensity profile. The fluorescence intensity of the oil phase (I_{oil}), the aqueous phase (I_{aq}) and the bilayer (I_{peak}) were extrated for further evaluation.

3.3.4 Atomic force microscopy

Atomic force microscopy (AFM) is a suitable tool to characterize the surface topography and the mechanical properties of artificial membrane systems. In the context of this work, PSMs derived from droplet-based microfluidics were analyzed and compared to PSMs created from electroformed GUVs.

General principle of atomic force microscopy

A common setup of an atomic force microscope is schematically illustrated in figure 3.23. The sample is scanned by a tip, which typically has a radius of a few nanometers and is mounted to a cantilever spring. Piezoelements allow to control the positioning of cantilever and sample relative to each other in x, y and z direction. When the cantilever approaches the surface of the sample, repulsive and attractive forces occur, leading to its deflection. Lateral and vertical deflection are detected by a laser, which is aligned to the cantilever and reflected from it towards a four quadrant photodiode (A-D, cf. figure 3.23).[139,140]
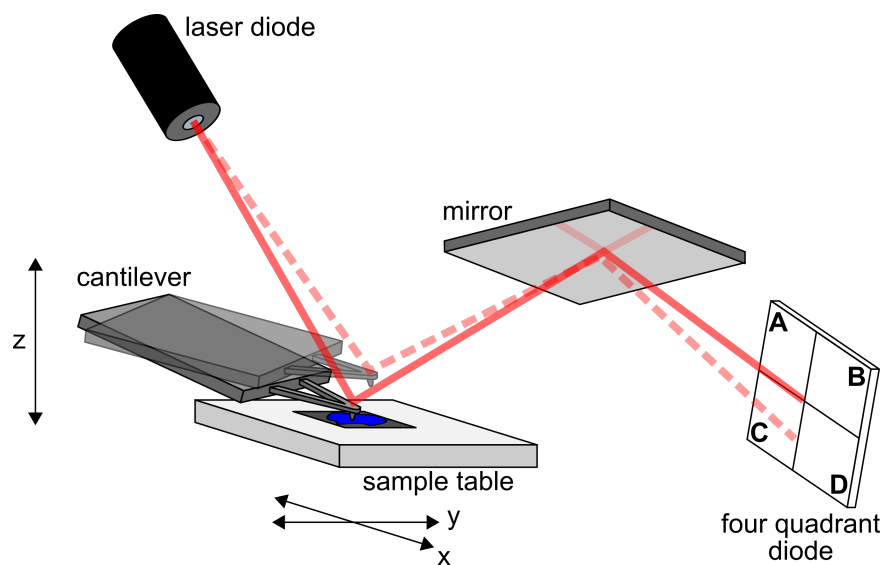
Figure 3.23: Schematic illustration of the setup of an atomic force microscope. A cantilever is scanning a sample by moving the sample in x-y-direction and the cantilever in z-direction using piezo actuators. The deflection of the cantilever is monitored by a laser beam which is reflected from the cantilever and a mirror towards a four quadrant photodiode.

Changes of the intensity of the laser beam in the quadrants of the photodiode can be used to determine the vertical deflection in % as described in equation 3.30. Analysis

of the lateral deflection can be performed analogously.[139,141]

$$A_{\text{vertical}} = \frac{I(\text{A} + \text{B}) - I(\text{C} + \text{D})}{I(\text{A} + \text{B}) + I(\text{C} + \text{D})} \tag{3.30}$$

Thus, the deflection of the cantilever as a function of the surface properties allows the imaging and characterization of the sample. Linewise scanning of the specimen is leading to a three-dimensional image offering the possibility of a resolution down to 1 nm in the x-y-direction and 0.1 nm in the z-direction.[139,140] According to the characteristics of the specimen, different imaging modi can be chosen. The quantitative imaging modus used in this work is described in more detail below.

Force distance curves

Force-distance curves (FDC) are a suitable tool for determining the mechanical properties of a specimen in the context of indentation experiments. Upon getting into contact with a surface of the specimen, the cantilever is deflected. The relation of the deflection z_{c} and the applied force F is dependent on the spring constant k_{c} of the cantilever and can be described by Hooke's law (cf. equation 3.31):

$$z_{\text{c}} = \frac{F}{k_{\text{c}}} = \frac{4FL_{\text{c}}^3}{Ew_{\text{c}}^2 t_{\text{c}}} \tag{3.31}$$

with the modulus of elasticity E, the length L_{c}, the width w_{c} and the thickness t_{c} of the cantilever. The cantilever's spring constant can be determined experimentally by a procedure described by Sader et al. analyzing its unloaded resonance frequency.[142] A thermal noise spectrum is recorded and the cantilever is assumed as a harmonic oszillator. Thus, the spring constant can be determined based on the knowledge about the obtained resonance frequency ω_{f}, the quality factor Q and the geometry of the cantilever.

$$k_{\text{c}} = 0.1906\rho_{\text{f}}w_{\text{c}}^2 L_{\text{c}}Q\Gamma_{\text{i}}(\omega_{\text{f}})\omega_{\text{f}}^2 \tag{3.32}$$

ρ_{f} is the density of the fluid and Γ_{i} the imaginary part of the hydrophobic function, which depends on the Reynolds number $Re = \rho_{\text{f}}\omega w_{\text{c}}^2/(4\eta)$, where η is the viscosity of the surrounding fluid. According to Hooke's law, the spring constant is required to

convert the deflection of the cantilever into a force.[141,142] A typical FDC is illustrated in figure 3.24.
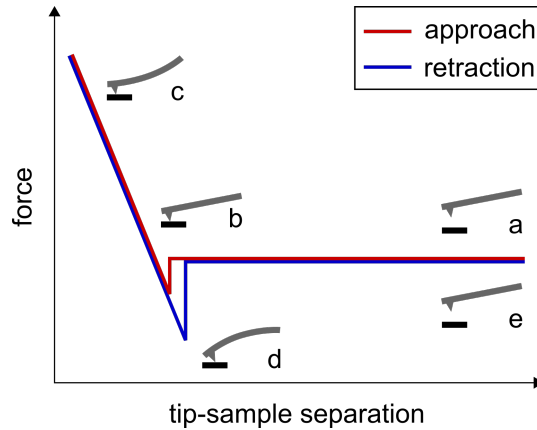
Figure 3.24: Schematic illustration of a typical FDC. Approaching the cantilever to the sample surface (red, a) leads to a snap on effect (b). The cantilever is deflected upon indentation (c). The response of the retraction (blue) reveals similar behavior as the approach. Potential adhesion forces lead to a snap-off effect (d). Total retraction positions the cantilever to the adjusted height (e).

At sufficiently large distance from the surface, no forces affect the cantilever and no deflection occurs. When the cantilever approaches to the sample, mediated by the z-piezo (cf. figure 3.24, red curve, a), attractive van-der-Waals or electrostatic interactions can result in a so-called a snap on effect (b). Further indentation leads to the deflection of the cantilever until the setted maximal force is reached (c). During retraction the response shows a similar behavior as before. If adhesion forces arise, a snap off effect can be monitored where the cantilever looses the contact to the surface of the specimen (d). Further retraction leads to position the cantilever to the adjusted height (e).[143]

As noted initially, the signal from the four quadrant diode is measured as a function of the z-piezo movement, which is converted in the deflection of the cantilever using its sensitivity S (in nm V^{-1}). The applied force is extracted by applying Hooke's law given by:[141]

$$F = -k_{\mathrm{c}} \cdot z_{\mathrm{p}} \tag{3.33}$$

To include not only the movement of the z-piezo but also the deflection and bending of the cantilever in the calculation, the tip sample separation d_{ts} is determined from

the piezo movement z_{p}, the deflection of the cantilever z_{c} and the indentation into the sample z_{s} by equation 3.34.[143]

$$d_{\mathrm{ts}} = z_{\mathrm{p}} - z_{\mathrm{c}} - z_{\mathrm{s}}. \tag{3.34}$$

Evaluation of the lateral membrane tension

Force distance curves measured in the center of f-PSMs provide information about their mechanical properties. The lateral membrane tension σ can be determined from the force-indentation relationship shown by equation 3.35.

$$F = 2\pi\sigma_{\mathrm{z}}R\frac{u(R)'}{\sqrt{1+u(R)'^2}} \tag{3.35}$$

The force F depends on the radius R of the f-PSM and the slope of $u(r)$ at the rim $r = R$. The free contour of the membrane $u(r)$ at $a \leq r \leq R$ is described by equation 3.36 assuming indentation with a conical tip.[141,144,145]

$$u(r) = d_1 + d_2 ln\left(\frac{r}{R}\right) \tag{3.36}$$

The tension σ_{z} acting on the system caused by the identation is defined by

$$\sigma_{\mathrm{z}} = \sigma + K_{\mathrm{A}}\left(\frac{\Delta A}{A_0}\right), \tag{3.37}$$

with σ being the pre-tension of the membrane, K_{A} the area compressibility modulus and $\Delta A/A_0 = (A - A_0)/A_0$ the increase of the membrane area. The initial area A_0 prior to the indentation is expressed by πR^2. The actual area $A = A_{\mathrm{cone}} + A_{\mathrm{catenoid}}$ can be calculated from $A_{\mathrm{cone}} = \pi a^2/cos(\theta)$ and A_{catenoid} (cf. equation 3.38) assuming the outer membrane geometry as a cantenoid and a conical indenter.[144,145]

$$A_{\mathrm{catenoid}} = \frac{\pi r_{\mathrm{N}}^2}{2}\left(\sinh\left(\frac{2u_{\mathrm{a}}}{r_{\mathrm{N}}}\right) + 2C - sinh\left(2C\right) + \frac{2u_{\mathrm{a}}}{r_{\mathrm{N}}}\right) \tag{3.38}$$

a denotes the contact radius of the membrane with the conical indenter, θ the opening angle of the cone, r_{N} the minimal radius of the catenoid, u_{a} the critical maximal

separation of tip and membrane and the constant $C = -cosh^{-1}(R/r_N)$.[144,145] Neglecting the influence of membrane bending is reasonable due to the dimension difference of the pores in the micrometer regime and the bilayer thickness in the nanometer regime.[144]

Quantitative imaging mode

Various operating modi are conceivable for imaging in atomic force microscopy, exhibiting different advantages and disadvantages. During measurements in contact mode, for instance, the constant contact of cantilever and surface can lead to deformations or damages of soft specimens due to high lateral forces. For this reason, a force distance curve (FDC) based imaging mode, the quantitative imaging (QI™) mode, developed by JPK instruments (Berlin, Germany) was selected here. The QI™mode is predicated on recording complete FDC for each pixel at high but constant indentation speed and constant force. While recording FDCs, the cantilever moves exclusively in z-direction. For x-y-movement, the cantilever is raised to a defined height to avoid lateral interaction with the surface of the specimen. Height information is determined on the basis of the contact point at each pixel.[146,147]

Experimental procedure

Pore-spanning membranes (POPC/POPG/Chol/Atto488 DPPE, 60/15/15/1, n/n) were prepared in a petri dish as described in chapter 3.2.4 using Aquamarijn substrates with a pore diameter of 1.2 µm. A portable BioMat™workstation (JPK instruments, Berlin, Germany) was used for the correlation of confocal laser scanning microscopy and atomic force microscopy. The Biomat station carries the actual sample and allows a precise alignment of the field of view and the scan range of both instruments and thus, the transport of the sample from AFM to CLSM or vice versa without losing the aligned position.

For atomic force microscopy the Nanowizard 4 (JPK instruments, Berlin, Germany) equipped with a triangular MLCT cantilever (Bruker AFM probes, Calle Tecate, USA) with tip radii of (20-60) nm and lenghts of (2.5-8.0) µm was used. Prior to all measurements, the cantilever was calibrated according to Sader et al. as specified before.[142] The sensitivity of the cantilever was determined from the slope of a FDC measured with a setpoint of 0.3 V and a velocity of 1 µm s^{-1}. QI images of pore-spanning membranes were monitored at a setpoint of (0.1-0.2) nN and a z length of at least 0.3 µm. Force-indentation experiments were performed by measuring FDCs in

the center of f-PSMs and for comparison in the area of the rim. The indentation speed was variied from (0.1-10) μm s^{-1} and the setpoint from (0.2-1.2) nN. The evaluation of FDCs in terms of the lateral membrane tension σ was performed by using a Matlab script from Prof. Dr. Andreas Janshoff (Georg-August Universität Göttingen), which is fundamentally based on the above defined equations (cf. equations 3.35-3.38).

4 Results

In the recent years, the concept of droplet-based microfluidics was established as a novel method, adressing a variety of scientific challenges in research fields such as soft matter physics, biochemistry and biophysics, biomedicine and chemical synthesis.[92,148–153] Conceivable applications range from droplet-based cell sorting[154], emulsion polymerase chain reactions (ePCR)[155], evolution of catalysts for chemical synthesis[153] as well as the production of droplet-stabilized giant unilamellar vesicles (dsGUVs)[54], the incorporation of proteins in dsGUVs and their biophysical investigation[45,156]. Microfluidic fabrication of GUVs represents the focus of this work as it offers various opportunities for the creation of artifical membrane systems and their sequential loading with proteins.[45] In the last decades, a wide range of methods for GUV production has been developed, however, they all exhibit limitations when it comes to the requisition of physiological buffer compositions or the incorporation of proteins.[10,43] The encapsulation and reconstitution of (transmembrane) proteins in artificial membranes is of great importance, on the one hand for the investigation of their activity and, on the other hand, in the field of synthetic biology, for the *bottom up* production of artificial cell systems. Droplet-based microfluidics were developed to open up a possibility for GUV production that is allows choice of physiological buffer conditions and reconstitution of proteins in GUVs.[93]

Here, a droplet-based microfluidic approach based on the works of Weiss et al. and Haller et al.[45,54] was established, modified and extensively analyzed to gather detailed knowledge about the biophysical properties of produced dsGUVs and GUVs, released from the microemulsion in an aqueous phase (cf. figure 4.1 A-I, B-I), using confocal laser scanning microscopy (CLSM) and fluorescence recovery after photobleaching (FRAP). In addition, the microfluidically manufactured GUVs were applied for the first time for preparation of pore-spanning membranes (PSMs, cf. figure 4.1 C). The characterization of resulting PSMs comprised the investigation of the diffusive behavior of the lipids by means of FRAP and fluorescence correlation spectroscopy (FCS) as well as the mechanical properties of the bilayers by means of atomic force microscopy (AFM). Parallel to this, transmembrane proteins such as the TF_OF_1 ATP synthase and synaptobrevin 2 (syb 2) were reconstituted in LUVs and subsequently in dsGUVs/released GUVs (cf. figure 4.1 A-II, B-II). Resulting TF_OF_1-lipsomes (dsGUVs/released GUVs) were examined by activity assays (luminescence

spectroscopy), while syb 2 reconsitution efficieny in dsGUVs/released GUVs was studied using a fluorescence-based approach (CLSM).
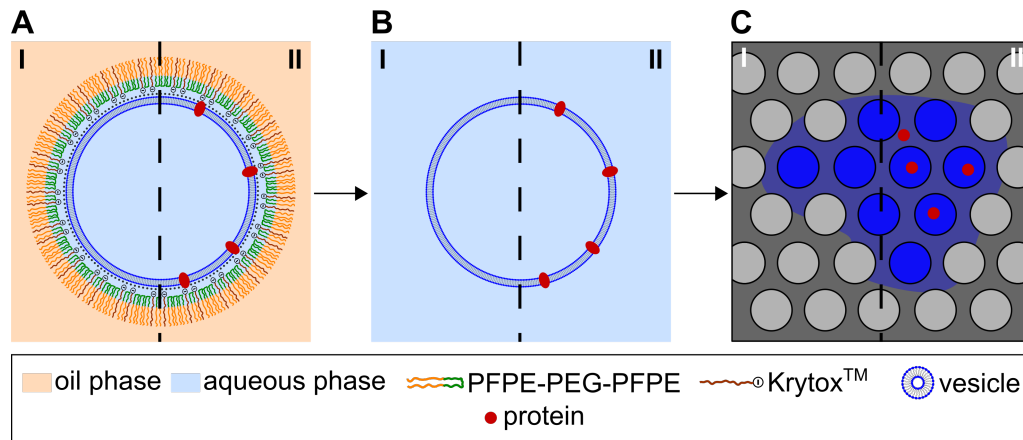
Figure 4.1: Schematic illustration of dsGUVs (A), GUVs (B) and PSMs (C) without (I) and with (II) reconstituted protein.

4.1 Production of giant unilamellar vesicles via droplet-based microfluidics

Parts of the CLSM measurements were carried out by Merve Sari as part of her master thesis.

The principle of common microfluidic approaches is based on the presence of surfactants that are able to stabilize the emulsion by decreasing the interfacial tension of the droplets.[100] In this work, the triblock copolymer PFPE-PEG-PFPE was a key component and an optimal concentration, providing sufficient long-term stability of droplets and allowing for dsGUV formation, was determined experimentally. Besides the surfactants, the buffer composition and lipid components likewise influence the success of dsGUV preparation and release of GUVs. Their effect was analyzed via confocal laser scanning microscopy.

4.1.1 Production of droplet-stabilized GUVs and release of GUVs

To analyze the impact of surfactant molecules, the microfluidic production of microemulsions was performed as described in chapter 3.2.3 based on the protocol of Haller et al.[54] The aqueous phase was composed of 30 mM Tris and 10 mM MgSO$_4$ (pH 7.4) and contained LUVs (POPC/POPG/Chol/TxR DHPE, 69/15/15/1, *n/n*) with a nominal diameter of 100 nm. The oil phase was composed of fluorocarbon oil (HFE-7500), doped with a charged surfactant (Krytox, PFPE-carboxylate) and an uncharged surfactant (PFPE-PEG-PFPE). While the concentration of Krytox (PFPE-carboxylate) was kept constant (9 mM), the impact of the PFPE-PEG-PFPE concentration was determined by varying the added weight percentage from 0.3 wt% to 1.4 wt% (0.01 mM to 0.04 mM). Confocal micrographs of the resulting dsGUVs are shown in figure 4.2 A. Success or failure of the subsequent release mediated by 1H,1H,2H,2H-perfluoro octanol (PFO) are represented by a check mark and a cross, respectively, in the upper right corner of each fluorescence micrograph. An efficient release of GUVs from the microemulsion into an aqueous environment was achievable by applying a mass fraction of 1.4 wt% PFPE-PEG-PFPE to the oil phase during the previous droplet production. It is noteworthy, that the measured fluorescence intensity in the outer oil phase changed with a decreasing mass fraction of the considered surfactant as illustrated in figure 4.2 B. Fluorescence intensities were extracted from line scans and normalized by means of equation 3.29 (cf. chapter 3.3.3.5). The normalized fluorescence intensity of the outer oil phase increases with decreasing surfactant concentration while the fluorescence intensity in the inner aqueous phase remains largely unaffected. In general, microemulsions with 1.4 wt% PFPE-PEG-PFPE demonstrated long-term stability over several days, whereas lower concentrations tended to droplet coalescence and separation of aqueous and oil phase, respectively.
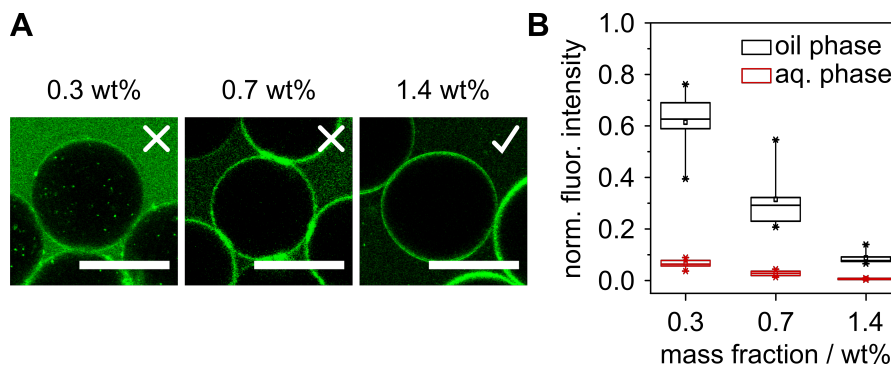
Figure 4.2: Influence of different mass fractions of the uncharged surfactant (PFPE-PEG-PFPE) on the production of dsGUVs. A: Fluorescence micrographs of dsGUVs (POPC/POPG/Chol/TxR DHPE, 69/15/15/1, *n/n*, aqueous phase: 30 mM Tris, 10 mM MgSO$_4$, pH 7.4, false colored in green) produced in an oil phase containing 0.3 wt%, 0.7 wt% respectively 1.4 wt% PFPE-PEG-PFPE. The concentration of Krytox was kept constant (9 mM). A check mark implies successful release of GUVs, whereas a cross signalizes that no released GUVs were found. Scale bars = 50 μm. **B:** Box plot diagramm of the fluorescence intensities of the outer oil phase (black box) and the inner aqueous phase (red box) of dsGUVs normalized to the fluorescence intensity of the bilayer as a condition of the mass fraction of PFPE-PEG-PFPE in the oil. Box plots extent from the 25th to 75th percentile and whiskers from 5th to 95th.

Other experiments represented in this work were performed at constant concentration of PFPE-PEG-PFPE of 1.4 wt%. Figure 4.3 A shows exemplary fluorescence micrographs of dsGUVs (POPC/POPG/Chol/Atto488 DPPE, 69/15/15/1, *n/n*, droplet-buffer) and the resulting GUVs released in release buffer (cf. chapter 3.2.3). A diameter analysis of fluorescence micrographs from several preparations of dsGUVs and their related released GUVs, was performed as described in chapter 3.3.3.5. Figure 4.3 B reveals for GUVs encapsulated in the microemulsion a more homogenous distribution with a mean diameter of (50 ± 6.7) μm ($n = 166$), while released GUVs exhibited a broader size distribution with a mean diameter of (18 ± 7.5) μm ($n = 549$). This becomes obvious when considering the middle 50 % of the respective data, which are marked by the box.
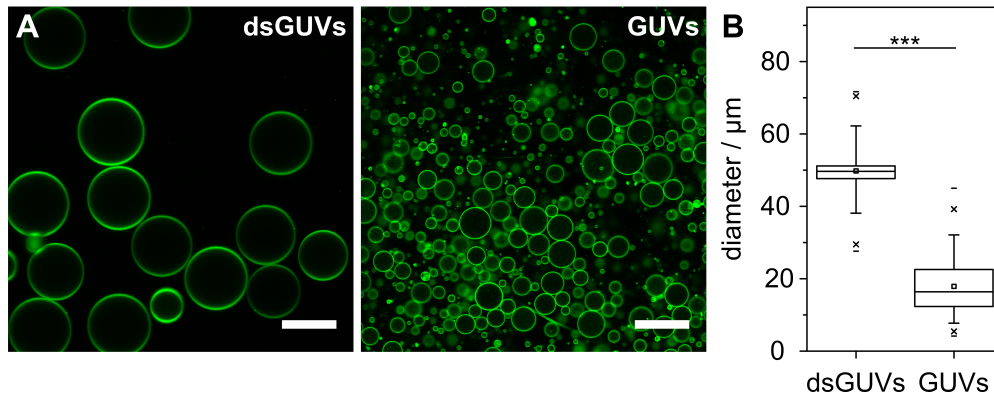
Figure 4.3: Comparison of diameters of dsGUVs and released GUVs. A: Fluorescence micrographs of dsGUVs and released GUVs (POPC/POPG/Chol/Atto488 DPPE, 69/15/15/1, *n/n*). The production of dsGUVs repectively the release were performed in standard droplet- respectively release-buffer. Scale bars = 50 µm. **B:** Box plot of the diameters of dsGUVs ((50 ± 6.7) µm, $n = 166$) and released GUVs ((18 ± 7.5) µm, $n = 549$). Box plots extent from the 25th to 75th percentile and whiskers from 5th to 95th. Statistical Mann-Whitney-test: $p \leq 0.001$ (***).

4.1.2 Impact of buffer and lipid components on the production of droplet-stabilized GUVs and the release of GUVs

The development of droplet-based microfluidics aims at the production of GUVs being free from limitations concerning buffer and lipid composition to achieve physiological conditions within the system.[10] In order to verify, that droplet-based microfluidics offers a tool for an efficient GUV production, allowing to add the mentioned components and, if necessary, to define limitations, dsGUVs and GUVs were produced according to chapter 3.2.3 in the course of this work, varying the concentrations of different supplements. Salts like potassium chloride (KCl), whose transport and occurence is given in almost every animal cell type, in particular are important components.[157] Besides, divalent cations like Mg^{2+} and Ca^{2+} are of central relevance in synthetic biology, since they are indispensable for the activity of many proteins, for example as cofactors[158], while other chemical components such as NaH_2PO_4 serve as substrates for example for ATP synthases.[115] In addition to these ionic buffer supplements, also lipids like POPS are of great significance in biological processes and are required for mimicking cellular membranes.[159] Moreover, the applicability of various buffer substances is crucial for a biological model system, since biochemical reactions mediated by proteins usually occur in a narrow pH range. The impact of

multiple factors was deciphered as described in the following and summarized in table 4.1.
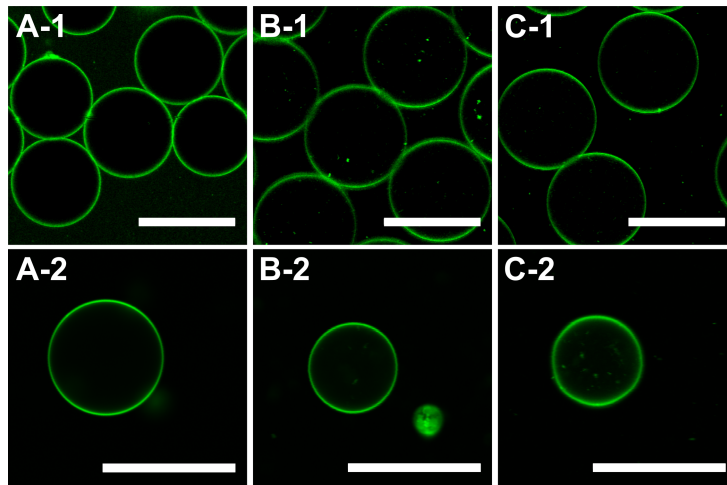
Figure 4.4: Influence of the KCl concentration on the production of ds-GUVs and release of GUVs. Droplet-stabilized GUVs (**1**) and released GUVs (**2**) (POPC/POPG/Chol/TxR DHPE, 69/15/15/1, *n/n*, aqueous phase: 20 mM Tris, 10 mM MgCl$_2$, pH 7.4, false colored in green) were produced in the presence of 0 mM (**A-1, A-2**), 50 mM (**B-1, B-2**) and 100 mM (**C-1, C-2**) KCl. Scale bars = 50 μm.

The basis for studying the effects of various components were dsGUVs, composed of a standard lipid mixture of POPC/POPG/Chol (70:15:15, *n/n*) doped with a lipid-coupled fluorophore (0.5 mol%-1 mol%) and partially BiotinCap18:1 (0.1 mol%), which allowed immobilization of the released GUVs at the bottom of a neutravidin-coated petri dish (cf. chapter 3.3.3.2). In order to dissect the effects of the composition of the aqueous phase, dsGUVs were produced from LUVs (d_{nom} = 100 nm) prepared via extrusion in the respective buffer.

Figure 4.4 represents dsGUVs and released GUVs, that are produced by using a buffer composed of 20 mM Tris and 10 mM MgCl$_2$ (pH 7.4) without (cf. figure 4.4 A) and with 50 mM and 100 mM KCl, respectively (cf. figure 4.4 B, C). The addition of different concentrations of KCl resulted in all cases in the observation of a homogeneous fluorescence intensity at the water-oil interface, indicating the formation of a continuous lipid bilayer. The success of the formation of a continuous lipid bilayer inside the droplets (dsGUVs, A-1 to C-1) was confirmed qualitatively by the observation of released GUVs (A-2 to C-2). Increasing concentrations of NaH$_2$PO$_4$ likewise led to successful production of dsGUVs and the subsequent release of GUVs as depicted in figure 4.5 (A, B). However, by increasing the concentration of NaH$_2$PO$_4$,

the normalized fluorescence intensity in the oil phase, calculated by equation 3.29 (cf. chapter 3.3.3.5), increased as well (cf. figure 4.5 C). Besides, areas of high fluorescence intensity, classified as vesicle aggregations or clusters, occured to a minor extent at $50\,\text{mM}$ NaH_2PO_4 (cf. figure 4.5 B-1). The normalized fluorescence intensity of the inner aqueous compartment (cf. equation 3.29) remained at a low level below 0.2, although it was comparatively increased for preparations with $5\,\text{mM}$ and $10\,\text{mM}$ NaH_2PO_4.
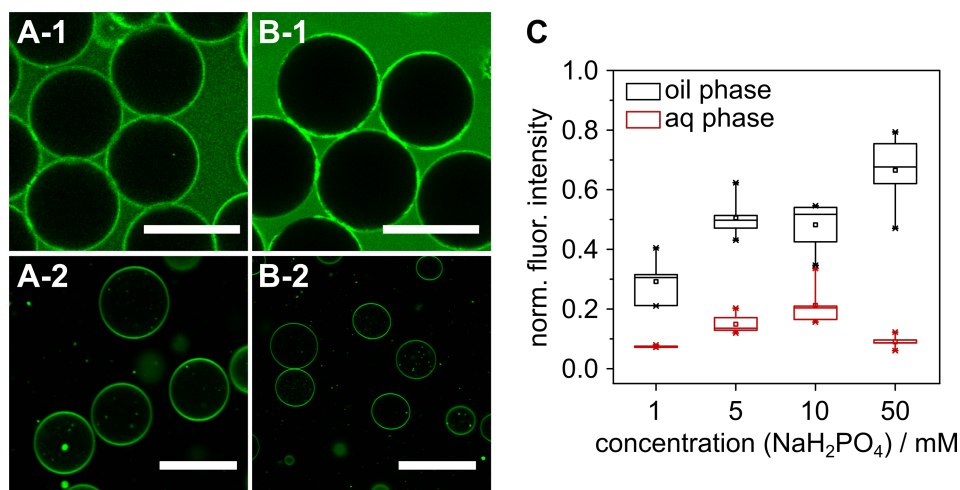
Figure 4.5: Impact of NaH_2PO_4 on the production of dsGUVs and the release of GUVs. The production of dsGUVs (**1**) and release of GUVs (**2**, POPC/POPG/Chol/TxR DHPE/BiotinCap18:1 68.9/15/15/1/0.1, *n/n*, false colored in green, aqueous phase: $20\,\text{mM}$ Tris, $10\,\text{mM}$ $MgCl_2$, pH = 7.4) were performed in the presence of $5\,\text{mM}$ (**A-1, A-2**) and $50\,\text{mM}$ (**B-1, B-2**) NaH_2PO_4. Scale bars = $50\,\text{µm}$. **C:** Box plot of the normalized fluorescence intensities of the outer oil phase (black box) and the inner aqueous phase (red box) of dsGUVs normalized to the fluorescence intensity of the bilayer as a function of the salt concentration (NaH_2PO_4). Box plots extent from the 25th to 75th percentile and whiskers from 5th to 95th.

The effect of a variation of the applied buffer substance was deciphered in the following and is illustrated in figure 4.6 (A-C). Success or failure of the release of GUVs is emblematized by a checkmark and a cross, respectively, in the upper right corner of each fluorescence micrograph. The usage of $20\,\text{mM}$ tris(hydroxymethyl)aminomethane (Tris, figure 4.6 A) or 4-(2-hydroxyethyl)-1-piperazineethanesulfonic acid (HEPES, figure 4.6 B), respectively, as buffer component, each doped with $10\,\text{mM}$ $MgCl_2$, led to dsGUVs revealing a homogeneous distribution of the fluorescence intensity at the water-oil interphase in the monitored micrographs. The addition of $20\,\text{mM}$ succinic acid (cf. figure 4.6 C) caused distinct regions of higher fluorescence intensity,

in particular at the interface of two adjacent droplets. In addition to these areas, assumed as lipid or vesicle clusters, it should be emphasized that the release of GUVs failed. Thus, the formation of a continuous bilayer at the interface remains questionable.

When using POPS (15 mol%) instead of POPG as the negatively charged lipid compound for the preparation of dsGUVs with an inner aqueous compartment composed of 20 mM HEPES and 10 mM MgCl$_2$ (pH = 7.4), areas of increased fluorescence intensity are even more prominent than described before (cf. figure 4.6 D). Likewise, the release of intact GUVs was not successful.
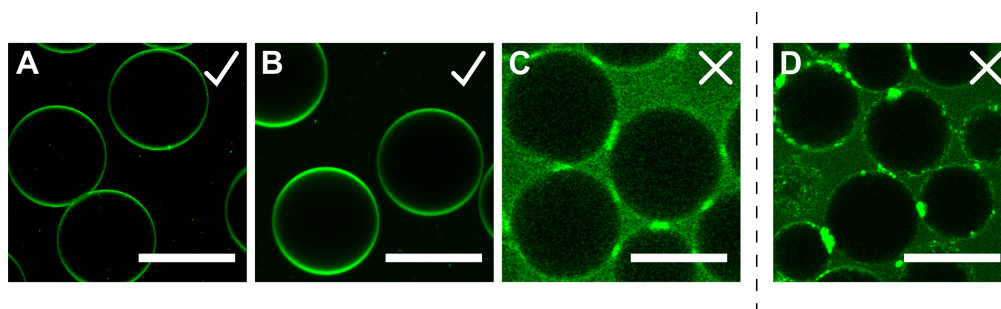
Figure 4.6: Influence of buffer components (TRIS, HEPES and succinic acid) and POPS on the production of dsGUVs and the release of GUVs. A-C: dsGUVs (POPC/POPG/Chol/Atto488 DPPE, 69/15/15/1, *n/n*) were produced in the presence of 20 mM Tris (**A**), 20 mM HEPES (**B**) or 20 mM Tris and 20 mM succinic acid (**C**). **D:** dsGUVs (POPC/**POPS**/Chol/Atto488 DPPE, 69/15/15/1,*n/n*) were prepared in 20 mM HEPES. A check mark means a release of GUVs was possible while a cross indicates that no released GUVs were found. All experiments were performed with 10 mM MgCl$_2$ and at pH = 7.4. Scale bars = 50 µm.

A summary of the results shown above and a selection of additional data can be found in table 4.1. Besides the ionic substances described above, the impact of Ca^{2+} (CaCl$_2$) as a second divalent cation in addition to Mg^{2+} was studied. Both, the addition of a low concentration (10 mM) as well as a high concentration (100 mM) of CaCl$_2$ to the respective buffer, containing 30 mM Tris (pH = 7.4), resulted in cluster formation at the water-oil interface and a high normalized fluorescence intensity within the oil phase. The release yielded in hardly any GUVs, thus a statement about the success would not be well-founded and therefore is labeled as not evaluable (n.e.). Apart from the buffer substances mentioned above, 2-(*N*-morpholino)ethanesulfonic acid (MES) was likewise analyzed, as an alternative for succinic acid(cf. chapter 4.3.2). However, similar observations to the case with additional succinic acid were made and no

GUVs were released from the dsGUVs. In further studies, the lipid composition was modified by total omission of negatively charged lipids (POPC/Chol/TxR DHPE, 84.5/15/0.5, n/n). Distinct areas of high fluorescence intensity (clustering) and an overall increased fluorescence intensity within the oil phase were monitored in the fluorescence micrographs and release of GUVs was not detectable. However, the preparation of dsGUVs from this lipid composition was improved by the addition of at least 50 mM KCl to the respective buffer, which allowed a release of GUVs.

Table 4.1: Impact of the buffer and lipid composition on the production of dsGUVs and the release of GUVs. (x: lipid-coupled fluorophore, n.e.: not evaluable, $I_{\text{oil,n}}$: normalized fluorescence intensity in the oil phase (cf. chapter 3.3.3.5, equation 3.29), ✓: yes, ✗: no).

lipid composition	aqueous phase	release success	$I_{\text{oil,n}}$	cluster form.
POPC/POPG/Chol/x 69/15/15/1	[a] 20 mM Tris, 10 mM MgCl$_2$	✓	-	✗
	[a] + 50 mM / 100 mM KCl	✓	-	✗
	[a] + 5 mM NaH$_2$PO$_4$	✓	0.5	✗
	[a] + 50 mM NaH$_2$PO$_4$	✓	0.7	(✓)
	[b] 30 mM Tris, 10 mM CaCl$_2$	n.e.	0.6	✓
	[b] + 100 mM CaCl$_2$	n.e.	0.5	✓
	[a] 20 mM HEPES, 10 mM MgCl$_2$	✓	-	✗
	20 mM Tris, 10 mM MgCl$_2$, [a]+ 20 mM succinic acid	✗	0.7	✓
	[b]+ 20 mM MES	✗	0.8	✓
POPC/POPS/Chol/x 69/15/15/1	[a] 20 mM HEPES, 10 mM MgCl$_2$	✗	0.8	✓
POPC/Chol/x 84.5/15/0.5	[b] 30 mM TRIS, 10 mM MgSO$_4$	✗	0.3	✓
	[b]+ 50 mM KCl	✓	0.6	✗

[a] shown in this work (cf. figures 4.4-4.6), [b] not shown in this work

4.2 Characterization of artificial membrane systems derived from droplet-based microfluidics

Artificial lipid bilayers allow to study membrane-associated biological processes in a more simplified system compared to the complex cellular membrane. However, various model lipid bilayer systems exhibit different properties regarding to membrane mechanics or mobility of membrane components (e.g. lipids, proteins), depending on, for example, remaining organic solvents from the preparation process (e.g. solvent containing micro BLMs)[160] or an underlying support (e.g. supported lipid bilayer, pore-spanning membranes)[33,35]. Thus, engineering a novel artificial membrane system requires simultaneous characterization of parameters such as lateral membrane tension and diffusion of lipids, in order to study its comparability to native membranes. As described previously (chapter 1.2), numerous possible model systems are available offering different advantages and disadvantages. In this work, artificial lipid bilayers produced from droplet-based microfluidics were extensively investigated with regard to their biophysical properties.

4.2.1 Lipid mobility in droplet-stabilized GUVs and GUVs

Parts of the FRAP measurements were carried out by Kathrin Schulze as part of her master thesis.

Lateral diffusion of molecules (e.g. lipids, proteins) is a basic property of biological membranes and essential when studying biological processes like cell adhesion, signal transduction or transport of biological components across the cellular membrane.[161–164] Analyzing these processes in a simplified artificial lipid bilayer system requires quantification of the lipid diffusion coefficient of the minimal system prior to addition of further components (e.g. proteins). Moreover, the diffusion coefficient can differ significantly between different model membrane systems, for example between free-standing and solid-supported bilayer systems[33], but also as a function of the influence of possible organic solvent residues from the respective preparation method[160]. Thus, extensive characterization of the lipid mobility in model membranes (like dsGUVs and the corresponding released GUVs) is required for comparison with native membranes, assessing its suitability as a biomimetic system

and distinguishing effects from proteins of interest and potential artifacts from the artificial system and its components (e.g. oil and surfactants).
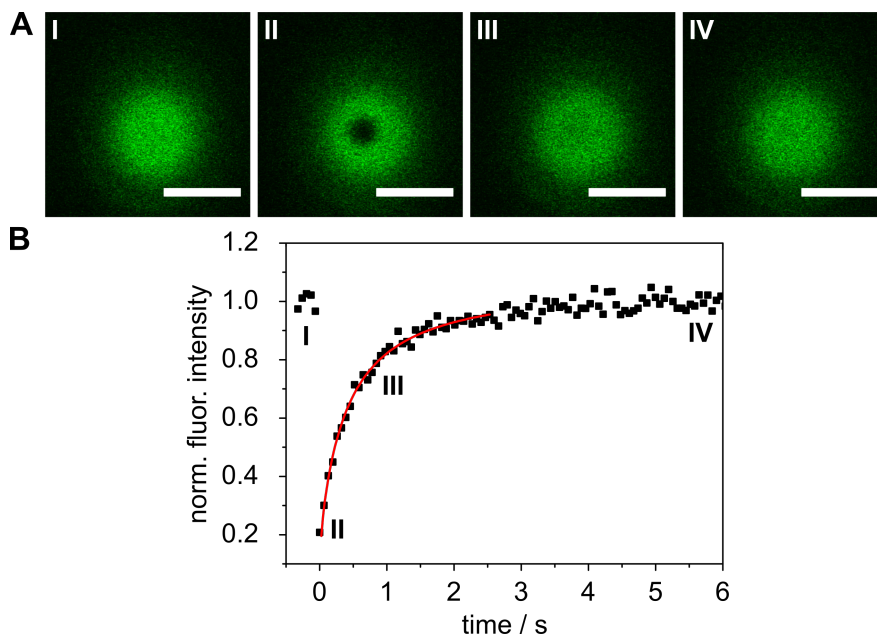
Figure 4.7: Exemplary FRAP experiment of a dsGUV. A: Fluorescence micrographs of a FRAP experiment on the bottom plane of a dsGUV (POPC/POPG/Chol/Atto488 DPPE, 69/15/15/1, n/n). After monitoring the pre bleach fluorescence intensity (I, $t = -0.3\,$s), lipid fluorophore molecules were bleached (II, $t = 0\,$s, $r_\mathrm{n} = 2.9\,\mu$m, $r_\mathrm{e} = 4.7\,\mu$m) and the fluorescence recovery was measured as a function of time (III, $t = 1\,$s and IV, $t = 6\,$s). Scale bars $= 20\,\mu$m. **B:** Normalized fluorescence intensity (ROI) as a function of time. The soumpasis fit (red, equation 3.16) leads to the diffusion time $\tau_{1/2} = 0.3\,$s.

In the present work, the lipid diffusion coefficient of the novel membrane system of dsGUVs and the respective released GUVs was quantified via fluorescence recovery after photobleaching (FRAP). Droplet-stabilized GUVs (POPC/POPG/Chol/Atto488 DPPE/BiotinCap18:1, 68.9/15/15/1/0.1, n/n) were prepared as described before (cf. chapter 3.2.3) and released GUVs were immobilized at the bottom of a functionalized petri dish via biotin-neutravidin interactions (cf. chapter 3.3.3.2). The fluorescence intensity was bleached in a circular ROI, which was set to the bottom plane of a dsGUV and the top plane of a GUV, to avoid in both cases an influence of the glass from the measurement chamber (cf. figure 3.18). The following fluorescence recovery was detected over time (cf. figure 4.7 A). Fluorescence intensity data, extracted from the ROI, were corrected concerning photofading and the background

intensity and normalized. Equation 3.16 was fitted to the data to determine the diffusion time $\tau_{1/2}$ (cf. figure 4.7 B). The nominal and the effective bleach radius, determined from the post bleach profile (cf figure 3.18 B), allowed to calculate the diffusion coefficient D from $\tau_{1/2}$ by equation 3.17.

The resulting diffusion coefficients D and mobile fractions F_m are shown in figure 4.8. Averaging of the data resulted in a mean diffusion coefficient for the dsGUVs of $(10 \pm 3)\,\mu m^2\,s^{-1}$ ($n = 77$) and for the GUVs of $(9 \pm 3)\,\mu m^2\,s^{-1}$ ($n = 33$) with errors representing the standard deviation. The lipid coupled fluorophore Atto488 DPPE was completely mobile in both, the dsGUVs ($F_m = (100 \pm 4)\,\%$) and the released GUVs ($F_m = (100 \pm 6)\,\%$). Statistical Welch's-t-test showed no significant difference of the diffusion coefficients and the mobile fractions, respectively ($p > 0.05$, ns).
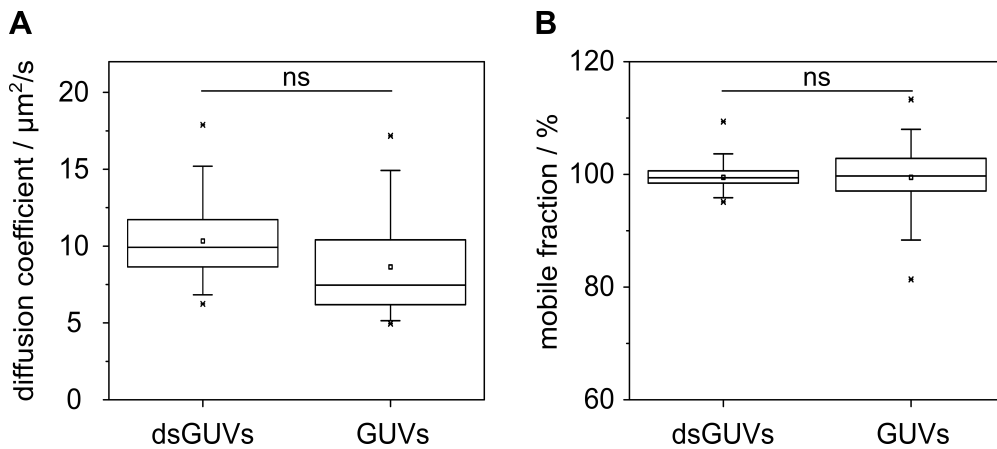
Figure 4.8: Lipid diffusion coefficients and mobile fraction in dsGUVs and GUVs. (POPC/POPG/Chol/Atto488 DPPE/BiotinCap18:1, 69.9/15/15/1/0.1, n/n) FRAP experiments resulted in a mean value for the lipid diffusion in dsGUVs of $(10 \pm 3)\,\mu m^2\,s^{-1}$ ($n = 77$) and in GUVs of $(9 \pm 3)\,\mu m^2\,s^{-1}$ ($n = 33$). The mean value of the mobile fraction for dsGUVs is $(100 \pm 4)\,\%$ and $(100 \pm 6)\,\%$ for released GUVs. The Box plots extent from the 25th to 75th percentile and whiskers from 5th to 95th. Statistical Welch's-t-test: $p > 0.05$ (ns).

4.2.2 Fabrication of pore-spanning membranes using microfluidic derived GUVs

Porous substrates exhibit an array of well-defined and highly ordered pores. Native or artificial lipid bilayers, covering the respective pores (pore-spanning membranes, PSMs), form a planar mimic of biological membranes with high long-term stability, separation of two aqueous compartments and accessibility of both sides. While the

solid-supported part (s-PSM) stabilizes the overall system, the free-standing part (f-PSM) provides properties of cellular membranes.[35] Therefore, PSMs represent a versatile tool for biophysical and biochemical research aiming at understanding complex processes at the cellular membrane.[35,36,144] In the present work, GUVs manufactured by droplet-based microfluidics were used as a starting point for the formation and characterization of pore-spanning membranes. Thus, the respective microfluidic-GUVs were spread on functionalized porous substrates (cf. chapter 3.2.4). Since microfluidically prepared GUVs are assumed to be more costumizable with respect to lipid and buffer composition, they might offer opportunities for the preparation of PSMs and the implementation of functional proteins.
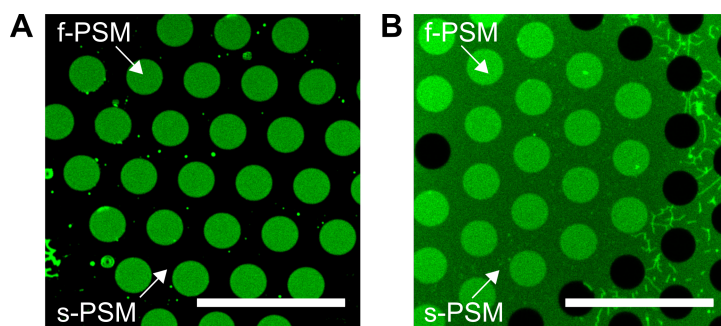
Figure 4.9: Fluorescence micrographs of pore spanning membranes (PSMs). PSMs (POPC/POPG/Chol/Atto488 DPPE, 69/15/15/1, *n/n*) on Aquamarijn substrates with a pore diameter of 5 μm functionalized with Au/6MH (**A**) or SiO$_x$ (1 ≤ *x* ≤ 2, **B**), respectively. Scale bars = 20 μm.

Preparation of PSMs consisting of POPC/POPG/Chol/Atto488 DPPE (69/15/15/1, *n/n*) aimed to be realized in this work with GUVs prepared from a microfluidic process. For this purpose, two different surface functionalizations known from literature were adopted, one with SiO$_x$ and the other one with Au and a SAM of 6-mercapto-1-hexanol (6MH).[36,106] GUVs were spread as described in chapter 3.2.4 and rinsed thoroughly with the respective buffer resulting in individual patches of pore-spanning membranes as depicted in figure 4.9. On SiO$_x$ functionalized substrates (cf. figure 4.9 A) fluorescence labeled PSMs were found, which can be identified by a high fluorescence intensity in the area of the f-PSM and a deminished fluorescence intensity in the solid-supported regions (s-PSM). In contrast, the fluorescence intensity for PSMs on Au/6MH functionalized substrates is entirely quenched at the rim, while the intensity in the f-PSM region remains high (cf. figure 4.9 B). For illustration purposes, exemplary fluorescence micrographs and their respective line profiles of the corrected

and normalized fluorescence intensities are shown in figure 4.10. For comparison, the fluorescence intensities were corrected to the fluorescence intensity at the uncovered pores serving as background and normalized to the maximal fluorescence intensity. The fluorescence intensity of the rim was 51% of that of the f-PSM for the SiO_x functionalization and 0% in case of the Au/6MH functionalization.
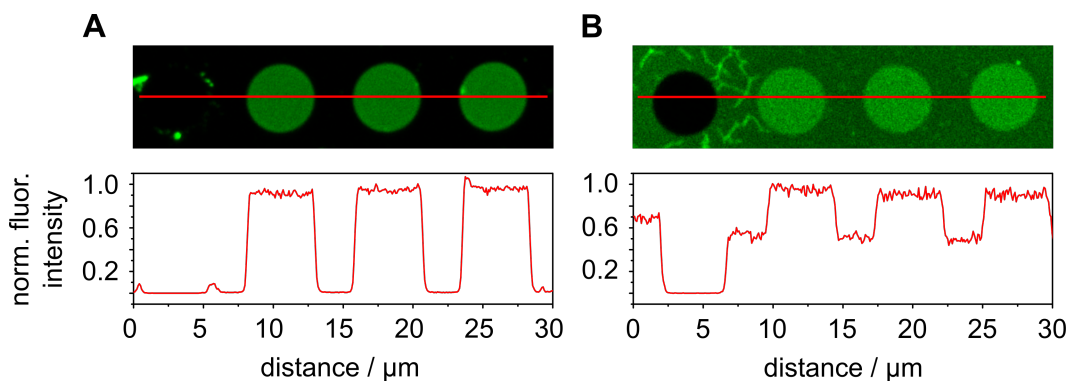
Figure 4.10: Fluorescence micrographs and corresponding normalized fluorescence intensity along the line. PSMs were prepared on Au/6MH (**A**) or SiO_x ($1 \leq x \leq 2$, **B**) functionalized substrates. The respective fluorescence intensities were extracted from the line profile and corrected to the background (uncovered pores) and normalized to the intensity of the free-standing membranes.

4.2.2.1 Characterization of the lipid mobility in pore-spanning membranes

The indirect FRAP measurements were carried out by Kathrin Schulze as part of her master thesis.

As mentioned initially, lipid mobility is an essential parameter differing between different types of model membrane systems. The two distinct parts of PSMs, the free-standing and the solid-supported part, exhibit characteristic properties of these different model systems. Whereas the s-PSM (rim area) is related to the system of solid supported membranes, the f-PSM (pore area) can be compared to free-standing membranes such as GUVs. Since lipids show different mobile behavior in s- and f-PSM, two distinct approaches have to be considered for their investigation. In order to investigate whether PSMs, produced on the basis of microfluidic GUVs, behave similar to those, obtained from electroformed GUVs, studies were carried out regarding the mobility of lipids via FCS (f-PSM) and indirect FRAP (s-PSM).

Z-scan FCS measurements were performed to investigate the mobile properties of lipids in the f-PSM region. GUVs (POPC/POPG/Chol/Atto390 DPPE/Atto655 DOPE, 69.999/15/15/1/0.001, n/n) were produced by droplet-based microfluidics (cf. chapter 3.2.3) or electroformation (cf. chapter 3.2.1.3), respectively, and spread on the functionalized porous substrates (cf. chapter 3.2.4). Atto655 DOPE was used to perform z-scan FCS measurement and thus, added in a low concentration (10^{-3} mol%). At the beginning of each measurement, the z-position of the membrane was adjusted approximately to the midpoint of the z-scan ($\Delta z = 0$). A set of autocorrelation functions from a z-scan FCS measurement, measured at ten different positions along the z-axis in the center of an f-PSM (Aquamarijn, 5 μm pore diameter, Au/6MH), is exemplified for both functionalization methods in figure 4.11 A. The lag times τ were extracted using equation 3.23 and plotted against the z distance Δz (cf figure 4.11 B) to calculate the diffusion time τ_D (cf. equation 3.25).
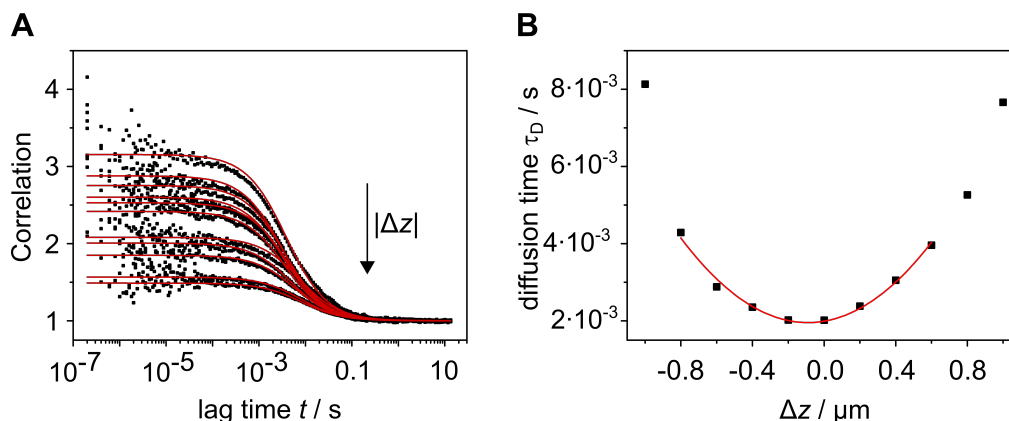
Figure 4.11: Exemplary autocorrelation function of a z-scan FCS at the f-PSM (5 μm Aquamarijn, Au/6MH). A: Fits of the autocorrelation function of a z-scan FCS of a f-PSM (POPC/POPG/Chol/Atto390 DPPE/Atto655 DOPE, 69.999/15/15/1/0.001, n/n). **B:** The extracted lag times were plotted against the z distance (Δz) and fitted for the determination of the diffusion time τ_D in the f-PSM.

The obtained averaged diffusion coefficient of lipids in the f-PSM in case of the Au/6MH functionalization were $D_{\text{f-PSM,Au,m}} = (13 \pm 4)\,\mu\text{m}^2\,\text{s}^{-1}$ ($n = 52$) for the microfluidic derived PSMs and $D_{\text{f-PSM,Au,e}} = (14 \pm 1)\,\mu\text{m}^2\,\text{s}^{-1}$ ($n = 7$) with the standard deviation as errors (cf. figure 4.12). PSMs on SiO$_x$ functionalized substrates represent diffusion coefficients for preparations obtained via microfluidics or electroformation, respectively, of $D_{\text{f-PSM,SiO,m}} = (14 \pm 3)\,\mu\text{m}^2\,\text{s}^{-1}$ ($n = 42$) and $D_{\text{f-PSM,SiO,e}} = (14 \pm 3)\,\mu\text{m}^2\,\text{s}^{-1}$ ($n = 9$). All data were found to be not significantly different by statistical Welch's-t-test respectively students t-test ($p > 0.05$).
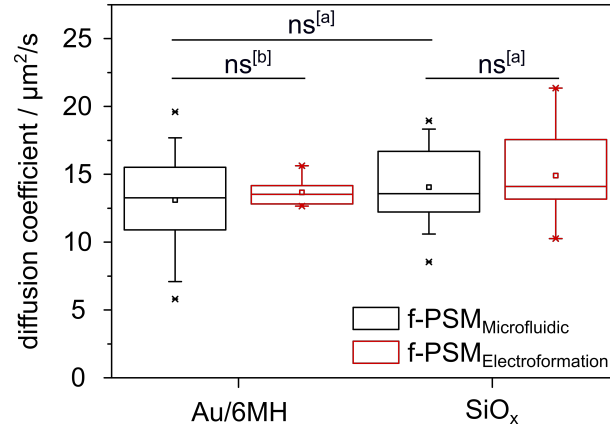
Figure 4.12: Diffusion coefficients of the f-PSMs determined by FCS. Diffusion coefficients of f-PSMs (POPC/POPG/Chol/Atto390 DPPE/Atto655 DOPE, 69.999/15/15/1/0.001, n/n) on Aquamarijn substrates (5 μm pore diameter) functionalized with SiO$_x$ ($1 \leq x \leq 2$) or Au/6MH. PSMs were prepared from microfluidic (black) and electroformed GUVs (red). The diffusion coefficients were found to be $D_{f\text{-PSM,Au,m}} = (13 \pm 4)\,\mu\text{m}^2\,\text{s}^{-1}$ ($n = 52$) and $D_{f\text{-PSM,Au,e}} = (14 \pm 1)\,\mu\text{m}^2\,\text{s}^{-1}$ ($n = 7$) for PSMs on Au/6MH functionalized substrates and $D_{f\text{-PSM,SiO,m}} = (14 \pm 3)\,\mu\text{m}^2\,\text{s}^{-1}$ ($n = 42$) and $D_{f\text{-PSM,SiO,e}} = (14 \pm 3)\,\mu\text{m}^2\,\text{s}^{-1}$ ($n = 9$) for PSMs on SiO$_x$ functionalized substrates prepared by spreading GUVs from microfluidics or electroformation, respectively. The Box plots extent from the 25$^{\text{th}}$ to 75$^{\text{th}}$ percentile and whiskers from 5$^{\text{th}}$ to 95$^{\text{th}}$. a: Statistical Welch's-t-test: $p > 0.05$ (ns). b: t-test: $p > 0.05$ (ns).

Due to the diminished or fully quenched fluorescence intensity in the rim area neither FCS nor common FRAP experiments provide a sufficient possibility to investigate the lipid mobility in the s-PSM. Thus, an indirect FRAP approach was considered, where an entire f-PSM was bleached. The following fluorescence recovery was predominantly realized by diffusion from the s-PSM into the f-PSM as described by Mühlenbrock et al.[36] Exemplary fluorescence micrographs of a FRAP experiment are shown in figure 4.13 A. Since conventional FRAP evaluation is not designed to adequately describe the two-component system used here, data evaluation was adapted to the described two-component system, which was influenced mainly by diffusion from the s-PSM but also from diffusion inside the f-PSM. Moreover, the inability to determine an effective bleaching radius contradicts the conventional evaluation, since the fluorescence quenching in the s-PSM region does not allow a gaussian intensity profile to be obtained. Thus, evaluation was performed semi-quantitatively by comparing experimental data to simulated FRAP experiments using FEM simulations for modeling 2D diffusion (COMSOL Multiphysics v4.4, Göttingen, Germany, chapter 3.3.3.3, cf. figure 4.13 B). The lipid diffusion coefficient

inside the f-PSM was fixed to $13\,\mu\text{m}^2\,\text{s}^{-1}$ as determined from FCS measurements previously, while the diffusion coefficient of the s-PSM was variied from $0.5\,\mu\text{m}^2\,\text{s}^{-1}$ to $3\,\mu\text{m}^2\,\text{s}^{-1}$. The modeled fluorescence recovery over time was extracted and plotted against experimental data. While lipids had a mobile fraction of $(97 \pm 6)\,\%$ using Au/6MH functionalized substrates, a mobile fraction of $(70 \pm 3)\,\%$ was observed for SiO_x substrates. Since the simulated 2D diffusion only considers mobile parts of the lipids, the experimental data had to be normalized to the maximal fluorescence recovery by substracting the immobile fraction from each data point and measured curve individually. Simulated and experimental data were shown in figure 4.13 C and D. Comparing individual measurements with the modeled data yielded mean lipid diffusion coefficients of $D_{\text{s-PSM,Au}} = (1.8 \pm 1.0)\,\mu\text{m}^2\,\text{s}^{-1}$ for Au/6MH functionalized substrates and $D_{\text{s-PSM,SiO}} = (1.7 \pm 0.7)\,\mu\text{m}^2\,\text{s}^{-1}$ for SiO_x functionalized substrates with the standard deviation as error.
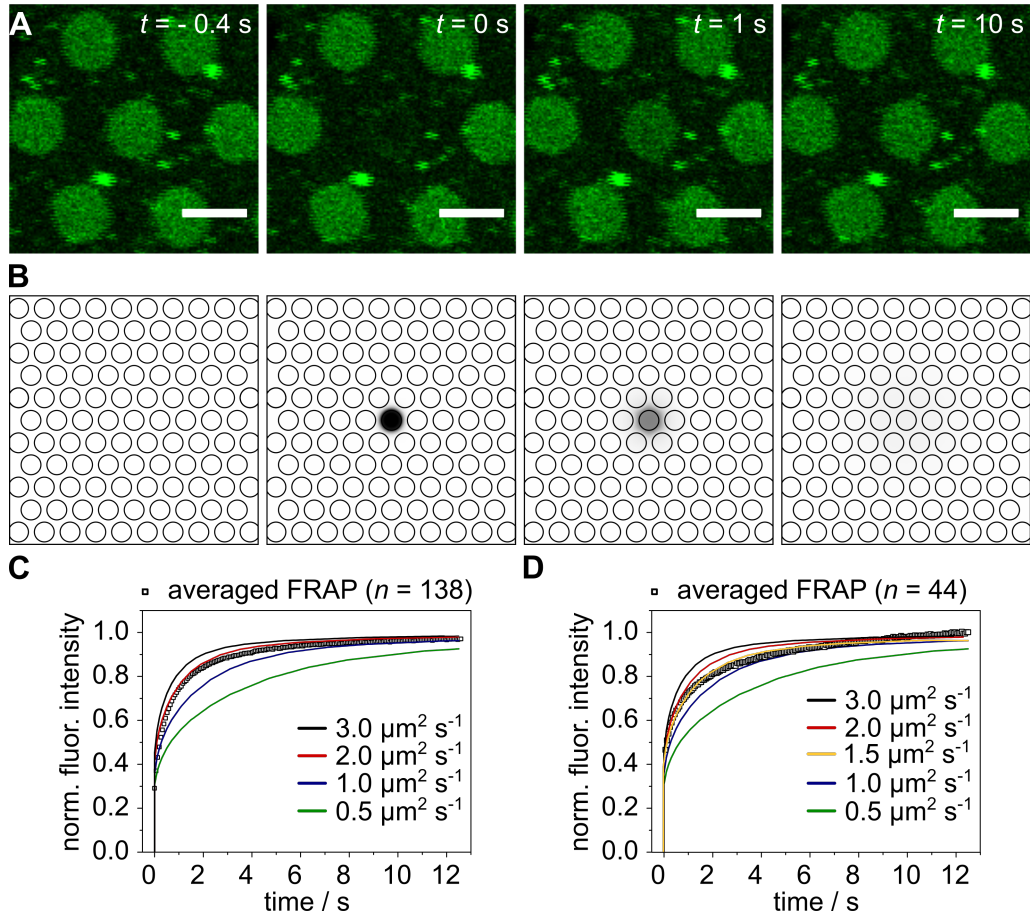
Figure 4.13: Indirect FRAP experiment and FEM simulations for the determination of the lipid diffusion coefficient of the s-PSM. A: Exemplary fluorescence micrographs of a FRAP experiment of a PSM (POPC/POPG/Chol/Atto488 DPPE, 69/15/15/1, n/n, Au/6MH functionalization, 5 μm pore diameter). Fluorescence intensity was bleached in a ROI (r_n = 2.2-2.3 μm) and the fluorescence recovery was observed over time. Scale bar = 5 μm. **B:** Snapshots of a simulated FRAP experiment (FEM simulations). **C and D:** Fluorescence recovery curves of indirect FRAP experiments of PSMS on Au/6MH (**C**) and SiO$_x$ ($1 \leq x \leq 2$, **D**) functionalized substrates were normalized, corrected and averaged. Simulated recovery curves were modeled for $D_{\text{f-PSM,sim}} = 13\,\mu\text{m}^2\,\text{s}^{-1}$ and different $D_{\text{s-PSM,sim}} = 0.5\,\mu\text{m}^2\,\text{s}^{-1}$ to $3\,\mu\text{m}^2\,\text{s}^{-1}$. The lipid diffusion coefficient of the s-PSM was found to be for Au/6MH functionalized substrates $D_{\text{s-PSM,Au}} = (1.8 \pm 1.0)\,\mu\text{m}^2\,\text{s}^{-1}$ and $D_{\text{s-PSM,SiO}} = (1.7 \pm 0.7)\,\mu\text{m}^2\,\text{s}^{-1}$ for SiO$_x$ functionalized substrates.

### 4.2.2.2 Mechanical properties of pore-spanning membranes prepared from microfluidics derived GUVs

The mechanical behavior of cellular membranes is crucial for a variety of biological processes such as division[165], adhesion[166], endo- and exocytosis[167], cellular growth[168] and several more.[144,169,170] The investigation of these processes via artificial membrane systems requires an extensive knowledge about parameters like the lateral membrane tension σ. Pore-spanning membranes offer a suitable system of free-standing membrane areas to scrutinize mechanical properties as a function of, for instance, the lipid composition, the preparational method and the surface functionalization.[169] Thus, in the present work, the mechanical properties of PSMs produced by electroformed GUVs and of PSMs produced by GUVs of microfluidic origin were compared, especially regarding to a possible influence of surfactants and fluorinated oil residues. Besides, the influence of the surface functionalization on microfluidic derived PSMs was investigated using Au/6MH and SiO_x ($1 \leq x \leq 2$) functionalized Aquamarijn substrates (pore diameter 1.2 μm).

The successful formation of PSMs (POPC/POPG/Chol/Atto488 DPPE, 69/15/15/1, n/n) was verified by fluorescence and atomic force measurements. Figure 4.14 depicts exemplary fluorescence (upper images) and atomic force (lower images) micrographs of PSMs, obtained from different preparational techniques using functionalized Aquamarijn substrates with a pore diameter of 1.2 μm (cf. chapter 3.2.4). Spreading GUVs, released from a microfluidic emulsion (cf. chapter 3.2.3), on substrates functionalized with Au/6MH or SiO_x, respectively, yielded in continuous bilayer patches as observed by the fluorescence of Atto488 DPPE (cf. figure 4.14 A and B, upper images). The f-PSMs were identified by high fluorescence intensity, while the s-PSMs show a diminished (SiO_x) or completely quenched (Au/6MH) fluorescence intensity. Uncovered pores can be recognized by a lack of measured fluorescence intensity in the pore region. Bright spots can be assigned to attached excess lipid material such as LUV clusters. The Biomat station allowed to precisely align the field of view of CLSM and AFM and to map the same image section topographically (cf. chapter 3.3.4). The resulting atomic force micrographs obtained from QI mode (set point: 0.1 nN-0.2 nN) were shown in the lower images of figure 4.14 A and B, respectively. The gray scale visualizes the relative depth of the contact point of each force distance curve and thus, the height profile. Rim area, membrane-covered and uncovered pores can be readily distinguished for both surface functionalizations by comparison with the

respective fluorescence micrograph. Extracted height profiles shown in figure 4.15 demonstrate an indentation depth in the f-PSM region of 300 nm in case of the Au/6MH functionalization (A) and 50 nm in case of the SiO_x functionalization (B) compared to the rim area. In contrast, a penetration depth of more than 1 μm was achieved in both cases with uncovered pores. Moreover, conventional PSMs were fabricated by spreading electroformed GUVs (cf. chapter 3.2.1.3) on porous substrates functionalized with SiO_x. Resulting membrane patches were visualized by fluorescence and atomic force microscopy (cf. figure 4.14 C) and the formation of a continuous bilayer was observed. The extracted height profile, shown in figure 4.15 C, indicates an indententation depth of 50 nm for membrane covered pores and more than 900 nm for uncovered pores.
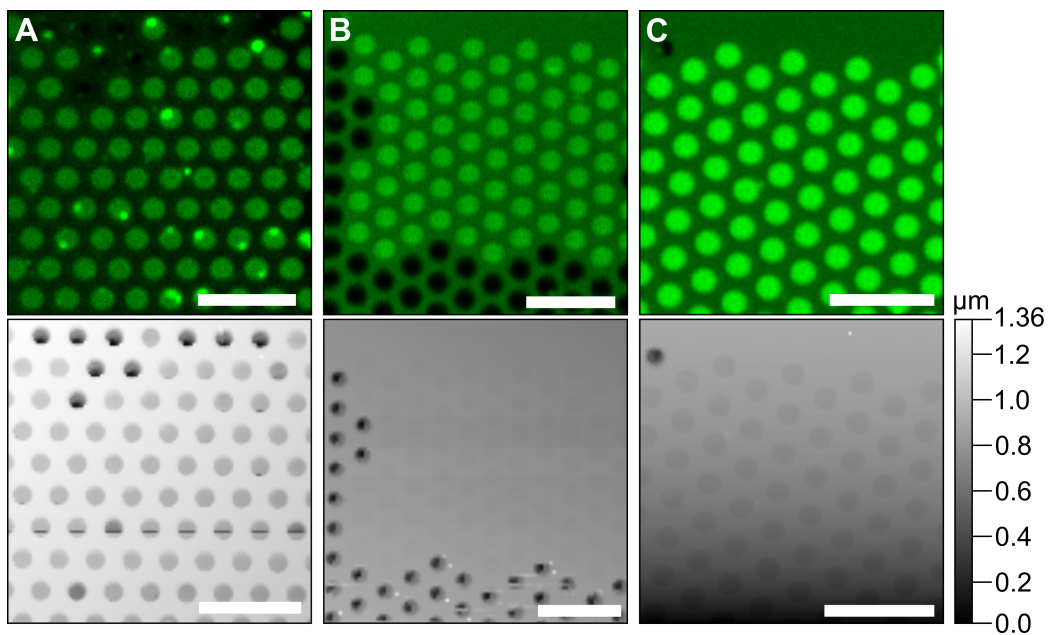
Figure 4.14: Fluorescence (upper images) and atomic force (lower images) micrographs of pore spanning membranes. PSMs (POPC/POPG/Chol/Atto488 DPPE, 69/15/15/1, n/n) prepared by spreading GUVs, originating from doplet-based microfluidics, on Aquamarijn substrates (pore diameter 1.2 μm) functionalized with **A:** Au/6MH respectively **B:** SiO_x ($1 \leq x \leq 2$). **C:** PSMs of the same lipid composition were prepared by spreading electroformed GUVs on SiO_x ($1 \leq x \leq 2$) functionalized Aquamarijn substrates (pore diameter 1.2 μm). Scale bars = 5 μm.
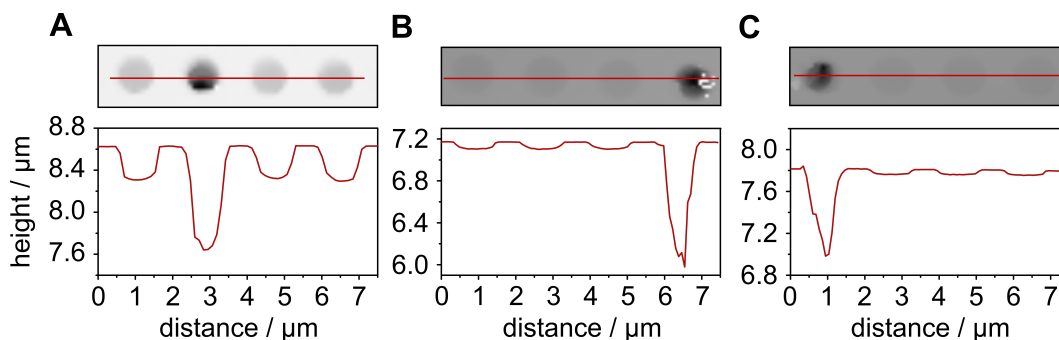
Figure 4.15: Atomic force micrographes and corresponding height profiles along the red line. PSMs (POPC/POPG/Chol/Atto48 DPPE, 69/15/15/1, n/n) prepared by spreading GUVs, originating from doplet-based microfluidics, on Aquamarijn substrates (pore diameter 1.2 μm) functionalized with **A:** Au/6MH respectively **B:** SiO$_x$ ($1 \leq x \leq 2$). **C:** PSMs of the same lipid composition were prepared by spreading electroformed GUVs on SiO$_x$ ($1 \leq x \leq 2$) functionalized Aquamarijn substrates (pore diameter 1.2 μm). Indentation depths for covered pores of 300 nm for PSMs on Au/6MH functionalized substrates and 50 nm for PSMs on SiO$_x$ functionalized substrates were found.

In order to determine mechanical properties of the presented PSMs, force-indentation experiments were performed. The lateral membrane tension of the pore covering bilayer, being a result of the free energy difference of s-PSM and f-PSM,[169] was investigated by measuring force-distance curves (FDCs) in the center of f-PSMs. Therefore, as described above, PSMs were prepared by spreading GUVs from different preparational methods (microfluidics, electroformation) on different functionalized substrates (Au/6MH, SiO$_x$) and imaged via CLSM and AFM. For the measurement of individual FDCs, the center of each pore was selected. Force-indentation experiments were performed by indenting the f-PSM and analyzing the applied force with respect to the tip-membrane separation at a loading force of 0.2 nN and an indentation speed of 1 μm s^{-1}. Figure 4.16 A displays a typical FDC of an f-PSM on a SiO$_x$ functionalized Aquamarijn substrate (pore diameter 1.2 μm) obtained from spreading microfluidic-GUVs, which is characteristic for all preparations. The course of indentation and retraction curve are super-imposed indicating a fully elastic behavior of the f-PSM upon indentation, which was observed during all experiments. The lateral membrane tensions σ were extracted from the slopes of the indentation curves as described in chapter 3.3.4 and are represented in figure 4.16 B. Spreading of microfluidic-GUVs on Au/6MH functionalized substrates resulted in PSMs exhibiting a mean lateral membrane tension σ of (2.1 ± 1.2) mN m^{-1} ($n = 40$). In contrast, a surface functionalization with SiO$_x$ led to higher membranes tensions. For PSMs produced

from microfluidic-GUVs, σ was found to be $(4.6 \pm 0.7)\,\mathrm{mN\,m^{-1}}$ ($n = 85$), while PSMs produced from electroformed GUVs exhibited a lateral membrane tension of $(7.1 \pm 0.6)\,\mathrm{mN\,m^{-1}}$ ($n = 62$).
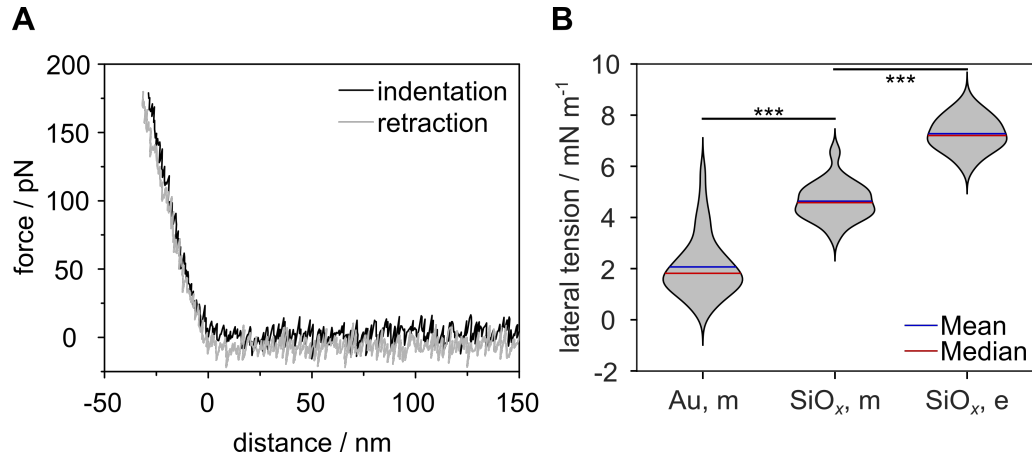
Figure 4.16: Lateral membrane tension of f-PSMs. A: Exemplary force distance curve measured in the center of an f-PSM (Aquamarijn, pore diameter 1.2 µm, funct. SiO_x) produced from microfluidic-derived GUVs (POPC/POPG/Chol/Atto488 DPPE, 69/15/15/1, n/n). **B:** Comparison of the lateral membrane tension of f-PSMs from different preparations. GUVs for the preparation of PSMs were produced by electroformation (e) and droplet-based microfluidics (m) and spread on Aquamarijn substrates (pore diameter 1.2 µm) functionalized with SiO_x ($1 \leq x \leq 2$) respectively Au/6MH. PSMs on Au/6MH functionalized substrates prepared from microfluidic GUVs (Au, m) exhibited a lateral membrane tension of $(2.1 \pm 1.2)\,\mathrm{mN\,m^{-1}}$ ($n = 40$), while PSMs on SiO_x functionalized substrates showed a lateral membrane tension of $(4.6 \pm 0.7)\,\mathrm{mN\,m^{-1}}$ ($n = 85$) for microfluidic-derived PSMs (SiO_x, m) and $(7.1 \pm 0.6)\,\mathrm{mN\,m^{-1}}$ ($n = 62$) for electroformation-derived PSMs (SiO_x, e), respectively. Statistical t-test: $p < 0.001$ (***).

As already described above, the membranes were fully elastic in all cases and thus, showed no hysteresis. To support this finding, the loading rate was varied between $0.1\,\mathrm{\mu m\,s^{-1}}$ and $10\,\mathrm{\mu m\,s^{-1}}$ during the repeated indentation of the same f-PSMs prepared by spreading microfluidic-GUVs on an SiO_x functionalized substrate. The resulting mean lateral membrane tensions σ ranged from $3.4\,\mathrm{mN\,m^{-1}}$ to $3.8\,\mathrm{mN\,m^{-1}}$ and were indistinguishable (cf. figure 4.17 A). Thus, no dependency of the membrane tension on the indentation speed was noted, supporting the hypothesis of a fully elastic behavior. Repeated measurements of FDCs on f-PSMs with varying loading forces ($0.2\,\mathrm{nN}$ to $1.2\,\mathrm{nN}$) had likewise no impact on the evaluated mean lateral membrane tensions, which ranged from $3.8\,\mathrm{mN\,m^{-1}}$ to $4.6\,\mathrm{mN\,m^{-1}}$ (cf. figure 4.17 B). A summary of all data is displayed in table 4.2.
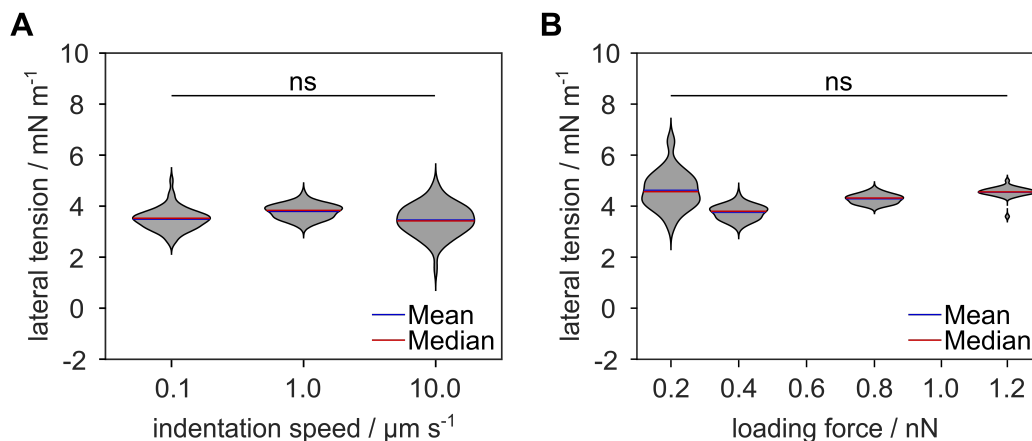
Figure 4.17: Influence of indentation speed and loading force on the lateral membrane tension. Force-distance curves were obtained from microfluidic prepared PSMs on SiO_x ($1 \leq x \leq 2$) functionalized substrates at different **A:** indentation speeds ($0.1\,\mu m\,s^{-1}$ to $10\,\mu m\,s^{-1}$, $n_{all} = 62$) and **B:** loading forces ($0.2\,nN$ to $1.2\,nN$, $n_{0.2} = 85$, $n_{0.4} = 62$, $n_{0.8} = 30$, $n_{1.2} = 32$). Statistical t-test: $p > 0.05$ (ns).

Table 4.2: Summary of the mean lateral membrane tension of all experiments with standard deviation as errors. GUVs were prepared via droplet based microfluidics (m) and electroformation (e) and spread on Aquamarijn substrates (pore diameter 1.2 µm) functionalized with SiO_x ($1 \leq x \leq 2$) and Au/6MH for the formation of PSMs. Force-indentation experiments were performed in the center of f-PSMs.

funct., prep. method	indentation speed	setpoint	σ / mN m^{-1}
Au/6MH, m ($n = 40$)	1.0 µm/s	0.22 nN	2.1 ± 1.2
SiO_x, m ($n = 85$)	1.0 µm/s	0.2 nN	4.6 ± 0.7
SiO_x, m ($n = 62$)	0.1 µm/s	0.4 nN	3.5 ± 0.4
SiO_x, m ($n = 62$)	1.0 µm/s	0.4 nN	3.8 ± 0.3
SiO_x, m ($n = 62$)	10 µm/s	0.4 nN	3.4 ± 0.6
SiO_x, m ($n = 30$)	1.0 µm/s	0.8 nN	4.3 ± 0.2
SiO_x, m ($n = 32$)	1.0 µm/s	1.2 nN	4.6 ± 0.2
SiO_x, e ($n = 62$)	1.0 µm/s	0.2 nN	7.1 ± 0.6

Besides the lateral membrane tension σ, the bending modulus κ of the f-PSMs was intended to be determined within the present work. For this purpose, an approach described by Kocun et al.[170] was followed, where both parameters can be extracted at the same location from a single force cycle. The basic experimental principle for the simultanous determination is depicted in figure 4.18 A. Approaching the

cantilever to the bilayer leads to an indentation, allowing to evaluate the lateral membrane tension σ. The subsequent tether formation upon retraction enables to determine the bending modulus when σ is known. An exemplary force distance curve is shown in figure 4.18 B. The lateral membrane tension (green) was extracted as described before (cf. chapter 3.3.4) from the indentation curve (black). If the retraction (grey) led to the formation of a membrane nanotube (tether), the tether force F_{tether} was extracted. The bending modulus was approximatly determined as described in equation 4.1.[35,170]

$$F_{\text{tether}} \approx 2\pi\sqrt{2\sigma\kappa} \qquad (4.1)$$
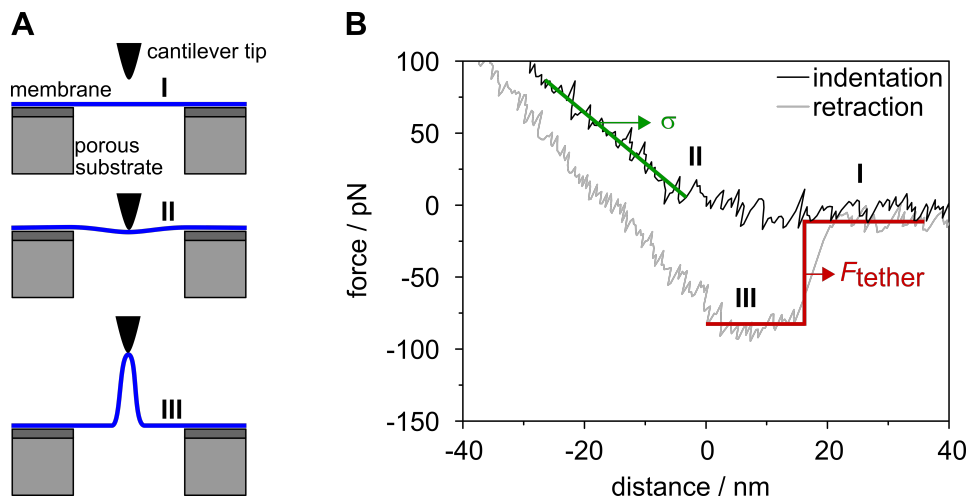
Figure 4.18: Tether formation during force-indentation experiments. A: Schematic illustration of approaching and indenting an f-PSM (I-II) and subsequently pulling a tether during the retraction. **B:** Exemplary force distance curve showing a formation of a nanotube during retraction (light gray) resulting in a plateau of the force (F_{tether}). The slope of the indentation (black) was used to calculate the lateral membrane tension σ (green) of the bilayer. A constant force plateau evidences the formation of a tether (F_{tether}).[170]

The bending modulus was determined for each above described experimental setup and summarized in table 4.3 using porous Aquamarijn substrates with a pore diameter of $1.2\,\mu\text{m}$. For PSMs prepared from microfluidic-GUVs spread on Au/6MH functionalized substrates a tether force a mean F_{tether} of $61.4\,\text{pN}$ and a bending modulus of $2.3\cdot10^{-20}\,\text{J}$ was determined. PSMs on substrates functionalized with SiO_x ($1 \leq x \leq 2$) resulted for PSMs prepared from microfluidic- and electroformed GUVs, respectively, in tether forces of $(65 \pm 6)\,\text{pN}$ and $(79 \pm 9)\,\text{pN}$. The bending

modulus σ calculated from these data yielded values of $(1.5 \pm 0.5) \cdot 10^{-20}$ J and $(1.2 \pm 0.2) \cdot 10^{-20}$ J, respectively.

Table 4.3: Summary of lateral tension, tether force and the calculated bending modulus. GUVs were prepared via droplet based microfluidics (m, $n = 4$) and electroformation (e, $n = 8$) and spread on Aquamarijn substrates (pore diameter 1.2 μm) functionalized with SiO_x and Au/6MH.

funct., prep. method	σ / mN m^{-1}	F_{tether} / pN	κ /10^{-20} J
Au/6MH, m	2.1 ± 1.2	61.4	2.3
SiO_x, m	4.6 ± 0.7	64.7 ± 5.9	1.5 ± 0.5
SiO_x, e	7.1 ± 0.6	78.5 ± 8.9	1.2 ± 0.2

4.3 Reconstitution of transmembrane proteins in artificial lipid bilayers

Studying individual integral membrane proteins requires either to deconstruct living cells in a top-down fashion or to assemble artificial model systems in a bottom-up approach from minimal components. Since the top-down approach has to deal with a high degree of complexity, reconstitution of the desired proteins in less complex model membrane systems is considered preferable oftentimes. [7,43] A multitude of different artificial membranes has been developed, such as lipid monolayers[171], lipid vesicles of different sizes (SUVs, LUVs, GUVs)[43], supported lipid bilayers[172], and pore-spanning membranes[35]. GUVs are particularly characterized by their cell-like size, which allows to image them for instance by fluorescence microscopy. Moreover, they serve as a starting point for the more sophisticated model system of pore-spanning membranes and for the design of artificial cells in the field of synthetic biology.[35,44] Diverse methods for the preparation of GUVs were established in the last decades, each exhibiting advantages as well as disadvantages particularly with regard to the reconstitution of membrane proteins (cf. chapter 1.3). Thus, developing and investigating novel methods to produce (proteo)-GUVs is an upcoming issue, which will be adressed in the following via droplet-based microfluidics.
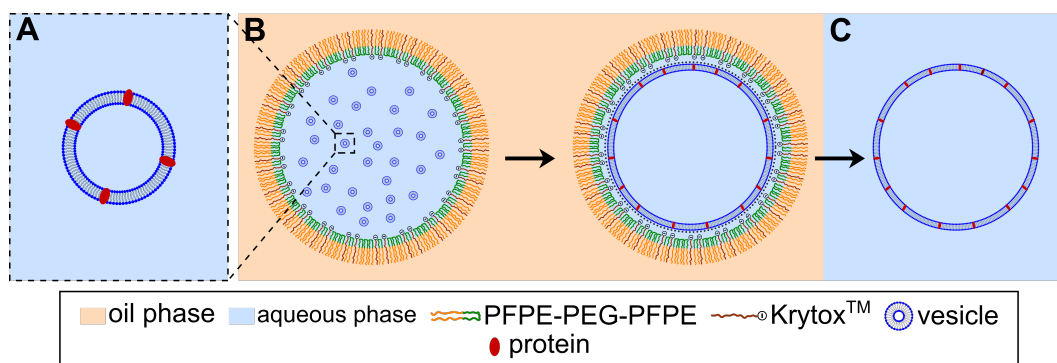
Figure 4.19: Schematic illustration of the injection of proteo-LUVs in surfactant stabilized droplets, the assembly of proteo dsGUVs and the release of proteo-GUVs. Proteo-LUVs (**A**) were produced via direct reconstitution or co-micellization, respectively. Injection of proteo-LUVs in surfactant stabilized droplets leads to the assembly of dsGUVs (**B**) which can be released to an aqueous phase (proteo-GUVs, **C**).

While Weiss et al. relied on the preliminary production of dsGUVs and their sequential loading with proteins by so-called picoinjection (cf. figure 5.4, chapter 5.3.2), a simplified approach was intended here to directly use proteo-LUVs for the assembly of protein-containing dsGUVs as illustrated schematically in figure 4.19. The TF_OF_1 ATP synthase and the less complex protein synaptobrevin 2 (syb 2) served as model proteins, each of which was first reconstituted in LUVs in a detergent-mediated manner before these proteo-LUVs were used to construct dsGUVs and to release GUVs.

4.3.1 Reconstitution of the TF_OF_1 ATP synthase in LUVs

Parts of the measurements were carried out by Roswitha Junker as part of her bachelor thesis.

4.3.1.1 Reconstitution of the TF_OF_1 ATP synthase in LUVs and determination of the activity by ATP synthesis assays

On average, F_OF_1 ATP synthases are responsible for more than $95\,\%$ of the total amount of synthesized ATP within different cell types. Therefore, they represent interesting drug targets, for example in cancer research.[173] In addition, ATP synthases are of great interest in the emerging field of synthetic biology, as they can supply artificial cells and tissues with energy in the form of ATP.[9] Reconstitution into model membrane systems and detailed study of their activity is required for accurate investigation. In order to transfer the TF_OF_1 ATP synthase from thermophillic *Bacillus* via microfluidics in the model membrane system of dsGUVs and released GUVs, reconstitution in LUVs was necessary (cf. figure 4.19). Subsequently, the proteo-LUVs were used analogously to protein-free LUVs for the fabrication of lipid based microemulsions containing droplet-stabilized proteo-GUVs according to chapter 3.2.3. However, prior to the microfluidic GUV production, the reconstitution success as well as the activity of the protein were studied extensively in LUVs, as described in the following.

Reconstitution of the TF$_O$F$_1$ ATP synthase in LUVs

Protein reconstitution in LUVs was performed as described in chapter 3.2.2 following the direct method (Triton™ X-100). LUVs (POPC) were produced via extrusion with a nominal diameter (d_{nom}) of 100 nm in reconstitution buffer R1 (cf. table 3.11) and destabilized by the detergent Triton™ X-100, allowing the insertion of the ATP synthase with a preferred orientation of the water soluble F$_1$ unit pointing to the extravesicular space.[174,175] The ATP synthase was added in a theoretical protein to lipid ratio of 1/20,000. Removal of the detergent was realized using Bio-Beads.

In order to analyze the reconstitution efficiency a density gradient centrifugation (flotation assay, cf. chapter 3.2.2.4) was performed to determine the amount of reconstituted protein ($n_{protein}$) within the bilayer as described by Miriam Schwamborn.[55] Proteoliposome samples were applied to a density gradient of the medium Nycodenz (0 %-40 %). Upon centrifugation proteoliposomes floated due to their inner aqueous compartment to the upper area of the gradient, while non-reconstituted protein accumulated on the bottom. Subsequent SDS PAGE of the fractions from the gradient and a protein standard of known concentration allowed to calculate the exact amount of reconstituted protein via the ImageJ feature *Analyze Gel* (Version 1.45s, W. Rasband, NIH, USA). With the help of the amount of lipid (n_{lipid}), determined via phosphate test (cf. chapter 3.2.1.4), an averaged protein to lipid ratio p/l of 1/19,600 was calculated by ($n_{protein}$)/(n_{lipid}). The mean reconstitution efficiency amounted to (102 ± 19) %. Values above 100 % can be explained by moderate loss of lipid material during the reconstitution procedure resulting in a higher final protein to lipid ratio than initially applied. Via dynamic light scattering (cf. chapter 3.2.2.3) the mean diameter (d_{eff}) of the proteoliposomes was determined to be (300 ± 40) nm. This information permits, with the help of the equations A.1 to A.4 (cf. chapter A.6), to estimate the number of ATP synthases per individual proteoliposome assuming an area of a single ATP synthase of $a_{protein} = 20 \, nm^2$, an area of a single lipid (POPC) of $a_{lipid} = 0.69 \, nm^2$ and a bilayer thickness of $h_{bilayer} = 4.0 \, nm$.[175–177] Thereby, it was calculated for an individual vesicle to contain approximately 45 ± 10 ATP synthases on average. Analyzed data result from five independent preparations (table 4.4).

Table 4.4: Results from the TF$_O$F$_1$ ATP synthase reconstlitution in LUVs (POPC) via Triton™ X-100. Reconstitution efficiency and protein to lipid ratio (p/l) were obtained from floatation assay and phosphate test. A nominal protein to lipid ratio of 1/20,000 was used. The diameter of the final proteoliposomes (d_{eff}) was determined by DLS and used for the calculation of the number of proteins per vesicle (N_{protein}). Data from five individual preparations were combined and averaged.

lipid mix.	averaged p/l (rec. efficiency)	d_{eff}	N_{protein}
POPC	$1/(19{,}600 \pm 4{,}200)$ $((102 \pm 19)\,\%)$	$(300 \pm 40)\,\text{nm}$	45 ± 10

Luminescence based activity assay of the TF$_O$F$_1$ ATP synthase

The preceding analysis of the reconstitution efficiency demonstrated successful reconstitution of the ATP synthase in LUVs. Next the activity was investigated and thereby, indirectly, the orientation of the ATP synthase, since a predominant orientation of the F$_1$ unit pointing to the interior of the vesicle would lead to inactive proteo-LUVs. Analysis of TF$_O$F$_1$-mediated ATP synthesis was performed using an assay, based on ATP-induced luminescence of a luciferin-luciferase-system, which is well-known in literature. [64,70,75,115,178]

The ATP synthesis assay was performed as described in chapter 3.3.1.1. Figure 4.20 A demonstrates an averaged exemplary time course from three measurements with proteo-LUVs (POPC) with a determined p/l of 1/19,500. Curves were background corrected and normalized to the produced amount of ATP, according to chapter 3.3.1.1 After the acidification of the proteo-LUVs using buffer A$_{4.7}$ (pH 4.7), a proton motive force pmf, generated from a membrane potential $\Delta\Psi$ and a ΔpH (cf. equation 4.2 and 4.3), was applied by adding buffer L$_{8.8}$ ($t = 0$, pH 8.8).

$$\Delta\psi = \frac{TR}{F} \cdot ln\frac{[K^+_{\text{out}}]}{[K^+_{\text{in}}]} = 135 \text{ mV} \tag{4.2}$$

$$pmf = \Delta\psi + 2.3 \cdot \frac{k_B T}{e} \cdot \Delta\text{pH} = \Delta\psi + 60\text{mV} \cdot \Delta\text{pH} \tag{4.3}$$

The theoretically created proton gradient amounted to ΔpH $= 4.1$ and thus a theoretical proton motive force of $pmf = 381$ mV ($\Delta\Psi = 135$ mV) was generated. The K$^+$ ionophore valinomycin was added to reach a valinomycin to lipid ratio (val/l) of 1:40,

enabling charge equilibration for the translocated protons. As a result, ATP synthesis by TF_OF_1, reconstituted in LUVs, was induced (cf. figure 4.20 A, lower right corner). The synthesized ATP was visualized by an increase of the luminescence intensity due to the reaction of the luciferin-luciferase-system as described in chapter 3.3.1. By fitting the initial slope (cf. figure 4.20 A, red line), the ATP synthesis rate v of the total amount of ATP synthases within the assay was determined (cf. equation 3.11 and 3.11). Figure 4.20 B represents the ATP synthesis rates plotted against the amount of TF_OF_1 ATP synthase per assay of four preparations, determined by flotation assay. The plot indicates a linear increase of the ATP synthesis rate with increasing amounts of reconstituted ATP synthases. Calculation of the rate per individual protein (turnover v_{cat}) was performed using equation 3.12 and yielded a mean value of $(10 \pm 3)\,\mathrm{s}^{-1}$ ($n = 18$) with the standard deviation as error.
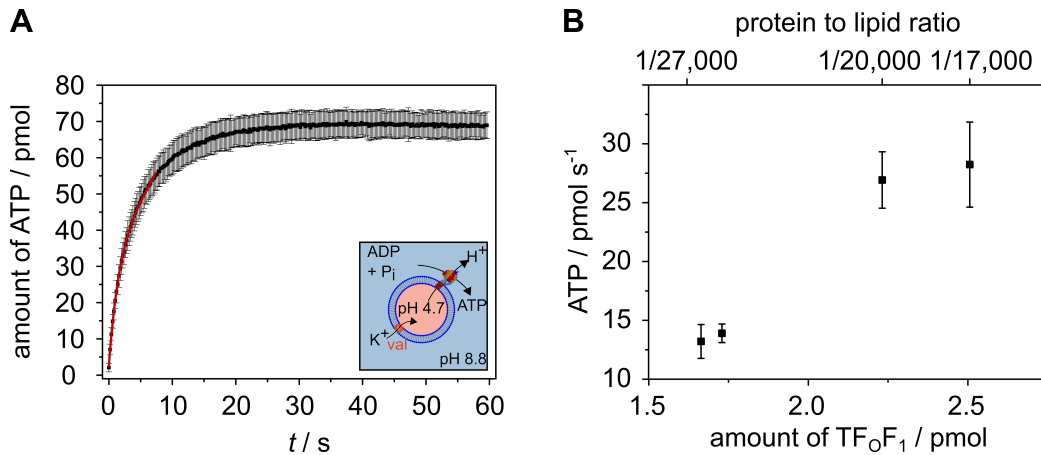
Figure 4.20: Measurement of the TF_OF_1 activity in large unilamellar vesicles. **A:** TF_OF_1 ATPase activity in LUVs (POPC, p/l 1/19,500) was determined by luminescence assays using a luciferin-luciferase system. The general procedure is schematically illustrated in the lower right corner. In the presence of a ΔpH between lumen and extravesicular compartement, a pmf was created, leading to ATP synthesis by TF_OF_1. **B:** ATP synthesis rate v is plotted against the amount of the TF_OF_1 ATP synthase per single assay (and the p/l). Measurements are shown with 1.66 pmol ($n = 9$), 1.73 pmol ($n = 3$), 2.23 pmol ($n = 3$) and 2.51 pmol ($n = 3$) TF_OF_1. ($T = 27.5\,°C$, $\Delta\Psi = 135$ mV, ΔpH = 4.1, $pmf = 381$ mV).

4.3.1.2 Quantitative analysis of the vesicle acidification step of the ATP synthesis assay

Pyranine based vesicle acidification assay

The presented ATP synthesis assay is widely used in literature. However, the data situation concerning the commonly used acidification step, which has to be conducted immediatly prior to the actual assay (cf. figure 3.13), is insufficient. As this acidification step greatly influences the achievable luminal pH of the proteoliposomes and thus, on the pmf and the overall activity of the ATP synthase, detailed investigation of vesicle acidification was performed in the course of this work. Thus, a fluorescence-based vesicle acidification assay, using the pH sensitive and water soluble dye pyranine was applied.

LUVs (POPC, $d_{\text{nom}} = 100\,\text{nm}$) were prepared via extrusion and filled with pyranine ($500\,\mu\text{M}$) as described in chapter 3.2.1.2 and 3.3.2 using reconstitution buffer $R1_{8.0}$ (pH = 8.0, cf. table 3.16). The lipid concentration was determined for each sample (cf. chapter 3.2.1.4) and kept constant ($50\,\mu\text{M}$) for all experiments. Via DLS, a mean effective diameter of the LUVs of $(101 \pm 3)\,\text{nm}$ ($n = 3$) was determined. The fluorimeter-based acidification assay was performed as described in chapter 3.3.2 at a constant temperature of $20\,°\text{C}$. Figure 4.21 A exemplifies the raw data of a typical fluorescence time course measurement ($\lambda_{\text{ex/em}} = 458/512\,\text{nm}$). After baseline detection (I), acidification buffer A_{pH} with a certain pH value (pH$_{\text{ac}}$, cf. table 3.15) was added and a ΔpH was generated across the lipid bilayer of the LUVs. The fast drop of the fluorescence intensity was initially caused by the dilution of the vesicle suspension (dilution factor $DF = 5$). The following decrease of the fluorescence intensity (II) resulted from proton influx into the vesicle lumen, which is schematically illustrated in 4.21 A (lower left corner), and the subsequent protonation of pyranine molecules. Since the acidification of proteoliposomes prior to the ATP synthesis assay was performed for 3 min, the fluorescence intensity was observed in the same time interval. By the addition of LDAO, vesicles were lysed to prove whether a complete pH equilibration between intra- and extravesicular compartment was reached (III). The data highlighted with a dashed box in figure 4.21 A were normalized to the fluorescence intensity of the baseline considering the dilution factor (DF) (cf. figure 4.21 B). The final normalized fluorescence intensities after vesicle acidification (I_{180s}) and subsequent LDAO addition (I_{LDAO}) were extracted from the normalized fluorescence

intensity data (cf. figure 4.21 B). A quantitative analysis of the resulting pH is described below.
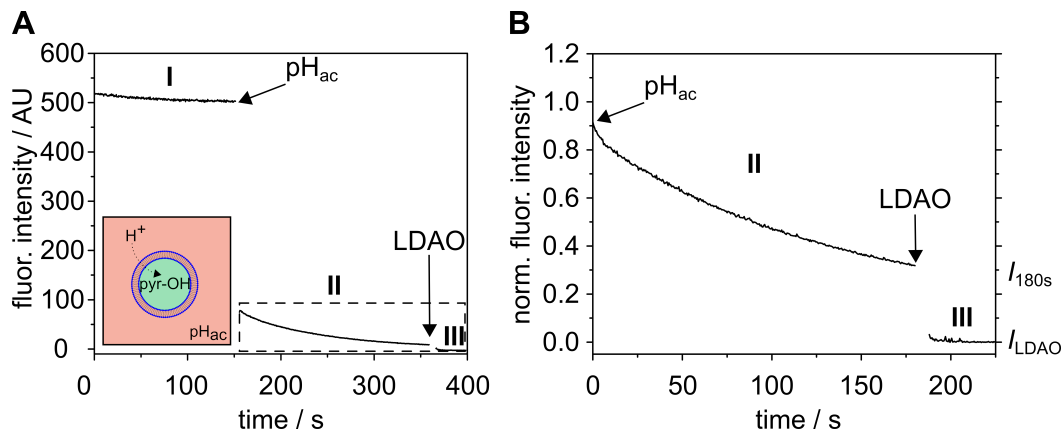
Figure 4.21: Investigation of the acidification step of the ATP synthesis assay. A: Typical fluorescence intensity curve of the acidification assay. The proton influx in LUVs (POPC, pH_{in} 8.0) as a function of external pH (pH_{ac} 5.8) was investigated using the pH sensitive fluorophore pyranine (500 µM). The addition of the acidification buffer A_{pH} led to a dilution ($DF = 5$) and subsequently an influx of protons in the lumen of the LUVs. The following addition of LDAO resulted in a release of the pyranine into the surrounding buffer. $\lambda_{ex/em} = 458/512$ nm. **B:** Data extracted from the dashed box were normalized to the fluorescence intensity of the baseline considering $DF = 5$.

Characterization and quantification of the pH dependent pyranine fluorescence

To quantify the intravesicular pH value after vesicle acidification, the fluorescent behavior of pyranine dependent on the pH value has to be known in detail. The literature known pK_a value of pyranine in aqueous solution amounts to 7.2, which makes it suitable for pH detection in the range of pH 5 to pH 8.[179] Since lipid or buffer components might alter the pK_a of a fluorophore, the exact pK_a was determined as described in the following for the employed conditions.

LUVs (POPC, $d_{nom} = 100$ nm) were prepared in reconstitution buffer $R1_{pH}$ (cf. table 3.16) with pH values of 8.0, 7.0, 6.0, 5.8, 5.0 and 4.0, respectively, and filled with pyranine (500 µM) as described in chapter 3.2.1.2 and 3.3.2. The lipid concentration was kept constant at 50 µM for all experiments. Subsequently, fluorescence emission spectra were measured ($\lambda_{ex} = 458$ nm, $\lambda_{em} = 485\text{-}580$ nm). The spectra were normalized to the maximal fluorescence intensity at $\lambda_{em,max} = 512$ nm from

the measurement at pH 8.0 (cf. figure 4.22 A). As can be seen in figure 4.22, the maximal fluorescence intensities decreased with decreasing luminal pH.
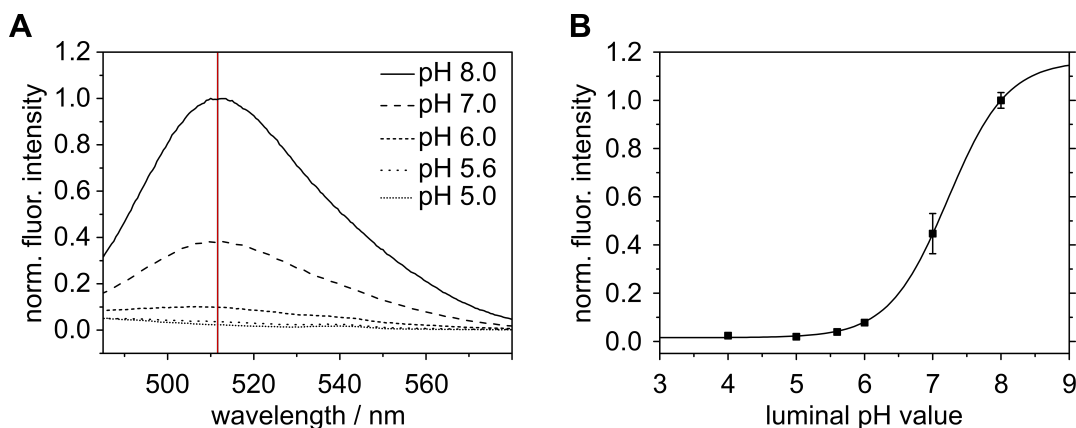
Figure 4.22: Fluorescence emission of LUVs (POPC, $d_{nom} = 100\,nm$) filled with pyranine (500 μm) at different pH-values. A: Spectra were measured from samples containing pyranine filled LUVs ($c_{lipid} = 50\,\mu M$) prepared at different luminal pH values (8.0, 7.0, 6.0, 5.8, 5.0, 4.0). With decreasing pH values, the fluorescence intensity at $\lambda_{em} = 512$ nm was reduced when exciting with $\lambda_{ex} = 458$ nm. **B:** The maxima of the normalized emission spectra of pyranine filled LUVs were plotted against the luminal pH. Fitting equation 4.4 to the pH dependent relative fluorescence intensities yielded in a pK_a value of 7.22.

For the determination of the pK_a value, the normalized maximal fluorescence intensity at $\lambda_{em,max} = 512$ nm (cf. figure 4.22 A, dashed red line) for each pH value was extracted from the spectra and plotted against the pH value (cf. figure 4.22 B). According to the works of Schwamborn et al. and Avnir et al., a variant of the Henderson Hasselbalch equation (cf. equation 4.4) was employed, allowing to describe the fluorescence intensity as a function of the luminal pH.[118,119]

$$I = I_{min} + \frac{I_{max} - I_{min}}{1 + 10^{pKa-pH}} \tag{4.4}$$

I_{min} and I_{max} represent the normalized minimal and maximal fluorescence intensities and were determined to values of 0.02 and 1.16, respectively. The pK_a value of pyranine was analyzed by fitting equation 4.4 to the data represented in figure 4.22 B. As a result, a pK_a of 7.22 was determined, which is in accordance with the literature.[179]
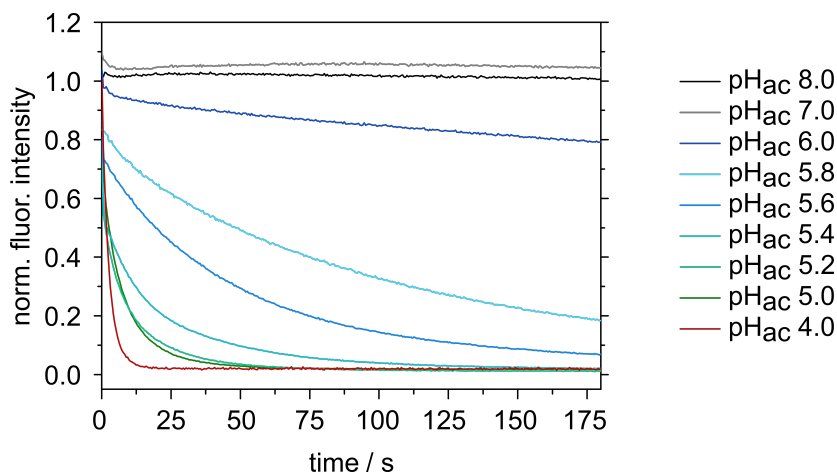
Figure 4.23: Acidification assay of LUVs (POPC) at different pH values. The normalized fluorescence intensity of LUVs filled with pyranine decreased after the influx of protons in the lumen of the LUVs due to the addition of the acidification buffer (pH_{ac}). Each curve was obtained from averaging at least three individual measurements.

For quantifying the acidification of the vesicle lumina as function of the pH of the acidification buffer, fluorescence spectroscopic measurements were performed as described above. Figure 4.23 reveals the normalized fluorescence intensity courses of the acidification of LUVs (POPC, $d_{\text{nom}} = 100\,\text{nm}$) with acidification buffer A_{pH} (cf. table 3.15) of pH values varying from 4.0 to 8.0. The final normalized fluorescence intensity at $t = 180\,\text{s}$ (I_{180s}) and the intensity after addition of LDAO (I_{LDAO}) were extracted and converted into pH values (pH_{180s}, pH_{LDAO}) by using equation 4.4. Extracted intensities and calculated pH values are listed in table 4.5. Since the LUVs were lysed after the addition of LDAO and thus the fluorophore entered the extravesicular solution, determination of pH_{LDAO} was a useful tool to prove, whether the pH value of the acidification buffer also led to the intended pH value of the external buffer during the assay. This requirement was complied since vesicle acidification assays with pH_{ac} values of 8.0, 7.0 or 6.0 resulted in mean pH_{LDAO} values of 7.9, 7.1 or 5.8, respectively. The analysis of I_{180s} revealed whether addition of acidification buffer A_{pH} caused total pH equilibration between the vesicle lumen and the outer buffer after the acidification period of 180 s. For an initial ΔpH of 0 or 1 ($\text{pH}_{\text{ac}} = 8.0, 7.0$), the resulting mean luminal pH_{180s} values were found to be 7.8 ± 0.2 or 8.1 ± 0.1, respectively, indicating that apparently no proton influx in the vesicles occured. In contrast, acidification with pH_{ac} 6.0, 5.8 and 5.6 led to luminal pH_{180s} values of 7.5 ± 0.3, 6.4 ± 0.3 and 5.8 ± 0.1, respectively. Thus, a proton influx occurred, however, a complete equilibration of the inner and

outer pH value was not reached. Calculated pH values below 6.0 are rather to be understood as approximations or can partly not be evaluated (n.e.), respectively, since the accuracy of the pH determination by means of equation 4.4 is limited. It is noteworthy to mention, that addition of valinomycin, which is part of buffers from the ATP synthesis assay (cf. chapter 4.3.1.1), has no impact on the acidification step, as presented in table 4.5. More detailed information can be found in the appendix (cf. chapter A.8).

Table 4.5: Summary of calculated luminal pH values obtained after the vesicle acidification assay. Normalized fluorescence intensities after vesicle acidification ($t = 180\,\text{s}$) and after the addition of LDAO (I_{180s}, I_{LDAO}) were extracted from measurements shown in figure 4.23 and A.1 B without and with valinomycin (val). For the calculation of the pH, equation 4.4 was recruited. Fluorescence intensity data from measurements performed with pH_{ac} lower than 5.4 were not shown, since they did not result in reliable values when applying the fit. Acidification assays were performed with pH_{ac} of 8.0 ($n = 5$), 7.0 ($n = 6$), 6.0 ($n = 6$), 5.8 ($n = 3$), 5.6 ($n = 3$) and 5.4 ($n = 3$). Displayed data with additional valinomycin result from single measurements ($n = 1$). (n.e.: not evaluable).

pHac	I_{180s}	I_{LDAO}	pH_{180s}	pH_{LDAO}
8.0	1.0 ± 0.2	1.0 ± 0.2	7.8 ± 0.2	7.9 ± 0.2
7.0	1.0 ± 0.1	0.5 ± 0.3	8.1 ± 0.1	7.1 ± 0.5
6.0	0.8 ± 0.2	0.1 ± 0.1	7.5 ± 0.3	5.8 ± 0.9
5.8	0.2 ± 0.1	0.01 ± 0.01	6.4 ± 0.3	< 5.8 (n.e.)
5.6	0.07 ± 0.01	0.002 ± 0.002	5.8 ± 0.1	< 5.8 (n.e.)
5.4	0.02 ± 0.003	0	< 5.8 (n.e.)	< 5.8 (n.e.)
7.0 (+ val)	1.0	0.4	8.0	7.0
6.0 (+ val)	0.6	0.04	7.3	5.4

4.3.1.3 Influence of the pH gradient on the TF$_O$F$_1$ activity

Proton-driven ATP synthesis by F$_O$F$_1$ ATP synthases plays an essential role in the chemiosmotic theory. The proton motive force *pmf* induces and influences the protein activity and is caused by the ΔpH and the transmembrane electrical potential $\Delta\psi$.[57,75] This section aims to investigate the influence of the applied proton gradient on the activity of TF$_O$F$_1$ ATP synthase in LUVs, while four other essential key factors were kept constant. First, the ATP synthesis assay was repeated as described in chapter 3.3.1.1 with the pre-step of the vesicle acidification being performed for precisely 3 min to consistently achieve the desired luminal pH. Second, the ATP synthesis assays were performed at a constant reaction temperature of 27.5 °C, although the physiological temperature optimum of TF$_O$F$_1$ ATPase is approximately 60 °C.[55,73,115] This difference results from the temperature sensitivity of the luciferase system, whose reactivity strongly decreases above 30 °C.[75] Third, the K$^+$-valinomycin diffusion potential was kept constant evoking a transmembrane electrical potential $\Delta\psi$ of 135 mV (cf. equation 3.6). Fourth, the pH$_{out}$ of the outer reaction buffer L$_{8.8}$ was fixed to 8.8. Phosphorylation and dephosphorylation of ATP *per se* are dependent on the pH value.[75,180] In the assay used here, the ATP-producing F$_1$ unit pointed to the outer solution. Therefore, the external pH was kept constant to avoid the phosphorylation reaction affecting the measured protein activity.

To investigate the impact of the ΔpH, proteoliposomes (POPC) were produced as described before (cf. chapter 3.2.2) and examined in terms of their diameter, protein-to-lipid ratio and the reconstitution efficiency. Results were presented in chapter 4.3.1.1. The respective ΔpH was formed by injecting the vesicles in different acidification buffers A$_{pH}$ (pH$_{ac}$, cf. table 3.15). By adding buffer L$_{8.8}$ (pH$_{out}$ = 8.8), the theoretical ΔpH$_{theor}$ (= pH$_{out}$ − pH$_{ac}$) and $\Delta\psi$ (135 mV) were generated and contributed to the applied *pmf*$_{theor}$ (cf. equations 4.2 and 4.3), which ranged from 423 mV (pH$_{ac}$ = 4.0) to 243 mV (pH$_{ac}$ = 7.0). ATP synthesis of the TF$_O$F$_1$ ATP synthase was induced and monitored as luminescence from the luciferin-luciferase system. Calibration of the signal was realized by the addition of ATP in a known concentration. By fitting the inital slope of the ATP synthesis curves, the turnover rate was determined using equations 3.10 to 3.12 and plotted against the theoretical luminal pH, equaling the pH$_{ac}$ of the acidification buffer. Reported turnover rates were obtained from six or more measurements from at least two independent reconstitutions.

Results are shown in figure 4.24. For the theoretical luminal pH_{ac} values, ranging from 4.0 to 7.0, mean turnover rates from $(13 \pm 2)\,s^{-1}$ to $(0.04 \pm 0.06)\,s^{-1}$ were determined and summarized in table 4.6. It is noteworthy that a maximal turnover rate of $\sim 13\,s^{-1}$ was reached at a luminal pH_{ac} of 4.0 and $\Delta pH_{theor} = 4.8$, respectively, which becomes evident by plotting the turnover rate against the difference in proton concentration between intra- and extravesicular volume (cf. figure 4.24 B).
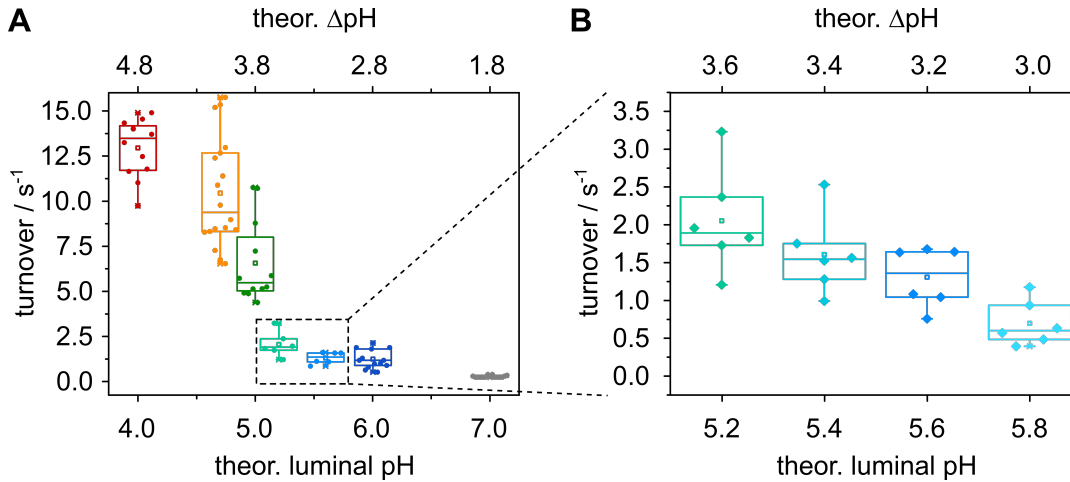
Figure 4.24: Turnover number of the TF_OF_1 ATP synthase in LUVs as a function of the theoretical luminal pH and ΔpH, respectively. The turnover rate was determined for different theoretical luminal pH values (pH_{in}) and a fixed pH_{out} of 8.8. The theoretical luminal pH value resulted from previous injection of the TF_OF_1-LUVs in acidification buffers with different pH values: **A:** 4.0 ($n = 12$, $N = 4$), 4.7 ($n = 18$, $N = 4$), 5.0 ($n = 12$, $N = 4$), 5.2 ($n = 6$, $N = 2$), 5.6 ($n = 6$, $N = 2$), 6.0 ($n = 13$, $N = 4$), 7.0 ($n = 15$, $N = 5$) and **B:** 5.2, 5.4, 5.6, 5.8 ($n = 6$, $N = 2$). $\Delta\psi$ was kept constant at 135 mV. Proteoliposomes (POPC) had a mean p/l of 1/19,600 and a mean diameter of $(300 \pm 40)\,nm$. The Box plots extent from the 25th to 75th percentile and whiskers from 5th to 95th.

However, as indicated in chapter 4.3.1.2, the injection of vesicles into the acidification buffer did not lead to a total equilibration of the pH value between vesicle lumen and the outer solution. Thus, it appeared interesting, to compare the curve shown in figure 4.24 with the course of the turnover rate as a function of the experimentally determined luminal pH value (pH_{exp}, cf. table 4.5). In figure 4.25 A, the mean turnover rates with standard deviation as error bars were plotted once against the theoretical pH_{ac} (black) and once against the mean experimentally determined luminal pH_{exp} (red). The respective experimentally determined luminal pH_{exp} values were taken from table 4.5 (mean value of pH_{180s}). For all assays, performed by using

acidification buffers of $pH_{ac} < 5.6$, the actual luminal pH_{exp} was not determinable (n.e.) and therefore respective data were not shown. The visual inspection of figure 4.25 A reveals a shift of the individual data points to the right. This finding indicates, that turnover resulted from lower ΔpH_{exp} (due to a higher luminal pH_{exp}) than actually anticipated based on the pH_{ac} of the acidification buffer. Therefore, the calculated theoretical pmf_{theor} for each turnover rate is overestimated and has to be corrected by using the determined ΔpH_{exp}. A summary of the data can be found in table 4.6.
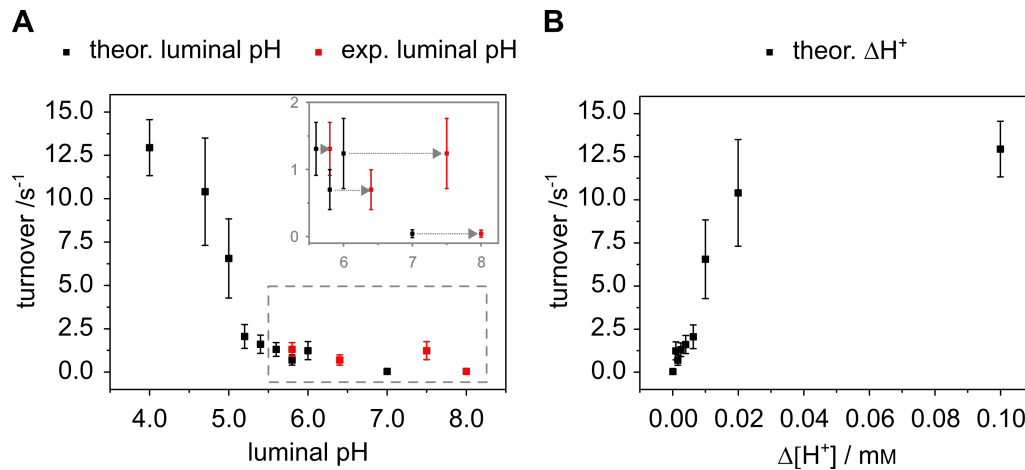
Figure 4.25: Impact of the vesicle acidification on the turnover rate of the TF_OF_1 ATP synthase. A: Dependency of the turnover rate v_{cat} on the theoretical (black) and the experimentally determined (red) luminal pH. The latter was obtained from vesicle acidification assays using pyranine (cf. table 4.5). **B:** Dependency of the turnover rate v_{cat} on the concentration gradient of protons $\Delta[H^+]$ across the lipid bilayer determined from the theoretical luminal pH values and the pH_{out} of the outer reation buffer $L_{8.8}$. Mean turnover with standard deviation as error bars were taken from figure 4.24. Proteoliposomes (POPC) had a mean p/l of $1/19{,}600$ and a mean diameter of (300 ± 40) nm.

Table 4.6: Summary of theoretical and experimental determined luminal pH, ΔpH, *pmf* and the resulting turnover rates of the TF_OF_1 ATP synthase. Theoretical values for the luminal pH were taken from the adjusted pH_{ac} of the acidification buffer, while pH_{exp} was determined from the vesicle acification assay using pyranine (cf. chapter 4.3.1.2). pH_{ac} and pH_{exp}, respectively, were used for the calculation of ΔpH and *pmf*. $\Delta\psi$ was kept constant at $135\,\mathrm{mV}$. The turnover rates were obtained from the ATP synthesis assay using fixed $pH_{out} = 8.8$ and different $pH_{ac} = 4.0$ ($n = 12$, $N = 4$), 4.7 ($n = 18$, $N = 4$), 5.0 ($n = 12$, $N = 4$), 5.2, 5.4, 5.6, 5.8 ($n = 6$, $N = 2$), 6.0 ($n = 13$, $N = 4$), 7.0 ($n = 15$, $N = 5$). (n.e.: not evaluable).

luminal pH		ΔpH		*pmf*		$v_{cat}\ /\ \mathrm{s}^{-1}$
theor.	exp.	theor.	exp.	theor.	exp.	
4.0	n.e.	4.8	n.e.	423	n.e.	13.0 ± 1.6
4.7	n.e.	4.1	n.e.	381	n.e.	10.4 ± 3.1
5.0	n.e.	3.8	n.e.	363	n.e.	6.5 ± 2.3
5.2	n.e.	3.6	n.e.	350	n.e.	2.1 ± 0.67
5.4	n.e.	3.4	n.e.	339	n.e.	1.6 ± 0.52
5.6	5.8	3.2	3.0	327	315	1.3 ± 0.39
5.8	6.4	3.0	2.4	315	279	0.70 ± 0.30
6.0	7.5	2.8	1.3	303	213	1.2 ± 0.52
7.0	8.1	1.8	0.7	243	177	0.042 ± 0.058

4.3.1.4 Influence of lipid composition on the activity TF_OF_1 ATP synthase

The lipid composition is an essential factor that has to be taken into consideration when working with membrane-associated proteins, regarding purification, crystallization, reconstitution in artificial membranes and activity determination.[181–183] In contrast to the native environment of transmembrane proteins, artificial membranes represent a highly simplified system scaled down to a limited set of lipids, allowing to analyze the influence on the protein activity of individual components. Representatively, the impact of two lipid components on the overall activity of the TF_OF_1 ATP synthase were investigated within this study. Since cellular membranes of bacteria, like thermophillic *Bacillus*, are negatively charged to a certain extend,[184] the percentage of POPG was variied in range from $0\,\%$ to $30\,\%$. Additionally, the influence of cholesterol was studied for two reasons, although this is not a common part of the bacterial membrane. First, glycolipids with a cholesterol-like function

have been found in *Bacillus* species,[185] wherefore the influence of cholesterol, serving as a simple mimicry, on the TF_OF_1 ATP synthase activity was analyzed here. Second, the lipid mixture should also be considered in the context of the acidification step of the ATP synthesis to investigate whether both negatively charged lipids and cholesterol can have an influence on membrane permeability.

To investigate the influence of POPG and cholesterol on the protein activity, the TF_OF_1 ATP synthase was reconstituted in LUVs composed of different lipid compositions as described previously. Reconstitution efficiency, protein to lipid ratio and effective vesicle diameter were obtained for POPG and cholesterol containing LUVs analogously to the procedure described in chapter 4.3.1.1. Proteo-LUVs composed of both POPC/POPG (0 mol% to 30 mol% POPG) and POPC/Chol (0 mol% to 30 mol% Chol) revealed similar reconstitution efficiencies of (96 ± 31) % ($n = 4$) and (97 ± 24) % ($n = 3$), respectively, yielding a mean protein to lipid (p/l) ratio of 1/21,000. The actual vesicle diameter d_{eff} after reconstitution was determined to be (330 ± 40) nm for POPC/POPG LUVs (85/15, n/n) and (360 ± 40) nm for POPC/Chol LUVs (85/15, n/n). Assuming an area of a single TF_OF_1 (a_{protein}) of 20 nm^2, a mean area of a single lipid (a_{lipid}) of 0.64 nm^2 for POPC/Chol and of 0.67 nm^2 for POPC/POPG, respectively, and a thickness of the bilayer of approximately 4.0 nm, the average number of proteins per individual vesicle was calculated to 49 ± 16 for POPG-containing vesicles and 56 ± 13 for cholesterol containing vesicles (cf. equations A.1 to A.4).[55,175–177] Overall, the data for both compositions were summarized in table 4.7 and is within the error range of the reconstitution analysis data for pure POPC proteo-LUVs, shown in chapter 4.3.1.1.

The TF_OF_1 activity was determined as described before via luminescence-based ATP synthesis assay (cf. chapter 3.3.1.1 and 4.3.1.3). Proteoliposomes were treated with acidification buffers of different pH ($pH_{\text{ac}} = 7.0, 6.0, 4.7$) to adjust the luminal pH. ATP synthesis was induced during the measurement by the addition of assay buffer $L_{8.8}$ ($pH_{\text{out}} = 8.8$), effecting a constant membrane electrical potential $\Delta\psi$ (135 mV) and a varying proton gradient ΔpH_{theor} (= 1.8, 2.8, 4.1). Both, electrical potential $\Delta\psi$ and ΔpH_{theor} contribute to the proton motive force pmf_{theor} (243 mV, 303 mV, 381 mV), which induces ATP synthesis by TF_OF_1. Production of ATP was monitored via the luciferin-luciferase system, yielding an ATP synthesis curve and allowing to estimate the ATP synthesis rate and thus the turnover rate v_{cat} per individual protein (cf. equation 3.11 to 3.12). Figure 4.26 displays the turnover rates of the TF_OF_1 ATP synthase, reconstituted in LUVs composed of different lipid compositions. For

the investigated $\Delta\text{pH}_{\text{theor}}$, no effect on the turnover rate was observed for either an increasing procentual amount of POPG or cholesterol within the bilayer of the LUVs.

Table 4.7: Results from the $\text{TF}_{\text{O}}\text{F}_1$ ATP synthase reconsitution in LUVs containing POPG and cholesterol, respectively, mediated by Triton™ X-100. Reconstitution efficiency and protein to lipid ratio (p/l) were obtained from floatation assay and phosphate test. A nominal protein to lipid ratio of 1/20,000 was used. The diameter of the final proteoliposomes (d_{eff}) was determined by DLS and used for the calculation of the number of proteins per vesicle (N_{protein}). Data from four (POPC/POPG) respectively three (POPC/Chol) preparations were combined and averaged.

lipid mix.	averaged p/l (rec. efficiency)	d_{eff}	N_{protein}
POPC/POPG	$1/(21{,}000 \pm 8{,}000)$ $(96 \pm 31\,\%)$	$(330 \pm 40)\,\text{nm}$	49 ± 16
POPC/Chol	$1/(21{,}000 \pm 4{,}000)$ $(97 \pm 24\,\%)$	$(360 \pm 40)\,\text{nm}$	56 ± 13
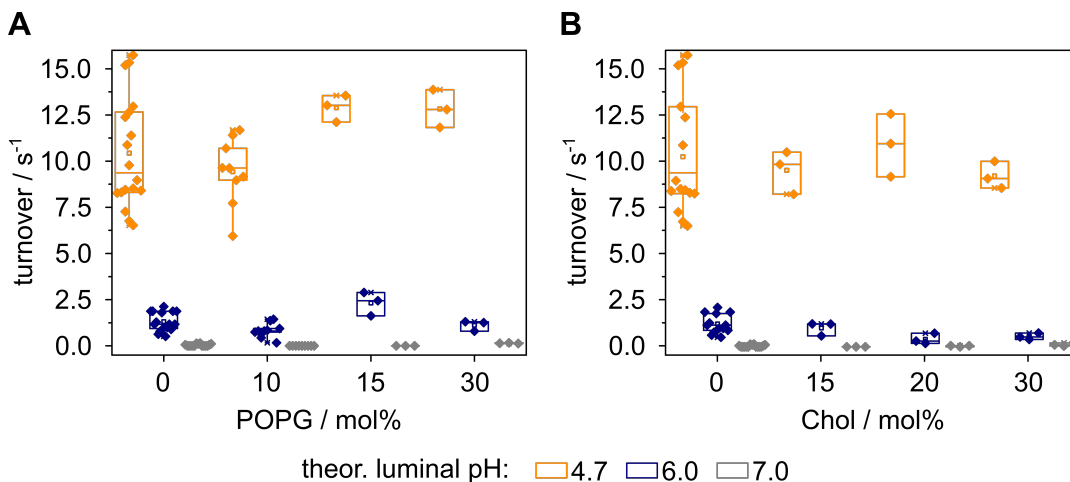
Figure 4.26: Impact of the lipid composition on the turnover rate of the $\text{TF}_{\text{O}}\text{F}_1$ ATP synthase. The turnover rate v_{cat} was determined for different amounts of the negatively charged POPG (10 mol%, 15 mol% and 30 mol%, **A**) and cholesterol (15 mol%, 20 mol% and 30 mol%, **B**), respectively, in the bilayer of the LUVs at luminal pH_{ac} values of 4.7 (orange), 5.0 (blue) and 7.0 (grey) and constant $\Delta\psi$ (135 mV). The basic component of the bilayer was POPC. The Box plots extent from the 25th to 75th percentile and whiskers from 5th to 95th.

Simultaneously, the possible impact of the lipid composition on the pre-assay acidification step, was analyzed analogously to chapter 4.3.1.2. Whether negatively charged POPG or cholesterol modulate the permeability of the membrane for protons was analyzed by the pyranine-based vesicle acidification assay as described in

chapter 4.3.1.2. The actual luminal pH was calculated from the normalized fluorescence intensity of pyranine filled LUVs composed of POPC/POPG (70/30, n/n) or POPC/Chol (70/30, n/n), respectively, measured after 3 min of vesicle acidification (I_{180s}) by applying equation 4.4. In Table 4.8 the obtained normalized fluorescence intensities I_{180s} and calculated actual luminal pH values (pH$_{exp}$) for acidification assays with pH$_{ac}$ = 7.0, 6.0 and 5.0 were summarized. For cholesterol containing LUVs, vesicle acidification assays with pH$_{ac}$ of 7.0 and 6.0 resulted in luminal pH values (pH$_{exp}$) of 8.0 ± 0.2 and 7.6 ± 0.1, respectively, which were similar to results for pure POPC vesicles (cf. table 4.5. Vesicles containing POPG appeared to reach moderately lower pH$_{exp}$ values of 7.7 ± 0.02 and 7.3 ± 0.07 after acidification with acidifiction buffer with pH$_{ac}$ 7.0 and 6.0, respectively. Acidification with pH$_{ac}$ 5.0 led to a drop in fluorescence intensity to almost zero in both cases, which precludes valid determination of the actual pH value with the aid of the calculation presented here. Assuming that these luminal pH$_{exp}$ values are reached upon acidification of proteoliposomes as a preliminary step prior to the ATP synthesis assay, these in turn can be used to calculate the pmf_{exp} from ΔpH$_{exp}$ (= pH$_{out}$ − pH$_{exp}$, pH$_{out}$ = 8.8). Theoretical and actual pmf are compiled in table 4.8.

Table 4.8: Effect of the lipid composition on the acidification of LUVs. LUVs composed of POPC/POPG (70/30, n/n) resp. POPC/Chol (70/30, n/n) were analyzed by the acidification assay using pyranine (luminal concentration of 500 µM). The pH value of the acidification buffer was decreased from 7.0 to 5.0 in steps of 1.0 ($n = 3$). Theoretical and actual pmf were determined from constant $\Delta\psi$ (135 mV) and ΔpH (= pH$_{out}$ − pH$_{ac/exp}$, pH$_{out}$ = 8.8).

lipid mixture	pH$_{ac}$	I_{180s}	pH$_{exp}$	pmf / mV	
				theor.	exp.
POPC/POPG	7.0	0.9 ± 0.01	7.7 ± 0.02	243	201
	6.0	0.6 ± 0.05	7.3 ± 0.07	303	225
	5.0	0.02 ± 0.01	< 5.8 (n.e.)	363	n.e.
POPC/Chol	7.0	1.0 ± 0.1	8.0 ± 0.2	243	183
	6.0	0.8 ± 0.1	7.6 ± 0.1	303	207
	5.0	0.02 ± 0.001	< 5.8 (n.e.)	363	n.e.

4.3.2 Reconstitution of the thermophillic F_OF_1 ATP synthase in GUVs via droplet-based microfluidics

Parts of the measurements were carried out by Merve Sari as part of her master thesis.

While reconstitution of F_OF_1 ATP synthases in LUVs has proven to be feasible since decades with high efficiency and reliability,[72,115,178,186] reconstitution in GUVs is still a challenge. Currently accessible methods for protein reconstitution in GUVs in general afford limited control of the GUV production and protein incorporation as well as low reproducibilty and inefficiency.[7,43,187] However, examination of proteins and their activity in a simplified but more cell-like shaped environment and the design of artificial cells can only be realized by their reconstitution in GUVs. To overcome the mentioned limitations, droplet-based microfluidics were applied recently for the production of droplet-stabilized GUVs (dsGUVs) and released GUVs, respectively, and their loading with biological components such as proteins. An approach based on studies from Weiss et al. was applied in a modified form (cf. figure 4.28 A).[45] The data shown in the following sections are taken from exemplary experiments which are representative for several preparations.

4.3.2.1 Reconstitution of TF_OF_1 ATP synthase in dsGUVs/GUVs

The TF_OF_1 ATP synthase was implemented in the lipid bilayer of preformed LUVs (d_{nom}) via direct reconstitution mediated by the detergent Triton™ X-100, as described in chapter 3.2.2 using reconstitution buffer R1 (cf. table 3.11). The lipid composition of POPC/POPG/Chol (70/15/15, n/n) was used to ensure comparability with previous results from the production of dsGUVs without protein. To verify the success of reconstitution in LUVs of this lipid composition, the protein to lipid ratio (1/14,000) was determined by flotation assay (cf. chapter 3.2.2.4). Additionally, the protein activity was analyzed by luminescence-based ATP synthesis assay (cf. chapter 3.3.1.1). A theoretical proton gradient ΔpH_{ac} of 4.1 was applied across the membrane resulting in a proton motive force *pmf* of $381\,mV$ ($\Delta\psi = 135\,mV$). ATP synthesis was monitored by a luciferin-luciferase system resulting in the ATP synthesis curve shown in figure 4.27 A. From the initial slope and the amount of

reconstituted protein, the turnover rate was examined equivalent to chapter 4.3.1.1 and calculated to be $7.4\,\mathrm{s}^{-1}$ ($\Delta\mathrm{pH}_{\mathrm{theor}} = 4.1$).
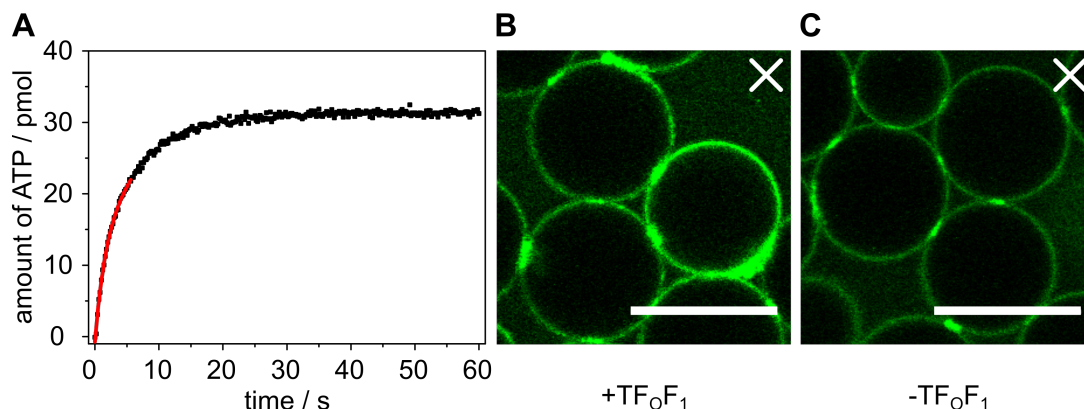
Figure 4.27: Influence of the detergent Triton™X-100 on the production of dsGUVs and the release of GUVs. A: The $\mathrm{TF_OF_1}$ ATP synthase was reconstituted in LUVs using the detergent Triton™X-100 (buffer R1, POPC/POPG/Chol 70/15/15, n/n). By means of an ATP synthesis assay the activity was verified and a turnover number of 7.4 s^{-1} was determined ($\Delta\mathrm{pH} = 4.1$, $\Delta\psi = 135\,\mathrm{mV}$, $pmf = 381\,\mathrm{mV}$). The protein to lipid ratio of 1/14,000 (n/n) was quantified by vesicle flotation assay. **B:** dsGUVs (POPC/POPG/Chol/TxR DHPE, 69/15/15/1, n/n, false colored in green) were prepared from proteoliposomes reconstituted with the help of Triton™X-100 (theor. p/l 1/80,000, n/n). Prior to injection into the droplets, the proteoliposomes were dialyzed and purified by size exclusion chromatography. **C:** dsGUVs (POPC/POPG/Chol/TxR DHPE, 69/15/15/1, n/n, false colored in green) were produced starting from LUVs treated with Triton™X-100 without reconstituting the $\mathrm{TF_OF_1}$ ATP synthase as a control. Buffers for **B**, **C**: reconstitution buffer R1 + 10 mm MgCl$_2$. Scale bars = 50 μm. A cross in the upper right corner of fluorescence micrograph indicates, that no released GUVs were found.

Subsequently, the $\mathrm{TF_OF_1}$-LUVs were used to produce dsGUVs following the general procedure described in chapter 3.2.3.2. For this purpose, a lipid-coupled fluorophore was added to the aforementioned lipid composition (POPC/POPG/Chol/TxR DHPE, 69/15/15/1, n/n) in order to visualize the membrane. The ATP synthase itself did not feature a fluorescent tag. A qualitative activity verification of $\mathrm{TF_OF_1}$ ATP synthase after reconstitution in LUVs was carried out in advance to each production of dsGUVs. Prior to the injection of the proteo-LUVs in the microfluidic device, the concentration of MgCl$_2$ was adjusted to 10 mm. Resulting dsGUVs are exemplarily depicted in figure 4.27 B. Visual inspection of the fluorescence micrograph reveals areas of high fluorescence intensity which can be classified as aggregations of lipid material. Moreover, the attempt to release GUVs from the microemulsion failed as indicated by the cross in the upper right corner of the fluorescence micrograph. In

order to verify, whether the presence of reconstituted protein itself led to the observed phenomena, LUVs were subjected to the procedure of TF_OF_1 reconstitution mediated by Triton™ X-100, but without adding protein. Subsequently these LUVs were used for the production of dsGUVs. An exemplary fluorescence micrograph is shown in figure 4.27 C. Again, areas of high fluorescence intensity were monitored in this case, and a release of GUVs was not observable. These findings led to the assumption, that the detergent Triton™ X-100 prevented the formation of a continuous bilayer within the droplets, independent of the presence of the protein. Instead aggregations of lipid material such as LUVs appear to occur.

As Triton™ X-100 seems to interfere with components from the dsGUVs production procedure, an alternative reconstitution procedure was required. Direct reconstitution of TF_OF_1 ATP synthases in LUVs was performed in a reliable and efficient manner by using the detergent nOG as described by Schwamborn et al.[119] The structural differences between nOG and Triton™ X-100 are, among other things, noticeable in a significantly higher CMC of nOG, enabling its removal from the LUVs suspension by gel filtration and dialysis.[22] The detailed reconstitution method involving membrane destabilization with nOG, protein addition and subsequent detergent removal by dialysis and size exclusion chromatography can be found in chapter 3.2.2.1. Success of functional protein reconstitution in LUVs ($d_{nom} = 100\,\text{nm}$, POPC/POPG, 90/10, n/n) was confirmed by a flotation assay (cf. chapter 3.2.2.4) and an activity assay (cf. chapter 3.3.1.1). Figure 4.28 B shows an exemplary ATP synthesis assay curve ($\Delta\text{pH}_{theor} = 4.1$, $\Delta\psi = 135\,\text{mV}$, $pmf = 381\,\text{mV}$) of the resulting proteoliposomes (p/l: 1/10,000) yielding in a turnover rate of $10\,\text{s}^{-1}$.

Next, TF_OF_1-LUVs (POPC/POPG/Chol/TxR DHPE, 69/15/15/1, n/n) obtained from nOG mediated reconstitution were used for the production of dsGUVs (cf. chapter 3.2.3.2). Reconstitution efficiency and protein activity in LUVs were verified in advance to each microfluidic preparation at least qualitatively. For the dsGUVs shown in figure 4.28 C, TF_OF_1-LUVs (p/l: 1/14,000) exhibited a turnover of $6.4\,\text{s}^{-1}$ ($\Delta\text{pH}_{theor} = 4.1$, $\Delta\psi = 135\,\text{mV}$, $pmf = 381\,\text{mV}$). The obtained dsGUVs revealed a homogeneous fluorescence intensity at the water-oil interface and were devoid of the areas of suspected lipid aggregations reported previously for Triton™ X-100 treated proteo-LUVs. Moreover, it was feasible to release GUVs from the oil phase in an aqueous environment by using the de-emulsifier PFO (cf. chapter 3.2.3.3) in a similar overall yield like protein-free GUVs and to image them by fluorescence microscopy (cf. figure 4.28 D).
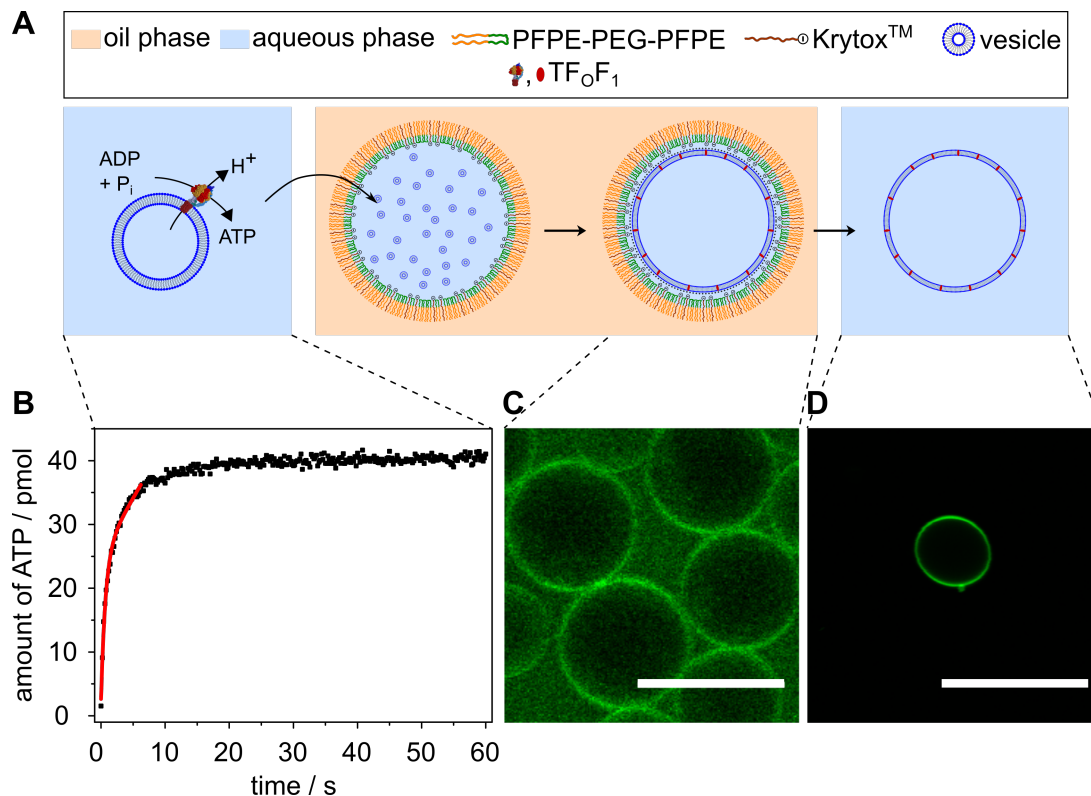
Figure 4.28: Reconstitution of active TF$_O$F$_1$ in LUVs mediated by the detergent *n*OG and subsequent formation of dsGUVs and GUVs. A: Schematic illustration of the ATP synthesis from TF$_O$F$_1$ reconstituted in LUVs, the following transfer in droplets for the formation of dsGUVs and the subsequent release of GUVs. **B:** LUVs (buffer R1, POPC/POPG, 90/10, *n/n*) were reconstituted with TF$_O$F$_1$ (*p/l*: 1/10,000). The activity was determined via ATP synthesis assay and resulted in a turnover rate of 10 s^{-1}. **C, D:** Fluorescence micrographs of dsGUVs and a released GUVs, respectively. dsGUVs (**C**, false colored in green) were prepared from proteo-LUVs (POPC/POPG/Chol/TxR DHPE, 69/15/15/1, *n/n*, 20 mM Tris, 10 mM MgCl$_2$, pH 7.4) and GUVs (**D**, false colored in green) were released. In advance to the injection into droplets, the activity of the proteo-LUVs (*p/l*: 1/14,000) was usually verified via ATP synthesis assays (here: 6.4 s^{-1} for ΔpH = 4.1, $\Delta\psi = 135$ mV, $pmf = 381$ mV).

4.3.2.2 Activity assessment of TF$_O$F$_1$ ATP synthases in dsGUVs/GUVs

So far, it has been proven that the TF$_O$F$_1$ ATP synthase can be actively reconstituted into LUVs using *n*OG. Resulting proteoliposomes were suitable to serve as basis for the formation of dsGUVs yielding free GUVs after release in aqueous buffer. However, it was of further interest to examine whether the protein was transferred in its active form from the LUVs to the assembled bilayer of the dsGUVs and

thus, to the GUVs. Besides, this included the question of protein orientation in the membrane of dsGUVS/GUVs. As mentioned before, the ATP-producing F_1 unit of the protein reconstituted in LUVs mainly points to the extravesicular space[174,175], while the orientation in dsGUVs/GUVs after the microfluidic process is still unknown.[45] Activity assays were intended to investigate these issues. Production of the dsGUVs (POPC/POPG/Chol/TxR DHPE, 69/15/15/1, *n,n*) occurred as previously described from proteo-LUVs (*p/l*: 1/28,000). Activity assessment of proteo-LUVs revealed a turnover rate of $v_{cat} = 9.2\,s^{-1}$ for a proton motive force $pmf = 381\,mV$ ($\Delta pH = 4.1$, $\Delta \psi = 135\,mV$), demonstrating active reconstitution in LUVs, which were subsequently employed for the production of dsGUVs and GUVs, respectively. Two separate approaches, each of which would require the opposite protein orientation in the membrane, were applied for activity assessment in dsGUVs/GUVs (cf. figure 4.29 A, B). First, an ATP synthesis assay of TF_OF_1 in the dsGUVs was performed, based on the work of Weiss et al.[45] with slight modifications (cf. chapter 3.3.1.2) as schematically illustrated in figure 4.29 A. This assay would allow observation of ATP production inside the dsGUVs mediated by proteins, pointing with the F_1 unit to the vesicle lumen. Thus, the required substrates ADP ($0.1\,mM$) and NaH_2PO_4 ($5\,mM$) were added to the respective reconstitution buffer R2 (cf. table 3.11). A proton gradient of $\Delta pH = 3$, serving as driving force for TF_OF_1 mediated ATP synthesis, was induced by incubating the dsGUVs for at least $2\,min$ in fluorinated oil, which was acidified by addition of TFA ($1/1,000$, *v/v*). By releasing the entire content of the dsGUVs by addition of the de-emulsifier PFO, the total amount of produced ATP was intended to be monitored by means of luciferin luminescence. Second, activity assessment of TF_OF_1 in released GUVs was intended to be determined by using the same procedure as for the proteo-LUVs, which would demonstrate a protein orientation with the F_1 unit pointing to the outside of the GUVs (cf. figure 4.29 B). Figure 4.29 C shows the resulting curves of both assay variants, each based on an exemplary measurement. The monitored luminescence was normalized to the measured ATP quantity using an ATP standard. It is apparent that both assay variants were not showing ATP production.
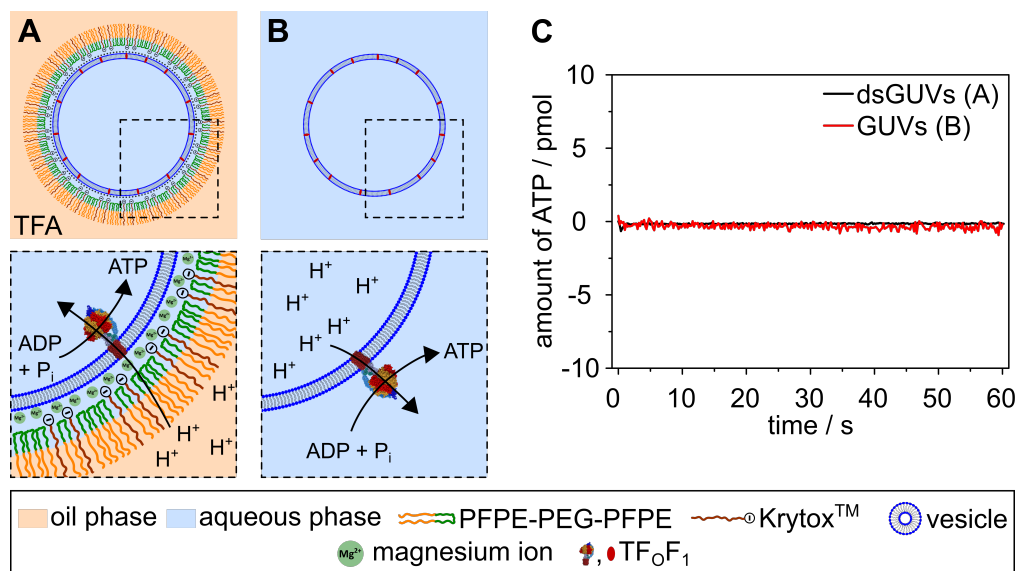
Figure 4.29: Exemplary ATP synthesis measurements with dsGUVs and released GUVs doped with reconstituted TF_OF_1 ATP synthase. A: Schematic illustration of TF_OF_1 ATP synthase reconstituted in a dsGUV and pointing with the F_1 unit to the vesicle lumen. ATP synthesis in the inside of dsGUVs is driven by a proton gradient achieved by addition of acidic oil (TFA) to the outside. **B:** Schematic illustration of TF_OF_1 ATP synthase reconstituted in a released GUV, pointing with the F_1 unit to the outside. Protein activity is induced from a proton gradient through addition of assay buffer of higher pH. **C:** Protein actitivity was monitored by detection of produced ATP through luciferin-luciferase luminescence. No activity of the protein in dsGUVs (black line) and released GUVs (red line), respectively, was detected. For preparation of both, proteo-LUVs (POPC/POPG/Chol/TxR DHPE, 69/15/15/1, *n,n*, buffer R2 + 10 mM MgCl$_2$, 0.1 mM ADP, 5 mM NaH$_2$PO$_4$, pH 7.4) were provided and the reconstitution was verified by a flotation assay (*p/l*: 1/28,000). The activity in LUVs was determined previously via ATP synthesis assay (9.2 s^{-1} for ΔpH = 4.1, $\Delta\psi$ = 135 mV, *pmf* = 381 mV).

4.3.3 Reconstitution of synaptobrevin 2 in GUVs via droplet-based microfluidics

So far, reconstitution of transmembrane proteins in GUVs was targeted by novel droplet-based microfluidics technique using the TF_OF_1 ATP synthase of thermophilic *Bacillus* PS3. Although ATP synthases are of broad interest for instance in pharmaceutical or biosynthetical research and thus, are highly studied, they remain very complex proteins. Overall, eight different types of subunits form the two greater units F_1 ($\alpha_3, \beta_3, \gamma, \epsilon$) and F_O (a, b_2, c_{10}). In total, 21 individual subunits are involved in the assembly of the total protein complex.[188] Since the present work aims at investigating a novel method for the production of GUVs and the reconstitution of transmembrane proteins in these, besides ATP synthases a further transmembrane protein was required, revealing a less complex structure. For this purpose, synaptobrevin 2 (syb 2) from *Rattus norvegicus*, which is anchored to the membrane via an α-helical transmembrane domain, was employed.[78] Furthermore, the recombinant protein offered the opportunity to add a fluorescence label to an additional *C*-terminal cystein residue, allowing on the one hand to visualize and quantify reconstituted protein in the bilayer via fluorescence microscopy and on the other hand to determine protein mobility via FRAP experiments.

4.3.3.1 Lipid and protein mobility in droplet stabilized GUVs

To analyze the lipid and protein mobility in dsGUVs quantitatively, FRAP experiments were performed to determine the diffusion coefficients of both. The lipid mobility was aimed to be compared to lipid diffusion of protein-free dsGUVs (cf. chapter 4.2.1). Moreover, investigation of the diffusive behavior of fluorescently labeled syb 2 can provide information about whether the protein is successfully integrated into the membrane of the dsGUVs. Proteo-LUVs as the starting point for the assembly of dsGUVs were produced via a direct reconstitution protocol based on nOG (cf. chapter 3.2.2.2) using LUVs ($d_{nom} = 100\,nm$, POPC/POPG/Chol/Atto488 DPPE, 69/15/15/1, n/n, buffer R3). The detergent nOG was chosen since preliminary experiments with the ATP synthase indicated its suitability for further use of the resulting proteoliposomes for microfluidic production of (ds)GUVs. Syb 2-Atto647N ($DOL = 35\,\%$), kindly provided by Peter Mühlenbrock (Georg-August Universität Göttingen), was added in a nominal protein to lipid ratio of 1/2,500. Microfluidic

production of dsGUVs was performed as described in chapter 3.2.3.2. Figure 4.30 A and B visualize fluorescence micrographs of the Atto488 DPPE labeled membrane and the fluorescence intensity of syb 2-Atto647N within water-in-oil droplets. The homogeneous fluorescence intensity of both, lipid- and protein-coupled fluorescent dyes, located at the water-oil interface indicates an assembly of a continuous bilayer and thus, the successful formation of dsGUVs reconstituted with syb 2. The checkmark in the upper right corner of figure 4.30 A demonstrates that the dsGUVs were able to be released as GUVs into an aqueous environment (release buffer) by adding de-emulsifier (cf. chapter 3.2.3.3), supporting the hypothesis that a continuous bilayer assembled within the droplets. The diffusion coefficients of lipids and labeled syb 2 were quantified by FRAP experiments (cf. chapter3.3.3.3) at the bottom plane of dsGUVs using a nominal bleaching radius of $r_n = 2.9\,\mu m$. The corrected and normalized fluorescence time course of the resulting recovery was fitted by equation 3.16 to extract the diffusion time $\tau_{1/2}$. From the postbleach profile of each experiment the respective effective bleach radius r_e was determined. The diffusion coefficient was calculated using equation 3.17 with the obtained parameters. Both, Atto488 DPPE and fluorescently labeled syb 2 were (nearly) fully mobile with $F_{m,DPPE} = (98 \pm 3)\,\%$ and $F_{m,syb2} = (97 \pm 5)\,\%$ ($n = 13$). Evaluation of diffusion coefficients resulted in $D_{DPPE} = (9 \pm 2)\,\mu m^2\,s^{-1}$ and $D_{syb\ 2} = (4 \pm 1)\,\mu m^2\,s^{-1}$.
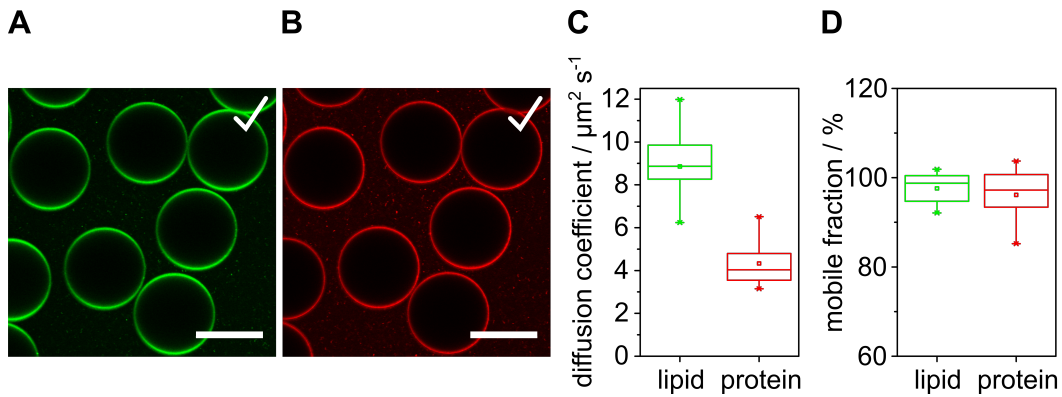
Figure 4.30: Reconstitution of syb 2 in dsGUVs. A,B: Fluorescence micrographs of the Atto488 DPPE labeled dsGUV membrane (**A**) and syb 2-Atto647N fluorescence intensity (**B**). For production of the dsGUVs, syb 2-Atto647N (DOL = 35 %) was inserted via direct reconstitution in the bilayer of LUVs ($d_{nom} = 100\,nm$, POPC/POPG/Chol/Atto488 DPPE, 69/15/15/1, n/n, buffer R3) with a nominal p/l of 1/2,500. Check mark in the upper right corner indicates that GUVs were found after release process. Scale bars = 50 μm. **C, D:** Box plots of diffusion coefficients (**C**) and mobile fractions (**D**) of lipids (green, $n = 13$) and syb 2-Atto647N (red, $n = 13$). The box plots extent from the 25th to 75th percentile and whiskers from 5th to 95th.

4.3.3.2 Investigation of the reconstitution efficiency of synaptobrevin 2 in GUVs

CLSM measurements were carried out by Miriam Stehr as part of her bachelor thesis.

So far, the efficieny of reconstitution of transmembrane proteins in GUVs mediated by microfluidics has not been quantitativly proven. For this purpose, a fluorescence-based method[36] was used, which will be described below. Initially, syb 2-Atto488 ($DOL = 92\,\%$) was directly reconstituted into preformed LUVs ($d_{nom} = 100\,nm$, POPC/POPG/Chol/Atto390 DPPE, 69/15/15/1, n/n) with a nominal protein to lipid ratio p/l of 1/500 as described in chapter 3.2.2.2. Reconstitution efficiency in LUVs was determined from two individual preparations by flotation assay (cf. chapter 3.2.2.4) to $\sim 90\,\%$, yielding in an actual mean p/l of 1/600, which is in accordance to results from Jan Kuhlmann.[81] Based on the resulting proteo-LUVs, dsGUVs were prepared as described in chapter 3.2.3.2. Membrane (Atto390 DPPE, green) and syb 2 (Atto488, red) were fluorescently labeled and respective exemplary fluorescence micrographs are shown in figure 4.31 A. Visual inspection of the micrographs revealed that both, lipid and protein coupled dyes were homogenously distributed between different dsGUVs and inside the bilayer. By adding de-emulsifier, GUVs were successfully transferred from the emulsion into an aqueous environment. To quantify the reconstition efficiency R_{GUV} of syb 2 in released GUVs, dsGUVs (POPC/POPG/Chol/Atto390 DPPE/Atto488 DPPE, $69-x/15/15/1/x$, n/n) were initially produced containing distinct concentrations of Atto488 DPPE (0.001 to 0.1 mol%) serving as a reference to the syb 2-Atto488 concentration. Exemplary fluorescence micrographs of the Atto390 DPPE and Atto488 DPPE (0.1 mol%) fluorescence intensity are shown in figure 4.31 B. Homogeneous distribution of the fluorescence intensity was observed for both fluorophores and GUVs were successfully released. The line profiles displayed in figure 4.31 provide information about the intensity along the white lines, illustrated in the micrographs of the syb 2-Atto488 (A) and the Atto488 DPPE (B) fluorescence intensity, respectively. Qualitative comparison reveals, that the peak intensities of both are approximately in the same order of magnitude, implying a similar amount of fluorescent molecules within the bilayer. Considering the DOL of syb 2-Atto488 (92%) and a total concentration of 0.1 mol% Atto488 DPPE in the reference-dsGUVs (B), this would indicate a protein to lipid ratio of approximately 1/1,000 and thus, a loss of protein compared to the

proteo-LUVs ($p/l = 1/600$). However, quantitative analysis was subsequently carried out on the basis of the released GUVs as described below.
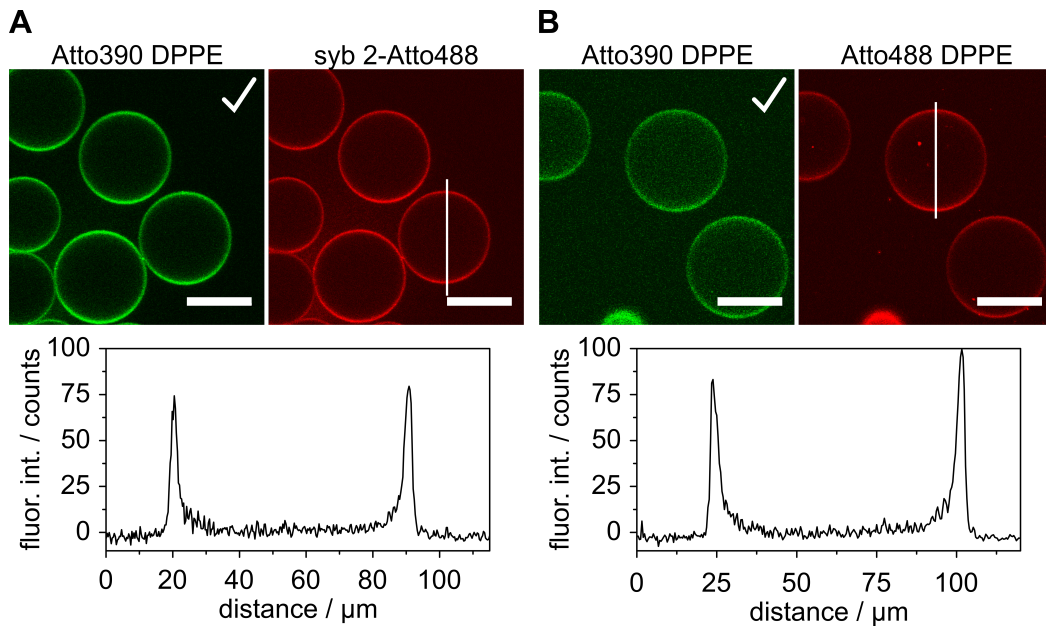
Figure 4.31: Reconstitution of syb 2 in dsGUVs. A Fluorescence micrographs of the Atto390 DPPE labeled dsGUV membrane, false-colored in green, and the syb 2-Atto488 fluorescence intensity, false-colored in red. Intensity of an exemplary line profile (white line) drawn through the center of an individual dsGUV is shown in the bottom. dsGUVs were produced from proteo-LUVs (POPC/POPG/Chol/Atto390 DPPE, 69/15/15/1, n/n, buffer R3) with syb 2-Atto488 in a p/l of 1/600. **B:** Fluorescence micrographs of the Atto390 DPPE labeled dsGUV membrane, false-colored in green, and the Atto488 DPPE fluorescence intensity as reference, false-colored in red. Intensity of an exemplary line profile (white line) drawn through the center of an individual dsGUV is shown in the bottom. dsGUVs were produced from LUVs (POPC/POPG/Chol/Atto390 DPPE/Atto488 DPPE, 69/15/15/1/0.1, n/n, buffer R3). Check marks in the upper right corner indicate that GUVs were found after release process. Scale bars = 50 µm.

GUVs containing syb 2-Atto488 were released from the microemulsion by addition of de-emulsifier and transferred in an aqueous environment (release buffer, cf. chapter 3.2.3.3). Figure 4.32 A-C exemplifies micrographs of the Atto390 DPPE (A) and syb 2-Atto488 (B) fluorescence intensity as well as a brightfield micrograph (C) of the same location in the sample. The brightfield micrograph allows the identification of an oil droplet in the lower corner which can be used as a reference point while comparing the fluorescence micrographs. Visual inspection reveals homogenous distributed Atto390 DPPE in the bilayer of released GUVs, while no intensity signal was visible for syb 2-Atto488, indicating that reconstitution in GUVs was not

successful. Findings were representative for all preparations exhibiting no or weak fluorescence intensity signals from syb 2-Atto488. For quantitative analysis, dsGUVs doped with a fixed concentration of Atto390 DPPE and different concentrations of Atto488 DPPE were released into an aqueous environment (release buffer, cf. chapter 3.2.3.3) by addition of de-emulsifier. An overall mean diameter of the obtained GUVs of $(12 \pm 5)\,\mu$m ($n = 173$) was evaluated as described in chapter 3.3.3.5. Released GUVs, containing known concentrations of Atto488 DPPE, were imaged in the equatorial plane, applying identical microscopy settings, and the membrane peak fluorescence intensities were acquired as described in chapter 3.3.3.5 from line profile analysis. Peak membrane fluorescence intensities were plotted against the fluorophore concentration (cf. figure 4.32 D). Fitting a linear function to the data resulted in a slope of $m = 18{,}000\,\mathrm{counts\,mol\%^{-1}}$. Equation 3.28 was used to determine the reconstitution efficiency of syb 2 in GUVs with c_{initial} of $0.17\,\mathrm{mol\%}$, calculated from the protein to lipid ratio of the proteo-LUVs ($p/l = 1/600$), and a *DOL* of 0.92. Three individual preparations resulted in a mean reconstitution efficiency R_{GUV} of syb 2 in GUVs of less than $0.1\,\%$ ($n = 21$), confirming that *de facto* no efficient reconstitution in GUVs was achieved. Comparable results were obtained from preparations with an initial p/l of 1/2,000 ($n = 16$) and 1/3,800 ($n = 5$) as well as reconstitution based the preparation of proteo-LUVs via comicellization (nominal $p/l : 1/500$, $n = 9$) (cf. chapter 3.2.2.2). A mean diameter of the released proteo-GUVs was determined to $(13 \pm 5)\,\mu$m ($n = 42$).
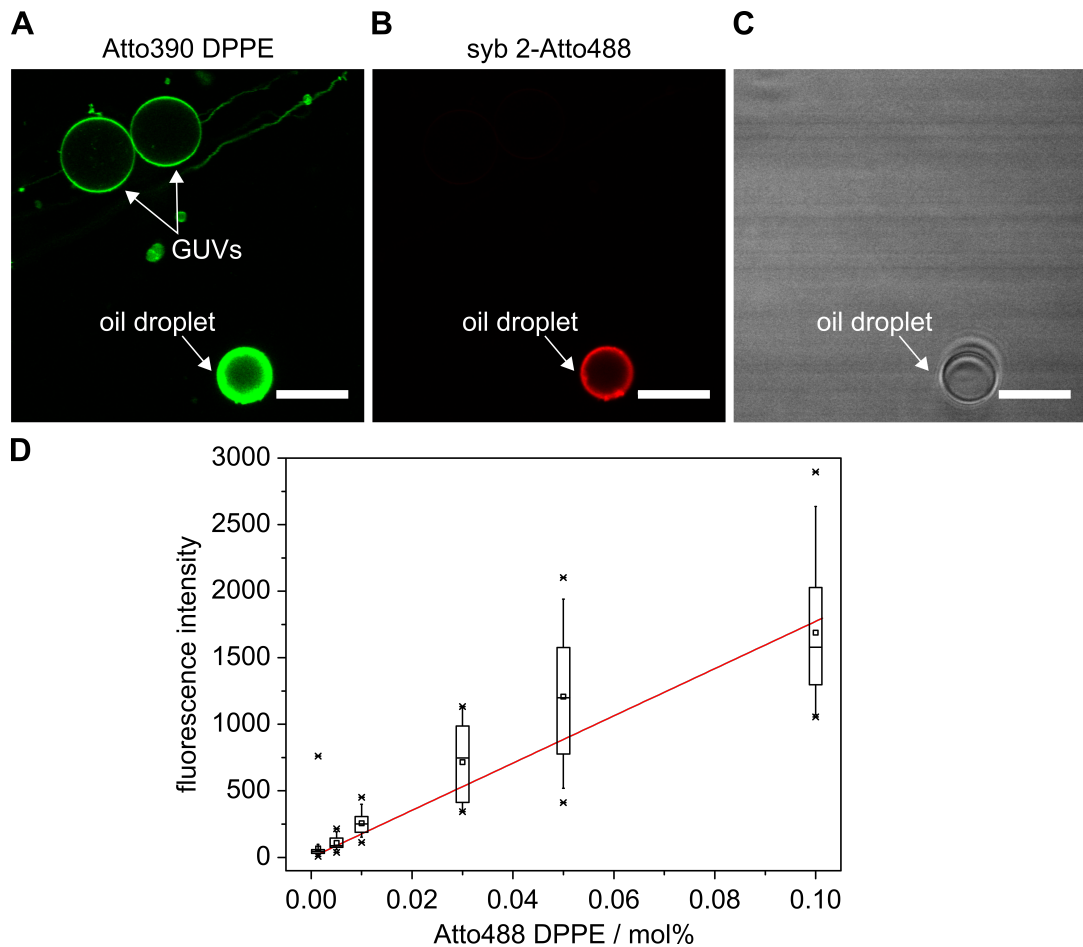
Figure 4.32: Fluorescence-based determination of the reconstitution efficiency R of syb 2 in GUVs. A-C: GUVs (POPC/POPG/Chol/Atto390 DPPE, 69/15/15/1, n/n) containing syb 2-Atto488 (nominal $p/l : 1/500$) were prepared via droplet-based microfluidics. Fluorescence micrographs represent the Atto390 DPPE labeled GUV membrane, false-colored in green (**A**) and the syb 2-Atto488 intensity, false-colored in red (**B**). The brightfield (**C**) reveals an oil droplet which was used as reference point. **D:** Fluorescence intensity as a function of the concentration of Atto488 DPPE in mol% of five different dye concentrations (0.001, 0.005, 0.01, 0.03, 0,05, 0.1, $n = 33, 30, 23, 11, 42, 30$). Linear regression of the data results in the extraction of calibration factor $m = 18,000 \, \text{counts mol\%}^{-1}$ from the slope.

5 Discussion

The main goal of this thesis was to establish novel droplet-based microfluidics as a potential tool for the preparation of model membrane systems and the subsequent functional reconstitution of transmembrane proteins. The formation of droplets, dsGUVs and release of free-standing GUVs was analyzed as a function of the buffer, lipid and oil composition by using confocal laser scanning microscopy (CLSM). Simultaneously, microfluidic-GUVs were utilized to produce the sophisticated model of pore-spanning membranes (PSMs). Lipid mobility was determined in all three systems (dsGUVs, GUVs and PSMs) by fluorescence recovery after photobleaching (FRAP) and fluorescence correlation spectroscopy (FCS), while mechanical properties of PSMs were adressed by force-indentation experiments using atomic force microscopy (AFM). Subsequently, protein reconstitution in dsGUVs/GUVs via droplet-based microfluidics was analyzed using two different model proteins: the TF_OF_1 ATP synthase and synaptobrevin 2. Proteo-LUVs, obtained from detergent-mediated reconstitution, served as starting material for the assembly of protein-containing dsGUVs. Initially, reconstitution efficiency of both proteins in LUVs was examined in greater detail, while TF_OF_1-LUVs were additionally studied extensively regarding the ATP synthesis activity via a luminescence-based assay. Microfluidic encapsulation of proteo-LUVs in water-in-oil droplets and subsequent spontaneous assembly of dsGUVs was proven by CLSM. The success of protein insertion in the membrane of released microfluidic-GUVs was adressed by activity determination (TF_OF_1) and fluorescence-based quantification of the reconstitution efficiency (syb 2), respectively.

5.1 Impact of buffer, lipid and oil composition on dsGUV and GUV preparation via droplet-based microfluidics

Production of GUVs using droplet-based microfluidics is an advanced process requiring a number of system components which can have an impact on the final yield. A charge-mediated approach based on Weiss et al.[45] and Haller et al.[54] was applied with slight modifications, where microemulsions of water-in-oil droplets were prepared by using a microfluidic device. While the oil phase was doped with two different

surfactant species to stabilize droplets (PFPE-PEG-PFPE) and to generate a negative net charge at the interface (Krytox, PFPE-carboxylate), the aqueous phase was loaded with LUVs harboring a negative net charge of the bilayer due to a certain amount of negatively charged lipids (POPG). By adding (divalent) cations to the aqueous phase, LUVs adhered, spread and fused at the water-oil interface and formed a continuous bilayer at the droplet periphery yielding dsGUVs which were released by addition of a de-emulsifier (PFO) (cf. figure 5.1).
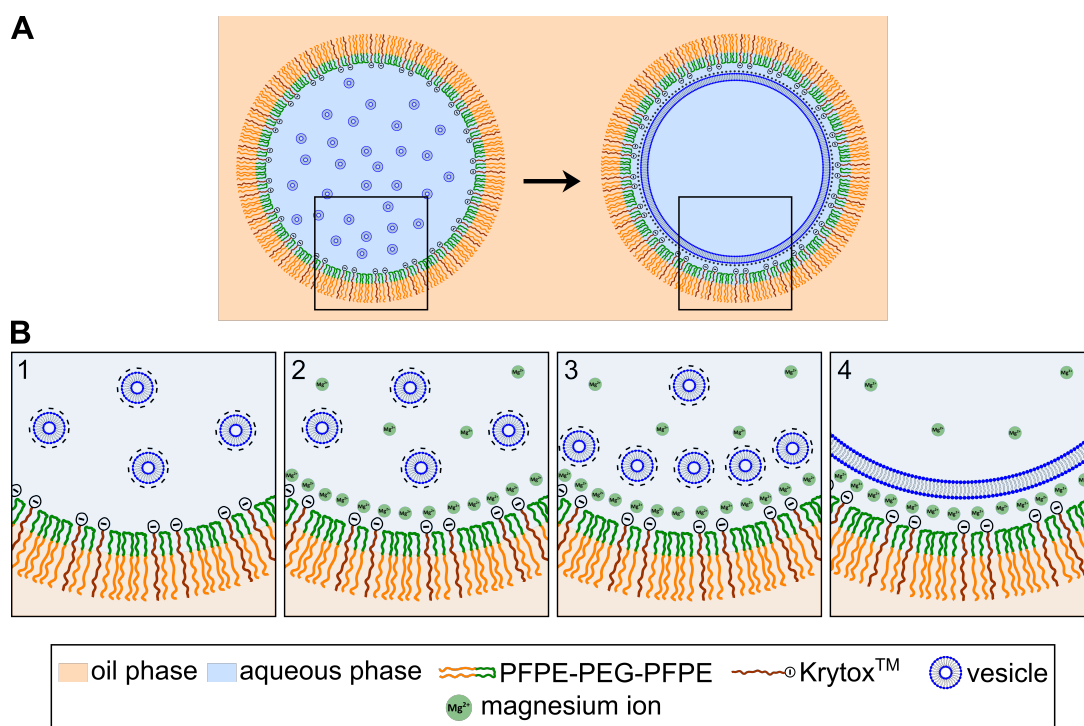
Figure 5.1: Schematic illustration of the formation of dsGUVs. A: Water-in-oil droplets stabilized by a surfactant shell were filled with LUVs which spread at the interface and form a continuous bilayer. **B:** Step-by-step illustration of the aforementioned spreading process. In the absence of Mg^{2+} ions, negatively charged LUVs are homogeneously distributed (1), whereas addition of Mg^{2+} ions (here: 10 mM) leads to their attraction to the negatively charged interface (2) and induces adsorption (3), rupture and fusion of LUVs and thus, the formation of a continuous bilayer (4) allowing the release of GUVs.

Thus, successful dsGUV formation requires a defined interplay of the charges provided from the surfactants *(1)*, ions *(2)* and lipids *(3)* allowing efficient release of GUVs *(4)*. Since the composition of oil phase, aqueous phase and lipid bilayer of LUVs might strongly influence the microfluidic manufacturing process, distinct components of all three have been investigated in the present work (cf. chapter 4.1) and will be discussed step by step in the following.

(1) Impact of surfactants

First, the impact of used surfactants dissolved in an inert fluorocarbon oil was studied. Providing long-term stability to water-in-oil droplets is a key step for the effective formation of dsGUVs, as the assembly of a continuous bilayer at the periphery may take several hours depending on the selected conditions.[189] Thus, initial analysis of an optimal concentration of the stabilizing surfactant was mandatory. Fluorinated oil was doped with different PFPE-PEG-PFPE concentrations and the impact on the droplet stability and dsGUV formation was analyzed at constant Krytox (PFPE-carboxylate) concentration ($9\,\mathrm{mM}$)(cf. figure 4.2, chapter 4.1.1). While microemulsions with low PFPE-PEG-PFPE concentrations ($0.3\,\mathrm{wt\%}$ and $0.7\,\mathrm{wt\%}$, $\sim 0.01\,\mathrm{mM}$ and $0.02\,\mathrm{mM}$) tended to coalesce, resulting partially in separation of the two distinct phases, addition of $1.4\,\mathrm{wt\%}$ ($\sim 0.04\,\mathrm{mM}$) to the oil yielded droplets, being stable up to several days which is consistent with results from Haller et al.[54] The long-term stability of the emulsion is associated with the interfacial tension between water and oil phase which is modulated by the used surfactants. Droplet stabilization can be described as a function of the surfactant adsorption rate at the interface, depending on the amount of surfactant added to the overall system.[99,190] Wagner et al. quantified a reduction of the interfacial tension of a microemulsion from $55\,\mathrm{mN\,m^{-1}}$ to $4.2\,\mathrm{mN\,m^{-1}}$ after addition of PFPF-PEG-PFPE in a low concentration ($0.04\,\mathrm{wt\%}$) and additionally demonstrated long-term stability of droplets after adding higher concentrations ($2\,\mathrm{wt\%}$) of a head group modified surfactant (poly(methyl glycerol, LPG(OMe)-PFPE$_2$) to the oil phase.[99] Moreover, the presented results are in good agreement with those of Haller et al. who were able to produce stable droplets in case of a surfactant mixture of $1.4\,\mathrm{wt\%}$ PFPE-PEG-PFPE and $9\,\mathrm{mM}$ Krytox (PFPE-carboxylate) and determined an interfacial tension of approximately $2.5\,\mathrm{mN\,m^{-1}}$, whereas no stable droplet formation was possible in the abscence of PFPE-PEG-PFPE.[54] Together with these findings, the results presented in this work indicate that although low PFPE-PEG-PFPE concentrations are sufficient to reduce surface tension, higher concentrations may be advantageous for sufficient long-term stability of water-in-oil droplets.

Apart from the stability of the droplets, bilayer formation at the droplet periphery as a function of the used surfactants was investigated based on the fluorescence intensity distribution of lipid-coupled fluorophores and the possibility of releasing GUVs in an aqueous environment. Formation of dsGUVs is mediated from the oil side mainly by anionic Krytox (PFPE-carboxylate), whose carboxylic acid group is deprotonated

$(pK_a < 0)$,[100,191] and from the aqueous side by ions and charged lipids. The exact process has not been elucidated yet, but is considered similar to the formation of supported lipid bilayers (SLB) on hydrophilic solid state supports which was studied in depth previously.[189,192] Electrostatic interactions between lipids and support, here the surfactant layer at the oil-water interface, have a key function and therefore must be considered. Göpfrich et al. and Haller et al., respectively, showed, that charge modulation of the inner droplet surface, mediated by surfactants like Krytox (PFPE-carboxylate), is a versatile tool to highly control dsGUV assembly.[54,189] Here, a Krytox concentration of 9 mM led to dsGUV formation and efficient release of GUVs (cf. figure 4.3 A) which is in agreement with Haller et al., who found similar results for 6 mM to 13.5 mM Krytox in a comparable system while experiments with lower or higher concentrations failed in dsGUV formation and GUV release.[54] While low Krytox (< 6 mM) concentrations provide insufficient negative charge at the interface, high concentrations (> 13.5 mM) lead to increased partitioning of lipid material into the oil phase, both of which counteract the formation of a continuous bilayer.[54] In this context it is noteworthy to highlight that adsorption and desorption processes of Krytox from the water-oil interface of the droplets are reported to induce micellar exclusion of (charged) molecules.[156] However, also the uncharged PFPE-PEG-PFPE appeared to affect dsGUV formation. Lower amounts (≤ 0.7 wt%) seemed to cause leakage of the lipid coupled fluorophore into the oil phase, indicated by an increasing fluorescence intensity of the oil phase with decreasing PFPE-PEG-PFPE concentration, and prevented efficient release of GUVs (cf. figure 4.2 B). Hence, the assembly of a continuous bilayer within the droplets was disturbed. A less dense layer of PFPE-PEG-PFPE at the interface might allow micellar exclusion of the molecules from the aqueous phase into the oil phase. However, while the uncharged PFPE-PEG-PFPE is considered to be biocompatible and inert to electrostatic interactions with biological components, it stands to reason that the leakage of (fluorescent) molecules in the oil phase was indirectly caused by the charged Krytox.[100,101,103] Supposing that a decrease of the PFPE-PEG-PFPE concentration in the bulk oil causes a change in the ratio of the two surfactants in favor of the total fraction of Krytox, a higher proportion of the latter would be provided for adsorption from the bulk reservoir to the droplet periphery. Surfactant layers at water-oil interfaces tend to induce micellar exclusion of certain molecules towards the oil phase dependent on the amount of provided Krytox.[54,156] Similar transfer events of molecules from the aqueous phase or interface, respectively, into the oil phase were described for instance

for lipid-coupled fluorophores (dsGUVs, $c_{\text{Krytox}} > 12\,\text{mM}$) and actin monomers (lipid-free water-in-oil droplets, $c_{\text{Krytox}} > 1.04\,\text{mM}$).[54,156] Following this hypothesis, it may be useful to consider the relative proportion of the surfactants in addition to their absolute concentrations when preparing GUVs by droplet-based microfluidics. Overall, the discussed data revealed, that the presented two-surfactant system for droplet stabilization and formation of a charged interface for GUV assembly is highly sensitive and based on a defined interplay of different components in a specific concentration ratio. Optimal concentrations of PFPE-PEG-PFPE (1.4 wt%, $\sim 0.04\,\text{mM}$) and Krytox (PFPE-carboxylate)(9 mM) for dsGUV assembly were found and are in agreement with the literature.[54,189]

(2) Impact of ions and water-soluble molecules added to the aqueous compartment of droplets

Second, the formation of the lipid bilayer within surfactant-stabilized droplets is influenced by ions and water-soluble molecules added to the aqueous compartment. Type and concentration of ions are of particular interest, since they represent an important factor when working with proteins and, moreover, mediate electrostatic attraction of vesicles to the water-oil interface, followed by the spreading and formation of a continuous bilayer at the droplet periphery (cf. figure 5.1 B-2 to B-4). In the absence of ions, vesicle accumulation and rupture at the water-oil interface and thus formation of dsGUVs and release of GUVs is not favored (cf. figure 5.1 B-1).[54] Similar to SLBs, the formation of a "surfactant supported" bilayer might be facilitated by addition of (divalent) cations like Ca^{2+} and Mg^{2+} due to electrostatically promoted adsorption and rupture of vesicles.[192–195] Addition of 10 mM MgCl_2 allowed effective attraction of LUVs to the interface, rupture and bilayer formation and was utilized in the present work in most experiments. It is noteworthy to mention, that the MgCl_2 concentration can be decreased to 5 mM when working with neutral lipids or replaced completely by addition of high concentrations of monovalent cations like K^+ or Na^+ replacing the positive charge of divalent cations.[54,94] Here, addition of both, KCl (50/100 mM) and MgCl_2 (10 mM) (cf. figure 4.4, chapter 4.1.2) allowed formation of dsGUVs and release of GUVs. Qualitatively, a higher amount of released GUVs was achieved from dsGUVs containing 100 mM KCl (cf. figure 4.3 A, chapter 4.1.1) which is in accordance to Witt et al. and Haller et al. who observed improved dsGUV formation, lower fluorophore leakage in the oil phase and enhanced release rates for experiments with additional monovalent cations.[54,94] However, no quantitative

analysis was carried out in the context of this work. Addition of Ca^{2+} $(10/100\,\text{mM})$ instead of Mg^{2+} (cf. table 4.1, chapter 4.1.2) unexpectedly led to clustering of vesicles at the interface and increased micellar exclusion of lipid-coupled fluorophores into the oil phase. Both, unspecific LUV-LUV aggregation and fusion in solution[195,196] as well as increased affinity to carboxylate- and phosphate-groups[197] present in surfactants and lipids, respectively, is enhanced for Ca^{2+} compared to Mg^{2+} and might contribute to the observed vesicle- and vesicle-surfactant clustering in dsGUVs and subsequent micellar exclusion into the oil phase. Results from Witt et al. confirmed these experimental findings and indicated an improvement for working with $CaCl_2$ by addition of increased NaCl concentrations $(100\,\text{mM})$.[94] Apart from mono- and divalent cations, the influence of additional $H_2PO_4^-$ (in presence of $10\,\text{mM}$ $MgCl_2$) on the described dsGUV system was tested (cf. figure 4.5, chapter 4.1.2). Although dsGUVs revealed an increasing fluorescence intensity of the oil phase and a slight clustering at the interface by increasing the NaH_2PO_4 concentration $(1\,\text{mM}$ to $50\,\text{mM})$, the release of GUVs was possible in all cases implying successful bilayer formation at the droplet periphery. Addition of both, NaH_2PO_4 and $10\,\text{mM}$ $MgCl_2$ to the aqueous phase might induce formation of hardly soluble magnesium salts (solubility product $L_p \leq 1.5 \cdot 10^{-6}$)[198] in the water-in-oil droplets, which precipitate and associate with lipid material from LUVs or dsGUV bilayers, as already observed in a comparable context with $CaCO_3$.[94] However, bilayer formation at the periphery was not disturbed, since first, an excess of vesicles was added in each preparation (as described below in more detail) allowing for a certain loss of lipid material and second, equally added Na^+ ions (NaH_2PO_4) are able to take over the mediation of bilayer formation from Mg^{2+} ions, lost by precipitation.[54] In addition to the impact of different ions, it is noteworthy to mention that different buffer substances, added to the aqueous phase, affected dsGUV/ GUV preparation (cf. figure 4.6 and table 4.1, chapter 4.1.2). While Tris and HEPES allowed formation of a bilayer at the droplet periphery in presence of $10\,\text{mM}$ $MgCl_2$, which is in agreement with divers various studies,[54,94,156,189] succinic acid and MES revealed a high degree of lipid leakage in the oil phase and lipid clusters at the interphase, implying the formation of a noncontinuous bilayer and resulting finally in a failed release of GUVs. Both, MES and succinic acid exhibit deprotonated carboxylic and sulfonic acid groups at the applied pH of 7.4, which could undergo complex formation with Mg^{2+} ions, that might associate to lipid material (POPG) resulting in uncontrolled clustering of cations, lipids and buffer substances.[199] Adjusting the pH and/or adding monovalent

cations in high concentration, respectively, might avoid this effect.

In summary, it was demonstrated, that addition of various salts and buffer substances to the aqueous compartment of droplets in different concentrations and combinations allowed the formation of a bilayer at the periphery and the subsequent release of GUVs in an aqueous environment. As this is an advantage against conventional methods like electroformation which are limited in terms of addition of high salt concentrations,[7] the presented method might offer new possibilities for the formation of artificial model systems in order to investigate transmembrane proteins in a more physiological environment.

(3) Impact of the lipid composition

Finally, the key element of the overall system is the lipid bilayer, formed at the droplet periphery which is affected by lipid concentration and composition of LUVs added to the aqueous compartment of the droplets. An important effect for formation of SLBs on solid support is the critical vesicular coverage, implying that a certain density of vesicles on the surface is essential to provoke spreading of surface-bound vesicles and to allow formation of a continuous bilayer.[192] The described cooperative effect of neighboring LUVs adhered to an interface can be transferred to the process of "surfactant supported" bilayer formation. Moreover, encapsulation of a crititical amount of LUVs allowing complete coverage of the droplet interface without any defects is necessary to form intact GUVs within the droplets, that can be successfully released.[189] Encapsulation of an excess of vesicles is required to compensate for a slight variation in the droplet diameter and a loss of lipid material during the microfluidic process. Based on the determined mean average diameter of the dsGUVs (50 µm, cf. figure 4.3 B, chapter 4.1.1) and the applied lipid composition (POPC/POPG/Chol, 70/15/15), a critical minimal lipid concentration of 640 µM was calculated using equations A.5 to A.8 (cf. chapter A.7) which was increased by 40 % to ∼1 mM (∼0.75 mg mL^{-1}). Since Weiss et al. recommended an excess lipid concentration of 15 %, a reduction could be considered.[45] Apart from concentration, the lipid composition of LUVs is a non-negligible factor for the formation of SLBs on solid support and "surfactant support" in general, especially concerning the net charge of the vesicles.[54,189,193] While Haller et al. and Weiss et al. utilized different concentrations of DOPG (0 to 30 %) to produce dsGUVs,[45,54] Göpfrich et al. further demonstrated successful mediation of bilayer formation at the droplet periphery by addition of positively charged lipids (30 % DOTAP) in the absence of cations.

Variation of negatively charged lipids (POPG, POPS) and their complete omission in the droplet-encapsulated LUVs were tested within the context of the present study in order to further define the limits of the entire system and to extend the findings presented in literature. POPG (15 %) was employed for all experiments discussed above and allowed reliable formation of a continuous bilayer at the interface (cf. figure 4.6 A, chapter 4.1.1). Replacing POPG with POPS (15 %) led to a failed bilayer formation, accompanied with high amount of vesicle clustering at the droplet periphery, lipid leakage in the oil phase and inability of GUV release (cf. figure 4.6 D, chapter 4.1.1), although Düzgüneş et al. revealed that Mg^{2+}, like Ca^{2+}, is able to induce fusion and aggregation of PS-containing SUVs in solution.[200] It is conceivable, that increased vesicle fusion and aggregation observed for PS-containing vesicles in the aqueous compartment of droplets resulted in clusters of larger vesicles, which accumulated at the water-oil interface, but without ruptering and forming of a continuous bilayer. Addition of monovalent ions (K^+, Na^+) or the complete replacement of Mg^{2+} by them could optimize the system towards effective bilayer formation, as they reduce or even prevent spontaneous vesicle fusion in solution[200] and thus might allow controlled vesicle attraction to the interface and formation of dsGUVs. Total omission of negatively charged lipids led to dsGUV formation only with the addition of both, di- and monovalent cations (10 mM Mg^{2+}, 50 mM K^+, cf. table 4.1, chapter 4.1.1), presumably since these ion composition leads to an enhanced vesicle attraction to the interphase. Results from Haller et al. add, that lower concentrations of divalent cations (5 mM Mg^{2+}) and/or addition of monovalent cations (50 mM K^+), respectively, improves dsGUV formation with net neutrally charged vesicles.[54]

In summary, a wide range of lipids can be applied for the formation of dsGUVs and subsequent release of GUVs, however adjustment of the applied ions and their concentrations might be required for example for utilization of positively charged or neutral lipids.[54,189]

(4) Release of GUVs

In the present work, a bulk release of GUVs from the oil phase into an aqueous environment was applied by covering the dsGUV microemulsion with buffer and de-emulsifier (PFO, 20 % v/v, cf. chapter 3.2.3.3).[54,189] It is noteworthy to mention that cholesterol (15 mol%) was added to the lipid mixture in all cases in order to enhance stability of GUVs during the release process as recommended from previous studies.[45] The

overall release success was not quantified in the present work, but a release efficiency of 0.3 % to 10 % can be assumed according to Haller et al. for the basic conditions (1.4 wt% PFPE-PEG-PFPE, 9 mM Krytox, POPC/POPG/Chol/Atto488 DPPE, 69/15/15/1, n/n).[54] Visual inspection of fluorescence micrographs revealed, that the diameter of GUVs was reduced compared to dsGUVs for all tested conditions. Quantification of dsGUVs/GUVs (cf. figure 4.3 B, cf. chapter 4.1.1) exhibited a rather homogeneous size distribution of dsGUVs and a mean diameter of (50 ± 6.7) μm, whereas released GUVs had a more heterogeneous size distribution and a mean diameter of (18 ± 7.5) μm. A reduction in GUV size was also observed by Haller et al. and Göpfrich et al. when using the bulk approach for GUV release with the de-emulsifier PFO.[54,189] Osmolarity differences between the inner and release buffers which could induce a shrinkage of the vesicles can be ruled out since precise adjustment was performed prior to all experiments. Göpfrich et al. assumed a favored release of smaller and thus, more stable GUVs, whereas larger GUVs rupture during the process.[189] This conjecture is reasonable for the shaking approach for droplet production which was used in the respective study and resulted in a broad size distribution of dsGUVs, but less reasonable for the microfluidic approach applied here which resulted in a narrow size distribution of dsGUVs being by factor two to three larger compared to the released GUVs. However, uncontrolled processes such as droplet splitting and merging during the bulk release might lead to a spontanously arising broader size distribution of dsGUVs as suggested from Haller et al.[54] Subsequently, the preferential release of rather smaller GUVs would be conceivable due to their higher stability. In contrast, a microfluidically controlled release approach developed by Weiss et al. resulted in released GUVs which revealed an average diameter of 26 μm and thus, differed hardly from the corresponding dsGUVs (28 μm).[45] These results support the aforementioned hypothesis and at the same time offer an option to obtain a more homogeneous size distribution of released GUVs, which are also closer to the size of the corresponding dsGUVs.

In summary, it was confirmed by this work, that the formation of dsGUVs and subsequent efficient release of GUVs is strongly dependent on a defined interaction of the oil and aqueous phase components. Here, the PFPE-PEG-PFPE and Krytox (PFPE-carboxylate) concentrations were optimized to 0.04 mM (1.4 wt%) and 9 mM (4.2 wt%), respectively. It was noticed, that the addition of high salt concentrations and different lipids to the aqueous phase is possible (cf. table 5.1), but requires a precise knowledge of the overall system and possibly certain adjustments. Application

of charged lipids (e.g. POPG) and/or ions (e.g. Mg^{2+}, Ca^{2+}, K^+) is necessary to mediate attraction of vesicles to the surface, rupture and bilayer formation,[54] but components causing strong vesicle fusion and aggregation already in solution (e.g. Ca^{2+}, POPS) are counterproductive and have to be balanced by addition of e.g. monovalent ions (K^+, Na^+).[94] Overall, droplet-based microfluidics opens up a wide range of possibilities for the preparation of dsGUVs and GUVs.

Table 5.1: Selection of lipid and salt conditions for dsGUVs/GUVs fabrication applied in literature and the present work. Fluorinated oil doped with $1.4\,\text{wt}\%$ PFPE-PEG-PFPE and $9\,\text{mM}$ Krytox (PFPE-carboxylate) and a lipid composition of POPC/charged lipid/Chol/dye (x/0-50/15/1, n/n) were applied unless otherwise noted. SUVs or LUVs were prepared in $20\,\text{mM}$-$30\,\text{mM}$ Tris or $20\,\text{mM}$ HEPES (pH 7.4).

charged lipids	salts	dsGUV formation & GUV release
no charged lipids[a,b]	$5\,\text{mM}$ MgCl$_2$	✓[54]
	(50-100) mM KCl	✓[54]
no charged lipids[a,b]	$10\,\text{mM}$ MgCl$_2$	✗[this work]
	$10\,\text{mM}$ MgCl$_2$ + $+\,50\,\text{mM}$ KCl	✓[this work]
no charged lipids	$100\,\text{mM}$ CaCl$_2$ + $100\,\text{mM}$ NaCl	✓[94]
DOPG $(0, 5\,\%)$[b]	$10\,\text{mM}$ MgCl$_2$	✗[54]
DOPG $(10, 15, 20, 30\,\%)$[b]	$10\,\text{mM}$ MgCl$_2$	✓[54]
POPG $(15\,\%)$	$10\,\text{mM}$ MgCl$_2$	✓[this work]
POPG $(15\,\%)$	$10\,\text{mM}$ MgCl$_2$ + (50-100) mM KCl	✓[this work]
POPG $(15\,\%)$	$10\,\text{mM}$ MgCl$_2$ + (5-50) mM NaH$_2$PO$_4$	✓[this work]
POPG $(15\,\%)$	$100\,\text{mM}$ CaCl$_2$ + $50\,\text{mM}$ KCl	✓[this work]
POPS $(15\,\%)$	$10\,\text{mM}$ MgCl$_2$	✗[this work]
DOTAP $(30, 50\,\%)$[a,c]	no salts	✓[189]

[a] $10.5\,\text{mM}$ Krytox

[b] DOPC/POPC/DOPG/Chol/Atto488 DOPE, x/x/0-50/15/0.5, n/n

[c] DOPC/POPC/DOTAP/Atto488 DOPE, x/x/0-50/15/0.5, n/n

5.2 Biophyscial characterization of model membrane systems derived from droplet-based microfluidics

5.2.1 Lipid mobility in model membrane systems derived from droplet-based microfluidics

Engineering novel artificial lipid bilayer systems allows detailed investigation of isolated biological processes like ATP biosynthesis mediated by F_OF_1 ATP synthases[75], neuronal fusion[36] or cortical actin arrangement[201] in a biomimetic environment, which is simplified compared to the cellular membrane. Lateral mobility of components (e.g. lipids, proteins, peptides) in the desired system is an influential element for mimicking physiological conditions and a specific parameter for various biological processes such as receptor-ligand interactions[161] or cell attachment and adhesion[162], respectively.[33] Thus, establishing model lipid systems requires profound knowledge about lipid mobility without the influence of associated components (e.g. proteins) enabling to assess their potential impact and the reliability of the chosen artificial system. Various components influence the lateral diffusion coefficient of lipids in a lipid bilayer such as an underlying support,[202] solvent residues from the preparation process,[160] salt concentrations[203], the overall lipid composition (cholesterol, saturation level, chain length of lipids),[204,205] the measurement technique[202] and the data evaluation[126]. In the present work, droplet-based microfluidics were applied for the formation of artificial but biomimetic membrane systems composed of POPC, POPG and cholesterol (20 mM HEPES, 100 mM KCl, 10 mM $MgCl_2$, pH 7.4). To investigate diffusive properties of lipids in the "surfactant supported" system of dsGUVs, the respective released GUVs *(1)* and PSMs (f- and s-PSM) *(2)*, FRAP and FCS measurements were performed at constant ambient conditions.

(1) Lipid mobility in dsGUVs and released GUVs

The mobility of Atto488 DPPE in dsGUVs and GUVs was analyzed by FRAP experiments on their bottom (dsGUVs) or top plane (GUVs), respectively, to avoid influence from adjacent glass of the measurement chamber (cf. figure 3.18, chapter 3.3.3.3), and yielded similar diffusion coefficients of $D_{\text{dsGUVs}} = (10 \pm 3)\,\mu m^2\,s^{-1}$ and $D_{\text{GUVs}} = (9 \pm 3)\,\mu m^2\,s^{-1}$ with a mobile fraction of each 100 % (cf. figure 4.8, chapter 4.2.1). Data evaluation was performed according to Soumpasis et al. and Kang et

al. including besides the nominal also the effective bleach radius to consider diffusion of lipid-coupled fluorophores into the bleach spot during the bleaching process.[125,126] Lipid mobility presented in this work differs compared to results from Weiss et al. and Haller et al., who determined diffusion coefficients of $\sim 4.2\,\mu m^2\,s^{-1}$ in dsGUVs and released GUVs.[45,54] However, they employed different lipid mixtures (cf. table 5.2) and a more simple evaluation method neglecting the potential difference in the nominal and effective bleach radius.[45,54] Thereby, the diffusion coefficient might be underestimated by a factor of two or more.[79,126] In general, it can be deduced from these data that there is no significant impact of the surfactant layer on lipid mobility in dsGUVs compared to the respective released compartment. Lipid mobility in electroformed GUVs composed of a slightly different lipid mixture was quantified analogously to the measurement and evaluation method presented here and yielded $D = (9 \pm 3)\,\mu m^2\,s^{-1}$ (cf. table 5.2) which is consistent to the values determined in the course of this work for dsGUVs and released GUVs. Moreover, including the effective bleaching radius leads to improved comparability with FCS measurements, which result in diffusion coefficients in electroformed GUVs between $6\,\mu m^2\,s^{-1}$ and $14\,\mu m^2\,s^{-1}$ depending on the applied conditions (lipids, salts, etc.).[33,202,205–209] It is noteworthy, that previous works studying black lipid membranes (BLMs) revealed an impact of trace amounts of solvents from the preparation method on the lipid mobility. The lipid diffusion coefficient of solvent-containing micro-BLMs ($D = (8.5 \pm 4.7)\,\mu m^2\,s^{-1}$) was increased compared to solvent-free micro-BLMs ($D = (4.0 \pm 1.9)\,\mu m^2\,s^{-1}$).[160] In contrast, lipid mobility in dsGUVs and GUVs was similar to solvent-free electroformed GUVs.[79] Overall, these findings from the literature and the present work allow the assumption that surfactants (PFPE-PEG-PFPE, Krytox/ PFPE-carboxylate) and fluorinated oil from the microfluidics production process do not effect lipid mobility in dsGUVs and released GUVs under the applied conditions allowing to hypothesize, that either surfactants and fluorinated oil have no impact on lipid mobility or do not intercalate in the bilayer.

(2) Lipid mobility in PSMs

Furthermore, microfluidic-GUVs were employed for the preparation of pore-spanning membranes on differently functionalized porous substrates (SiO_x, Au/6MH) and investigated with respect to the diffusive properties of the lipids in the free-standing (f-PSM) and the solid-supported parts (s-PSM) via FCS (Atto655 DOPE) or indirect FRAP measurements (Atto488 DPPE). PSMs prepared from electroformed GUVs

of the same lipid composition were used for control experiments. All obtained data are summarized in table 5.2. Diffusion coefficients of lipids in the f-PSM were obtained via FCS and resulted for both, microfluidic- and electroformation-derived PSMs on SiO_x functionalized substrates, in $D_{\text{f-PSM,SiOx}} = (14 \pm 3)\,\mu\text{m}^2\,\text{s}^{-1}$. The diffusion coefficients of f-PSMs in case of the Au/6MH functionalization were found to be $D_{\text{f-PSM,Au,m}} = (13 \pm 4)\,\mu\text{m}^2\,\text{s}^{-1}$ for microfluidic-derived PSMs and $D_{\text{f-PSM,Au,e}} = (14 \pm 1)\,\mu\text{m}^2\,\text{s}^{-1}$ for electroformation-derived PSMs (cf. figure 4.12, chapter 4.2.2.1). One finds, that obtained values for lipid diffusion in the f-PSM are not significantly different for all preparation approaches. Lipid diffusion inside the f-PSM behaves similar to that in the GUV membrane.[35] Comparison with the literature revealed that the obtained values range at the upper limit of lipid diffusion coefficients determined for f-PSMs $(7\,\mu\text{m}^2\,\text{s}^{-1}$ to $13\,\mu\text{m}^2\,\text{s}^{-1})$[105,210] and electroformed GUVs $(6\,\mu\text{m}^2\,\text{s}^{-1}$ to $14\,\mu\text{m}^2\,\text{s}^{-1})$[33,202,205–209] via FCS. Additionally, diffusion coefficients in the f-PSM are increased by factor ~ 1.5 compared to values determined for dsGUVs and released GUVs via FRAP which might be attributable to the different measurement methods (FRAP, FCS)[202], the applied fluorophores or a combination of both. Measurements of dsGUVs/GUVs (FRAP) and f-PSMs (FCS) were performed by adding DPPE- or DOPE-coupled fluorophores, respectively, to a constant overall lipid mixture, which might have a minor influence on the obtained diffusion coefficients.[205,211,212] According to Guo et al., it is more likely that the choice of the measurement method is the main cause affecting an increased diffusion coefficients obtained via FCS for f-PSMs compared to the dsGUV/GUV system analyzed by the FRAP method.[202] They found an increase of diffusion coefficients by factor two when the (z-scan) FCS method was performed instead of FRAP experiments. Overall, no impact on the lipid diffusion in the f-PSM of fluorinated oil or surfactant residues from the microfluidic production route was identified, supporting the above described findings for dsGUVs and GUVs.

In contrast to f-PSMs, lipid mobility inside the s-PSM was analyzed by combining indirect FRAP experiments and FEM simulations for microfluidic derived PSMs (cf. chapter 3.3.3.3). This approach was required as the fluorescence intensity of lipid-coupled fluorophores in the s-PSM was reduced for the SiO_x functionalization and completely quenched for the Au/6MH functionalization, as described previously.[106,169,213] Similar values of $D_{\text{s-PSM,SiOx,m}} = (1.7 \pm 0.7)\,\mu\text{m}^2\,\text{s}^{-1}$ and $D_{\text{s-PSM,Au,m}} = (1.8 \pm 1.0)\,\mu\text{m}^2\,\text{s}^{-1}$ were determined for s-PSMs in case of both surface functionalizations by comparing each individual measurement with FEM simulated curves indicating a reduced

lipid mobility compared to the f-PSM. However, averaging the measurements and comparing the mean curves with simulated data (cf. figure 4.13) reveals, that FRAP data gained from SiO_x supported s-PSMs tend to overlap with the simulated curve modeled for $D = 1.5\,\mu m^2\,s^{-1}$. In contrast, the averaged FRAP curve determined for Au/6MH supported s-PSMs is most coincident with the model for $D = 2\,\mu m^2\,s^{-1}$. Overall, it must be noted that this is a rather semi-quantitative evaluation and it remains to be assumed whether the mobility on SiO_x is actually slightly reduced. Diffusion coefficients of lipids in SLBs on glass[202,214], mica[33,215] and hydrohilic SiO_2 functionalized surfaces[216] were determined in various studies and obtained values ranged between $0.1\,\mu m^2\,s^{-1}$ and $9\,\mu m^2\,s^{-1}$ being at least more than two times lower than similar free-standing membrane systems.[33,202] Diffusion coefficients of s-PSMs on Au/6MH functionalized porous substrates were analyzed by a similar measurement and evaluation method by Mühlenbrock et al. and resulted in a diffusion coefficient of $(2 \pm 1)\,\mu m^2\,s^{-1}$ for lipids which is in good agreement with the findings presented in this thesis for microfluidic derived PSMs.[36,79,81] Overall, the reduced diffusion coefficients of lipids in solid-supported compared to free-standing membranes is reasonable due to membrane-surface interactions depending on the presence and extent of the water layer between substrate and bilayer,[131] the surface roughness,[131] adsorption and desorption processes of lipids to the surface[217] and overall sticking behavior[33,202,217]. High frictional coupling of the two leaflets leads to similar lipid mobility in both layers although only the lower one interacts directly with the substrate.[131] Interestingly, there was no significant difference in diffusion coefficients between the two surface functionalizations, but the s-PSMs on SiO_x functionalized substrates were found to have a mobile fraction of $(70 \pm 3)\,\%$ while s-PSMs on Au/6MH functionalized substrates exhibited almost full mobility ($(97 \pm 6)\,\%$). The latter is in agreement with earlier observations and can be attributed to the fact that a sufficiently large spacer between substrate and lipids is created by the SAM (6MH).[36] However, in the case of SiO_x functionalization, it remains to hypothesize that enhanced lipid-surface interactions create a diffusion barrier between the rim and the pore, which accounts for the higher immobile fraction. Overall, lower mobile fractions were found for proteins ($0\,\%$ to $7\,\%$) and lipids ($50\,\%$ to $75\,\%$) in direct contact with the surface as on Si/SiO_2 chips,[34] quartz[218] or in micro-BLMs[160] while Au/6MH functionalization allows full lipid and enhanced protein ($70\,\%$) mobility[36].

In the context of this thesis, microfluidic-GUVs were applied for the first time for preparation of PSMs. Diffusive properties of lipids were investigated in detail from the stage of dsGUVs, via GUVs to PSMs, and compared with the literature. For all analyzed model membrane systems, no significant impact of components from the microfluidic production pathway (e.g. residual oil, surfactants) was monitored. In comparison, studies on cells ($\sim 1\,\mu\mathrm{m}^2\,\mathrm{s}^{-1}$)[206], giant plasma membrane vesicles ($1\,\mu\mathrm{m}^2\,\mathrm{s}^{-1}$ to $5\,\mu\mathrm{m}^2\,\mathrm{s}^{-1}$)[206,219,220] and supported plasma membrane bilayers ($0.4\,\mu\mathrm{m}^2\,\mathrm{s}^{-1}$ to $1\,\mu\mathrm{m}^2\,\mathrm{s}^{-1}$)[219] revealed reduced lipid diffusion due to their complexity and high content of various cellular components like proteins.[206] Lipid mobility in the presented less complex model systems is increased by factor two or more, which has to be taken into consideration. However, taken together, all these findings highlight the suitability of the microfluidic approach for the production of various biomimetic model membrane systems as tool for studying lateral diffusion of divers components.

Table 5.2: Selection of diffusion coefficients of lipids in different model systems. a: POPC/POPG/Chol/Atto488 DPPE or Atto655 DOPE (69-$70/15/15/10^{-3}$-1), **b:** DOPC/RhB DOPE ($99/1$), **c:** POPC/DOPC/DOPG/Chol/Atto488 DOPE ($27/27/30/15/1$), **d:** DOPC/DOPS/Chol/Atto488 DOPE ($79/10/10/1$), **e:** POPC/ Rho PE (99.5-$100/0.0025$-0.5), **f:** DOPC/Bodipy500/510 PC ($100/5 \cdot 10^{-5}$) , **g:** DOPC/Atto647N DPPE (unknown), **h:** DOPC/POPE/POPS/Chol/Atto488 DPPE or KK114 DPPE (49.5-$50/20/10/20/10^{-4}$-0.5), **i:** DOPC/DOPG/DiD ($0.75/0.25/10^{-3}$), **j:** DOPC/Atto655 DOPE ($100/10^{-3}$), **k:** DPhPC/DPPE/Chol/DSPE-KK114 ($35/35/30/0.01$), **l:** DPhPC/Bodipy500/510 PC (99.95-$99.9/0.05$-0.1).

system	lipids, fluorophore	method	D / $\mu m^2\,s^{-1}$	F_m / %
dsGUVs *	a, Atto488 DPPE	FRAP	10 ± 3	100 ± 4
released GUVs *	a, Atto488 DPPE	FRAP	9 ± 3	100 ± 6
dsGUVs[45]	b, RhB DOPE	FRAP	4.11 ± 0.59	
dsGUVs[54]	c, Atto488 DOPE	FRAP	4.2 ± 0.3	
released GUV[45]	d, Atto488 DOPE	FRAP	4.24 ± 0.94	
GUVs[202]	e, Rho PE	FRAP	3.3 ± 1.8	
GUVs[202]	e, Rho PE	FCS	6.1 ± 1.8	
GUVs[33]	f, Bodipy500/510 PC	z-scan FCS	7.8 ± 0.8	
GUVs[206]	g, Atto647N DPPE	FCS	8.5	
GUVs[79]	h, Atto488 DPPE	FRAP	9 ± 3	100 ± 8
GUVs[207]	i, DiD	FCS	11.3 ± 0.6	
f-PSM, SiO_x *,**	a, Atto655 DOPE	z-scan FCS	14 ± 3	
f-PSM, SiO_x *,***	a, Atto655 DOPE	z-scan FCS	14 ± 3	
f-PSM, Au/6MH *,**	a, Atto655 DOPE	z-scan FCS	13 ± 4	
f-PSM, Au/6MH *,***	a, Atto655 DOPE	z-scan FCS	14 ± 1	
f-PSM, SiO_x[105]	j, Atto655 DOPE	z-scan FCS	11.2 ± 0.9	
f-PSM, Au/6MH[210]	h, KK114 DPPE	FCS	7.7 ± 0.4	
s-PSM, SiO_x *,**	a, Atto488 DPPE	FRAP	1.7 ± 0.7	70 ± 3
s-PSM, Au/6MH *,**	a, Atto488 DPPE	FRAP	1.8 ± 1.0	97 ± 6
s-PSM, Au/6MH[79]	h, Atto488 DPPE	FRAP	2 ± 1	100
s-PSM, Au/6MH[81]	h, Atto488 DPPE	FRAP	3	
SLB, mica[33]	f, Bodipy500/510 PC	FCS	1.8	
SLB, mica[215]	k, KK114 DSPE	FCS	3.1 ± 0.3	
micro BLM, solvent[160]	l, Bodipy500/510 PC	FRAP	8.5 ± 4.7	75
micro BLM, solv.-free[160]	l, Bodipy500/510 PC	FRAP	4.0 ± 1.9	50

* this work, ** prepared from microfluidic-GUVs, *** prepared from electroformed GUVs.

5.2.2 Mechanical properties of pore-spanning membranes derived from microfluidic-GUVs

Mechanical properties of membranes have a major impact on living organisms and are involved in a variety of mechanochemical processes like exo- and endocytosis, blebbing, cell adhesion or division.[165,166,221,222] The membrane tension of living cells ranging from $0.01\,\mathrm{mN\,m^{-1}}$ to $0.1\,\mathrm{mN\,m^{-1}}$ is mainly caused by the underlying actin cytoskeleton.[221,222] Investigating the aforementioned processes and understanding mechanics of native systems requires simplification of cellular systems for example by consulting model membrane systems and addition of a minimal set of desired biological components of interest (e.g. proteins). Among the available model membranes, pore-spanning membranes offer a suitable and biomimetic system being accessible by fluorescence and atomic force spectroscopic approaches and reminiscent of the cellular membrane supported by a mesh.[41] A variety of surface functionalizations of porous substrates has been applied in the past to allow PSM formation, like for instance self assembled monolayers (SAM) of 2-mercaptoethanol associated to a gold surface.[41] In contrast to hybride PSMs ($20\,\mathrm{mN\,m^{-1}}$ to $30\,\mathrm{mN\,m^{-1}}$),[169] these PSMs exhibit moderate lateral membrane tensions ($\sim 2\,\mathrm{mN\,m^{-1}}$)[41] due to the comparatively lower adhesion energy between SAM and membrane. Moreover, it was observed that the membrane is able to flow from the rim into the pores upon indentation, which allows an area dilatation of more than $5\,\%$ being typically the point of bilayer rupturing and highlighting the suitability of PSMs as a model membrane system.[35,41,169,223] PSMs, which were generated for the first time by spreading GUVs prepared from droplet-based microfluidics, were characterized previously regarding lipid mobility (cf. chapter 5.2.1). Additionally, mechanical behavior of the microfluidic derived PSMs was characterized allowing comparisons to conventional PSMs prepared from electroformed GUVs. Thus, a novel pathway for PSM formation might be established to pave the way for the subsequent equipment with various components like transmembrane proteins.

PSMs prepared by spreading microfluidic- or electroformed GUVs on SiO_x and Au/6MH functionalized substrates were successfully imaged via AFM and thereby exhibited mechanical robustness (cf. figure 4.14, chapter 4.2.2.2). The lateral membrane tension was systematically analyzed by force indentation measurements with respect to the surface functionalization and the origin of spreaded GUVs (cf. chapter 4.2.2.2).

Obtained data were summarized in table 5.3. Fully elastic behavior was noticed since curves of indentation and retraction were super-imposed (cf. figure 4.16 A, chapter 4.2.2.2) and no significant impact of the applied loading rate or force on the mechanical response was found (cf. figure 4.17, chapter 4.2.2.2) which is in good agreement with earlier studies on PSMs.[81,169] Spreading microfluidic-GUVs on hydrophilic 6MH SAMs revealed a lateral membrane tension of $\sigma_{\text{Au,m}} = (2.1 \pm 1.2)\,\text{mN m}^{-1}$ and a bending modulus of $\kappa_{\text{Au,m}} = 2.3 \cdot 10^{-20}\,\text{J}$ which is in accordance to results from Kocun at al., who found lateral membrane tensions ranging from $1\,\text{mN m}^{-1}$ to $4\,\text{mN m}^{-1}$ ($\kappa = (0.8\text{-}9) \cdot 10^{-20}\,\text{J}$) depending on the applied lipid composition (cf. table 5.3).[41,170] In contrast, PSMs prepared on SiO_x functionalized substrates exhibited a similar bending modulus ($1.2 \cdot 10^{-20}\,\text{J}$ to $1.5 \cdot 10^{-20}\,\text{J}$), but by factor two to four increased lateral membrane tensions revealing an enhanced adhesion energy between lipid headgroups of the bilayer and surface of the pore rim.[41,105] Lateral membrane tension amounts to $\sigma_{\text{SiOx,m}} = (4.6 \pm 0.7)\,\text{mN m}^{-1}$ for microfluidic derived PSMs and $\sigma_{\text{SiOx,e}} = (7.1 \pm 0.6)\,\text{mN m}^{-1}$ for PSMs prepared from electroformed GUVs. Sibold et al. determined lateral membrane tensions of PSMs prepared from spreading electroformed GUVs on SiO_x functionalized substrates in a similar order of magnitude like the data obtained in this work ranging from $\sigma = (10.5 \pm 4.3)\,\text{mN m}^{-1}$ for pure DOPC bilayers to $\sigma = (6.7 \pm 4.0)\,\text{mN m}^{-1}$ for bilayers composed of sphingomyelin and cholesterol ($60/40$, n/n) (cf. table 5.3).[39,105] Although the lateral membrane tension of microfluidic-derived PSMs on Au/6MH functionalized substrates is almost consistent with values from Kocun et al.,[41,170] direct comparison of values obtained in this work for PSMs on SiO_x functionalized substrates revealed a reduced lateral membrane tension for microfluidic-derived PSMs compared to PSMs prepared from electroformed GUVs. Notably, exposing (hybrid-) PSMs to organic solvents like isopropanol leads to similar findings of decreased lateral membrane tension as described by Mey et al. and Kocun et al. (cf. table 5.3).[35,170] The authors explained a reduction of lateral tension with reservoirs of the respective solvent formed at the pore rims facilitating the overall membrane to flow into the pore upon indentation.[35] Although in recent studies no traces of residual oil or surfactants (PFPE-PEG-PFPE, PFPE-carboxylate, cf. figure 5.2 A) of the preparation process were detected in microfluidic-GUV suspensions by means of Raman spectroscopy[45,54] and no alteration of lipid mobility was determined for microfluidic-derived bilayers (cf. chapter 5.2.1), the question arises, whether any of the aforementioned components caused the demonstrated influence on the lateral membrane tension. Tri- or di-block

co-polymers composed of poly(ethylene oxide) (PEO) and poly(propylene oxide) (PPO) resembling the surfactants employed in the present thesis are extensively used to stabilize cellular membranes, protect cells from external injuries and thus apparently alter biophysical characteristics of lipid bilayers.[224–226] Although the exact mechanism of lipid-co-polymer (surfactant) interactions is still elusive, ealier works hypothesize that hydrophobic blocks of co-polymers incorporate into the hydrophobic region of the bilayer, while hydrophilic blocks are loosely adsorbed to lipid headgroups (cf. figure 5.2 B, C).[225] Depending on the length of the hydrophobic block relative to the lipid bilayer, block co-polymers either partially insert (i) or span the entire membrane (ii).[225,227–229]
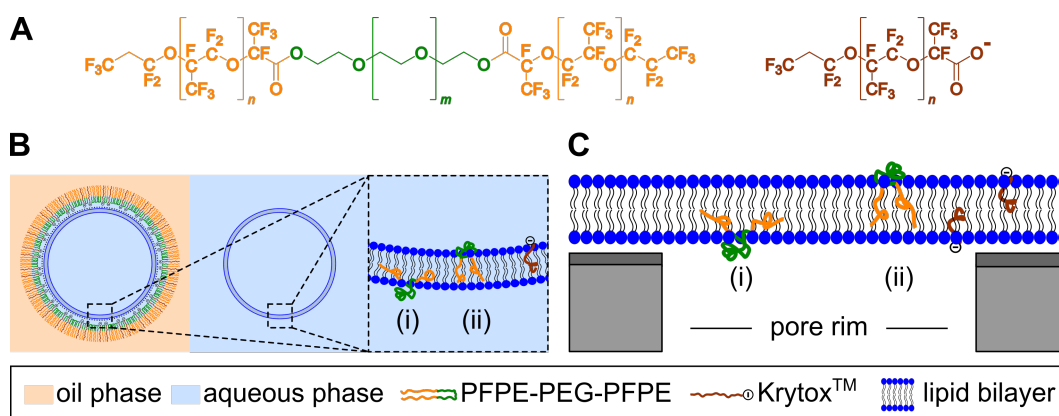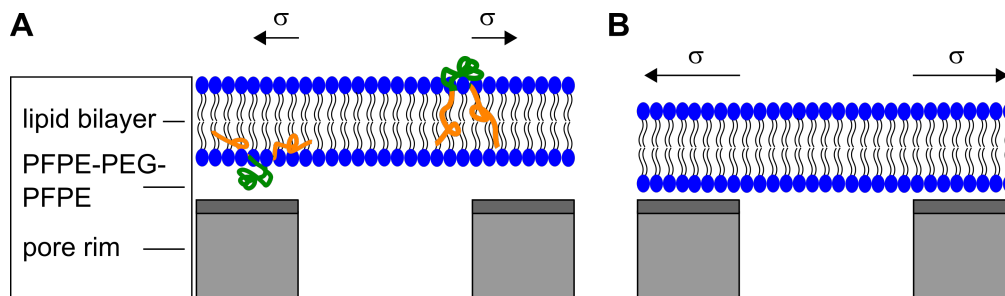

Figure 5.2: Schematic illustration of the insertion of block co-polymers in lipid bilayers. A: Chemical structures of PFPE-PEG-PFPE (left) and PFPE-carboxylate (Krytox, right). **B:** Schematic illustration of block co-polymers (surfactants) penetrating the lipid bilayer of GUVs during microfluidic production. **C:** Pore-spanning membranes prepared from microfluidic GUVs with residual surfactants inserted within the lipid bilayer.

An increasing ratio of hydrophobic to hydrophilic parts (i.e. total hydrophobicity) and an increasing molecular weight of the block co-polymers contribute to an enhanced percentage of co-polymer insertion or binding (PEO-PPO-PEO, MW = 2,000 g mol^{-1} to 15,000 g mol^{-1}) to lipid bilayers as demonstrated by Zhang et al.[225] In comparison, the surfactants PFPE-PEG-PFPE ($\leq$ 20,000 g mol^{-1}) and Krytox ($\leq$ 7,500 g mol^{-1}) applied for microfluidic GUV production exhibit high molecular weights and thus, are supposed to reveal similar membrane penetration properties. It has been shown by Kim et al. that membranes can be loaded with up to 30 % (v/v) of the respective block co-polymer, which presumably would affect their overall biophysical behavior.[224] While breakthrough forces for penetrating solid-supported lipid bilayers with

an AFM tip seem to be unaffected by the presence of block co-polymers,[224] membrane permeation, membrane thickness and lipid diffusion were altered.[228,230,231] Interestingly, no change in lipid mobility was noted for surfactant-treated lipid bilayers in this thesis, which is consistent with the results of Wang et al., as they determined significant block co-polymer-induced hindrance of diffusion only with temperatures of $T \geq 30\,°\text{C}$ while measurements in the present work were performed at $T = 20\,°\text{C}$.[228] Moreover, further experimental[232] and modulation[231] studies specified the altered mechanical properties of (cellular) membranes linked to the addition of block co-polymers. Molecular simulations revealed an increased area compressibility modulus (K_A) and increased critical rupture tensions for block co-polymer treated membranes[231] while optical tweezer studies on saponin-treated cells demonstrated a correlation of increasing block co-polymer concentration and reduced membrane tensions[232]. The here observed alteration of the lateral membrane tension of microfluidically produced PSMs likewise suggests surfactant(block co-polymer)-based modulation of the mechanical membrane properties, although the exact mechanism can only be hypothesized and requires prospective systematic investigation. It is possible that a similar effect of reservoir formation as observed for solvent-treated PSMs[169,170] occurs, or that surfactants in the area of the pore rims change the surface-membrane distance and thus reduce interaction of lipids and surface (cf. figure 5.3). Briefly, surfactants inserted in the bilayer might act as spacer when facing with their hydrophilic parts towards the substrates evoking reduced adhesion of lipids to the pore rims and thus a reduced lateral membrane tension σ. Enhanced insertion of surfactants to the outer leaflet of the microfluidic-GUVs and therefore the lower leaflet of the PSM is reasonable as it is directly exposed to the surfactant layer within the droplets (cf. figure 5.2 B) and might magnify the described spacing effect. Finally, changed lipid packing observed for block co-polymer treated membranes might also contribute to the modulation of their mechanical properties.[230]

Figure 5.3: Schematic illustration surfactant-based alteration of the lateral membrane tension of pore-spanning membranes. Surfactants act as spacer between membrane and pore rim. Thus, adhesion energy between lipid headgroups and pore rim and consequently lateral membrane tension σ is reduced for surfactant-exposed PSMs (prepared from microfluidic-GUVs, **A**) compared to surfactant-free PSMs (prepared from electroformed GUVs, **B**).

In summary, mechanical studies revealed successful formation of stable and fully elastic PSMs by spreading microfluidic-GUVs on functionalized porous substrates. Determined parameters like bending modulus and lateral membrane tension were found to range in a similar order of magnitude determined for conventional PSMs prepared by electroformed GUVs. Nevertheless, direct comparison of the lateral membrane tension of PSMs on SiO_x-functionalized substrates revealed a potential influence of the surfactants (block co-polymers) used for the microfluidic GUV-production, which has to be taken into account in prospective studies. It is likely that an interplay of lipid packing, reservoir formation and/or bilayer-surface interactions mediate the observed alteration of mechanical properties. Interestingly, the lateral membrane tension of microfluidic-PSM indicated no reduction in the case of Au/6MH functionalization of the underlying substrate compared to the literature.[41,170] However, a comparison is only possible to a limited extent, since both the lipid mixture and the functionalization (Au/2Me, Au/6MH) variied (cf. table 5.3). Finally, it is noteworthy to mention that co-polymer insertion in lipid bilayers can be reduced by decreasing POPG[233] and increasing cholesterol concentrations[234] which might be adressed in further studies.

Table 5.3: Selection of lateral membrane tensions and bending moduli of PSMs prepared on different functionalizations of porous substrates. 2ME: 2-mercaptethanol, 6MH: 6-mercaptohexanol, OT: octanthiol.

surface	preparation	lipids	σ / mN m^{-1}	κ / 10^{-20} J
Au/6MH	GUVs (m)	POPC/POPG/Chol **	2.1 ± 1.2	2.3
Au/6MH[105]	GUVs (e)	DOPC	0.6 ± 0.4	
Au/6MH[235]	GUVs (e)	DPhPC	1.4	
Au/2ME[170]	GUVs (e)	POPC	2.4 ± 0.5	6.7 ± 2.0
Au/2ME[170]	GUVs (e)	POPC, isopropanol	0.86 ± 0.13	2.8 ± 3.0
Au/2ME[170]	GUVs (e)	POPC/Chol (75/25)	2.6 ± 0.9	8.7 ± 3.0
Au/2ME[41]	GUVs (e)	DOPC	1.018 ± 0.014	5
Au/2ME[41]	GUVs (e)	DOPC/Chol (70/30)	3.5 ± 0.15	10
SiO$_x$	GUVs (m)	POPC/POPG/Chol **	4.6 ± 0.7	1.5 ± 0.5
SiO$_x$	GUVs (e)	POPC/POPG/Chol **	7.1 ± 0.6	1.2 ± 0.2
SiO$_x$[39,105]	GUVs (e)	SM/Chol (60/40)	6.7 ± 4.0	
SiO$_x$[39,105]	GUVs (e)	DOPC	10.5 ± 4.3	
OT[169] *	painting	DPhPC	18 ± 3	
OT[169] *	GUV	DPhPC	26 ± 4	

* hybrid PSM. ** (70/15/15).

5.3 Reconstitution of transmembrane proteins in model membrane systems

Creation of artificial minimal cell compartments capturing essential facets of living organisms requires insertion of biological components in model membrane systems like GUVs. In particular, reconstitution of ATP synthases is indispensable for provision of energy in the form of ATP being an important hallmark of living cells.[11,12] Considering the microfluidic approach for production of protein-containing GUVs presented in this thesis requires previous functional reconstitution of proteins in LUVs (cf. chapter 5.3.1). Subsequently, proteo-LUVs can be employed for the assembly of dsGUVs (cf. chapter 5.3.2).

5.3.1 Reconstitution and activity assessment of TF_OF_1 ATP synthases in LUVs

In this thesis, the TF_OF_1 ATP synthase from thermophilic *Bacillus* PS3 was considered for probing the microfluidic approach as it is a stable protein which can be functionally reconstituted in LUVs in a reliable manner as verified in previous studies.[75,119,236] Initially, the protein was produced recombinantly in *E. coli* DK8 harboring the pTR19-ASDS vector achieving typical protein yields in a similar order of magnitude as described by Schwamborn et al. (cf. chapter 3.1.1).[72,76,77,119] After inserting the protein in LUVs composed of varying lipid compositions (POPC, POPG, Chol) the reconstitution efficiency *(1)* and protein activity *(2)* were analyzed in detail to probe suitability of the proteoliposomes for the following transfer in droplets for the formation of dsGUVs (cf. chapter 5.3.2). Finally, the ATP synthesis assay was analyzed in greater detail considering the effect of membrane permeability for protons *(3)*.

(1) Reconstitution of the TF_OF_1 ATP synthases in LUVs

Reconstitution of F_OF_1 ATP synthases in LUVs was performed in the past by various protocols and detergents.[72,75,89,119,178,236] Reliable methods revealing high functionality of the proteoliposomes were for example presented by Schwamborn

et al. using the detergent nOG [119] and Fischer et al. applying Triton™ X-100 [178]. Although ATP synthases have been reconstituted and studied for decades, a detailed examination of reconstitution efficiency in LUVs was first performed by Miriam Schwamborn in 2017. [55] It was shown that saturation was achieved at a protein to lipid ratio of 1/20,000 corresponding to four reconstituted proteins per vesicle at a vesicle diameter of 95 nm. [55] Thus, in this work, the TF_OF_1 ATP synthase was reconstituted in a nominal protein to lipid ratio of 1/20,000 via Triton™ X-100 in LUVs (d_{nom} = 100 nm) composed of different lipid mixtures (POPC, POPG, Chol). The effective diameter of the resulting proteoliposomes was determined by DLS measurements and amounted to averaged values of 300 nm for POPC, 330 nm for POPC/POPG (85/15, n/n) and 360 nm for POPC/Chol (85/15, n/n). Mean reconstitution efficiencies of each nearly 100 % were analyzed by flotation assays ($R_{LUV,PC} \approx 102\,\%$, $R_{LUV,PC/PG} \approx 96\,\%$, $R_{LUV,PC/Chol} \approx 97\,\%$). Values above 100 % can be explained by moderate loss of lipid material during the reconstitution procedure resulting in a higher final protein to lipid ratio than initially applied. According to these parameters, an approximate number of 45 to 56 TF_OF_1 ATP synthases per liposome was calculated which is an order of magnitude higher than the value obtained by Miriam Schwamborn. [55] However, proteoliposomes produced by Triton™ X-100 mediated reconstitution revealed significantly larger diameters and thus also membrane surface area was found to be increased by a factor of nine to twelve. It is most likely, that the bulky F_1 unit of the TF_OF_1 ATP synthase restricts reconstitution of the protein in a vesicle size dependent manner. The increase in vesicle diameter observed here from ~ 100 nm, which was checked before reconstitution in each case, to ≥ 300 nm after reconstitution can be attributed to vesicle aggregation, reorganization or fusion of the vesicles induced by Triton™ X-100. Evidence for such a phenomenon has already been described in various studies for instance by Alonso et al. and Urbaneja et al. even though it has not been mechanistically elucidated until now. [237–240] As such an alteration of the vesicle diameter was not described by Schwamborn et al. their reconstitution method based on nOG is recommended when constant vesicle diameters are required. [55,119] It is noteworthy to mention, that lipid and detergent concentrations were carefully chosen with respect to the critical micelle concentration (CMC) of Triton™ X-100 (~ 0.2 mM) [22] and its R_{sat}-value (~ 0.64) [26] guaranteeing preferred destabilization of the vesicular membrane and thus a mostly unidirectional orientation of the protein with the water-soluble F_1 unit pointing to the outside of the liposomes. In contrast, higher detergent concentrations

would lead to the formation of mixed micelles and as a consequence to a mixed protein orientation.[26] Thus, required concentrations were determined by equation 5.1. Rigaud et al. described a preferred protein orientation with the F_1 unit facing to the outside of more than 80 % for a comparable direct reconstitution method using Triton™ X-100.

$$R_{sat} = \frac{c_{detergent} - CMC}{c_{lipid}} \tag{5.1}$$

It is worth emphasizing that the effective protein orientation was not controlled within the course of this work. Thus, no correction was applied for misoriented proteins resulting presumably in moderate underestimation of the protein activity in the following discussion. However, as this procedure was common practice also in the majority of earlier studies on F_OF_1 ATP synthases comparison of those and results presented here appears to be reasonable.[115]

(2) Activity assessment of the TF$_O$F$_1$ ATP synthase

Functionality of the protein was proven by a luminescence-based ATP synthesis assay (cf. chapter 4.3.1.1). After reconstituting the protein in LUVs, acidification of the interior of the vesicles was performed by injecting and incubating them in a buffer of the desired luminal pH. Subsequently, the proton motive force *pmf* was generated by addition of the assay buffer (containing the luciferin-luciferase mixture) which applies a constant $\Delta\psi$ (135 mV) and the respective ΔpH (cf. figure 3.13). This so-called acid-base transition was commonly applied for driving ATP synthesis in liposomes in ealier studies.[64,75,115,178,241,242]

In this thesis, the ATP synthesis activity of TF$_O$F$_1$-LUVs (POPC) was determined as a function of the applied ΔpH (4.8 to 1.8) at constant $\Delta\psi$ (135 mV) resulting in *pmf*s ranging from 243 mV to 423 mV and leading to turnover rates of 0.042 s^{-1} to 13 s^{-1} (cf. figure 4.24, chapter 4.3.1.3). Earlier works demonstrated that ATP synthesis mediated by different bacterial ATP synthases occurs only at *pmf*s greater than $\sim$ 200 mV.[236,243,244] This finding is only partially reflected by the data presented here since only minimal activity was observed at 243 mV ($v_{cat} = 0.042$ s^{-1}) while reliable activity started at 303 mV and greater *pmf*s. So far, no systematic examination of the TF$_O$F$_1$ ATP synthase activity as a function of the pH gradient was reported in

literature. However, various studies described turnover rates at defined pmfs which can be consulted for comparison. Overall, turnover rates of $0.7\,\mathrm{s}^{-1}$ to $2\,\mathrm{s}^{-1}$ were reported for pmfs between $275\,\mathrm{mV}$ and $330\,\mathrm{mV}$ in the temperature range of $30\,°\mathrm{C}$ to $40\,°\mathrm{C}$.[115,236,245,246] These findings are in good agreement to the data obtained here at a pmf of $303\,\mathrm{mV}$ to $327\,\mathrm{mV}$ accounting to turnover rates of the $\mathrm{TF_OF_1}$ ATP synthase between $1.2\,\mathrm{s}^{-1}$ to $1.3\,\mathrm{s}^{-1}$ ($T = 27.5\,°\mathrm{C}$). In contrast, $\mathrm{F_OF_1}$ ATP synthases originating from other organisms revealed significantly higher overall activities compared to $\mathrm{TF_OF_1}$ from thermophilic *Bacillus*. The ATP synthesis actitivity amounted to $30\,\mathrm{s}^{-1}$ to $78\,\mathrm{s}^{-1}$ for the *E. coli* $\mathrm{F_OF_1}$ ($\mathrm{EF_OF_1}$, $pmf = (330\text{-}386)\,\mathrm{mV}$),[64,178,241,247] $120\,\mathrm{s}^{-1}$ for the yeast mitochondrial $\mathrm{F_OF_1}$ ($\mathrm{MF_OF_1}$, $pmf = 325\,\mathrm{mV}$)[248] and $400\,\mathrm{s}^{-1}$ for $\mathrm{F_OF_1}$ from spinach chloroplasts ($\mathrm{CF_OF_1}$, $pmf = 320\,\mathrm{mV}$)[249]. All data were summarized in table 5.4. The comparatively low activity of the $\mathrm{TF_OF_1}$ ATP synthase may be attributed to the high physiological temperature optimum of $T_\mathrm{opt} = 60\,°\mathrm{C}$ of the thermophilic *Bacillus* PS3 compared to for instance *E. coli* ($T_\mathrm{opt} = 37\,°\mathrm{C}$).[247,250] In this study, measurements were performed at $T = 27.5\,°\mathrm{C}$ due to the temparature limitation of the luciferin-luciferase system (cf. chapter 4.3.1.3). Thus, significantly higher protein activity can be expected when increasing the temperature to $60\,°\mathrm{C}$. This assumption is supported by studies analyzing the proton pumping and ATPase activity, respectively, of $\mathrm{TF_OF_1}$.[55,250] In addition, Soga et al. assumed an increase of the activity of a mutated $\mathrm{TF_OF_1^{\epsilon\Delta c}}$ at $T = 60\,°\mathrm{C}$ compared to measurements at $T = 30\,°\mathrm{C}$ by at least a factor of six (and at most a factor of ~ 66).[115] However, besides the temperature limitation of the luciferin-luciferase system also the increased proton permeability of the membrane incapacitates application of high temperatures during the measurements performed in this work.[55,251] Furthermore, it is noteworthy to highlight that the aforementioned $\mathrm{TF_OF_1^{\epsilon\Delta c}}$ ATP synthase is a mutated version of the wildtype protein lacking the *C*-terminal inhibitory segment of the ϵ subunit and enabling increased ATP synthesis rates (by a factor ~ 20).[115] Thus, a direct comparison is only possible to a limited extent. Yet, equivalent studies on the pH dependence of the ATP synthesis were performed by Soga et al. with the mutated $\mathrm{TF_OF_1^{\epsilon\Delta c}}$ revealing a similar general behavior, but with higher overall activities at similar pmfs.[75] Interestingly, application of a luminal pH < 5.8 resulted in a drop of the protein activity which was not observed here.[75] Whether this is related to the mutation of the ϵ subunit is still elusive and cannot be ascertained within the scope of this work.

Thus, within the context of this work, functional and reliable reconstitution of the

TF_OF_1 ATP synthase was achieved exhibiting an activity comparable to previously reported values (cf. table 5.4). Moreover, detailed characterization of the protein activity as a function of the applied pH gradient allows novel insights in the function of ATP synthases which supports and complements the existing literature. Furthermore, the application of TF_OF_1 ATP synthase as a model protein for the preparation of protein-containing dsGUVs using droplet-based microfluidics appears to be feasible (cf. chapter 5.3.2).

Table 5.4: Selection of turnover rates of F_OF_1 ATP synthases from different organisms reconstituted in small and large liposomes. Substrates ADP and phosphate were adjusted to saturating concentrations.

protein	lipids	T / °C	pmf / mV	mean turnover / s^{-1}
TF_OF_1	POPC	27.5	303-327	1.2-1.3
TF_OF_1	POPC/POPG**	27.5	303	0.8
TF_OF_1	POPC/Chol***	27.5	303	1.0
TF_OF_1 [115]	L-α PC	30	330	0.7
$TF_OF_1^{\epsilon\Delta c}$ [115]	L-α PC	30	330	15
TF_OF_1 [236]	soy bean p-lipids	36	275	2
TF_OF_1 [186]	PC/PA (9/1)	40	143	1
TF_OF_1 [245]	soy bean p-lipids	36	unknown*	0.1
TF_OF_1 [246]	soy bean p-lipids	40	unknown*	2.2-7.8
EF_OF_1 [241]	soy bean p-lipids	RT	330	30
EF_OF_1 [178]	soy bean p-lipids	RT	360-386	50-78
EF_OF_1 [64]	L-α PC	RT	364	20
$EF_OF_1^{\epsilon\Delta c}$ [64]	L-α PC	RT	364	66
MF_OF_1 (yeast) [248]	PC/PA (19/1)	RT	325	120
CF_OF_1 (spinach) [249]	asolectin	RT	320	400

* pH gradient generated light-induced from co-reconstituted bacteriorhodopsin.

** (90/10, n/n), *** (85/15, n/n).

Apart from the already discussed impact of the pmf and the temperature, further parameters like the protein to vesicle (and protein to lipid) ratio, the applied lipid mixture or detergent for reconstitution may affect the protein activity. As noted initially, systematic analysis of the reconstitution effiency of TF_OF_1 ATP synthases in LUVs revealed saturation at a protein to lipid ratio of 1/20,000 corresponding

to approximately four proteins per vesicle with a diameter of 95 nm.[55] Here, a comparable p/l of 1/20,000 led to 40 to 50 proteins for the determined final vesicle diameter of > 300 nm. Soga et al. reported a decrease in the activity ($\mathrm{TF_OF_1^{\epsilon \Delta c}}$) when increasing the number of proteins per vesicle ($d = 170$ nm) from five ($p/l \approx 1/68,000$) to 50 ($p/l \approx 1/6,800$).[75] However, as they did not perform a characterization of the reconstitution efficiency, a high amount of non-reconstituted protein can be assumed for all $p/l > 1/20,000$[55] leading to an underestimation of the respective turnover rates und thus explaining the observed decrease of the activity which was not observed here. Moreover, impact of the lipid mixture on the protein activity was addressed in this work by supplementing the LUVs (POPC) with cholesterol (0 % to 30 %) and net negatively charged POPG (0 % to 30 %). In general, it would be conceivable that the lipid composition alters the observed protein activity indirectly by influencing the proton transport at the membrane surface,[252,253] the membrane permeability[254,255] or the reconstitution efficiency[256]. Although previous studies with the $\mathrm{CF_OF_1}$ from Grotjohann et al. and $\mathrm{TF_OF_1}$ from Pitard et al. suggested an influence of the lipid composition on the protein activity, results from this work do not reflect these findings.[186,249] The mentioned previous studies revealed a conducive influence of cholesterol on the ATP synthesis rate, whereas contrary results were obtained for the addition of a net negatively charged lipid (phosphatidic acid, PA). While Pitard et al. revealed an increased protein activity by addition of PA,[186] Grotjohann et al. demonstrated a decreased activity in their studies[249]. However, here, the activity of the $\mathrm{TF_OF_1}$ ATP synthase was unaffected by the addition of POPG or cholesterol (cf. chapfer 4.3.1.4). It may be assumed that these contrary findings from the literature are a result of an under- or overestimation of the turnover rate as no evaluation of the actual reconstitution efficiency was performed. Lastly, the detergent selected for the reconstitution may influence, besides the reconstitution efficiency, the activity of the protein. Whereas previous works with the $\mathrm{EF_OF_1}$ ATP synthase indicated up to 6-fold increased protein activities after reconstituting the protein in LUVs via Triton™ X-100 compared to nOG,[89,186] contrary results were obtained in this work. Reconstitution with Triton™ X-100 or nOG, respectively, revealed turnover rates of $v_{\mathrm{cat,Triton\ X\text{-}100}} = (10.4 \pm 3.1)\,\mathrm{s}^{-1}$ and $v_{\mathrm{cat,nOG}} = (6.4\text{-}10.0)\,\mathrm{s}^{-1}$ (for different lipid mixtures, cf. chapter 4.3.2) being in the same order of magnitude. However, depending on the reconstitution method and the choice of the detergent the reconstitution efficiency may be altered as described before. Thus, the supposed amount of proteins contributing to the observed activity

might be under- or overestimated leading to inaccurate assumptions of the overall turnover rate.

The contrasting results found here compared to data from the literature highlight the necessity of a precise determination of the actual reconstitution efficiency for each individual experiment by means of flotation assays, for example, as carried out in this work. Quantifying turnover rates relies on reliable information on total amount of reconstituted protein to be able to compare results and draw conclusions from the influence of varied parameters like the lipid composition or the applied detergent for reconstitution. Moreover, a further key parameter for the observed protein activity is the efficiency of the acidification step of proteoliposomes to produce the proton gradient and thus the pmf. Therefore, the passive membrane permeability of liposomes for protons was probed and quantified in the following also with respect to detergents and lipid compositions.

(3) Detailed investigation of luminal acidification of liposomes during the acid-base transition

As mentioned above, the acid-base transition of $(T)F_OF_1$-liposomes is a common practice for establishing a proton gradient to analyze the activity of ATP synthases.[64,75,115,178,241,242] The so-called acidification step of the ATP synthesis assay relies on the assumption of a proton permeability of the liposomal membrane leading to a total equilibration of pH value und thus of the proton concentration between inter- and extravesicular volume. Thereby, the pH gradient contributing to the activity of F_OF_1 ATP synthases is affected by the efficiency of the acidification step. Thus, in this work the pH-sensitive fluorophore pyranine was entrapped in LUVs for quantifying the luminal pH after treating them with different acidification buffers (pH_{ac}) from the ATP synthesis assay. This assay will be referred to as acidification assay in the following. For this purpose, pyranine was found to be suitable as it does not leak out of liposomes after its entrapment.[257] Initially, the pK_a value of pyranine was determined to 7.2 which is in good accordance to the literature-known value.[179] Converting measured fluorescence intensities of pyranine into the mean luminal pH value required a calibration curve prepared from LUVs with defined luminal pH values (cf. figures 4.22 and 4.23, chapter 4.3.1.2). Consulting a modified Henderson-Hasselbalch equation allowed calculation of pH values from the normalized fluoresence intensities of pyranine after vesicle acidification (cf. equation 4.4,

table 4.5 and 4.8, chapter 4.3.1). Given its anionic character, no interaction with net negatively charged lipids such as POPG is expected for pyranine.[257] Therefore the calibration curve was used to quantify acidification experiments with LUVs composed of not only POPC and POPC/Chol (70/30, n/n) but also POPC/POPG (70/30, n/n). Acidification with pH_{ac} of 7.0 and 6.0 of LUVs composed of POPC and an initial luminal pH of 8.0 resulted in final luminal pH values of 8.1 ± 0.1 and 7.5 ± 0.3, respectively. Thus no or incomplete equilibration of the pH across the lipid bilayer was reached. Similar results were obtained for cholesterol containing LUVs yielding luminal pH values of 8.0 ± 0.2 and 7.6 ± 0.1 while slightly lower luminal pH values of 7.7 ± 0.02 and 7.30 ± 0.07 are indicated for POPG-containing vesicles after acidification with pH_{ac} values of 7.0 and 6.0. Therefore, lipid composition does not seem to affect the membrane permeability to a greater extent. Likewise, acidification of LUVs (POPC) with pH_{ac} 5.8 and 5.6 did not result in a complete equilibration of the inner and outer pH value. Reached luminal pH values were determined to 6.4 ± 0.3 and 5.8 ± 0.1, respectively. Interestingly, the extent of proton influx was increased with increasing pH gradient. Acidification assays with $pH_{ac} < 5.6$ yielded luminal pH values that were not evaluable due to the complete fluorescence quenching of pyranine and thus were not taken into account here.

The precise mechanism of passive proton transfer across lipid membranes is still elusive.[258–260] Membrane permeability in general is dependent on a wide range of parameters like the temperature,[261] membrane thickness,[262], the lipid composition[263] and the type of ion (size, charge)[260]. Compared to other monovalent cations like potassium ($P_{K^+} = (10^{-9}\text{-}10^{-13})\,\mathrm{cm\,s^{-1}}$) the permeability coefficient of protons (at pH = 7.0) is several orders of magnitude greater ($P_{H^+} = (10^{-2}\text{-}10^{-7})\,\mathrm{cm\,s^{-1}}$).[260,262] Studies analyzing the passive proton transport across membranes by means of lipid and hybrid lipid/polymer vesicles observed a biphasic mechanism of a faster pH drop followed by a slower diffusion which was more prominent for hybrid systems.[71,264,265] A similar behavior is indicated by the acidification assays measured here (cf. chapter 4.3.1.2, figure 4.23). The mentioned biphasic mechanism has been ascribed to a faster passive H^+ translocation across the bilayer building up a charge and leading in the following to a slower H^+ flux limited by the membrane permeability of other ions, that are able to compensate the charge.[264] As a result, some studies have shown that the rate of passive proton flux across the membrane is increased depending on the presence of the ionophore valinomycin and K^+.[71,264,265] In this work, however, no significant difference was found with and without valinomycin, even though a

slightly faster influx was indicated for acidification with $pH_{ac} = 6.0$ (cf. table 4.5, chapter 4.3.1.2 and figure A.1, chapter A.8). However, proton influx may also be facilitated by the presence of membrane-permeable buffer substances like succinate (and bis-tris).[266,267] In brief, the proton influx into the vesicle lumen builds up a charge gradient, whereupon the above-mentioned slower phase of the proposed two-step mechanism occurs. Succinate, in its neutral and monoanionic form, can cross the membrane due to the formation of an intramolecular hydrogen bridge, thus providing charge balance.[266] Several mechanisms have been considered to explain the passive proton flux across lipid bilayers including for example the transient pore formation, the solubility diffusion mechanism and formation of water wires.[260,262,265,268,269] The model of transient pore formation suggests temporary opening of a (hydrophilic) pore due to thermal fluctuations allowing ions to pass the membrane.[265,268,269] Formation of such pores may be facilitated by osmotic and electrical gradients[265,269] as occured here by injecting the LUVs with an initial luminal pH of 8.0 (20 mM Tricine, 20 mM succinic acid, 0.6 mM KCl, 2.5 mM $MgCl_2$) in an outer solution with $pH_{ac} \leq 7.0$ and a varied overall buffer composition (20 mM Bis-Tris or succinic acid, 0.6 mM KCl, 5 mM NaH_2PO_4, 2.5 mM $MgCl_2$). Thus, it appears to be conceivable that a higher pH gradient and, associated with this, the evoked increased electrical potential across the lipid bilayer promotes transient pore formation which may explain the observed enhanced proton influx in the intervesicular volume at lower extravesicular pH values. The solubility diffusion model proposes partitioning of the proton in the outer leaflet followed by its diffusion through the hydrophobic core and exclusion from the inner leaflet.[265,268] In contrast, another mechanism supposes formation of membrane spanning water wires or water wire networks along which proton can be transported from one side of the lipid bilayer to the other.[259] Further mechanisms such as the packing defect model, lipid headgroup-gated model and the lipid carrier model which may also contribute to the observed permeability of the membrane for protons, shall be mentioned here only by name for the sake of completeness.[268] It can be proposed that a combination of more of these proposed mechanisms contribute to the increased proton permeability of membranes compared to other small monovalent cations. Moreover, there is evidence that the lipid composition affects membrane permeability. While cholesterol was found to reduce leakage of small cations like protons across lipid bilayers, negatively charged lipids seem to increase membrane permeability.[260,270] Interestingly, as mentioned at the beginning, no explicit influence of the lipid mixture was found in this work. The proton permeability of the

membrane appears to be slightly increased when POPG was added, while addition of cholesterol had no effect. Finally, it must be taken into account that proteoliposomes subjected to the acidification step during the ATP synthesis assay have been treated with detergents (e.g. Triton™ X-100, nOG) during the reconstitution. Potential residual detergents may contribute to an increased membrane permeability. [23,271] For Triton™ X-100 a concentration of $0.05\,\text{mM}$ would be required to affect the membrane permeability. [271] Nevertheless, in this work, acidification assays with Triton™ X-100-treated and pyranine-filled LUVs revealed unaltered results compared to detergent-free LUVs (cf. figure A.2, chapter A.9) implying that little or no residual detergent is left in the proteoliposome suspension after reconstitution. Interestingly, studies by Fischer and Richard et al. found an increase of ATP synthesis activity by increasing the amount of Triton™ X-100 during reconstitution and decreasing the degree of its removal. [89,272] Residual detergent may increase membrane permeability und thus the efficiency of the acidification step yielding a higher ΔpH (and pmf) compared to detergent-free proteoliposomes. However, remaining detergents may also increase passive backflow of protons from the vesicle lumen in the outer solution rather than driving the $\text{TF}_\text{O}\text{F}_1$ ATP synthase during the ATP synthesis assay.

All in all, it has been shown that the common acid-base transition procedure for establishing the required pH gradient and electrochemical potential to drive ATP synthases is based on a highly complex and not fully understood process of passive proton transport across lipid bilayers. Moreover, incomplete pH equilibration was observed which may lead to an overestimation of the pmf and thus misinterpretation of ATP synthase activity (cf. figure 4.25 and table 4.6, chapter 4.3.1.2). The effect of incomplete pH equilibration appears to be particularly pronounced for smaller ΔpH-values during the acidification step. Based on the determined effective luminal pH values after vesicle acidification the statement about the minimal pmf required for ATP synthesis by $\text{TF}_\text{O}\text{F}_1$ has to be corrected from $243\,\text{mV}$ to $177\,\text{mV}$. Additionally, passive backflow of protons across the membrane competes with proton translocation through the ATP synthase and thus with its ATP synthesis activity. These findings have to be taken into consideration when working with ATP synthases and comparing turnover rates from literature.

## 5.3.2 Reconstitution of transmembrane proteins in dsGUVs/GUVs via droplet-based microfluidics

Reconstitution of transmembrane proteins in GUVs is required for the characterization of protein activity in a cell-like but defined system composed of a minimal set of components and, to go one step further, for the formation of artificial cell mimicries.[7] Various approaches were evolved including gentle hydration,[273] electroformation,[274] fusion-based methods[53] and double emulsion,[275] to name a few, all exhibiting certain drawbacks like restricted lipid compositions, low ion strength or low protein reconstitution efficiencies.[43] Especially when it comes to the reconstitution of complex proteins or simultaneous reconstitution of two or more proteins current methods are limited.[7] Nevertheless, different approaches were reported in the recent past aiming at overcoming the aforementioned challenges.[7] For instance, parallel reconstitution of two transmembrane proteins (F_OF_1 ATP synthase, bo_3 oxidase) was provided by charged mediated fusion of proteo-LUVs and protein-free GUVs.[52] However, high amounts of positively and negatively charged lipids are required providing a less physiological environment for transmembrane proteins in the final proteo-GUVs.[52,276] In this thesis, reconstitution of transmembrane proteins (TF_OF_1 ATP synthase, syb 2) followed basically the droplet-based microfluidic approach first introduced by Weiss et al. with modifications.[45] Here, the preparation of dsGUVs was performed by direct encapsulation of proteo-LUVs within surfactant-stabilized water-in-oil droplets whereas Weiss et al. described a more complicated variant of subsequent loading of preformed dsGUVs with proteo-LUVs via so-called picoinjection (cf. figure 5.4).[45] So far, model membranes derived from droplet-based microfluidics (dsGUVs, GUVs, PSMs) were studied in this thesis in terms of their biophysical properties (lipid mobility, mechanical behavior, cf. chapter 5.2.1, 5.2.2) in the absence of proteins. Here, formation of dsGUVs from proteo-LUVs (proteo-dsGUVs) and subsequent release of GUVs (proteo-GUVs) will be analyzed regarding bilayer formation at the water-oil interface, protein activity and reconstitution efficiency taking the proteins TF_OF_1 ATP synthase and syb 2 as examplary proteins.

Reconstitution of the TF_OF_1 ATP synthase in (ds)GUVs via droplet-based microfluidics

The TF_OF_1 ATP synthase was inserted into preformed LUVs ($d_{nom} = 100\,nm$) at a nominal protein to lipid ratio of 1/20,000 as described in previous studies via direct,

detergent-mediated reconstitution relying either on nOG[119] or Triton™ X-100[178] (cf. chapter 4.3.2). Reconstitution efficiency and protein activity were proven by flotation (cf. chapter 3.2.2.4) and ATP synthesis assays (cf. chapter 3.3.1.1), respectively, yielding for both applied detergents functional proteo-LUVs ($v_{cat} \approx 6\,\mathrm{s}^{-1}$ to $10\,\mathrm{s}^{-1}$, $pmf = 381\,\mathrm{mV}$). Detailed analysis of reconstitution efficiency and ATP synthesis actitivity of the $\mathrm{TF_OF_1}$ ATP synthase in LUVs can be found in chapter 5.3.1. Microfluidic production of dsGUVs using Triton™ X-100 treated LUVs (with and without reconstituted $\mathrm{TF_OF_1}$ ATP synthase) led to the formation of distinct areas of high fluorescence intensity at the droplet periphery indicating clustering of vesicles and/or lipid debris and thus disturbed bilayer formation at the water-oil interface. It is noteworthy to mention that the attempt to release GUVs from this approach failed (cf. figure 4.27, chapter 4.3.2). In contrast, $\mathrm{TF_OF_1}$-LUVs prepared by nOG-mediated reconstitution resulted in (proteo-)dsGUVs with a homogeneous fluorescence intensity at the interface and successful release of (proteo-)GUVs. Thus, while dsGUV formation is feasible with nOG-treated proteo-LUVs, residual Triton™ X-100 seems to hinder the assembly of a continuous bilayer at the droplet periphery. Reason for this observation may be the low critical micelle concentration of Triton™ X-100 ($\mathrm{CMC_{TritonX\text{-}100}} = (0.17\text{-}0.3)\,\mathrm{mM}$) compared to nOG ($\mathrm{CMC_{nOG}} = (20\text{-}25)\,\mathrm{mM}$) complicating its removability from proteoliposome suspensions during reconstitution.[22] Although the applied Bio-Beads SM-2® are mostly reported as a reliable method to remove detergents, retention of minor residues cannot be excluded.[25,277,278] It remains to be hypothesized what impact even minimal residues of detergents have on the surfactant-stabilized droplets, which, as described in chapter 5.1, rely on a sensitive interplay of the individual components. Conceivable would be either an influence of residual detergent on vesicles in the aqueous phase (e.g. vesicle clustering) or detergent insertion into the surfactant layer (PFPE-PEG-PFPE, Krytox/PFPE-carboxylate) resulting in disturbed vesicle adsorption to the surfactant shell and subsequent hindered spreading and bilayer formation at the droplet periphery. However, none of these effects were described in detail in the literature so far, although Triton™ X-100 was used in the past as a surfactant for studying water-in-oil emulsions highlighting its potential impact on the system of interest of this thesis.[101] Moreover, there is evidence that Triton™ X-100 can cause structural changes of small vesicles up to an increase in their diameter (cf. chapter 5.3.1),[237,238] which could contribute to a lack of continuous bilayer formation in the droplets. Interestingly, Weiss et al. reconstituted the $\mathrm{EF_OF_1}$ ATP synthase in LUVs, likewise based on Triton™ X-100,

and subsequently used the resulting proteoliposomes for dsGUVs production.[45] The authors did not report of a disturbed bilayer formation and show activitiy measurements (ATP synthesis assays) indicating low protein activity in the proteo-dsGUVs. However, a different approach based on the picoinjection technology was applied by them.[45] The picoinjection technology relies on poration of the surfactant layer by an alternating electric potential allowing injection of defined volumes into the water-in-oil droplets (cf. figure 5.4). In the referred study, protein-free dsGUVs and thus a continuous bilayer at the water-oil interface were preformed. Subsequent picoinjection of a defined volume containing proteoliposomes within the droplets allows their fusion with the existing bilayer at the water-oil interface and thereby the transfer of the protein from LUVs in the bilayer of the dsGUVs.[45] One can suggest, that a significantly lower proportion of proteoliposomes is inserted by using the picoinjection approach and therefore a lower concentration of potentially residual detergent (Triton™ X-100) is present in the droplets compared to direct formation of dsGUVs from proteo-LUVs. Furthermore, the bilayer is already preformed which might reduce impact of detergents and support the assembly of proteo-dsGUVs. Both assumptions may explain that Weiss et al. were able to produce dsGUVs without noticeable vesicle aggregations (as observed here). Overall, it should be noted, that the choice of detergent for protein reconstitution in LUVs and its complete removal plays a pivotal role for the success of subsequent (proteo-)dsGUV formation. In the course of this work, nOG proved to be suitable and was therefore used for further experiments.
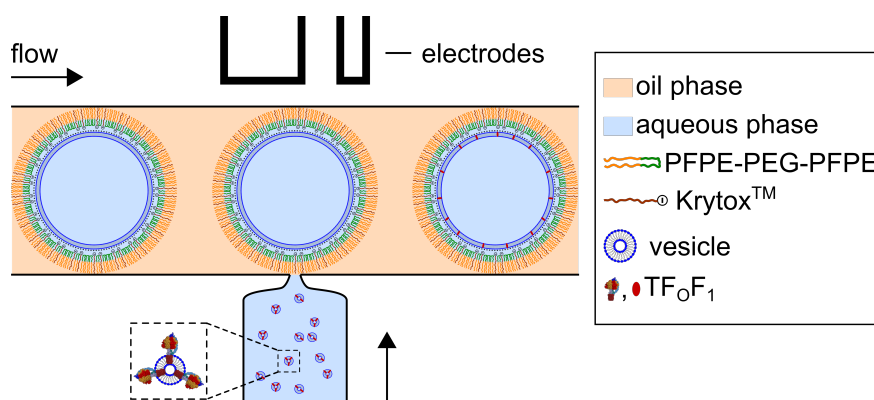
Figure 5.4: Schematic illustration of the picoinjection technology for incorporating transmembrane proteins in dsGUVs. Controlled volumes of proteoliposome suspension were added into each droplet containing a protein-free dsGUV triggered by an electric field.

Luminescence-based ATP synthesis assays were perfomed to determine the activity of the TF_OF_1 ATP synthase in dsGUVs and released GUVs, respectively (cf. figure 4.29, chapter 4.3.2). So far, the exact process of bilayer formation at water-oil interfaces and thus protein orientation after dsGUV formation is still elusive. Therefore, different approaches were taken into consideration addressing the two conceivable orientations of the protein within the lipid bilayer (cf. figure 5.5). First, an approach adopted from Weiss et al. was performed, using the (proteo-)dsGUVs and establishing the required proton gradient by acidification of the outer oil phase.[45] Thus, protein orientation with the F_1 unit pointing to the inside of dsGUVs was required to produce ATP by this method (cf. figure 5.5 A). Total amount of ATP synthesized from the ATP synthase was monitored by addition of the ATP sensitive luciferin-luciferase system after releasing the content of dsGUVs (cf. figure 4.29 A, chapter 4.3.2). Unexpectedly, in contrast to the study of Weiss et al. no ATP and therefore no protein activity could be detected.[45] One can assume that the picoinjection-based production of (proteo-)dsGUVs applied by the aforementioned authors leads to a protein orientation with the F_1 unit pointing to the inside (cf. figure 4.29 A1, chapter 4.3.2) while the direct production pathway applied in this work yields the opposite orientation within the lipid bilayer of the dsGUVs (cf. figure 4.29 A2, chapter 4.3.2). Thus, a second approach was used to probe the aformentioned assumption (cf. figure 4.29 B, chapter 4.3.2). Since the interior of dsGUVs cannot be readily acidified due to the external oil phase and surfactant layer, TF_OF_1 activity was aimed to be monitored in released (proteo-)GUVs by subjecting them to an assay procedure as applied for proteo-LUVs (cf. chapter 5.3.1). However, no protein activity could be detected in this approach neither.

Potential explanations include low reconstitution efficiency of the protein in (ds)GUVs and/or low release rate of the (proteo-)GUVs leading to amounts of synthesized ATP during the ATP synthesis assay below the detection limit of the luciferin-luciferase system ($c_{ATP,minimal} \approx 10^{-11}$ M)[114]. Another factor may be the influence of co-block polymers (surfactants) increasing the membrane permeability for protons and causing the proton gradient built up by the ATP synthesis assay to be degraded by passive transport across the membrane rather than being utilized by ATP synthase.[228,230,231,279] Furthermore, denaturation and loss of function of the protein during microfluidic dsGUV production or bulk release of the GUVs might occur. To adress these open questions a second less complex protein featuring a fluorescence tag (syb 2) was employed in order to visualize protein localization after microfluidic

production of dsGUVs and the subsequent release process.
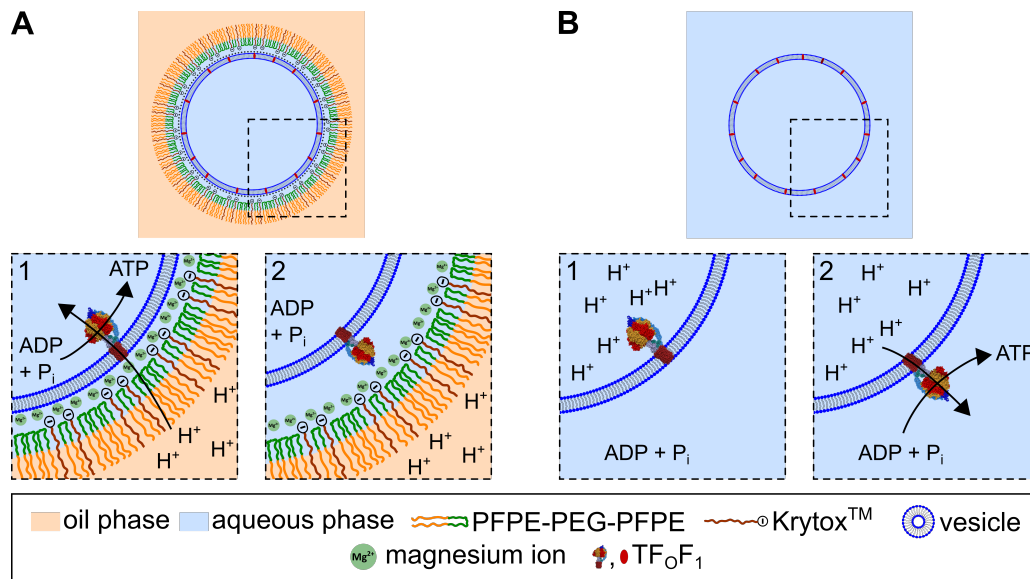
Figure 5.5: Schematic illustration of conceivable protein orientations in dsGUVs and released GUVs. A: TF_OF_1 ATP synthase in dsGUVs with the F_1 unit pointing to the inside (1) or outside (2). The ATP synthesis assay in dsGUVs adopted from Weiss et al. addresses orientation (1) due to the direction of the proton gradient. No activity would be measured for proteins oriented as depicted in (2). **B:** TF_OF_1 ATP synthase in released GUVs with the F_1 unit pointing to the inside (1) or outside (2). The ATP synthesis assay was performed as described for proteo-LUVs (cf. chapter 5.3.1) and addresses orientation (2) due to the inverted direction of the proton gradient.

Reconstitution of syb 2 in (ds)GUVs via droplet based microfluidics

The v-SNARE synaptobrevin 2 (syb 2) featuring an additional *C*-terminal cystein residue for fluorescence labeling was inserted via direct, *n*OG-mediated reconstitution in LUVs ($d_{nom} = 100$ nm) in nominal protein to lipid ratios between 1/500 and 1/2,500. Quantitative analysis by flotation assays yielded an effective reconstitution efficiency of $\sim 90\%$ which is in accordance to previous studies although a modified protein reconstitution protocol was applied here.[79,81] The resulting proteoliposomes were used for the microfluidic preparation of dsGUVs revealing homogeneous fluorescence intensity of lipid- and protein-coupled dyes at the droplet periphery (cf. figure 4.31, chapter 4.3.3.2) indicating formation of a continous bilayer doped with the labeled syb 2. This finding was supported by a successful release of GUVs from the microemulsion. The mobility of labeled syb 2 (Atto647N) and lipids (Atto488 DPPE) in dsGUVs was analyzed by FRAP experiments at the bottom plane of the dsGUVs

(cf. chapter 4.3.3.1). Data evaluation followed Soumpasis et al. and Kang et al. considering the effective bleach radius as discussed in chapter 5.2.1[125,126] and led to diffusion coefficients (and mobile fractions) of $D_{\mathrm{DPPE}} = (9 \pm 2)\,\mathrm{\mu m^2\,s^{-1}}$ $((98 \pm 3)\,\%)$ and $D_{\mathrm{syb\,2}} = (4 \pm 2)\,\mathrm{\mu m^2\,s^{-1}}$ $((97 \pm 5)\,\%)$ (cf. figure 4.30 C, D, chapter 4.3.3.1). Lipid mobility is in good agreement to the results discussed in chapter 5.2.1 and thus unaffected from the incorporated protein. The obtained diffusion coefficient of the protein is in the same order of magnitude than results of protein mobility in electroformed GUVs ranging from $1\,\mathrm{\mu m^2\,s^{-1}}$ to $8\,\mathrm{\mu m^2\,s^{-1}}$ determined by FRAP or FCS experiments.[79,207,280–282] In particular, studies on the mobility of ΔN49 in electroformed GUVs by a similar FRAP and evaluation method showed with $D_{\Delta\mathrm{N49}} = (5 \pm 3)\,\mathrm{\mu m^2\,s^{-1}}$ a good accordance to the diffusion coefficient presented here. Thus, successful formation of dsGUVs and insertion of proteins can be assumed. However, qualitative comparison of the membrane peak fluorescence intensities of dsGUVs doped with syb 2-Atto488 and Atto488 DPPE, respectively, indicated a loss of protein after dsGUV production compared to the expected fluorescence intensity based on the reconstitution efficiency in the LUVs (cf. figure 4.31, chapter 4.3.3.2). The loss of protein increased even more after releasing GUVs from the oil phase in an aqueous environment. In this thesis, the reconstitution efficiency of syb 2 in the released GUVs was quantified by a fluorescence-based approach and resulted in $< 0.1\,\%$ (cf. figure 4.32 D, chapter 4.3.3.2). In various studies, reconstitution of (SNARE) proteins in GUVs via electroformation yielded a wide range of reconstitution efficiencies between $1\,\%$ and $100\,\%$.[79,81,281] Reconstitution of ΔN49 in GUVs by means electroformation was examined by Mühlenbrock et al. with a fluorescence-based method comparable to the approach used here and resulted in a reconstitution efficiency of $\sim 26\,\%$.[36,79]

Together with findings from the above described $\mathrm{TF_O F_1}$ ATP synthase reconstitution, the observed decrease of the amount of reconstituted protein during microfluidic dsGUV production and total loss of protein after release of GUVs leads to the assumption of an interaction of the proteins and the surfactant-doped oil phase. This hypothesis is supported by the observation of accumulation of labeled lipids and syb 2 at residual oil droplets (cf. figure 4.32 A-C, chapter 4.3.3.2) and will be discussed in greater detail below.

Protein-surfactant interactions at water-oil interfaces

Using water-in-oil droplets for production of dsGUVs requires a defined interplay of lipids from the aqueous phase and surfactants from the oil phase, but simultaneously minimal interactions with other encapsulated biochemical components (e.g. proteins). Since protein adsorption and denaturation at water-(hydrocarbon)oil interfaces is a known phenomenon[283,284] mainly fluorinated oils are used for biochemical applications as they revealed excellent biocompatibility in cell experiments[101,285]. However, reliable prevention of nonspecific protein adsorption at water-oil interfaces can be highly controlled via interface chemistry at the droplet periphery by surfactants.[283] The aforementioned biocompatibility is an important prerequisite also for droplet-stabilizing surfactants used for biochemical applications. Design of surfactants aims at fulfilling criteria like an inert behavior to the droplet content and minimization of interfacial effects which is combined for the commonly used tri-block co-polymers (PFPE-PEG-PFPE).[101] Nevertheless, as already mentioned the formation of a continuous bilayer at the droplet periphery is based on electrostatic interactions between the surfactant shell and the encapsulated liposomes mediated by anionic Krytox (PFPE-carboxylate) (cf. chapter 5.1).[54] This desired negatively charged interface of the droplets can lead not only to interactions with liposomes but also with other encapsulated components like proteins[101] which might explain findings like the monitored inactivity of the TF_OF_1 ATP synthase in dsGUVs and the respective released GUVs as well as the total loss of syb 2 during the overall preparation described in the present thesis. While Johnston et al. performed toxicological studies and attributed a biologically non-inert behavior to Krytox (PFPE-carboxylate),[286] Roach et al. were able to show adsorption of proteins to water-oil interfaces stabilized by surfactants as a function of their hydrophilic headgroups (cf. figure 5.6 C).[283] The authors demonstrated by fluorescence microscopy and surface tension measurements with labeled fibrinogen non-specific interactions of the protein with surfactants harboring a polar or charged headgroup at water-oil interfaces. Effects were demonstrated for alcoholic headgroups and found to be increased when using carboxylic acid capped surfactants like Krytox (PFPE-carboxylate).[103,283] Consequences include unfolding of biological components (e.g. protein, RNA, DNA), loss of functionality and micellar exclusion of (water soluble) proteins in the oil phase due to Krytox ad- and desorption processes at the interface.[103,156,283] Besides Krytox also the de-emulsifier PFO harbors a hydrophilic headgroup (alcoholic) and thus may contribute to the observed effects when GUVs are released from the microemulsion.[283]
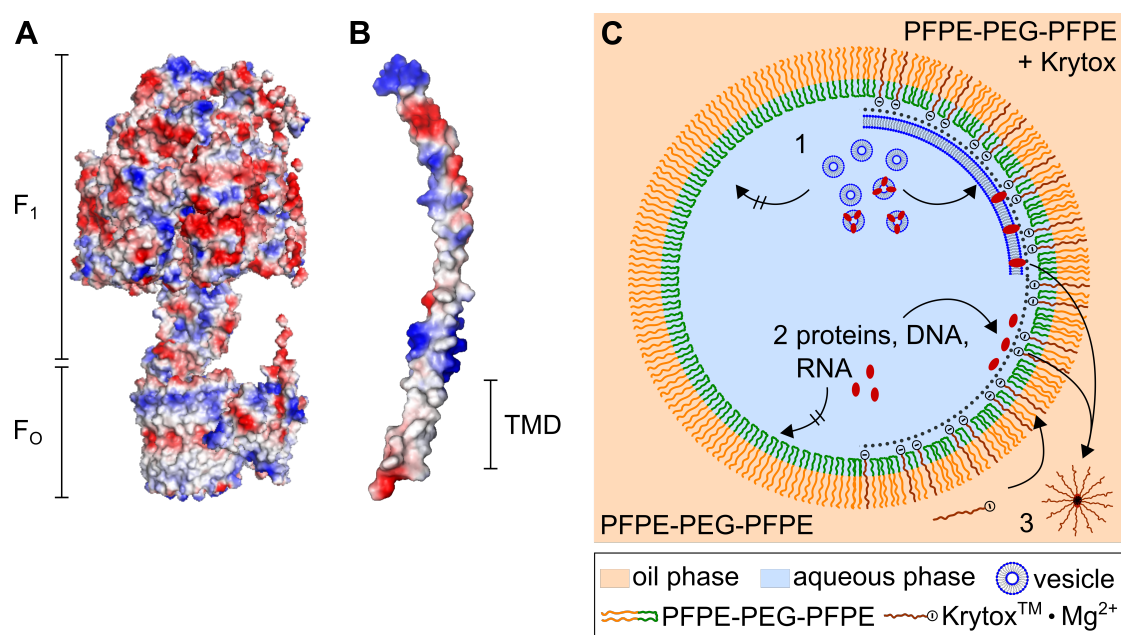
Figure 5.6: Schematic illustration of charge-mediated interactions of proteins and surfactants at water-oil interfaces. A, B: Surface charge distribution of the TF_OF_1 ATP synthase (**A**, PDB: 6N2Y) and syb 2 (**B**, PDB: 3ND7). Red areas represent negatively charged, blue positively charged and white neutral regions. **A:** The TF_OF_1 ATP synthase consists of various subunits forming a water-soluble F_1 unit and a membrane-spanning F_O unit. **A:** Syb 2 consists of the water-soluble SNARE-motif and the transmembrane domain (TMD). Images were created via *PyMOL* with kind assistance of Merve Sari (Insitute of Organic and Biomolecular Chemistry, University of Göttingen). [60,188,287] **C:** Schematic illustration of charge-mediated processes at surfactant-stabilized water-oil interphases. While PFPE-PEG-PFPE creates a biocompatible and inert inner surface (left), (proteo-)lipsomes (1) and biological compounds (e.g. proteins, RNA, DNA) (2) are electrostatically attracted to the surfactant shell in the presence of anionic Krytox (right). Ad- and desorption of Krytox leads to micellar exclusion of individual components like proteins (3).

Thus, findings reported in the literature support the proposed hypothesis that interactions of the hydrophilic domains of proteins and anionic Krytox (PFPE-carboxylate) at the water-oil interface led to the observed inactivity of the TF_OF_1 ATP synthase and the loss of syb 2 during formation of dsGUVs and release of GUVs (cf. figure 5.6 C). Both proteins were first reconstituted by direct reconstitution in LUVs, leaving them largely oriented with the water-soluble region facing outward. [23] This places them in close contact with the surfactant layer after encapsulation of the proteo-LUVs in the water-in-oil droplets and their electrostatic attraction to the interface (cf. chapter 5.1), whereby the processes described above may occur. In the following, these processes will be analyzed in detail on the basis of the two proteins

described in this thesis.

The F_1 unit of the ATP synthase exhibits predominantly negatively charged regions at its surface (cf. figure 5.6 A, pI = 5.8, pH = 7.4)[60,188] and therefore can interact electrostatically with the negatively charged surfactant layer mediated by magnesium ions whereby denaturation and a loss of functionality may occur. Moreover, disassembly of the overall protein complex and extraction from the membrane may happen during the release of GUVs since the F_1 unit may remain at the interface due to strong electrostatic interactions with Krytox (PFPE-carboxylate) and the de-emulsifier PFO.[101,283] In comparison, syb 2 displays more positively charged domains on the surface (cf. figure 5.6 B, pI = 7.8, pH = 7.4)[287] and thus presumably directly interacts with Krytox electrostatically. The total loss of reconstituted syb 2 can be explained by two conceivable processes. First, micellar exclusion from the interface to the aqueous phase may occur due to Krytox ad- and desorption processes (cf. figure 5.6 C).[156] Its extraction from the bilayer may be provided by known penetration of lipid bilayers by the surfactants.[224,225] Second, the complete loss of the remaining syb 2 during the release implies its complete extraction from the bilayer as a result from the strong electrostatic interactions of charged or polar surfactants (Krytox, PFO) and the hydrophilic regions of the protein. Presumably, it remains at the interface after separation of the oil and water phase. Interestingly, similar observations were made for syb 2-LUVs prepared by co-micellization resulting in a equal distribution of the protein orientation in the membrane.[23] This observation suggests that either minor interactions of the small *C*-terminal charged region with the surfactants are sufficient to cause the aforementioned effects or that further so far unknown processes are involved.

In summary, both transmembrane proteins feature charged regions at the interface (PDB (TF_OF_1): 6N2Y, PDB (syb 2): 3ND7)[60,188,287] which are known to interact with Krytox.[100] These interactions may result after encapsulation in surfactant-stabilized water-in-oil droplets in protein denaturation, loss of functionality, extraction from the lipid bilayer and micellar exclusion in the oil phase. While Krytox concentrations between $6\,\mathrm{mM}$ and $13\,\mathrm{mM}$ are required for the bilayer formation at the droplet periphery und thus dsGUV assembly,[54] protein adsorption and denaturation seems to occur already at $c_{\mathrm{Krytox}} = 0.54\,\mathrm{mM}$[156]. Thus, it must be questioned whether the charge-controlled microfluidic production of GUVs is suitable for the reconstitution of proteins with charged or hydrophilic domains, respectively. It is advisable to verify protein activity and reconstitution efficiency in each individual case and for the

specific protein of interest. Thus, a surfactant-free and additive-free approach based on water-octanol double emulsion as introduced from Yandrapalli et al. may be a suitable advancement for the microfluidic production of GUVs, the incorporation of proteins and subsequent creation of biomimetic artificial cells and may be considered for further studies.[288] Their evaluation of lipid diffusion, protein incorporation and membrane leakage assays revealed high similarities to solvent-free lipid bilayers and was recently applied for cell-free gene expression in artificial cells.[288,289] However, residual solvent (octanol) may remain in the bilayer and has to be carefully controlled and a reconstitution strategy for complex transmembrane proteins is still has to be developed.[288]

6 Conclusion

The bottom-up assembly of model membrane systems equipped with a minimal set of biological components like transmembrane proteins is an essential step to investigate and disentangle complex processes at cellular membranes. Thus, reconstitution of proteins in giant unilamellar vesicles (GUVs) is highly relevant as they represent a suitable cell mimicking system and can also act as starting point for further model systems like pore-spanning membranes (PSMs). Goal of this thesis was to probe droplet-based microfluidics as a tool for the production of (protein-containing) model membranes and to analyze their biophysical properties.

Droplet-based microfluidics were employed for producing droplet-stabilized GUVs (dsGUVs) which were subsequently released as free GUVs in an aqueous environment by de-emulsification. The approach was probed by applying multiple oil-surfactant-, buffer- and lipid-compositions revealing a defined interplay of the charged components (e.g. surfactants, ions, lipids) at the water-oil interface. It was demonstrated that the microfluidic method for producing (ds)GUVs offers high flexibility concerning buffer and lipid additives allowing to maintain biomimetic conditions during the preparation. Moreover, the released microfluidic-GUVs were applied to produce PSMs. For this purpose, GUVs were spread on porous Si_3N_4 substrates functionalized with a thin layer of SiO_x or gold and 6-mercapto-1-hexanol. Probing the diffusive properties by fluorescence recovery after photobleaching and fluorescence correlation spectroscopy revealed that the lipid mobility in microfluidic-derived systems (dsGUVs, microfluidic-GUVs and -PSMs) is unaltered compared to electroformed GUVs and the respective PSMs. Additionally, atomic force microscopy was employed to investigate the membrane mechanics by means of force-indentation experiments showing high stability and a fully elastic behavior of the microfluidic-PSMs. The bending modulus κ, determined by these experiments, was found to be unaffected by the preparation method, whereas the lateral membrane tension σ was decreased by factor 1.5 for microfluidic-PSMs compared to PSMs derived from electroformed GUVs on SiO_x functionalized porous substrates. The latter observation suggests a potential impact of trace amounts of surfactants from the preparation procedure which remains to be systematically analyzed in prospective studies.

Furthermore, the TF_OF_1 ATP synthase and fluorescently labeled synaptobrevin 2 (syb 2) were recruited as model proteins to scrutinize functional and efficient protein reconstitution under biomimicking conditions in the membrane of dsGUVs and

released GUVs. Reconstituting transmembrane proteins in microfluidic-GUVs requires their initial detergent-mediated insertion into the bilayer of large unilamellar vesicles (LUVs). It was found that potential trace amounts of the detergent Triton™X-100 from the preparation of proteo-LUVs might interfere with the GUV formation at the droplet periphery while utilizing nOG instead allowed to successfully assemble dsGUVs and release GUVs. While FRAP experiments revealed that syb 2 is present and mobile in the bilayer of dsGUVs, activity assessments (TF_OF_1) and fluorescence-based quantification of the reconstitution efficiency (syb 2) in dsGUVs and GUVs revealed a loss of protein during the microfluidic preparation pathway and the following de-emulsification presumably as a consequence of electrostatic interactions between proteins and charged surfactants. Thus, the reconstitution of transmembrane proteins in (ds)GUVs requires adaptation of the charged surfactants since no evidence of quantitative and functional protein reconstitution has been demonstrated to date.

ATP synthases are of particular interest in living organisms as they play an essential role as universal energy suppliers. Thus, besides its reconstitution in (ds)GUVs the TF_OF_1 ATP synthase was characterized concerning the ATP synthesis actitivity in LUVs in the course of this work.

Therefore, the protein was reconstituted in LUVs composed of different lipid mixtures in order to determine its activity as a function of the applied proton motive force (pmf) using a luminescence-based ATP synthesis assay. Both, reconstitution efficiency ($R_{LUV} \approx 100\%$) and protein activity were unaffected by the applied lipid composition. Varying the pH gradient across the lipid bilayer yielded turnover rates of $0.043\,s^{-1}$ to $13.0\,s^{-1}$. Simultaneously, the acid-base transition of the ATP synthesis assay, which has been commonly applied in previous works for establishing the required proton gradient and relies on passive proton transport across the lipid bilayer, was analyzed by a pyranine-based acidification assay. Thereby, incomplete pH equilibration during the acidification of the inner compartment of the vesicles was observed leading to an overestimation of the pmf in the ATP synthesis assay and thus potential misinterpretation of the activity of ATP synthases. It was found that TF_OF_1 activity started at a minimal pmf of $177\,mV$ ($\Delta\psi = 135\,mV$, $\Delta pH_{exp} = 0.7$) according to the experimentally quantified luminal pH_{in}. This pmf is thus considerably lower than the expected one ($243\,mV$, $\Delta\psi = 135\,mV$, $\Delta pH_{theor} = 1.8$), which was assumed based on the nominal pH-value of the acidification buffer. Overall, the shown data allow novel insights in the function of the TF_OF_1 ATP synthase and the luminescence-based ATP synthesis assay complementing the existing literature.

7 Bibliography

[1] M. Eeman, M. Deleu, From biological membranes to biomimetic model membranes, *Biotechnologie, Agronomie, Société et Environnement* **2010**, *14*(4), 719–736.

[2] V. Malinova, M. Nallani, W. Meier, E. Sinner, Synthetic biology, inspired by synthetic chemistry, *FEBS letters* **2012**, *586*(15), 2146–2156.

[3] J. C. Xavier, K. R. Patil, I. Rocha, Systems biology perspectives on minimal and simpler cells, *Microbiology and Molecular Biology Reviews* **2014**, *78*(3), 487–509.

[4] Y. Elani, Interfacing living and synthetic cells as an emerging frontier in synthetic biology, *Angewandte Chemie* **2021**, *133*(11), 5662–5671.

[5] M. Nie, S. Takeuchi, Bottom-up biofabrication using microfluidic techniques, *Biofabrication* **2018**, *10*(4), 044103.

[6] P. Walde, K. Cosentino, H. Engel, P. Stano, Giant vesicles: preparations and applications, *ChemBioChem* **2010**, *11*(7), 848–865.

[7] T. Litschel, P. Schwille, Protein reconstitution inside giant unilamellar vesicles, *Annual Review of Biophysics* **2021**, *50*, 525–548.

[8] K. Y. Lee, S.-J. Park, K. A. Lee, S.-H. Kim, H. Kim, Y. Meroz, L. Mahadevan, K.-H. Jung, T. K. Ahn, K. K. Parker, S. Kwanwoo, Photosynthetic artificial organelles sustain and control ATP-dependent reactions in a protocellular system, *Nature Biotechnology* **2018**, *36*(6), 530–535.

[9] S. Berhanu, T. Ueda, Y. Kuruma, Artificial photosynthetic cell producing energy for protein synthesis, *Nature Communications* **2019**, *10*(1), 1–10.

[10] S. Matosevic, Synthesizing artificial cells from giant unilamellar vesicles: State-of-the art in the development of microfluidic technology, *Bioessays* **2012**, *34*(11), 992–1001.

[11] N. Yeh Martín, L. Valer, S. S. Mansy, Toward long-lasting artificial cells that better mimic natural living cells, *Emerging Topics in Life Sciences* **2019**, *3*(5), 597–607.

[12] N. A. Yewdall, A. F. Mason, J. C. Van Hest, The hallmarks of living systems: towards creating artificial cells, *Interface Focus* **2018**, *8*(5), 20180023.

[13] A. Oshima, Structure and closure of connexin gap junction channels, *FEBS letters* **2014**, *588*(8), 1230–1237.

[14] S. M. Bartelt, E. Chervyachkova, J. Ricken, S. V. Wegner, Mimicking adhesion in minimal synthetic cells, *Advanced Biosystems* **2019**, *3*(6), 1800333.

[15] R. B. Lira, R. Dimova, Fusion assays for model membranes: a critical review, *Advances in Biomembranes and Lipid Self-Assembly* **2019**, *30*, 229–270.

[16] M. Loose, P. Schwille, Biomimetic membrane systems to study cellular organization, *Journal of Structural Biology* **2009**, *168*(1), 143–151.

[17] J. I. Korenbrot, Ion transport in membranes: incorporation of biological ion-translocating proteins in model membrane systems, *Annual Review of Physiology* **1977**, *39*(1), 19–49.

[18] V. Kobliakov, Role of proton pumps in tumorigenesis, *Biochemistry (Moscow)* **2017**, *82*(4), 401–412.

[19] J. Knobloch, D. K. Suhendro, J. L. Zieleniecki, J. G. Shapter, I. Köper, Membrane–drug interactions studied using model membrane systems, *Saudi Journal of Biological Sciences* **2015**, *22*(6), 714–718.

[20] A. Jesorka, O. Orwar, Liposomes: technologies and analytical applications, *Annual Review of Analytical Chemistry* **2008**, *1*, 801–832.

[21] E. Rideau, R. Dimova, P. Schwille, F. R. Wurm, K. Landfester, Liposomes and polymersomes: a comparative review towards cell mimicking, *Chemical society reviews* **2018**, *47*(23), 8572–8610.

[22] D. Linke, Detergents: an overview, *Methods in Enzymology* **2009**, *463*, 603–617.

[23] J.-L. Rigaud, D. Lévy, Reconstitution of membrane proteins into liposomes, *Methods in Enzymology* **2003**, *372*, 65–86.

[24] D. Lévy, A. Bluzat, M. Seigneuret, J.-L. Rigaud, A systematic study of liposome and proteoliposome reconstitution involving Bio-Bead-mediated Triton X-100 removal, *Biochimica et Biophysica Acta (BBA)-Biomembranes* **1990**, *1025*(2), 179–190.

[25] J.-L. Rigaud, D. Lévy, G. Mosser, O. Lambert, Detergent removal by non-polar polystyrene beads, *European Biophysics Journal* **1998**, *27*(4), 305–319.

[26] J.-L. Rigaud, B. Pitard, D. Lévy, Reconstitution of membrane proteins into liposomes: application to energy-transducing membrane proteins, *Biochimica et Biophysica Acta (BBA)-Bioenergetics* **1995**, *1231*(3), 223–246.

[27] A. S. Ladokhin, S. Jayasinghe, S. H. White, How to measure and analyze tryptophan fluorescence in membranes properly, and why bother?, *Analytical Biochemistry* **2000**, *285*(2), 235–245.

[28] T. Robinson, Microfluidic handling and analysis of giant vesicles for use as artificial cells: a review, *Advanced Biosystems* **2019**, *3*(6), 1800318.

[29] Y. Lu, G. Allegri, J. Huskens, Vesicle-based artificial cells: materials, construction methods and applications, *Materials Horizons* **2022**.

[30] E. Sezgin, P. Schwille, Model membrane platforms to study protein-membrane interactions, *Molecular Membrane Biology* **2012**, *29*(5), 144–154.

[31] E. Sezgin, Giant plasma membrane vesicles to study plasma membrane structure and dynamics, *Biochimica et Biophysica Acta (BBA)-Biomembranes* **2022**, 183857.

[32] A. Janshoff, C. Steinem, Scanning force microscopy of artificial membranes, *ChemBioChem* **2001**, *2*(11), 798–808.

[33] M. Przybylo, J. Sỳkora, J. Humpolícková, A. Benda, A. Zan, M. Hof, Lipid diffusion in giant unilamellar vesicles is more than 2 times faster than in supported phospholipid bilayers under identical conditions, *Langmuir* **2006**, *22*(22), 9096–9099.

[34] S. Ramakrishnan, M. Bera, J. Coleman, S. S. Krishnakumar, F. Pincet, J. E. Rothman, Synaptotagmin oligomers are necessary and can be sufficient to form a Ca2+-sensitive fusion clamp, *FEBS letters* **2019**, *593*(2), 154–162.

[35] I. Mey, C. Steinem, A. Janshoff, Biomimetic functionalization of porous substrates: towards model systems for cellular membranes, *Journal of Materials Chemistry* **2012**, *22*(37), 19348–19356.

[36] P. Mühlenbrock, K. Herwig, L. Vuong, I. Mey, C. Steinem, Fusion pore formation observed during SNARE-mediated vesicle fusion with pore-spanning membranes, *Biophysical Journal* **2020**, *119*(1), 151–161.

[37] S. Spindler, J. Sibold, R. Gholami Mahmoodabadi, C. Steinem, V. Sandoghdar, High-speed microscopy of diffusion in pore-spanning lipid membranes, *Nano Letters* **2018**, *18*(8), 5262–5271.

[38] D. Frese, S. Steltenkamp, S. Schmitz, C. Steinem, In situ generation of electrochemical gradients across pore-spanning membranes, *RSC Advances* **2013**, *3*(36), 15752–15761.

[39] J. Sibold, V. E. Tewaag, T. Vagedes, I. Mey, C. Steinem, Phase separation in pore-spanning membranes induced by differences in surface adhesion, *Physical Chemistry Chemical Physics* **2020**, *22*(17), 9308–9315.

[40] A. Janshoff, C. Steinem, Mechanics of lipid bilayers: What do we learn from pore-spanning membranes?, *Biochimica et Biophysica Acta (BBA)-Molecular Cell Research* **2015**, *1853*(11), 2977–2983.

[41] M. Kocun, T. D. Lazzara, C. Steinem, A. Janshoff, Preparation of solvent-free, pore-spanning lipid bilayers: modeling the low tension of plasma membranes, *Langmuir* **2011**, *27*(12), 7672–7680.

[42] P. Mühlenbrock, M. Sari, C. Steinem, In vitro single vesicle fusion assays based on pore-spanning membranes: merits and drawbacks, *European Biophysics Journal* **2021**, *50*(2), 239–252.

[43] I. L. Jørgensen, G. C. Kemmer, T. G. Pomorski, Membrane protein reconstitution into giant unilamellar vesicles: a review on current techniques, *European Biophysics Journal* **2017**, *46*(2), 103–119.

[44] P. Supramaniam, O. Ces, A. Salehi-Reyhani, Microfluidics for artificial life: techniques for bottom-up synthetic biology, *Micromachines* **2019**, *10*(5), 299.

[45] M. Weiss, J. P. Frohnmayer, L. T. Benk, B. Haller, J.-W. Janiesch, T. Heitkamp, M. Börsch, R. B. Lira, R. Dimova, R. Lipowsky, E. Bodenschatz, J.-C. Baret, T. Vidakovic-Koch, K. Sundmacher, I. Platzman, J.-P. Spatz, Sequential bottom-up assembly of mechanically stabilized synthetic cells by microfluidics, *Nature Materials* **2018**, *17*(1), 89–96.

[46] P. Girard, J. Pécréaux, G. Lenoir, P. Falson, J.-L. Rigaud, P. Bassereau, A new method for the reconstitution of membrane proteins into giant unilamellar vesicles, *Biophysical journal* **2004**, *87*(1), 419–429.

[47] S. Aimon, J. Manzi, D. Schmidt, J. A. Poveda Larrosa, P. Bassereau, G. E. Toombes, Functional reconstitution of a voltage-gated potassium channel in giant unilamellar vesicles, *PloS One* **2011**, *6*(10), e25529.

[48] T. Bhatia, F. Cornelius, J. Brewer, L. A. Bagatolli, A. C. Simonsen, J. H. Ipsen, O. G. Mouritsen, Spatial distribution and activity of $Na+/K+$-ATPase in lipid bilayer membranes with phase boundaries, *Biochimica et Biophysica Acta (BBA)-Biomembranes* **2016**, *1858*(6), 1390–1399.

[49] M. Kreir, C. Farre, M. Beckler, M. George, N. Fertig, Rapid screening of membrane protein activity: electrophysiological analysis of OmpF reconstituted in proteoliposomes, *Lab on a Chip* **2008**, *8*(4), 587–595.

[50] A. R. Battle, E. Petrov, P. Pal, B. Martinac, Rapid and improved reconstitution of bacterial mechanosensitive ion channel proteins MscS and MscL into liposomes using a modified sucrose method, *FEBS letters* **2009**, *583*(2), 407–412.

[51] M. Dezi, A. Di Cicco, P. Bassereau, D. Lévy, Detergent-mediated incorporation of transmembrane proteins in giant unilamellar vesicles with controlled physiological contents, *Proceedings of the National Academy of Sciences* **2013**, *110*(18), 7276–7281.

[52] O. Biner, T. Schick, Y. Müller, C. von Ballmoos, Delivery of membrane proteins into small and giant unilamellar vesicles by charge-mediated fusion, *FEBS Letters* **2016**, *590*(14), 2051–2062.

[53] N. Kahya, E.-I. Pécheur, W. P. de Boeij, D. A. Wiersma, D. Hoekstra, Reconstitution of membrane proteins into giant unilamellar vesicles via peptide-induced fusion, *Biophysical Journal* **2001**, *81*(3), 1464–1474.

[54] B. Haller, K. Göpfrich, M. Schröter, J.-W. Janiesch, I. Platzman, J. P. Spatz, Charge-controlled microfluidic formation of lipid-based single-and multicompartment systems, *Lab on a Chip* **2018**, *18*(17), 2665–2674.

[55] M. Schwamborn, PhD thesis, Georg-August-Universität Göttingen, **2017**.

[56] C. von Ballmoos, G. M. Cook, P. Dimroth, Unique rotary ATP synthase and its biological diversity, *Annual Review of Biophysics* **2008**, *37*, 43–64.

[57] P. Mitchell, Coupling of phosphorylation to electron and hydrogen transfer by a chemi-osmotic type of mechanism, *Nature* **1961**, *191*(4784), 144–148.

[58] C. von Ballmoos, A. Wiedenmann, P. Dimroth, Essentials for ATP synthesis by F1F0 ATP synthases, *Annual Review of Biochemistry* **2009**, *78*, 649–672.

[59] M. Sobti, C. Smits, A. S. Wong, R. Ishmukhametov, D. Stock, S. Sandin, A. G. Stewart, Cryo-EM structures of the autoinhibited E. coli ATP synthase in three rotational states, *Elife* **2016**, *5*, e21598.

[60] ProteinDataBase, Biological Macromolecular Structures Enabling Breakthroughs in Research and Education, `https://www.rcsb.org/`, **accessed: Feb. 2022**.

[61] M. Yoshida, E. Muneyuki, T. Hisabori, ATP synthase—a marvellous rotary engine of the cell, *Nature Reviews Molecular Cell Biology* **2001**, *2*(9), 669–677.

[62] S. A. Ferguson, S. Keis, G. M. Cook, Biochemical and molecular characterization of a Na+-translocating F1Fo-ATPase from the thermoalkaliphilic bacterium Clostridium paradoxum, *Journal of Bacteriology* **2006**, *188*(14), 5045–5054.

[63] B. A. Feniouk, M. Yoshida, Regulatory mechanisms of proton-translocating F O F 1-ATP synthase, *Bioenergetics* **2007**, 279–308.

[64] R. Iino, R. Hasegawa, K. V. Tabata, H. Noji, Mechanism of Inhibition by C-terminal α-Helices of the ϵ Subunit of Escherichia coli FoF1-ATP Synthase, *Journal of Biological Chemistry* **2009**, *284*(26), 17457–17464.

[65] H. Sielaff, T. M. Duncan, M. Börsch, The regulatory subunit ε in Escherichia coli FOF1-ATP synthase, *Biochimica Et Biophysica Acta (BBA)-Bioenergetics* **2018**, *1859*(9), 775–788.

[66] D. Okuno, R. Iino, H. Noji, Rotation and structure of F o F 1-ATP synthase, *The Journal of Biochemistry* **2011**, *149*(6), 655–664.

[67] T. Xu, V. Pagadala, D. M. Mueller, Understanding structure, function, and mutations in the mitochondrial ATP synthase, *Microbial Cell* **2015**, *2*(4), 105.

[68] P. Neupane, S. Bhuju, N. Thapa, H. K. Bhattarai, ATP synthase: structure, function and inhibition, *Biomolecular Concepts* **2019**, *10*(1), 1–10.

[69] J. Berg, L. Stryer, J. Tymoczko, G. Gatto, *Biochemistry*, Macmillan Learning, **2015**.

[70] E. Usukura, T. Suzuki, S. Furuike, N. Soga, E.-i. Saita, T. Hisabori, K. Kinosita, M. Yoshida, Torque generation and utilization in motor enzyme F0F1-ATP synthase: half-torque F1 with short-sized pushrod helix and reduced ATP synthesis by half-torque F0F1, *Journal of Biological Chemistry* **2012**, *287*(3), 1884–1891.

[71] C. Kleineberg, PhD thesis, Otto-von-Guericke-Universität Magdeburg, **2021**.

[72] T. Suzuki, H. Ueno, N. Mitome, J. Suzuki, M. Yoshida, F0 of ATP Synthase Is a Rotary Proton Channel, *Journal of Biological Chemistry* **2002**, *277*(15), 13281–13285.

[73] H. Ueno, T. Suzuki, K. Kinosita, M. Yoshida, ATP-driven stepwise rotation of FoF1-ATP synthase, *Proceedings of the National Academy of Sciences* **2005**, *102*(5), 1333–1338.

[74] T. Suzuki, C. Wakabayashi, K. Tanaka, B. A. Feniouk, M. Yoshida, Modulation of Nucleotide Specificity of Thermophilic FoF1-ATP Synthase by epsilon-Subunit, *Journal of Biological Chemistry* **2011**, *286*(19), 16807–16813.

[75] N. Soga, K. Kinosita, M. Yoshida, T. Suzuki, Kinetic equivalence of transmembrane pH and electrical potential differences in ATP synthesis, *Journal of Biological Chemistry* **2012**, *287*(12), 9633–9639.

[76] D. Klionsky, W. Brusilow, R. Simoni, In vivo evidence for the role of the epsilon subunit as an inhibitor of the proton-translocating ATPase of Escherichia coli, *Journal of Bacteriology* **1984**, *160*(3), 1055–1060.

[77] S. Schenck, S. M. Wojcik, N. Brose, S. Takamori, A chloride conductance in VGLUT1 underlies maximal glutamate loading into synaptic vesicles, *Nature Neuroscience* **2009**, *12*(2), 156–162.

[78] R. B. Sutton, D. Fasshauer, R. Jahn, A. T. Brunger, Crystal structure of a SNARE complex involved in synaptic exocytosis at 2.4 Å resolution, *Nature* **1998**, *395*(6700), 347–353.

[79] P. Mühlenbrock, PhD thesis, Georg-August-Universität Göttingen, **2021**.

[80] R. Hubrich, PhD thesis, Georg-August-Universität Göttingen, **2018**.

[81] J. W. Kuhlmann, PhD thesis, Georg-August-Universität Göttingen, **2017**.

[82] U. K. Laemmli, Cleavage of structural proteins during the assembly of the head of bacteriophage T4, *Nature* **1970**, *227*(5259), 680–685.

[83] H. Schägger, G. Von Jagow, Tricine-sodium dodecyl sulfate-polyacrylamide gel electrophoresis for the separation of proteins in the range from 1 to 100 kDa, *Analytical Biochemistry* **1987**, *166*(2), 368–379.

[84] H. Schägger, Tricine–sds-page, *Nature Protocols* **2006**, *1*(1), 16–22.

[85] ExPasy, Bioinformatics Recource Portal ProtParam Tool, `https://web.expasy.org/protparam/`, **accessed: Nov. 2021**.

[86] Y. Kim, S. O. Ho, N. R. Gassman, Y. Korlann, E. V. Landorf, F. R. Collart, S. Weiss, Efficient site-specific labeling of proteins via cysteines, *Bioconjugate Chemistry* **2008**, *19*(3), 786–791.

[87] D. P. Nair, M. Podgorski, S. Chatani, T. Gong, W. Xi, C. R. Fenoli, C. N. Bowman, The thiol-Michael addition click reaction: a powerful and widely used tool in materials chemistry, *Chemistry of Materials* **2014**, *26*(1), 724–744.

[88] R. J. Mrsny, J. J. Volwerk, O. H. Griffith, A simplified procedure for lipid phosphorus analysis shows that digestion rates vary with phospholipid structure, *Chemistry and Physics of Lipids* **1986**, *39*(1-2), 185–191.

[89] S. Fischer, PhD thesis, Universität Stuttgart, **1999**.

[90] I. Starke, PhD thesis, Albert-Ludwigs-Universität Freiburg, **2015**.

[91] D. Rickwood, T. Ford, J. Graham, Nycodenz: a new nonionic iodinated gradient medium, *Analytical Biochemistry* **1982**, *123*(1), 23–31.

[92] T. Fujii, PDMS-based microfluidic devices for biomedical applications, *Microelectronic Engineering* **2002**, *61*, 907–914.

[93] Y. Ai, R. Xie, J. Xiong, Q. Liang, Microfluidics for biosynthesizing: from droplets and vesicles to artificial cells, *Small* **2020**, *16*(9), 1903940.

[94] H. Witt, N. Yandrapalli, M. Sari, L. Turco, T. Robinson, C. Steinem, Precipitation of Calcium Carbonate Inside Giant Unilamellar Vesicles Composed of Fluid-Phase Lipids, *Langmuir* **2020**, *36*(44), 13244–13250.

[95] Y. Elani, Construction of membrane-bound artificial cells using microfluidics: a new frontier in bottom-up synthetic biology, *Biochemical Society Transactions* **2016**, *44*(3), 723–730.

[96] L. Mazutis, J. Gilbert, W. L. Ung, D. A. Weitz, A. D. Griffiths, J. A. Heyman, Single-cell analysis and sorting using droplet-based microfluidics, *Nature Protocols* **2013**, *8*(5), 870–891.

[97] A. Abate, A. Poitzsch, Y. Hwang, J. Lee, J. Czerwinska, D. Weitz, Impact of inlet channel geometry on microfluidic drop formation, *Physical Review E* **2009**, *80*(2), 026310.

[98] P. Garstecki, M. J. Fuerstman, H. A. Stone, G. M. Whitesides, Formation of droplets and bubbles in a microfluidic T-junction—scaling and mechanism of break-up, *Lab on a Chip* **2006**, *6*(3), 437–446.

[99] O. Wagner, J. Thiele, M. Weinhart, L. Mazutis, D. A. Weitz, W. T. Huck, R. Haag, Biocompatible fluorinated polyglycerols for droplet microfluidics as an alternative to PEG-based copolymer surfactants, *Lab on a Chip* **2016**, *16*(1), 65–69.

[100] C. J. DeJournette, J. Kim, H. Medlen, X. Li, L. J. Vincent, C. J. Easley, Creating biocompatible oil–water interfaces without synthesis: direct interactions between primary amines and carboxylated perfluorocarbon surfactants, *Analytical Chemistry* **2013**, *85*(21), 10556–10564.

[101] J.-C. Baret, Surfactants in droplet-based microfluidics, *Lab on a Chip* **2012**, *12*(3), 422–433.

[102] P. W. Atkins, J. De Paula, *Physikalische Chemie*, John Wiley & Sons, **2013**.

[103] C. Holtze, A. Rowat, J. Agresti, J. Hutchison, F. Angile, C. Schmitz, S. Köster, H. Duan, K. Humphry, R. Scanga, et al., Biocompatible surfactants for water-in-fluorocarbon emulsions, *Lab on a Chip* **2008**, *8*(10), 1632–1639.

[104] M. Karbaschi, P. Shahi, A. R. Abate, Rapid, chemical-free breaking of microfluidic emulsions with a hand-held antistatic gun, *Biomicrofluidics* **2017**, *11*(4), 044107.

[105] J. Sibold, PhD thesis, Georg-August-Universität Göttingen, **2019**.

[106] N. Teske, J. Sibold, J. Schumacher, N. K. Teiwes, M. Gleisner, I. Mey, C. Steinem, Continuous Pore-Spanning Lipid Bilayers on Silicon Oxide-Coated Porous Substrates, *Langmuir* **2017**, *33*(49), 14175–14183.

[107] L. B. McGown, K. Nithipatikom, Molecular fluorescence and phosphorescence, *Applied Spectroscopy Reviews* **2000**, *35*(4), 353–393.

[108] M. Vacher, I. Fdez. Galvan, B.-W. Ding, S. Schramm, R. Berraud-Pache, P. Naumov, N. Ferre, Y.-J. Liu, I. Navizet, D. Roca-Sanjuan, et al., Chemi- and bioluminescence of cyclic peroxides, *Chemical Reviews* **2018**, *118*(15), 6927–6974.

[109] T. Wilson, J. W. Hastings, Bioluminescence, *Annual Review of Cell and Developmental Biology* **1998**, *14*(1), 197–230.

[110] I. Navizet, Y.-J. Liu, N. Ferré, D. Roca-Sanjuán, R. Lindh, The chemistry of bioluminescence: an analysis of chemical functionalities, *ChemPhysChem* **2011**, *12*(17), 3064–3076.

[111] T. A. Hopkins, H. H. Seliger, E. H. White, M. W. Cass, Chemiluminescence of firefly luciferin. Model for the bioluminescent reaction and identification of the product excited state, *Journal of the American Chemical Society* **1967**, *89*(26), 7148–7150.

[112] A. Lundin, A. Thore, Analytical information obtainable by evaluation of the time course of firefly bioluminescence in the assay of ATP, *Analytical Biochemistry* **1975**, *66*(1), 47–63.

[113] A. Lundin, B. Jäderlund, T. Lövgren, Optimized bioluminescence assay of creatine kinase and creatine kinase B-subunit activity., *Clinical Chemistry* **1982**, *28*(4), 609–614.

[114] Roche, ATP Bioluminescence Assay Kit CLS II, `https://www.sigmaaldrich.com/deepweb/assets/sigmaaldrich/product/documents/118/678/11699695001bul.pdf`, **accessed: Nov. 2021**.

[115] N. Soga, K. Kinosita Jr, M. Yoshida, T. Suzuki, Efficient ATP synthesis by thermophilic Bacillus FoF1-ATP synthase, *The FEBS journal* **2011**, *278*(15), 2647–2654.

[116] J. R. Lakowicz, in *Principles of Fluorescence Spectroscopy*, Springer, **1999**, 1–23.

[117] J. J. Hurley, Q. J. Meisner, C. Huang, L. Zhu, Hydroxyaromatic Fluorophores, *ACS Omega* **2021**, *6*(5), 3447–3462.

[118] Y. Avnir, Y. Barenholz, pH determination by pyranine: medium-related artifacts and their correction, *Analytical Biochemistry* **2005**, *347*(1), 34–41.

[119] M. Schwamborn, J. Schumacher, J. Sibold, N. K. Teiwes, C. Steinem, Monitoring ATPase induced pH changes in single proteoliposomes with the lipid-coupled fluorophore Oregon Green 488, *Analyst* **2017**, *142*(14), 2670–2677.

[120] J.-A. Conchello, J. W. Lichtman, Optical sectioning microscopy, *Nature Methods* **2005**, *2*(12), 920–931.

[121] J. Piehler, A. Brecht, R. Valiokas, B. Liedberg, G. Gauglitz, A high-density poly (ethylene glycol) polymer brush for immobilization on glass-type surfaces, *Biosensors and Bioelectronics* **2000**, *15*(9-10), 473–481.

[122] P. Jönsson, M. P. Jonsson, J. O. Tegenfeldt, F. Höök, A method improving the accuracy of fluorescence recovery after photobleaching analysis, *Biophysical Journal* **2008**, *95*(11), 5334–5348.

[123] N. Lorén, J. Hagman, J. K. Jonasson, H. Deschout, D. Bernin, F. Cella-Zanacchi, A. Diaspro, J. G. McNally, M. Ameloot, N. Smisdom, et al., Fluorescence recovery after photobleaching in material and life sciences: putting theory into practice, *Quarterly Reviews of Biophysics* **2015**, *48*(3), 323–387.

[124] D. Axelrod, D. Koppel, J. Schlessinger, E. Elson, W. W. Webb, Mobility measurement by analysis of fluorescence photobleaching recovery kinetics, *Biophysical Journal* **1976**, *16*(9), 1055–1069.

[125] D. Soumpasis, Theoretical analysis of fluorescence photobleaching recovery experiments, *Biophysical Journal* **1983**, *41*(1), 95–97.

[126] M. Kang, C. A. Day, A. K. Kenworthy, E. DiBenedetto, Simplified equation to extract diffusion coefficients from confocal FRAP data, *Traffic* **2012**, *13*(12), 1589–1600.

[127] L. Danos, R. Greef, T. Markvart, Efficient fluorescence quenching near crystalline silicon from Langmuir–Blodgett dye films, *Thin Solid Films* **2008**, *516*(20), 7251–7255.

[128] K. Vasilev, W. Knoll, M. Kreiter, Fluorescence intensities of chromophores in front of a thin metal film, *The Journal of Chemical Physics* **2004**, *120*(7), 3439–3445.

[129] Y. S. Chi, H. R. Byon, B. S. Lee, B. Kong, H. C. Choi, I. S. Choi, Polymeric Rulers: Distance-Dependent Emission Behaviors of Fluorophores on Flat Gold Surfaces and Bioassay Platforms Using Plasmonic Fluorescence Enhancement, *Advanced Functional Materials* **2008**, *18*(21), 3395–3402.

[130] G. Schneider, G. Decher, N. Nerambourg, R. Praho, M. H. Werts, M. Blanchard-Desce, Distance-dependent fluorescence quenching on gold nanoparticles ensheathed with layer-by-layer assembled polyelectrolytes, *Nano Letters* **2006**, *6*(3), 530–536.

[131] R. Macháň, M. Hof, Lipid diffusion in planar membranes investigated by fluorescence correlation spectroscopy, *Biochimica et Biophysica Acta (BBA)-Biomembranes* **2010**, *1798*(7), 1377–1391.

[132] S. Rüttinger, PhD thesis, Technical University Berlin, **2007**.

[133] B. Zhang, J. Zerubia, J.-C. Olivo-Marin, Gaussian approximations of fluorescence microscope point-spread function models, *Applied Optics* **2007**, *46*(10), 1819–1829.

[134] R. Rigler, Ü. Mets, J. Widengren, P. Kask, Fluorescence correlation spectroscopy with high count rate and low background: analysis of translational diffusion, *European Biophysics Journal* **1993**, *22*(3), 169–175.

[135] T. Wohland, R. Rigler, H. Vogel, The standard deviation in fluorescence correlation spectroscopy, *Biophysical Journal* **2001**, *80*(6), 2987–2999.

[136] J. Enderlein, I. Gregor, D. Patra, J. Fitter, Art and artefacts of fluorescence correlation spectroscopy, *Current Pharmaceutical Biotechnology* **2004**, *5*(2), 155–161.

[137] A. Benda, M. Beneš, V. Marecek, A. Lhotskỳ, W. T. Hermens, M. Hof, How to determine diffusion coefficients in planar phospholipid systems by confocal fluorescence correlation spectroscopy, *Langmuir* **2003**, *19*(10), 4120–4126.

[138] E. Gielen, A. Margineanu, P. Dedecker, M. Van der Auweraer, Y. Engelborghs, J. Hofkens, M. Ameloot, et al., On the use of Z-scan fluorescence correlation experiments on giant unilamellar vesicles, *Chemical Physics Letters* **2009**, *469*(1-3), 110–114.

[139] H.-J. Butt, B. Cappella, M. Kappl, Force measurements with the atomic force microscope: Technique, interpretation and applications, *Surface Science Reports* **2005**, *59*(1-6), 1–152.

[140] T. Ando, T. Uchihashi, S. Scheuring, Filming biomolecular processes by high-speed atomic force microscopy, *Chemical Reviews* **2014**, *114*(6), 3120–3188.

[141] I. P. Mey, PhD thesis, Johannes Gutenberg-Universität Mainz, **2009**.

[142] J. E. Sader, J. W. Chon, P. Mulvaney, Calibration of rectangular atomic force microscope cantilevers, *Review of Scientific Instruments* **1999**, *70*(10), 3967–3969.

[143] M. Gleisner, PhD thesis, Georg-August-Universität Göttingen, **2016**.

[144] S. Nehls, A. Janshoff, Elastic properties of pore-spanning apical cell membranes derived from MDCK II cells, *Biophysical Journal* **2017**, *113*(8), 1822–1830.

[145] A. Janshoff, Viscoelasticity of basal plasma membranes and cortices derived from MDCK II cells, *bioRxiv* **2021**.

[146] L. Chopinet, C. Formosa, M. Rols, R. Duval, E. Dague, Imaging living cells surface and quantifying its properties at high resolution using AFM in QI™ mode, *Micron* **2013**, *48*, 26–33.

[147] JPK-instruments, QI mode - Quantitative Imaging with the NanoWizard 3 AFM, `https://www.jpk.com/app-technotes-img/AFM/pdf/jpk-tech-quantitative-imaging.14-1.pdf`, **accessed: Dec. 2021**.

[148] R. Seemann, M. Brinkmann, T. Pfohl, S. Herminghaus, Droplet based microfluidics, *Reports on Progress in Physics* **2011**, *75*(1), 016601.

[149] A. B. Theberge, F. Courtois, Y. Schaerli, M. Fischlechner, C. Abell, F. Hollfelder, W. T. Huck, Microdroplets in microfluidics: an evolving platform for discoveries in chemistry and biology, *Angewandte Chemie International Edition* **2010**, *49*(34), 5846–5868.

[150] S. Vyawahare, A. D. Griffiths, C. A. Merten, Miniaturization and parallelization of biological and chemical assays in microfluidic devices, *Chemistry & Biology* **2010**, *17*(10), 1052–1065.

[151] N. Wu, J. Oakeshott, S. Brown, C. Easton, Y. Zhu, Microfluidic droplet technique for in vitro directed evolution, *Australian Journal of Chemistry* **2010**, *63*(9), 1313–1325.

[152] X. Wang, J. Liu, P. Wang, A. DeMello, L. Feng, X. Zhu, W. Wen, R. Kodzius, X. Gong, Synthesis of biomaterials utilizing microfluidic technology, *Genes* **2018**, *9*(6), 283.

[153] J. E. Kreutz, A. Shukhaev, W. Du, S. Druskin, O. Daugulis, R. F. Ismagilov, Evolution of catalysts directed by genetic algorithms in a plug-based microfluidic device tested with oxidation of methane by oxygen, *Journal of the American Chemical Society* **2010**, *132*(9), 3128–3132.

[154] J.-C. Baret, O. J. Miller, V. Taly, M. Ryckelynck, A. El-Harrak, L. Frenz, C. Rick, M. L. Samuels, J. B. Hutchison, J. J. Agresti, et al., Fluorescence-activated droplet sorting (FADS): efficient microfluidic cell sorting based on enzymatic activity, *Lab on a Chip* **2009**, *9*(13), 1850–1858.

[155] Y. Schaerli, F. Hollfelder, The potential of microfluidic water-in-oil droplets in experimental biology, *Molecular Biosystems* **2009**, *5*(12), 1392–1404.

[156] B. Haller, K. Jahnke, M. Weiss, K. Göpfrich, I. Platzman, J. P. Spatz, Autonomous Directional Motion of Actin-Containing Cell-Sized Droplets, *Advanced Intelligent Systems* **2021**, *3*(5), 2000190.

[157] J. M. Russell, Sodium-potassium-chloride cotransport, *Physiological Reviews* **2000**, *80*(1), 211–276.

[158] W. Jahnen-Dechent, M. Ketteler, Magnesium basics, *Clinical Kidney Journal* **2012**, *5*(Suppl 1), i3–i14.

[159] W. Breckenridge, I. Morgan, J. Zanetta, G. Vincendon, Adult rat brain synaptic vesicles II. Lipid composition, *Biochimica et Biophysica Acta (BBA)-General Subjects* **1973**, *320*(3), 681–686.

[160] D. Weiskopf, PhD thesis, Georg-August-Universität Göttingen, **2010**.

[161] V. Yamazaki, O. Sirenko, R. J. Schafer, J. T. Groves, Lipid mobility and molecular binding in fluid lipid membranes, *Journal of the American Chemical Society* **2005**, *127*(9), 2826–2827.

[162] D. Thid, M. Bally, K. Holm, S. Chessari, S. Tosatti, M. Textor, J. Gold, Issues of ligand accessibility and mobility in initial cell attachment, *Langmuir* **2007**, *23*(23), 11693–11704.

[163] M. J. Akhunzada, F. D'Autilia, B. Chandramouli, N. Bhattacharjee, A. Catte, R. Di Rienzo, F. Cardarelli, G. Brancato, Interplay between lipid lateral diffusion, dye concentration and membrane permeability unveiled by a combined

spectroscopic and computational study of a model lipid bilayer, *Scientific Reports* **2019**, *9*(1), 1–12.

[164] M. Rose, N. Hirmiz, J. M. Moran-Mirabal, C. Fradin, Lipid diffusion in supported lipid bilayers: a comparison between line-scanning fluorescence correlation spectroscopy and single-particle tracking, *Membranes* **2015**, *5*(4), 702–721.

[165] M. Louveaux, O. Hamant, The mechanics behind cell division, *Current Opinion in Plant Biology* **2013**, *16*(6), 774–779.

[166] J. Schmitz, K.-E. Gottschalk, Mechanical regulation of cell adhesion, *Soft Matter* **2008**, *4*(7), 1373–1387.

[167] G. Apodaca, Modulation of membrane traffic by mechanical stimuli, *American Journal of Physiology-Renal Physiology* **2002**, *282*(2), F179–F190.

[168] A. Geitmann, J. K. Ortega, Mechanics and modeling of plant cell growth, *Trends in Plant Science* **2009**, *14*(9), 467–478.

[169] I. Mey, M. Stephan, E. K. Schmitt, M. M. Mueller, M. Ben Amar, C. Steinem, A. Janshoff, Local membrane mechanics of pore-spanning bilayers, *Journal of the American Chemical Society* **2009**, *131*(20), 7031–7039.

[170] M. Kocun, A. Janshoff, Pulling Tethers from Pore-Spanning Bilayers: Towards Simultaneous Determination of Local Bending Modulus and Lateral Tension of Membranes, *Small* **2012**, *8*(6), 847–851.

[171] H. Brockman, Lipid monolayers: why use half a membrane to characterize protein-membrane interactions?, *Current Opinion in Structural Biology* **1999**, *9*(4), 438–443.

[172] V. Kiessling, M. K. Domanska, D. Murray, C. Wan, L. K. Tamm, Supported lipid bilayers, *Wiley Encyclopedia of Chemical Biology* **2007**, 1–12.

[173] B. A. Patel, T. L. D'Amico, B. S. Blagg, Natural products and other inhibitors of F1FO ATP synthase, *European Journal of Medicinal Chemistry* **2020**, 112779.

[174] A. M. Seddon, P. Curnow, P. J. Booth, Membrane proteins, lipids and detergents: not just a soap opera, *Biochimica et Biophysica Acta (BBA)-Biomembranes* **2004**, *1666* (1-2), 105–117.

[175] M. Tutus, F. F. Rossetti, E. Schneck, G. Fragneto, F. Förster, R. Richter, T. Nawroth, M. Tanaka, Orientation-Selective Incorporation of Transmembrane F0F1 ATP Synthase Complex from Micrococcus luteus in Polymer-Supported Membranes, *Macromolecular Bioscience* **2008**, *8* (11), 1034–1043.

[176] L. Janosi, A. A. Gorfe, Simulating POPC and POPC/POPG bilayers: conserved packing and altered surface reactivity, *Journal of Chemical Theory and Computation* **2010**, *6* (10), 3267–3273.

[177] CharmmGui, Membrane Builder, `https://charmm-gui.org/`, **accessed: Jan. 2022**.

[178] S. Fischer, P. Gräber, Comparison of ΔpH-and $\Delta \varphi$-driven ATP synthesis catalyzed by the H+-ATPases from Escherichia coli or chloroplasts reconstituted into liposomes, *FEBS letters* **1999**, *457* (3), 327–332.

[179] J. Han, K. Burgess, Fluorescent indicators for intracellular pH, *Chemical Reviews* **2010**, *110* (5), 2709–2728.

[180] J. Rosing, E. Slater, The value of ΔG for the hydrolysis of ATP, *Biochimica et Biophysica Acta (BBA)-Bioenergetics* **1972**, *267* (2), 275–290.

[181] C. Hunte, S. Richers, Lipids and membrane protein structures, *Current Opinion in Structural Biology* **2008**, *18* (4), 406–411.

[182] I. Arechaga, P. C. Jones, The rotor in the membrane of the ATP synthase and relatives, *FEBS letters* **2001**, *494* (1-2), 1–5.

[183] R. Tunuguntla, M. Bangar, K. Kim, P. Stroeve, C. M. Ajo-Franklin, A. Noy, Lipid bilayer composition can influence the orientation of proteorhodopsin in artificial membranes, *Biophysical Journal* **2013**, *105* (6), 1388–1396.

[184] S. Clejan, T. Krulwich, K. Mondrus, D. Seto-Young, Membrane lipid composition of obligately and facultatively alkalophilic strains of Bacillus spp, *Journal of Bacteriology* **1986**, *168* (1), 334–340.

[185] K. Poralla, E. Kannenberg, A. Blume, A glycolipid containing hopane isolated from the acidophilic, thermophilic bacillus acidocaldarius, has a cholesterol-like function in membranes, *FEBS letters* **1980**, *113*(1), 107–110.

[186] B. Pitard, P. Richard, M. Duñarach, G. Girault, J.-L. Rigaiud, ATP synthesis by the F0F1 ATP synthase from thermophilic Bacillus PS3 reconstituted into liposomes with bacteriorhodopsin: 1. Factors defining the optimal reconstitution of ATP synthases with bacteriorhodopsin, *European Journal of Biochemistry* **1996**, *235*(3), 769–778.

[187] D. van Swaay, A. DeMello, Microfluidic methods for forming liposomes, *Lab on a Chip* **2013**, *13*(5), 752–767.

[188] H. Guo, T. Suzuki, J. L. Rubinstein, Structure of a bacterial ATP synthase, *Elife* **2019**, *8*, e43128.

[189] K. Goepfrich, B. Haller, O. Staufer, Y. Dreher, U. Mersdorf, I. Platzman, J. P. Spatz, One-pot assembly of complex giant unilamellar vesicle-based synthetic cells, *ACS Synthetic Biology* **2019**, *8*(5), 937–947.

[190] J.-C. Baret, F. Kleinschmidt, A. El Harrak, A. D. Griffiths, Kinetic aspects of emulsion stabilization by surfactants: a microfluidic analysis, *Langmuir* **2009**, *25*(11), 6088–6093.

[191] J. Wang, E. Kang, U. Sultan, B. Merle, A. Inayat, B. Graczykowski, G. Fytas, N. Vogel, Influence of Surfactant-Mediated Interparticle Contacts on the Mechanical Stability of Supraparticles, *The Journal of Physical Chemistry C* **2021**, *125*(42), 23445–23456.

[192] R. P. Richter, R. Bérat, A. R. Brisson, Formation of solid-supported lipid bilayers: an integrated view, *Langmuir* **2006**, *22*(8), 3497–3505.

[193] R. Richter, A. Mukhopadhyay, A. Brisson, Pathways of lipid vesicle deposition on solid surfaces: a combined QCM-D and AFM study, *Biophysical Journal* **2003**, *85*(5), 3035–3047.

[194] P. Nollert, H. Kiefer, F. Jähnig, Lipid vesicle adsorption versus formation of planar bilayers on solid surfaces, *Biophysical Journal* **1995**, *69*(4), 1447–1455.

[195] Z. D. Schultz, I. M. Pazos, F. K. McNeil-Watson, E. N. Lewis, I. W. Levin, Magnesium-induced lipid bilayer microdomain reorganizations: implications for membrane fusion, *The journal of physical chemistry B* **2009**, *113*(29), 9932–9941.

[196] S. Ohki, H. Ohshima, Interaction and aggregation of lipid vesicles (DLVO theory versus modified DLVO theory), *Colloids and Surfaces B: Biointerfaces* **1999**, *14*(1-4), 27–45.

[197] G. Löffler, P. E. Petrides, *Biochemie und Pathobiochemie*, Springer-Verlag, **2019**.

[198] A. Taylor, A. Frazier, E. Gurney, J. Smith, Solubility products of di-and tri-magnesium phosphates and the dissociation of magnesium phosphate solutions, *Transactions of the Faraday Society* **1963**, *59*, 1585–1589.

[199] A. Kondoh, T. Oi, Interaction of alkaline earth metal ions with carboxylic acids in aqueous solutions studied by 13C NMR spectroscopy, *Zeitschrift für Naturforschung A* **1998**, *53*(1-2), 77–91.

[200] N. Düzgünes, J. Wilschut, R. Fraley, D. Papahadjopoulos, Studies on the mechanism of membrane fusion. Role of head-group composition in calcium-and magnesium-induced fusion of mixed phospholipid vesicles, *Biochimica et Biophysica Acta (BBA)-Biomembranes* **1981**, *642*(1), 182–195.

[201] H. Nöding, M. Schön, C. Reinermann, N. Dörrer, A. Kürschner, B. Geil, I. Mey, C. Heussinger, A. Janshoff, C. Steinem, Rheology of membrane-attached minimal actin cortices, *The Journal of Physical Chemistry B* **2018**, *122*(16), 4537–4545.

[202] L. Guo, J. Y. Har, J. Sankaran, Y. Hong, B. Kannan, T. Wohland, Molecular diffusion measurement in lipid bilayers over wide concentration ranges: a comparative study, *ChemPhysChem* **2008**, *9*(5), 721–728.

[203] R. A. Böckmann, A. Hac, T. Heimburg, H. Grubmüller, Effect of sodium chloride on a lipid bilayer, *Biophysical Journal* **2003**, *85*(3), 1647–1655.

[204] N. Kahya, P. Schwille, How phospholipid-cholesterol interactions modulate lipid lateral diffusion, as revealed by fluorescence correlation spectroscopy, *Journal of Fluorescence* **2006**, *16*(5), 671–678.

[205] S. Ladha, A. Mackie, L. Harvey, D. Clark, E. Lea, M. Brullemans, H. Duclohier, Lateral diffusion in planar lipid bilayers: a fluorescence recovery after photobleaching investigation of its modulation by lipid composition, cholesterol, or alamethicin content and divalent cations, *Biophysical Journal* **1996**, *71*(3), 1364–1373.

[206] F. Schneider, D. Waithe, M. P. Clausen, S. Galiani, T. Koller, G. Ozhan, C. Eggeling, E. Sezgin, Diffusion of lipids and GPI-anchored proteins in actin-free plasma membrane vesicles measured by STED-FCS, *Molecular Biology of the Cell* **2017**, *28*(11), 1507–1518.

[207] S. Ramadurai, A. Holt, V. Krasnikov, G. van den Bogaart, J. A. Killian, B. Poolman, Lateral diffusion of membrane proteins, *Journal of the American Chemical Society* **2009**, *131*(35), 12650–12656.

[208] N. Kahya, D. Scherfeld, K. Bacia, B. Poolman, P. Schwille, Probing lipid mobility of raft-exhibiting model membranes by fluorescence correlation spectroscopy, *Journal of Biological Chemistry* **2003**, *278*(30), 28109–28115.

[209] F. Heinemann, V. Betaneli, F. A. Thomas, P. Schwille, Quantifying lipid diffusion by fluorescence correlation spectroscopy: a critical treatise, *Langmuir* **2012**, *28*(37), 13395–13404.

[210] L. L. Schwenen, R. Hubrich, D. Milovanovic, B. Geil, J. Yang, A. Kros, R. Jahn, C. Steinem, Resolving single membrane fusion events on planar pore-spanning membranes, *Scientific Reports* **2015**, *5*(1), 1–15.

[211] W. L. Vaz, R. M. Clegg, D. Hallmann, Translational diffusion of lipids in liquid crystalline phase phosphatidylcholine multibilayers. A comparison of experiment with theory, *Biochemistry* **1985**, *24*(3), 781–786.

[212] S. Ollila, M. T. Hyvönen, I. Vattulainen, Polyunsaturation in lipid membranes: dynamic properties and lateral pressure profiles, *The Journal of Physical Chemistry B* **2007**, *111*(12), 3139–3150.

[213] D. Weiskopf, E. K. Schmitt, M. H. Klühr, S. K. Dertinger, C. Steinem, Micro-BLMs on highly ordered porous silicon substrates: rupture process and lateral mobility, *Langmuir* **2007**, *23*(18), 9134–9139.

[214] L. M. Solanko, A. Honigmann, H. S. Midtiby, F. W. Lund, J. R. Brewer, V. Dekaris, R. Bittman, C. Eggeling, D. Wüstner, Membrane orientation and lateral diffusion of BODIPY-cholesterol as a function of probe structure, *Biophysical Journal* **2013**, *105*(9), 2082–2092.

[215] A. Honigmann, V. Mueller, S. W. Hell, C. Eggeling, STED microscopy detects and quantifies liquid phase separation in lipid membranes using a new far-red emitting fluorescent phosphoglycerolipid analogue, *Faraday Discussions* **2013**, *161*(0), 77–89.

[216] N. Teske, PhD thesis, Georg-August-Universität Göttingen, **2020**.

[217] T. Dertinger, I. von der Hocht, A. Benda, M. Hof, J. Enderlein, Surface sticking and lateral diffusion of lipids in supported bilayers, *Langmuir* **2006**, *22*(22), 9339–9344.

[218] M. E. Bowen, K. Weninger, A. T. Brunger, S. Chu, Single molecule observation of liposome-bilayer fusion thermally induced by soluble N-ethyl maleimide sensitive-factor attachment protein receptors (SNAREs), *Biophysical Journal* **2004**, *87*(5), 3569–3584.

[219] N. K. Teiwes, I. Mey, P. C. Baumann, L. Strieker, U. Unkelbach, C. Steinem, Pore-Spanning Plasma Membranes Derived from Giant Plasma Membrane Vesicles, *ACS Applied Materials & Interfaces* **2021**, *13*(22), 25805–25812.

[220] I. Levental, F. J. Byfield, P. Chowdhury, F. Gai, T. Baumgart, P. A. Janmey, Cholesterol-dependent phase separation in cell-derived giant plasma-membrane vesicles, *Biochemical Journal* **2009**, *424*(2), 163–167.

[221] M. P. Sheetz, Cell control by membrane–cytoskeleton adhesion, *Nature Reviews Molecular Cell Biology* **2001**, *2*(5), 392–396.

[222] J. Dai, M. P. Sheetz, Membrane tether formation from blebbing cells, *Biophysical Journal* **1999**, *77*(6), 3363–3370.

[223] R. Lipowsky, E. Sackmann, *Structure and Dynamics of Membranes-from Cells to Vesicles (Handbook of Biological Physics Vol 1)*, Elsevier, **1995**.

[224] M. Kim, F. Heinrich, G. Haugstad, G. Yu, G. Yuan, S. K. Satija, W. Zhang, H. S. Seo, J. M. Metzger, S. M. Azarin, et al., Spatial Distribution of PEO–PPO–PEO Block Copolymer and PEO Homopolymer in Lipid Bilayers, *Langmuir* **2020**, *36*(13), 3393–3403.

[225] W. Zhang, K. J. Haman, J. M. Metzger, B. J. Hackel, F. S. Bates, T. P. Lodge, Quantifying binding of ethylene oxide–propylene oxide block copolymers with lipid bilayers, *Langmuir* **2017**, *33*(44), 12624–12634.

[226] K. Flandez, S. Bonardd, M. Soto-Arriaza, Physicochemical properties of L-alpha dipalmitoyl phosphatidylcholine large unilamellar vesicles: Effect of hydrophobic block (PLA/PCL) of amphipathic diblock copolymers, *Chemistry and Physics of Lipids* **2020**, *230*, 104927.

[227] S. Hezaveh, S. Samanta, A. De Nicola, G. Milano, D. Roccatano, Understanding the interaction of block copolymers with DMPC lipid bilayer using coarse-grained molecular dynamics simulations, *The Journal of Physical Chemistry B* **2012**, *116*(49), 14333–14345.

[228] J. Wang, L. Segatori, S. L. Biswal, Probing the association of triblock copolymers with supported lipid membranes using microcantilevers, *Soft Matter* **2014**, *10*(34), 6417–6424.

[229] M. A. Firestone, A. C. Wolf, S. Seifert, Small-angle X-ray scattering study of the interaction of poly (ethylene oxide)-b-poly (propylene oxide)-b-poly (ethylene oxide) triblock copolymers with lipid bilayers, *Biomacromolecules* **2003**, *4*(6), 1539–1549.

[230] J.-Y. Wang, J. Chin, J. D. Marks, K. Y. C. Lee, Effects of PEO- PPO- PEO triblock copolymers on phospholipid membrane integrity under osmotic stress, *Langmuir* **2010**, *26*(15), 12953–12961.

[231] A. M. Zaki, P. Carbone, How the incorporation of Pluronic block copolymers modulates the response of lipid membranes to mechanical stress, *Langmuir* **2017**, *33*(46), 13284–13294.

[232] C. Maatouk, M. Ling, I. Titushkin, M. Cho, C. A. McFaul, R. C. Lee, Amphiphilic Block Copolymer-Catalyzed Cell Membrane Sealing Is Linked to

Decreased Membrane Tension, *Regenerative Engineering and Translational Medicine* **2021**, 1–11.

[233] W. Zhang, J. M. Metzger, B. J. Hackel, F. S. Bates, T. P. Lodge, Influence of the Headgroup on the Interaction of Poly (ethylene oxide)-Poly (propylene oxide) Block Copolymers with Lipid Bilayers, *The Journal of Physical Chemistry B* **2020**, *124*(12), 2417–2424.

[234] W. Zhang, M. L. Coughlin, J. M. Metzger, B. J. Hackel, F. S. Bates, T. P. Lodge, Influence of Cholesterol and Bilayer Curvature on the Interaction of PPO–PEO Block Copolymers with Liposomes, *Langmuir* **2019**, *35*(22), 7231–7241.

[235] J. W. Kuhlmann, I. P. Mey, C. Steinem, Modulating the lateral tension of solvent-free pore-spanning membranes, *Langmuir* **2014**, *30*(27), 8186–8192.

[236] N. Sone, M. Yoshida, H. Hirata, Y. Kagawa, Adenosine triphosphate synthesis by electrochemical proton gradient in vesicles reconstituted from purified adenosine triphosphatase and phospholipids of thermophilic bacterium., *Journal of Biological Chemistry* **1977**, *252*(9), 2956–2960.

[237] A. Alonso, A. Villena, F. Goñi, Lysis and reassembly of sonicated lecithin vesicles in the presence of Triton X-100, *FEBS letters* **1981**, *123*(2), 200–204.

[238] M.-A. Urbaneja, F. M. Goñi, A. Alonso, Structural changes induced by Triton X-100 on sonicated phosphatidylcholine liposomes, *European Journal of Biochemistry* **1988**, *173*(3), 585–588.

[239] N. Maru, K.-i. Shohda, T. Sugawara, Successive fusion of vesicles aggregated by DNA duplex formation in the presence of triton X-100, *Chemistry Letters* **2008**, *37*(3), 340–341.

[240] J. Lasch, J. Hoffman, W. Omelyanenko, A. Klibanov, V. Torchilin, H. Binder, K. Gawrisch, Interaction of Triton X-100 and octyl glucoside with liposomal membranes at sublytic and lytic concentrations. Spectroscopic studies, *Biochimica et Biophysica Acta (BBA)-Biomembranes* **1990**, *1022*(2), 171–180.

[241] S. Fischer, C. Etzold, P. Turina, G. Deckers-Hebestreit, K. Altendorf, P. Gräber, ATP synthesis catalyzed by the ATP synthase of Escherichia coli reconstituted into liposomes, *European Journal of Biochemistry* **1994**, *225*(1), 167–172.

[242] A. T. Jagendorf, E. Uribe, ATP formation caused by acid-base transition of spinach chloroplasts., *Proceedings of the National Academy of Sciences* **1966**, *55*(1), 170.

[243] D. M. Wilson, J. Alderette, P. C. Maloney, T. H. Wilson, Protonmotive force as the source of energy for adenosine 5'-triphosphate synthesis in Escherichia coli, *Journal of Bacteriology* **1976**, *126*(1), 327–337.

[244] P. C. Maloney, T. H. Wilson, ATP synthesis driven by a protonmotive force inStreptococcus lactis, *The Journal of Membrane Biology* **1975**, *25*(1), 285–310.

[245] M. Yoshida, N. Sone, H. Hirata, Y. Kagawa, ATP synthesis catalyzed by purified DCCD-sensitive ATPase incorporated into reconstituted purple membrane vesicles, *Biochemical and Biophysical Research Communications* **1975**, *67*(4), 1295–1300.

[246] P. Richard, B. Pitard, J.-L. Rigaud, ATP Synthesis by the F0F1-ATPase from the Thermophilic Bacillus PS3 Co-reconstituted with Bacteriorhodopsin into Liposomes: evidence for stimulation of ATP synthesis by ATP bound to a noncatalytic binding site, *Journal of Biological Chemistry* **1995**, *270*(37), 21571–21578.

[247] C. Etzold, G. Deckers-Hebestreit, K. Altendorf, Turnover number of Escherichia coli F0F1 ATP synthase for ATP synthesis in membrane vesicles, *European Journal of Biochemistry* **1997**, *243*(1-2), 336–343.

[248] K. Förster, P. Turina, F. Drepper, W. Haehnel, S. Fischer, P. Gräber, J. Petersen, Proton transport coupled ATP synthesis by the purified yeast H+-ATP synthase in proteoliposomes, *Biochimica et Biophysica Acta (BBA)-Bioenergetics* **2010**, *1797*(11), 1828–1837.

[249] I. Grotjohann, P. Gräber, The H+-ATPase from chloroplasts: effect of different reconstitution procedures on ATP synthesis activity and on phosphate dependence of ATP synthesis, *Biochimica et Biophysica Acta (BBA)-Bioenergetics* **2002**, *1556*(2-3), 208–216.

[250] G. M. Cook, S. Keis, H. W. Morgan, C. von Ballmoos, U. Matthey, G. Kaim, P. Dimroth, Purification and biochemical characterization of the F1Fo-ATP

synthase from thermoalkaliphilic Bacillus sp. strain TA2. A1, *Journal of Bacteriology* **2003**, *185*(15), 4442–4449.

[251] M. Rossignol, P. Thomas, C. Grignon, Proton permeability of liposomes from natural phospholipid mixtures, *Biochimica et Biophysica Acta (BBA)-Biomembranes* **1982**, *684*(2), 195–199.

[252] Y. Georgievskii, E. S. Medvedev, A. A. Stuchebrukhov, Proton transport via the membrane surface, *Biophysical Journal* **2002**, *82*(6), 2833–2846.

[253] S. Serowy, S. M. Saparov, Y. N. Antonenko, W. Kozlovsky, V. Hagen, P. Pohl, Structural proton diffusion along lipid bilayers, *Biophysical Journal* **2003**, *84*(2), 1031–1037.

[254] G. Szabo, Dual mechanism for the action of cholesterol on membrane permeability, *Nature* **1974**, *252*(5478), 47–49.

[255] P. Yeagle, Modulation of membrane function by cholesterol, *Biochimie* **1991**, *73*(10), 1303–1310.

[256] K. R. Daghastanli, R. B. Ferreira, G. Thedei Jr, B. Maggio, P. Ciancaglini, Lipid composition-dependent incorporation of multiple membrane proteins into liposomes, *Colloids and Surfaces B: Biointerfaces* **2004**, *36*(3-4), 127–137.

[257] N. R. Clement, J. M. Gould, Pyranine (8-hydroxy-1, 3, 6-pyrenetrisulfonate) as a probe of internal aqueous hydrogen ion concentration in phospholipid vesicles, *Biochemistry* **1981**, *20*(6), 1534–1538.

[258] N. Yandrapalli, T. Robinson, Ultra-high capacity microfluidic trapping of giant vesicles for high-throughput membrane studies, *Lab on a Chip* **2019**, *19*(4), 626–633.

[259] H. L. Tepper, G. A. Voth, Protons may leak through pure lipid bilayers via a concerted mechanism, *Biophysical journal* **2005**, *88*(5), 3095–3108.

[260] D. W. Deamer, Proton permeation of lipid bilayers, *Journal of Bioenergetics and Biomembranes* **1987**, *19*(5), 457–479.

[261] D. W. Deamer, J. Bramhall, Permeability of lipid bilayers to water and ionic solutes, *Chemistry and Physics of Lipids* **1986**, *40*(2-4), 167–188.

[262] S. Paula, A. Volkov, A. Van Hoek, T. Haines, D. W. Deamer, Permeation of protons, potassium ions, and small polar molecules through phospholipid bilayers as a function of membrane thickness, *Biophysical Journal* **1996**, *70*(1), 339–348.

[263] J. De Gier, J. Mandersloot, L. Van Deenen, Lipid composition and permeability of liposomes, *Biochimica et Biophysica Acta (BBA)-Biomembranes* **1968**, *150*(4), 666–675.

[264] W. F. Paxton, P. T. McAninch, K. E. Achyuthan, S. H. R. Shin, H. L. Monteith, Monitoring and modulating ion traffic in hybrid lipid/polymer vesicles, *Colloids and Surfaces B: Biointerfaces* **2017**, *159*, 268–276.

[265] C. L. Kuyper, J. S. Kuo, S. A. Mutch, D. T. Chiu, Proton permeation into single vesicles occurs via a sequential two-step mechanism and is heterogeneous, *Journal of the American Chemical Society* **2006**, *128*(10), 3233–3240.

[266] G. Kaim, P. Dimroth, ATP synthesis by F-type ATP synthase is obligatorily dependent on the transmembrane voltage, *The EMBO Journal* **1999**, *18*(15), 4118–4127.

[267] C. L. Andrew, A. R. Klemm, J. B. Lloyd, Lysosome membrane permeability to amines, *Biochimica et Biophysica Acta (BBA)-Biomembranes* **1997**, *1330*(1), 71–82.

[268] S. S. Mansy, Membrane transport in primitive cells, *Cold Spring Harbor Perspectives In Biology* **2010**, *2*(8), a002188.

[269] S. A. Kirsch, R. A. Böckmann, Membrane pore formation in atomistic and coarse-grained simulations, *Biochimica et Biophysica Acta (BBA)-Biomembranes* **2016**, *1858*(10), 2266–2277.

[270] T. H. Haines, Do sterols reduce proton and sodium leaks through lipid bilayers?, *Progress in Lipid Research* **2001**, *40*(4), 299–324.

[271] J. Bangham, E. Lea, The interaction of detergents with bilayer lipid membranes, *Biochimica et Biophysica Acta (BBA)-Biomembranes* **1978**, *511*(3), 388–396.

[272] P. Richard, J.-L. RIGAUD, P. Gräber, Reconstitution of CF0F1 into liposomes using a new reconstitution procedure, *European Journal of Biochemistry* **1990**, *193*(3), 921–925.

[273] K.-i. Akashi, H. Miyata, H. Itoh, K. Kinosita Jr, Preparation of giant liposomes in physiological conditions and their characterization under an optical microscope, *Biophysical Journal* **1996**, *71*(6), 3242–3250.

[274] M. Angelova, D. S. Dimitrov, A mechanism of liposome electroformation, *Trends in Colloid and Interface Science II* **1988**, 59–67.

[275] S. Okushima, T. Nisisako, T. Torii, T. Higuchi, Controlled production of monodisperse double emulsions by two-step droplet breakup in microfluidic devices, *Langmuir* **2004**, *20*(23), 9905–9908.

[276] R. R. Ishmukhametov, A. N. Russell, R. M. Berry, A modular platform for one-step assembly of multi-component membrane systems by fusion of charged proteoliposomes, *Nature Communications* **2016**, *7*(1), 1–10.

[277] P. Holloway, A simple procedure for removal of Triton X-100 from protein samples, *Analytical Biochemistry* **1973**, *53*(1), 304–308.

[278] P. S. Cheetham, Removal of Triton X-100 from aqueous solution using Amberlite XAD-2, *Analytical Biochemistry* **1979**, *92*(2), 447–452.

[279] C. Kleineberg, C. Wölfer, A. Abbasnia, D. Pischel, C. Bednarz, I. Ivanov, T. Heitkamp, M. Börsch, K. Sundmacher, T. Vidaković-Koch, Light-driven ATP regeneration in diblock/grafted hybrid vesicles, *ChemBioChem* **2020**, *21*(15), 2149–2160.

[280] K. Bacia, C. G. Schuette, N. Kahya, R. Jahn, P. Schwille, SNAREs Prefer Liquid-disordered over "Raft"(Liquid-ordered) Domains When Reconstituted into Giant Unilamellar Vesicles*[boxs], *Journal of Biological Chemistry* **2004**, *279*(36), 37951–37955.

[281] A. Witkowska, R. Jahn, Rapid SNARE-mediated fusion of liposomes and chromaffin granules with giant unilamellar vesicles, *Biophysical Journal* **2017**, *113*(6), 1251–1259.

[282] M. K. Doeven, J. H. Folgering, V. Krasnikov, E. R. Geertsma, G. van den Bogaart, B. Poolman, Distribution, lateral mobility and function of membrane proteins incorporated into giant unilamellar vesicles, *Biophysical Journal* **2005**, *88*(2), 1134–1142.

[283] L. S. Roach, H. Song, R. F. Ismagilov, Controlling nonspecific protein adsorption in a plug-based microfluidic system by controlling interfacial chemistry using fluorous-phase surfactants, *Analytical Chemistry* **2005**, *77*(3), 785–796.

[284] C. Beverung, C. J. Radke, H. W. Blanch, Protein adsorption at the oil/water interface: characterization of adsorption kinetics by dynamic interfacial tension measurements, *Biophysical Chemistry* **1999**, *81*(1), 59–80.

[285] I. Giaever, C. R. Keese, Behavior of cells at fluid interfaces, *Proceedings of the National Academy of Sciences* **1983**, *80*(1), 219–222.

[286] K. P. Johnston, T. Randolph, F. Bright, S. Howdle, Toxicology of a PFPE surfactant, *Science* **1996**, *272*(5269), 1726–1726.

[287] H.-J. Yoon, J. Y. Kang, B. Mikami, H. H. Lee, S. W. Suh, Crystal structure of phosphopantetheine adenylyltransferase from Enterococcus faecalis in the ligand-unbound state and in complex with ATP and pantetheine, *Molecules and Cells* **2011**, *32*(5), 431–435.

[288] N. Yandrapalli, J. Petit, O. Bäumchen, T. Robinson, Surfactant-free production of biomimetic giant unilamellar vesicles using PDMS-based microfluidics, *Communications Chemistry* **2021**, *4*(1), 1–10.

[289] D. T. Gonzales, N. Yandrapalli, T. Robinson, C. Zechner, T. D. Tang, Cell-Free Gene Expression Dynamics in Synthetic Cell Populations, *ACS Synthetic Biology* **2022**, *11*(1), 205–215.

A Appendix

A.1 List of Figures

A.2 List of Tables

A.3 Abbreviations and symbols

2ME	2-mercapto ethanol
6MH	6-mercapto-1-hexanol
A	absorbance
AC	alternating current
ADP	adenosine 5'-diphosphate
AMP	adenosine 5'-monophosphate
APS	ammonium persulfate
ATP	adenosine 5'-triphosphate
BLM	black lipid membrane
c	concentration
C_a	capillary number
CAD	computer-aided design
CF	correction factor
CHAPS	(3-((3-cholamidopropyl) dimethylammonio)-1-propane -sulfonate)
Chol	cholesterol
CLSM	confocal laser scanning microscopy
CMC	critical micelle concentration
CV	column volume
Cys	cysteine
D	diffusion coefficient
DDM	n-dodecyl-β-D-maltosid
DHPE	1,2-dihexadecanoyl-sn-glycerin-3-phosphoethanolamine
DiD	[1,1-Dioctadecyl-3,3,3,3-tetramethylindodicarbocyanine]
DMβCD	heptakis(2,6-di-O-methyl)-β-cyclodextrin
DOL	degree of labeling
DOPE	1,2-dioleoyl-sn-glycero-3-phosphoethanolamine
DOTAP	1,2-dioleoyl-3-trimethylammonium-propane
DPhPC	1,2-diphytanoyl-sn-glycero-3-phosphocholine
DPPE	1,2-dipalmitoyl-sn-glycero-3-phosphoethanolamine
dsGUV	droplet-stabilized GUV
DTT	dithiothreitol

E. coli	*Escherichia coli*
EDTA	ethylenediaminetetraacetic acid
F	fluorescence intensity
FCS	fluorescence correlation spectroscopy
FEM	finite element method
FRAP	fluorescence recovery after photobleaching
f-PSM	free-standing part of the PSM
g	gravity
GUV	giant unilamellar vesicle
$G(\tau)$	autocorrelation function
h	hour
HEPES	2-[4-(2-hydroxyethyl)piperazin-1-yl]ethanesulfonic acid
HPTS	trisodium 8-hydroxypyrene-1,3,6-trisulfonate
I_0, I_1	Bessel function of the 0th and 1st order
I	intensity
IMAC	immobilized metal ion affinity chromatography
IPTG	isopropyl β-D-1-thiogalactopyranosid
ITO	indium tin oxide
K	bleach depth
k_{B}	Boltzmann constant
L-α PC	L-α phosphatidylcholine
l	thickness (cuvette)
LB	lysogeny broth
LDAO	N,N-dimethyldodecan-1-amine N-oxide
Lp	solubility product
LUV	large unilamellar vesicle
m	reference slope
MES	2-(*N*-Morpholino)ethansulfonsäure
min	minute
MLV	multilamellar vesicle
n	amount of substance, sample number
$N_{(0)}$	particle number (in focus waist)
NA	numeric aperture

n_{r}	refractive index
n/n	ratio of substance amounts
nOG	n-octyl-β-D-glucoside
NTA	nitrilotriacetic acid
OD_{600}	optical density at 600 nm
OG488	OregonGreen 488
OT	octanthiol
P	permeability coefficient
p-lipid	phospholipid
PA	phosphatidic acid
PDB	protein data base
PDMS	polydimethylsiloxane
PEG	polyethylene glycol
PEO	poly (ethylene oxide)
PFO	1H,1H,2H,2H-perfluoro octanol
PFPE	perfluoropolyether
pH	negative decimal logarithm of proton concentration
pI	isoelectric point
pK_{a}	acid dissociation constant
p/l	protein to lipid ratio
pmf	proton motive force
PMT	photon multiplier tube
POPC	1-palmitoyl-2-oleoyl-sn-glycero-3-phosphocholin
POPG	1-palmitoyl-2-oleoyl-sn-glycero-3-phospho-rac-1-glycerol
POPS	1-palmitoyl-2-oleoyl-sn-glycero-3-phospho-L-serine
PPO	poly (propylene oxide)
PSF	point spread function
PSM	pore-spanning membrane
R	gas constant
$r_{\mathrm{e/n}}$	effective/nominal bleach radius
R_{e}	Reynolds number
$R_{\mathrm{GUV/LUV}}$	reconstitution efficiency in GUVs/LUVs
ROI	region of interest

rpm	rounds per minute
S_0, S_1	electronic states
SDS PAGE	sodium dodecyl sulfate polyacrylamide gel electrophoresis
SLB	supported lipid bilayer
s-PSM	solid-supported part of the PSM
surfactant	surface active agent
syb 2	synaptobrevin 2
t	time
T	temperature
TB	terrific broth
TCEP	Tris(2-carboxyethyl)phosphine hydrochloride
TEMED	tetramethyethylenediamine
TMD	transmembrane domain
Tris	tris(hydroxymethyl)aminomethane
Tx / Triton X-100	2-[4-(2,4,4-trimethylpentan-2-yl)phenoxy]ethanol
TxR	Texas Red
UV	ultraviolett
v/ v_{cat}	ATP synthesis rate/ turnover rate
val	valinomycin
val/l	valinomycin to lipid ratio
v/v	volume to volume
wt%	weight percent
w/v	weight to volume
w/w	weight to weight
γ	interfacial tension
Γ	excess surface concentration
ε	extinction coefficient
κ	bending modulus
λ	wavelength
μ	viscosity
ν	flow rate
ρ	fluid density
τ	lag time

$\tau_{1/2}$	half time of fluorescence recovery
τ_{D}	diffusion time
ψ	membrane potential
$\omega_{xy/z}$	radial and axial radii of the PSF

A.4 Chemicals and consumables

Chemicals

008-Fluorosurfactant (PFPE-PEG-PFPE)	Ran Biotechnologies, Beverly, USA
1-methoxy-2-propyl acetate	Sigma Aldrich, Taufkirchen, Germany
3-glycidyloxipropyl-trimethoxy-silane	Sigma Aldrich, Taufkirchen, Germany
6-mercapto-1-hexanol	Sigma Aldrich, Taufkirchen, Germany
ADP	Sigma Aldrich, Taufkirchen, Germany
ampicillin	Carl Roth GmbH, Karlsruhe, Germany
argon	Air Liquide Deutschland GmbH, Düsseldorf, Germany
ascorbic acid	Merck, Darmstadt, Germany
ATP	Sigma Aldrich, Taufkirchen, Germany
ATP Bioluminescence Kit CLSII	Sigma Aldrich, Taufkirchen, Germany
Atto390/488/655 DPPE/DOPE	Atto-tec, Siegen, Germany
Atto488 maleimide	Atto-tec, Siegen, Germany
Bio-Beads SM-2®	Bio-Rad Laboratories GmbH, München, Germany
Cap-biotin-DOPE	Avanti Polar Lipids, Alabaster, USA
CHAPS	Carl Roth GmbH, Karlsruhe, Germany
chloroform	VWR international, Darmstadt, Germany
cholesterol	Sigma Aldrich, Taufkirchen, Germany
Complete-mini, EDTA-free	Roche, Mannheim, Germany
DDM	Carl Roth GmbH, Karlsruhe, Germany
DMβDM	Sigma Aldrich, Taufkirchen, Germany
DTT	Carl Roth GmbH, Karlsruhe, Germany
DNase	Applichem, Darmstadt, Germany
EDTA	Carl Roth GmbH, Karlsruhe, Germany

ethanol	VWR international, Darmstadt, Germany
glucose	Sigma Aldrich, Taufkirchen, Germany
glycerol	Merck, Darmstadt, Germany
gold, 99.99 %	Allg. Gold- und Silberscheideanstalt, Pforzheim, Germany
$HClO_4$	Merck, Darmstadt, Germany
HEPES	Carl Roth GmbH, Karlsruhe, Germany
hexokinase	Merck, Darmstadt, Germany
imidazole	Sigma Aldrich, Taufkirchen, Germany
IPTG	Sigma Aldrich, Taufkirchen, Germany
isopropanol	Merck, Darmstadt, Germany
KCl	Merck, Darmstadt, Germany
KH_2PO_4	Sigma Aldrich, Taufkirchen, Germany
K_2HPO_4	Sigma Aldrich, Taufkirchen, Germany
Krytox (157 FSL)	Costenoble, Eschborn, Germany
LDAO	Sigma Aldrich, Taufkirchen, Germany
lysozyme	Merck, Darmstadt, Germany
MES	Merck, Darmstadt, Germany
methanol	VWR international, Darmstadt, Germany
$MgCl_2$	Merck, Darmstadt, Germany
NaCl	Merck, Darmstadt, Germany
NaH_2PO_4	Merck, Darmstadt, Germany
NaH_4MoO_4	Merck, Darmstadt, Germany
Na_3PO_4	Merck, Darmstadt, Germany
Neutravidin	Thermo Fisher Scientific, Waltham, USA
Ni-NTA	Qiagen GmbH, Venlo, Netherlands
nitrogen	Air Liquide Deutschland GmbH, Düsseldorf, Germany
nOG	Carl Roth GmbH, Karlsruhe, Germany
non-binding plates	Fisher Scientific, Hampton, USA
n-propanol	VWR international, Darmstadt, Germany
Nycodenz	Axis-shield Alere Technologies AS, Oslo, Norway

OG488 DHPE	Thermo Fisher Scientific, Waltham, USA
oil (HFE 7,500 3M)	Sigma Aldrich, Taufkirchen, Germany
oxygen	Air Liquide Deutschland GmbH, Düsseldorf, Germany
PDMS (Sylgard 184)	Farnell, Leeds, United Kingdom
perchloric acid	
Photoresist SU8 3050	Micro resist technology, Berlin, Germany
POPC, POPG, POPS	Avanti Polar Lipids, Alabaster, USA
pyranine	Fisher Scientific, Hampton, USA
SDS	AppliChem GmbH, Darmstadt, Germany
Sigmacoat®	Sigma Aldrich, Taufkirchen, Germany
SiO	Merck, Darmstadt, Germany
sodium cholate	Carl Roth GmbH, Karlsruhe, Germany
succinic acid	Carl Roth GmbH, Karlsruhe, Germany
sucrose	Acros Organics, New Jersey, USA
TALON Metal Affinity Resin	Clontech, Takara Bio Europe Saint-Germain-en-Laye, France
TCEP	Carl Roth GmbH, Karlsruhe, Germany
TxR DHPE	Sigma Aldrich, Taufkirchen, Germany
tryptone	Carl Roth GmbH, Karlsruhe, Germany
tricine	Carl Roth GmbH, Karlsruhe, Germany
Tris	Carl Roth GmbH, Karlsruhe, Germany
Triton™X-100	Merck, Darmstadt, Germany
valinomycin	Sigma Aldrich, Taufkirchen, Germany
yeast extract	Carl Roth GmbH, Karlsruhe, Germany

Consumables

MLCT cantilever	Bruker AFM Probes, Camarillo, USA
cover glass (22 × 22 mm)	VWR international, Darmstadt, Germany
glass slides	Fisher Scientific, Hampton, USA
ITO slides	Präzision Glas and Optic GmbH, Iserlohn, Germany

MonoQ 5/50 column	GE Healthcare Europe, Freiburg, Germany
MonoS 5/50 column	GE Healthcare Europe, Freiburg, Germany
NAP10/NAP25 column	GE Healthcare, Solingen, Germany
polycarbonate membrane	Avestin, Ottawa, Canada
porous substrates (1.2 μm & 5 μm)	Aquamarijn, Zutphen, Netherlands
PTFE tubes (0.12 x 0.3 mm)	Cole Parmer, Wertheim, Germany
puncher (0.75 mm)	Science Services, München, Germany
self adhesice copper stripe	Präzisions Glas & Optik GmbH, Iserlohn, Germany
teflon spacer	
wafer (silicon)	Active Business Company GmbH, Brunnthal, Germany
ZelluTrans® dialysis tubes	Carl Roth GmbH, Karlsruhe, Germany

A.5 Devices and software

Protein isolation

ÄKTA Purifier 10	GE Healthcare Europe, Freiburg, Germany
Centricon T-1065	Kontron Instruments, Rossdorf, Germany
centrifuge Allegra X22R	Beckmann Coulter, Krefeld, Germany
centrifuge Sigma 3K30	Sigma GmbH, Osterode, Harz, Germany
gel imager c300	Azure Biosystems, Dublin, USA
incubator Shaker Innova 44	New Brunswick Scientific, Enfield, USA
Microfluidizer LM 10	Microfluidics, Westwook, USA
Mini Protean gel system	Bio Rad Lab. GmbH, München, Germany
Nanodrop 2000c	Thermo Fisher Scientfic, Waltham, USA
power supply Power Pac 200	Bio Rad Lab. GmbH, München, Germany
Stuart tube roller SRT 6	Cole Parmer, Stone, USA
ThermoMix Compact	Eppendorf AG, Hamburg, Germany

Vesicle preparation

LiposoFast Basic	Avestin, Ottawa, Canada
frequency generator Agilent 3220A	Agilent Technologies, Santa Clara, USA
Varian Cary Scan 50	Varian, Darmstadt, Germany

Microfluidics

Axiovert 200 Zeiss	Carl Zeiss Microscopy, Thornwood, USA
Photron FASTCAM SA1.1	Photron, Reutlingen, Germany
pressure controller OB1 MK3+ system	Elveflow, Paris, France

Surface coating

Coating System MED020	Bal-Tec, Balzers, Lichtenstein
Sputtercoater 108 auto	Cressington Scientific Instruments, Watford, United Kingdom
Zepto plasma cleaner	Diener Electronics, Ebbhausen, Germany

Spectroscopy

Fluorescence spectrometer Jasco FP6500	JASCO, Easton, USA
Luminometer Centro LB 963	Berthold Technologies, Bad Wildbad, Deutschland

CLSM

FluoView 1200	Olympus, Tokyo, Japan
objective: LUMFLN 60XW, NA 1.1	Olympus, Tokyo, Japan
objective: LUMFLN 40X, NA 0.6	Olympus, Tokyo, Japan
SM 880 Examiner	Carl Zeiss Microscopy GmbH, Oberkochen, Germany
objective: 40X A Plan Apochromat, NA 1.0	Carl Zeiss Microscopy GmbH, Oberkochen, Germany

Software

COMSOL Multiphysics v4.4	COMSOL, Göttingen, Germany
FluoView 1200	Olympus, Tokyo, Japan
Gwyddion 2.45	http://gwyddion.net
ImageJ 1.52t	http://imagej.nih.gov/ij
JPK Data Processing	Instruments AG, Berlin, Germany
Matlab R2019b	Math Works, Natick, USA
OriginPro 8.5G	OriginLab Corporation, Northampton, USA
PyMOL	https://pymol.org/2/
Zen 2.3	Carl Zeiss Microscopy GmbH, Oberkochen, Germany

Miscelanous

Osmomat 030	Gonotec, Berlin, Germany
pH meter Calimatic 766	Knick, Berlin, Germany
thermomixer compact	Eppendorf,Hamburg, Germany

Ultrapure Water System	MilliQ Gradient A10 Merck Millipore, Darmstadt, Germany
Zetasizer NanoS	Malvern Instruments, Herrenberg, Germany

A.6 Determination of ATP synthase molecules per individual vesicle

In order to calculate the number of ATP synthase molecules N_{protein} per individual vesicle, the mean diameter of the vesicle (d_{LUV}, determined via DLS), the protein to lipid ratio (p/l, determined via flotation assay), the bilayer thickness h_{bilayer} as well as the areas of a single ATP synthase a_{protein} and a lipid a_{lipid} were needed. N_{protein} was calculated using equation A.1.

$$N_{\text{protein}} = N_{\text{lipid}} \frac{p}{l} \tag{A.1}$$

The number of lipids N_{lipid} can be determined from equation A.2 with A_{lipid} being the total area of lipids and A_{protein} being the total area of proteins. The outer surface area is defined by $A_{\text{out}} = \pi d_{\text{LUV}}^2$ while the inner surface area is calculated from $A_{\text{in}} = \pi(d_{\text{LUV}} - 2h_{\text{bilayer}})^2$.

$$N_{\text{lipid}} = \frac{A_{\text{lipid}}}{a_{\text{lipid}}} = \frac{A_{\text{out}} + A_{\text{in}} - A_{\text{protein}}}{a_{\text{lipid}}} \tag{A.2}$$

A_{protein} is determined from the area fraction χ as described in equation A.3 and A.4.

$$\chi = \frac{a_{\text{protein}}}{a_{\text{protein}} + (p/l)^{-1} a_{\text{lipid}}} \tag{A.3}$$

$$A_{\text{protein}} = \chi(\pi d_{\text{LUV}}^2 + \pi(d_{\text{LUV}} - 2h_{\text{bilayer}})^2) \tag{A.4}$$

All needed parameters are listed in the respected chapter.

A.7 Calculation of minimal lipid concentration for dsGUV formation

The mean diameter of produced droplets was found to be $50\,\mu\text{m}$ (cf. figure 4.3) and was assumed for the following equations. Volume V_{droplet} and surface area A_{droplet} of a droplet are given by equations A.5 and equations A.6.

$$V_{\text{droplet}} = \frac{4}{3}\pi r^3 = 6.5 \cdot 10^{-14}\text{m}^3 \tag{A.5}$$

$$A_{\text{droplet}} = 4\pi r^2 = 7.9 \cdot 10^{-9}\text{m}^2 \tag{A.6}$$

A mean average headgroup area of the used lipids was determined to be $a_{\text{lipid}} = 0.63\,\text{nm}^2$ for a lipid mixture of POPC/POPG/Chol (70/15/15).[177] Therefore, the amount of lipids required for the formation of a bilayer inside the spherical droplet ($r = 25\,\mu\text{m}$) can be determined by equation A.7.

$$N_{\text{lipid}} = 2\frac{A_{\text{droplet}}}{a_{\text{lipid}}} = 2.5 \cdot 10^{10} \tag{A.7}$$

The required minimal lipid concentration for covering the complete interface is

$$c = \frac{N_{\text{lipid}}}{V_{\text{droplet}} \cdot N_{\text{A}}} = 640\mu\text{M} \tag{A.8}$$

An excess of $40\,\%$ was added to compensate for a slight variation in the droplets diameter and a loss of lipid material during the process. Thus, lipid concentration of all experiments was adjusted to $1\,\text{mM}$ ($\sim 0.75\,\text{mg}\,\text{mL}^{-1}$). Since this is a significant excess, the concentration was maintained for experiments with POPS and various added lipid-coupled fluorophores and was assumed to be sufficient.

## A.8 Impact of valinomycin on vesicle acidification
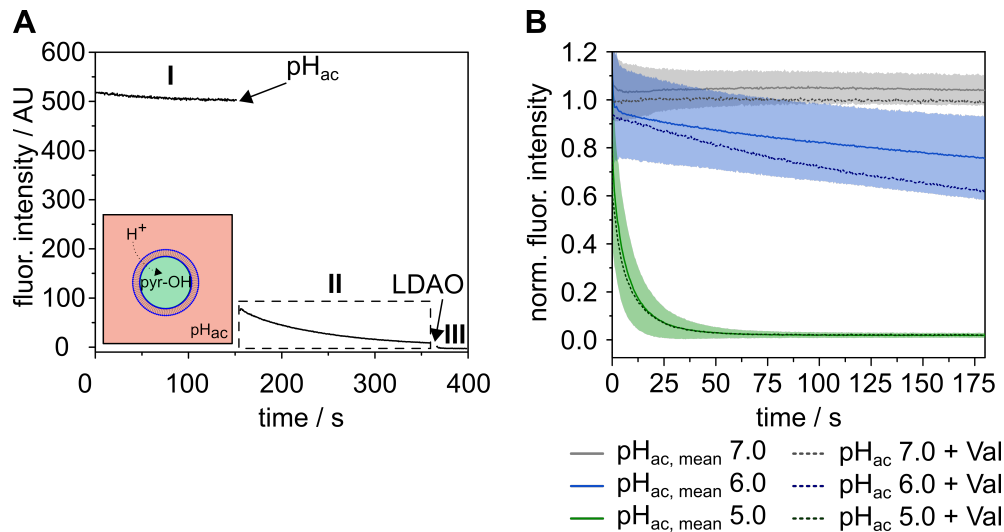
Figure A.1: Investigation of the acidification step of the ATP synthesis assay.
A: Typical fluorescence intensity curve of the acidification assay. The proton influx in LUVs (POPC, pH_{in} 8.0) as a function of external pH (pH_{ac} 5.8) was investigated using the pH sensitive fluorophore pyranine (500 μM). The addition of the acidification buffer A_{pH} led to a dilution ($DF = 5$) and subsequently an influx of protons in the lumen of the LUVs. The following addition of LDAO resulted in a release of the pyranine into the surrounding buffer. $\lambda_{ex/em} = 458/512$ nm. **B:** Acidification assay with pH 7.0 (grey), 6.0 (blue) and 5.0 (green) with (dashed line, $n = 1$) or without (continuous line, $n = 5$) valinomycin (val/l 1:40).

Vesicle acidification was performed analogously to chapter 4.3.1.2. Figure A.1 displays the normalized fluorescence intensity courses of assays with pH_{ac} of 7.0, 6.0 and 5.0 containing (dashed lines) and lacking valinomycin (continuous line, error band). Valinomycin was added in a valinomycin to lipid ratio (val/l) of 1:40, which is equivalent to the ratio used during the ATP synthesis assay. For varied pH values of the acidification buffers, measurements that were carried out in the presence of valinomycin, lay within the error range of measurements performed without valinomycin. The final normalized fluorescence intensity was extracted at $t = 180$ s (I_{180s}). While no reduction of fluorescence intensity was observed for $\Delta pH = 1$ (buffer $A_{7.0}$, $pH_{ac} = 7.0$), $\Delta pH = 2$ (buffer $A_{6.0}$, $pH_{ac} = 6.0$) led to a slow decrease, ending with final normalized fluorescence intensity I_{180s} of 0.75 ± 0.18 ($n = 5$) in the absence and 0.61 in the presence of valinomycin. After addition of LDAO the normalized intensity I_{LDAO} for $\Delta pH = 1$ dropped to 0.42 ± 0.36 (0.41 with

valinomycin) and for ΔpH $= 2$ to 0.11 ± 0.14 (0.03 with valinomycin). Measurements with ΔpH $= 3$ (buffer $A_{5.0}$, $pH_{ac} = 5.0$) triggered a fast drop of the normalized fluorescence intensity and a final normalized fluorescence intensity I_{180s} of 0.02 ± 0.01 ($n = 5$) and 0.03 when adding valinomycin, respectively. I_{LDAO} was found to be 0 with and without valinomycin.
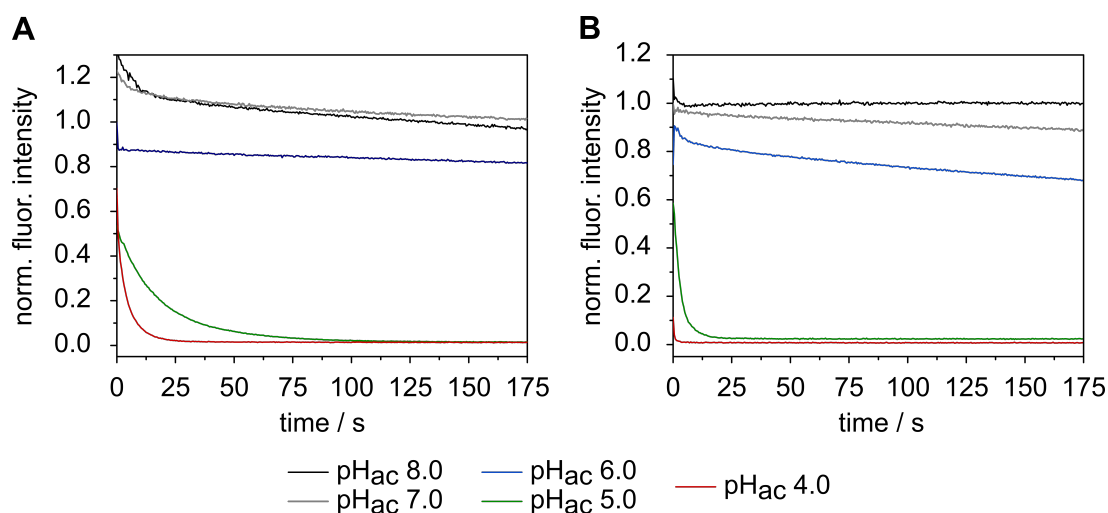
A.9 Impact of Triton™ X-100 on vesicle acidification
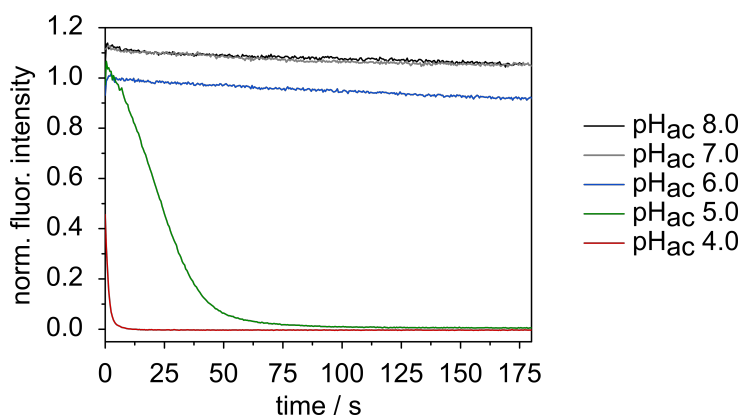
Figure A.2: Investigation of the acidification step of the ATP synthesis assay with Triton™ X-100 treated LUVs. Pyranine-filled LUVs ($d_{nom} = 100\,nm$, POPC) were treated with the reconstitution procedure as described in chapter 3.2.2.1. Addition of protein solution was replaced by a comparable volume of reconstitution buffer A (cf. chapter 3.1.1, table 3.1).

Pyranine-filled LUVs (POPC) were treated with the reconstitution procedure using Triton™ X-100 as described in chapter 3.2.2.1. Adding a defined volume of the protein solution was replaced by the same volume of buffer A (cf. chapter 3.1.1, table 3.1). Vesicle acidification assay was conducted analogously to chapter 4.3.1.2. Figure A.2 displays the normalized fluorescence intensity of pyranine as a function of time after addition of acidification buffer of differen pH_{ac} (8.0 to 4.0). Final normalized fluorescence intensities were extracted at $t = 180\,s$ and amounted to $I_{180s,8.0} = 1.1$, $I_{180s,7.0} = 1.0$, $I_{180s,6.0} = 0.92$, $I_{180s,5.0/4.0} \approx 0.0$. Thus, the final fluorescence intensities lay within the error range of measurements with detergent-free LUVs. Interestingly, the proton influx appears to be slowed down for Triton™ X-100 treated bilayers (in particular for $pH_{ac} = 5.0$). However, this may be attributed to either the increased diameter of Triton™ X-100-treated LUVs (cf. chapter 4.3.1.1, table 4.4) or to measurement artefacts as the shown data originate from single measurements.

A.10 Impact of the lipid composition on vesicle acidification

Figure A.3: Investigation of the acidification step of the ATP synthesis assay as a function of the lipid composition. Acidification assays were performed with pyranine-filled LUVs ($d_{nom} = 100\,\text{nm}$) composed of **A:** POPC/Chol (70/30, n/n) Chol and **B:** POPC/POPG (70/30, n/n). Data from at least three individual measurements were averaged for each curve.

Pyranine-filled LUVs composed of POPC/Chol (70/30, n/n) and POPC/POPG (70/30, n/n) were subjected to the vesicle acidification assay as described in chapter 4.3.1.4 by applying an outer pH_{ac} ranging from 8.0 to 4.0. Results were described in detail in chapter 4.3.1.4 and table 4.8.